

# IN-SITU MAGNESIUM BASED COMPOSITES - DEVELOPMENT AND TRIBOLOGICAL BEHAVIOUR

## A THESIS

*Submitted in partial fulfilment of the  
requirements for the award of the degree*

*of*

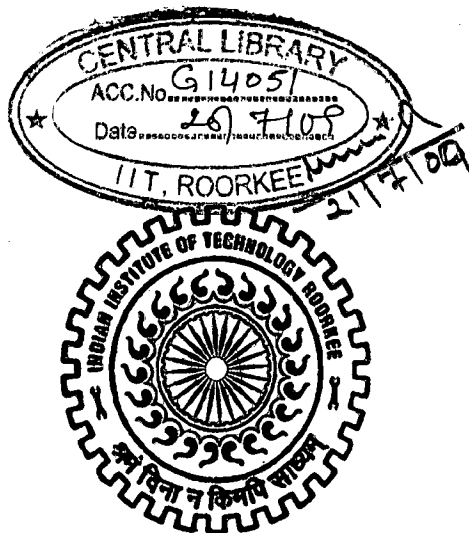
DOCTOR OF PHILOSOPHY

*in*

METALLURGICAL AND MATERIALS ENGINEERING

*By*

**SHIVALINGAPPA. D.**



DEPARTMENT OF METALLURGICAL AND MATERIALS ENGINEERING  
INDIAN INSTITUTE OF TECHNOLOGY ROORKEE  
ROORKEE-247 667 (INDIA)

AUGUST, 2007

**© INDIAN INSTITUTE OF TECHNOLOGY ROORKEE, ROORKEE, 2007  
ALL RIGHTS RESERVED**



# INDIAN INSTITUTE OF TECHNOLOGY ROORKEE ROORKEE

## CANDIDATE'S DECLARATION


I hereby certify that the work which is being presented in the thesis entitled **IN-SITU MAGNESIUM BASED COMPOSITES – DEVELOPMENT AND TRIBOLOGICAL BEHAVIOUR** in partial fulfilment of the requirements for the award of the degree of Doctor of Philosophy, submitted in the Department of Metallurgical and Materials Engineering, Indian Institute of Technology Roorkee, Roorkee is an authentic record of my own work carried out during a period from July 2004 to August 2007 under the supervision of Dr. Subrata Ray, Professor and Dr. B.S. Sundar Daniel, Asstt. Professor, Department of Metallurgical and Materials Engineering, Indian Institute of Technology Roorkee, Roorkee.

The matter embodied in this thesis has not been submitted by me for the award of any other degree of this or any other University/Institute.

  
(SHIVALINGAPPA. D.)

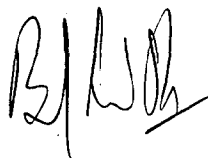
This is to certify that the above statement made by the candidate is correct to the best of our knowledge.

  
(Subrata Ray)  
Supervisor

  
(B.S. Sundar Daniel)  
Supervisor

Date: August 8, 2007

The Ph.D. Viva-Voce examination of **Mr. Shivalingappa. D.**, Research Scholar, has been held on 23.4.08.

   
Signature of Supervisors

  
Signature of External Examiner

# ABSTRACT

---

---

Particle reinforced cast metal matrix composites (PMMCs) result from solidification of a metal or alloy in the restricted spaces between the reinforcing phases. By carefully controlling the relative amounts and distributions of the ingredients constituting a composite and by controlling the solidification conditions, one may synergize the constituents to impart a tailored set of useful engineering properties that cannot be realized in conventional monolithic materials. In addition, the microstructure of the of the matrix is often refined and modified because of solidification in presence of the reinforcing particles, indicating the possibility of controlling micro-segregation, macro-segregation and grain size in the matrix.

PMMCs combine metallic properties (ductility and toughness) of the matrix with the characteristics of particle reinforcements, often leading to greater strength, higher wear resistance and higher elevated temperature properties. Stable properties at elevated temperatures require thermally stable reinforcements. In PMMC's where reinforcement is added externally, the resulting combination in *ex-situ* composite may not be thermodynamically stable at elevated temperatures. Over the last two decades, considerable research efforts have been directed towards the production of *in-situ* PMMCs, in which the reinforcements are formed *in-situ* in a metallic matrix by chemical reaction between the constituents during the fabrication of composites. Compared to conventional *ex-situ* PMMCs, the *in-situ* PMMCs exhibits the following advantages: (a) the *in-situ* formed reinforcements are thermodynamically stable and do not dissolve at higher temperature or do not generally have a reaction layer, thereby leading to less degradation during elevated-temperature services; (b) the *in-situ* generated reinforcements are finer in size and their distribution in the matrix is relatively more uniform, which may lead to better mechanical properties; and (c) the reinforcement-matrix interfaces are clean and uncontaminated which may result in good interfacial bonding, leading to higher ductility and toughness and also, improved wettability during melt processing.

The tribological behaviour of particulate composites depends mainly on the type, size and volume fraction of the reinforcing particles. Friction and wear in a material observed during its dry sliding against the counterface of another material depends on the nature, the extent and the strength of contact between the asperities of the mating surfaces. The hardness of the materials in dry sliding contact determines its extent. Higher hardness at the contact reduces the wear of the material significantly. Therefore, it is desirable to design the metal



matrix composites which contain hard *in-situ* formed reinforcing particles like alumina. Solidification processing offers a low cost route for synthesizing such *in-situ* composites but the resulting cast *in-situ* composite may often have significant porosity content. The impact of porosities on the tribological properties is of practical concern. However, these porosities may not necessarily be a handicap as they will provide space for storage of lubricants and improve the performance of these cast *in-situ* composites under lubricated conditions.

The rising oil prices compelled the automobile industries to look for better fuel economy and lighter vehicles which has opened the door to expanded usage of lightweight metal matrix composites. Weight saving in a vehicle reduces the requirement of the engine capacity for the same performance and thereby, results in better fuel economy. Therefore, the agenda of weight saving in a car is alive in the automobiles sector which is a high volume material consumer. Development of cast metal matrix composites, the cheapest material in its category, is primarily motivated by the interest of automobile industries which can afford its price range. It is perceived that composite materials are going to make a big difference in automobiles, particularly in view of escalating oil prices.

Engines including those used in automobiles have a number of bearings. In addition, there are components like valve seat/valve insert and gudgeon pin where tribological properties are important factors deciding their service life. By replacing the currently used denser alloy based components made of lead, tin, copper or iron by those made of lightweight materials, it is possible to achieve reduction in the weight of engines resulting in considerable fuel economy. Magnesium and its alloys being soft materials, may provide a suitable matrix of a composite for developing bearing by incorporation hard load bearing constituents in it. Recent efforts have led to the development of PMMCs with magnesium as matrix material, and borides, carbides, nitrides, oxides, silicides and their mixtures as second-phase particles.

Magnesium and its alloys, owing to their uniquely low density, good damping characteristics, dimensional stability and excellent machinability have become potential candidates for light-weight structural materials. It is easy to fabricate this metal and its alloys by a number of conventional techniques. The demand for magnesium alloys has increased rapidly owing to increased efforts by the automotive industry to adopt light-weight materials in order to achieve improved fuel economy and lower emission levels. The use of magnesium in automobile parts is predicted to increase globally at an average rate of 15% per year. As the usage of magnesium alloy components in automobiles and other energy saving applications increase, the demand also increased for further improvement of some the properties of these materials, such as high elastic modulus, hardness, wear resistance and

lower thermal coefficient of expansion etc. Chapter 1 presents the general context of the present investigation as explained above.

Literature review of the last two decades given in chapter 2 indicates that extensive research has been conducted on the development of *in-situ* composites. These studies show that the objectives for the synthesis of *in-situ* composites are to generate finer particles with cleaner interfaces, which has been achieved by many novel processing techniques developed. Synthesis of *in-situ* magnesium based composites has just been initiated and literature is sparse. Therefore, the present study has been undertaken to explore solidification processing of *in-situ* magnesium based composites with a new approach to inherit constituents of another composite or to initiate the reaction between the matrix alloy of magnesium and minor phase of another alloy. The aim of developing these composites is to employ them in components used in automobiles, particularly components having relative motion, and readily acceptable by the industry people from economical as well as product development and fabrication point of view.

In view of the gaps in the present state of knowledge of cast *in-situ* composites as outlined in literature review on cast *in-situ* magnesium based composites, the present study has been formulated with the following objectives:

1. To explore the feasibility of solidification synthesis of low cost magnesium alloy based *in-situ* composite via stir casting in such a way as to generate reinforcing intermetallics ( $\text{Al}_3\text{Ti}$ ,  $\text{Mg}_2\text{Si}$ ) and/or oxides particles (such as  $\text{Al}_2\text{O}_3$ ) *in-situ* from a different composite developed by addition of low cost metal oxide, such as titanium dioxide ( $\text{TiO}_2$ ) or the minor phase of silicon existing in an alloy.
2. To determine the influences of different key processing parameters like processing temperature and the amount of titanium dioxide ( $\text{TiO}_2$ )/silicon content in the constituent composite/alloy added to magnesium melt, on the evolution of microstructure and their impact on the mechanical properties of the resulting magnesium based cast *in-situ* composites.
3. To evaluate the tribological behaviour of the resulting cast *in-situ* composites including interaction between particle/intermetallic content and porosity in the context of dry sliding friction and wear properties.

The experimental procedure followed in the present investigation is given in chapter 3. Special purpose furnace has been designed and fabricated for the solidification processing of intended cast *in-situ* magnesium or magnesium alloy composites in inert atmosphere. Comprehensive experimental studies have been carried out to achieve the objectives outlined above, in order to enable and to identify the most promising combination of parameters in the context of mechanical and tribological properties.

maximum size up to 2  $\mu\text{m}$ . Formation of intermetallic,  $\text{Mg}_2\text{Si}$ , in another type of composite, cast *in-situ* Mg-Al/ $\text{Mg}_2\text{Si}$  composite, has been observed from the XRD pattern of the composite powder and further confirmed in the microstructures of *in-situ* composite through EDS analysis. In the cast *in-situ* Mg-Al/ $\text{Mg}_2\text{Si}$  composites, the intermetallic,  $\text{Mg}_2\text{Si}$ , occurs in blocky shapes with an average size of about 20  $\mu\text{m}$ .

In both the types of cast *in-situ* composites, relatively higher porosities are observed at the top than at the bottom of cast ingot and relatively higher volume fraction of intermetallics are observed at the bottom than at the top of cast ingots. It may be due to gravity segregation due to settling of intermetallics, being heavier than the matrix alloy. In the cast *in-situ* Mg-Al/ $\text{Mg}_2\text{Si}$  composites, the volume fraction of  $\text{Mg}_2\text{Si}$  and the porosity increases with increasing addition of silicon. Also, the porosity increases with increasing volume fraction of  $\text{Mg}_2\text{Si}$ .

In both the cast *in-situ* composites - Mg-Al/ $\text{Al}_3\text{Ti-Al}_2\text{O}_3$  and Mg-Al/ $\text{Mg}_2\text{Si}$ , Brinell hardness decreases gradually along the height of cast ingot from the bottom to top, which may be due to combined effect of decreasing reinforcing phases and increasing porosity along the height of cast ingot from the bottom to the top. Brinell hardness values for both the types of cast *in-situ* composites are significantly higher than those observed in cast Mg-9 wt% Al alloy and cast commercial magnesium. Brinell hardness decreases with increasing processing temperature in the cast *in-situ* Mg-Al/ $\text{Al}_3\text{Ti-Al}_2\text{O}_3$  composites, while, in case of the cast *in-situ* Mg-Al/ $\text{Mg}_2\text{Si}$  composites, Brinell hardness increases slightly with increasing processing temperature, however, at higher processing temperatures it decreases, which may be attributed to higher porosities. Brinell hardness increases with increasing reinforcing phases, for both the types of cast *in-situ* composites. In both the types of cast *in-situ* composites, comparatively better tensile properties (UTS and percentage elongation) are observed at the bottom than at the top of cast ingots where particle content is relatively more and porosity is less. In cast *in-situ* Mg-Al/ $\text{Mg}_2\text{Si}$  composites, both of the tensile properties, UTS and percent elongation increase initially but decreases at higher processing temperatures. While, in the case of cast *in-situ* Mg-Al/ $\text{Al}_3\text{Ti-Al}_2\text{O}_3$  composites, UTS increases with increasing processing temperature, but the percentage elongation show slightly decreasing trend with increasing processing temperature. In both the types of cast *in-situ* composites, both of the tensile properties, UTS and percent elongation, decrease with increasing porosity. In both the types of cast *in-situ* composites, lower values of tensile properties, UTS and percentage elongation, are observed over Mg-9 wt% Al alloy.

The results on tribological behaviour of both the cast *in-situ* composites as well as of cast commercial magnesium and Mg-9 wt% Al alloy are given in chapter 5 and it is observed that the cumulative volume loss increases linearly with increasing normal load for all these materials. In cast commercial magnesium, the wear rate initially increases gradually with increasing normal load but at higher loads it increases rapidly. In Mg-9 wt% Al alloy, the wear rate increases with increasing normal load. In both the types of cast *in-situ* composites, the wear rate increases with increasing normal load and at higher normal loads. In both the types of cast *in-situ* composites, the cumulative volume loss and wear rate decreases considerably, particularly at higher loads, compared to those observed in cast commercial magnesium and Mg-9 wt% Al alloy. In both the types of cast *in-situ* composites, the wear coefficient decreases gradually with increasing porosity. In both the cast *in-situ* composites containing similar porosity content, the wear rate decreases gradually and continuously with increasing reinforcing phase whereas the wear coefficient increases with increasing reinforcing phase. In cast *in-situ* Mg-Al/Al<sub>3</sub>Ti-Al<sub>2</sub>O<sub>3</sub> composites, the average value of coefficient of friction is slightly higher than those observed in cast Mg-9 wt% Al base alloy whereas its value for cast *in-situ* Mg-Al/Mg<sub>2</sub>Si composites is similar to those observed in cast Mg-9 wt% Al alloy. The coefficient of friction decreases with increasing normal load in both type of *in-situ* composites and Mg-9 wt% Al alloy and it decreases at a higher rate for lower loads than that at higher normal loads. The decreasing rate of coefficient of friction is relatively more for cast commercial magnesium and the coefficient of friction decreases from about 0.53 at 10 N to 0.27 at 40 N. In both type of *in-situ* composites and Mg-9 wt% Al alloy, there are large fluctuations in the coefficient of friction during sliding only at the lowest load, 10 N whereas large fluctuations in the coefficient of friction are observed at all the normal loads for cast commercial magnesium. From the examination of the worn surfaces of wear specimens and the debris, oxidative and abrasive wear mechanisms are observed in both the types of cast *in-situ* composites.

Finally, chapter 6 summarizes the conclusion of the present investigation.

# ACKNOWLEDGEMENTS

---

---

It is my great privilege and pleasure to record my heartiest thanks and deep sense of gratitude to my respected Guru, **Professor Subrata Ray**, for his valuable guidance and untiring efforts throughout the tenure of this work. He has been my inspiration and constant driving force when targets appeared to be difficult to achieve during the course of my PhD work. His timely help, constructive criticism, positive attitude, painstaking efforts, humanistic and warm personal approaches enabled me to compile the thesis in its present form. I also express my sincere gratitude and indebtedness to **Dr. B.S.S. Daniel**, for his invaluable guidance, cooperation, encouragement and providing all assistance to complete this work. His painstaking efforts in going through the manuscript, giving good suggestions for its improvement are gratefully acknowledged.

I am deeply indebted to Dr. S.K. Nath, Professor and Head of the Department of Metallurgical and Materials Engineering, Indian Institute of Technology Roorkee, for his help and providing the excellent facilities in the department for the research work. I wish to also record my gratitude to Dr. Satya Prakash, Dr. V.K. Tiwari and Dr. P.S. Misra, Professors and former Heads of Metallurgical and Materials Engineering dept. and The Head, Institute Instrumentation Centre (IIC), for their co-operation in providing excellent facilities during the entire course of my experimental work.

I wish to express my heartfelt gratitude to the Management and the Principal of Bapuji Institute of Engineering and Technology, Davangere for deputing me to IIT Roorkee to carry out my PhD work. I am also indebted to friends and staff of Bapuji Institute of Engineering and Technology, Davangere, who have to put in extra efforts. So that I could ensure my PhD work at IIT Roorkee. The financial support rendered by All India Council of Technical Education (AICTE) New Delhi under Quality Improvement Programme (QIP) through QIP centre, IITR, is gratefully acknowledged.

I wish to place on record my sincere thanks to the technical and administrative staff of the Department of Metallurgical and Materials Engineering, especially to Mr. Shamsheer Singh, Mr. Dharam Pal, Mr. S. K. Seth, Mr. Vidya Prakash, Mr. S. N. Kaushik, Mr. Shakti Gupta, Mr. Balesh Sharma, Mr. Rajinder Sharma, Mr. T. K. Sharma, Mr. R. K. Sharma, Mr. H.K. Ahuja, Mr. S.M. Giri, Mr. Y.K Goel, Mr. V. P. Verma, Mr. M. Aslam and Mr. Sanjay, who have helped in many ways during the course of my experimental work. Thanks are also

<b>2.5</b>	<b>Tribological Behaviour of Light Weight PMMCs</b>	<b>37</b>
2.5.1	Friction Behaviour	37
2.5.2	Dry Sliding Wear	41
2.5.3	Influence of Variables on Dry Sliding Wear	45
<b>2.6</b>	<b>Problem Formulation</b>	<b>52</b>
<i>Chapter 3</i>	<b>EXPERIMENTAL WORK</b>	<b>58</b>
<b>3.1</b>	<b>Design and Fabrication of Experimental Set-up</b>	<b>58</b>
<b>3.2</b>	<b>Selection of Stirrer</b>	<b>62</b>
<b>3.3</b>	<b>Solidification Processing of <i>In-Situ</i> Composites</b>	<b>62</b>
3.3.1	Materials for Processing of <i>In-Situ</i> Composites	62
3.3.2	Cast Mg-Al/Al <sub>3</sub> Ti-Al <sub>2</sub> O <sub>3</sub> <i>In-Situ</i> Composite	63
3.3.3	Cast Mg-Al/Mg <sub>2</sub> Si <i>In-Situ</i> Composite	68
3.3.4	Cast Mg-Al base alloy and commercial Mg	69
<b>3.4</b>	<b>Specimens Location</b>	<b>69</b>
<b>3.5</b>	<b>Chemical Analysis</b>	<b>71</b>
<b>3.6</b>	<b>X-Ray Diffraction Analysis</b>	<b>71</b>
<b>3.7</b>	<b>Microstructural Studies</b>	<b>72</b>
3.7.1	Optical Microscopy and Scanning Electron Microscopy (SEM)	72
3.7.2	Electron Probe Micro-Analysis (EPMA) and Energy Dispersive Spectroscopy (EDS)	72
<b>3.8</b>	<b>Estimation of Reinforcement Content</b>	<b>73</b>
3.8.1	Estimation of Oxide Particles	73
3.8.2	Estimation of Intermetallics	73
<b>3.9</b>	<b>Estimation of Porosity Content</b>	<b>74</b>
<b>3.10</b>	<b>Studies on Mechanical Properties</b>	<b>75</b>
3.10.1	Hardness Testing	75
3.10.2	Tensile Testing	75
<b>3.11</b>	<b>Wear and Friction Testing</b>	<b>76</b>

**Processing, Microstructural Studies  
and Mechanical Properties of  
Cast *In-Situ* Composites**

78

<b>4.1</b>	<b>Structural Characterization of Cast <i>In-Situ</i> Mg- Al/Al<sub>3</sub>Ti-Al<sub>2</sub>O<sub>3</sub> Composites</b>	78
4.1.1	X-ray Diffraction Analysis	78
4.1.2	Microstructural Studies	79
	(a) <i>Influence of Amount of TiO<sub>2</sub> Particles Addition</i>	83
	(b) <i>Influence of Processing Temperature</i>	90
4.1.3	Mechanical Properties of Cast <i>In-Situ</i> Mg- Al/Al <sub>3</sub> Ti-Al <sub>2</sub> O <sub>3</sub> Composites	90
	(a) <i>Hardness Measurement</i>	91
	(b) <i>Tensile Properties</i>	96
4.1.4	Fractography	
<b>4.2</b>	<b>Structural Characterization of Cast <i>In-Situ</i> Mg-Al/Mg<sub>2</sub>Si Composites</b>	105
4.2.1	X-ray Diffraction Analysis	105
4.2.2	Microstructural Studies	105
	(a) <i>Influence of Amount of Si Particles Addition</i>	111
	(b) <i>Influence of Processing Temperature</i>	111
4.2.3	Mechanical Properties of Cast <i>In-Situ</i> Mg-Al/ Mg <sub>2</sub> Si Composites	121
	(a) <i>Hardness Measurement</i>	121
	(b) <i>Tensile Properties</i>	121
4.2.4	Fractography	122
<b>4.3</b>	<b>Discussion</b>	128

<b>Fig. 4.2</b>	SEM/EDS point analysis of a cast <i>in-situ</i> Mg-Al/Al <sub>3</sub> Ti-Al <sub>2</sub> O <sub>3</sub> composite designated as MT14/80 at various locations; (a) spot 1, (b) spot 2, (c) spot 3, (d) spot 4 and (e) spot 5.	81
<b>Fig. 4.3</b>	(a) SEM micrograph and (b) distribution of various elements of a cast <i>in-situ</i> Mg-Al/Al <sub>3</sub> Ti-Al <sub>2</sub> O <sub>3</sub> composite designated as MT12/85; the label (1) indicates the intermetallic phase, Al <sub>3</sub> Ti, (2) the oxide particle, Al <sub>2</sub> O <sub>3</sub> and (3) the β-phase, Al <sub>12</sub> Mg <sub>17</sub> .	84
<b>Fig. 4.4</b>	SEM micrograph and EDS X-ray mapping for various elements of a cast <i>in-situ</i> Mg-Al/Al <sub>3</sub> Ti-Al <sub>2</sub> O <sub>3</sub> composite designated as MT14/80.	85
<b>Fig. 4.5</b>	Typical optical micrograph of cast Al-based composite of nominal composition of Al(5%Mg)-10%TiO <sub>2</sub> processed at 940 °C; the label (1) indicates the intermetallics, Al <sub>3</sub> Ti and (2) the oxide.	86
<b>Fig. 4.6</b>	a) Lower and (b) higher magnification optical micrographs of a cast <i>in-situ</i> Mg-Al/Al <sub>3</sub> Ti-Al <sub>2</sub> O <sub>3</sub> composite designated as MT12/80; the label (1) indicates the intermetallics, Al <sub>3</sub> Ti, (2) the oxide and (3) the β-phase, Al <sub>12</sub> Mg <sub>17</sub> .	86
<b>Fig. 4.7</b>	Lower and higher magnification optical micrographs of a cast <i>in-situ</i> Mg-Al/Al <sub>3</sub> Ti-Al <sub>2</sub> O <sub>3</sub> composite designated as MT12/80; at the bottom (a) & (b), the middle (c) & (d) and the top (e) & (f).	87
<b>Fig. 4.8</b>	Optical micrographs of cast Al-based composites synthesized at 940 °C with different nominal composition of TiO <sub>2</sub> particles; (a) 8 wt% (b) 10 wt% (c) 12 wt% and (d) 14 wt%.	88
<b>Fig. 4.9</b>	SEM micrographs of different cast <i>in-situ</i> Mg-Al/Al <sub>3</sub> Ti-Al <sub>2</sub> O <sub>3</sub> composites developed by increasing amounts of TiO <sub>2</sub> particles, respectively 10, 12 and 14 wt% and designated as; (a) & (b) MT10/80, (c) & (d) MT12/80 and (e) & (f) MT14/80; at lower and higher magnification.	89
<b>Fig. 4.10</b>	The variation of amount of reinforcing particles extracted at the bottom, the middle and the top of cast ingots of cast <i>in-situ</i> Mg-Al/Al <sub>3</sub> Ti-Al <sub>2</sub> O <sub>3</sub> composites with amount of TiO <sub>2</sub> particles added.	92



<b>Fig. 4.11</b>	The variation of porosity at the bottom, the middle and the top of cast ingots of cast <i>in-situ</i> Mg-Al/Al <sub>3</sub> Ti-Al <sub>2</sub> O <sub>3</sub> composites with amount of TiO <sub>2</sub> particles added.	92
<b>Fig. 4.12</b>	The variation of difference in weight fraction extracted particles at the top and bottom of cast ingot of <i>in-situ</i> Mg-Al/Al <sub>3</sub> Ti-Al <sub>2</sub> O <sub>3</sub> composites with varying amounts of TiO <sub>2</sub> particles.	93
<b>Fig. 4.13</b>	The variation of porosity with amount of particles extracted at the bottom, the middle and the top of cast ingot of <i>in-situ</i> Mg-Al/Al <sub>3</sub> Ti-Al <sub>2</sub> O <sub>3</sub> composites.	93
<b>Fig. 4.14</b>	Optical micrographs of cast Al-based composites developed using 10 wt% TiO <sub>2</sub> particles at different processing temperatures; (a) 800 °C and (b) 1040 °C.	94
<b>Fig. 4.15</b>	SEM micrographs of different cast <i>in-situ</i> Mg-Al/Al <sub>3</sub> Ti-Al <sub>2</sub> O <sub>3</sub> composites developed by varying the processing temperature, respectively, 750, 800 and 850 °C and designated as; (a) & (b) MT12/75, (c) & (d) MT12/80 and (e) & (f) MT12/85; at lower and higher magnification.	95
<b>Fig. 4.16</b>	Brinell hardness measurement along the height from the bottom to top of cast ingot of a <i>in-situ</i> Mg-Al/Al <sub>3</sub> Ti-Al <sub>2</sub> O <sub>3</sub> composite designated as MT12/80.	98
<b>Fig. 4.17</b>	The variation in hardness with processing temperature for cast <i>in-situ</i> Mg-Al/Al <sub>3</sub> Ti-Al <sub>2</sub> O <sub>3</sub> composite, synthesized using cast Al-based composite developed with 12 wt% TiO <sub>2</sub> .	98
<b>Fig. 4.18</b>	The variations of hardness with (a) amount of extracted particles and (b) amount of intermetallics, Al <sub>3</sub> Ti, for cast <i>in-situ</i> Mg-Al/Al <sub>3</sub> Ti-Al <sub>2</sub> O <sub>3</sub> composites, synthesized at 800 °C using cast Al-based composites processed with different amounts of TiO <sub>2</sub> particles.	99
<b>Fig. 4.19</b>	Comparison between average Brinell hardness for cast <i>in-situ</i> Mg-Al/ Al <sub>3</sub> Ti-Al <sub>2</sub> O <sub>3</sub> composite containing 2.14 ± 0.43 wt% extracted particles and 1 vol% porosity, cast Mg-9 wt% Al alloy containing 0.6 vol% porosity and cast commercially pure Mg containing 0.2 vol% porosity.	99

<b>Fig. 4.20</b>	The comparison between tensile properties for the three segments, the bottom, middle and top, of a cast <i>in-situ</i> Mg-Al/Al <sub>3</sub> Ti-Al <sub>2</sub> O <sub>3</sub> composite designated as MT8/80.	100
<b>Fig. 4.21</b>	The variation of tensile properties with processing temperature for cast <i>in-situ</i> Mg-Al/Al <sub>3</sub> Ti-Al <sub>2</sub> O <sub>3</sub> composite, synthesized using cast Al-based composite developed with 12 wt%TiO <sub>2</sub> particles.	100
<b>Fig. 4.22</b>	Effect of porosity content on ln( $\sigma_{ut}$ ) for cast <i>in-situ</i> Mg-Al/Al <sub>3</sub> Ti-Al <sub>2</sub> O <sub>3</sub> composites.	101
<b>Fig. 4.23</b>	Variation of weakening factor, $\alpha$ , with particle content for the cast <i>in-situ</i> Mg-Al/Al <sub>3</sub> Ti-Al <sub>2</sub> O <sub>3</sub> composites.	102
<b>Fig. 4.24</b>	Effect of particle content on the tensile strength at zero porosity for cast <i>in-situ</i> Mg-Al/Al <sub>3</sub> Ti-Al <sub>2</sub> O <sub>3</sub> composites.	102
<b>Fig. 4.25</b>	Effect of porosity content on ln(percentage elongation) for cast <i>in-situ</i> Mg-Al/Al <sub>3</sub> Ti-Al <sub>2</sub> O <sub>3</sub> composites.	103
<b>Fig. 4.26</b>	Effect of particle content on the percentage elongation at zero porosity for cast <i>in-situ</i> Mg-Al/Al <sub>3</sub> Ti-Al <sub>2</sub> O <sub>3</sub> composites.	103
<b>Fig. 4.27</b>	The variation of ultimate tensile strength with porosity content for cast <i>in-situ</i> Mg-Al/Al <sub>3</sub> Ti-Al <sub>2</sub> O <sub>3</sub> composite containing $1.74 \pm 0.24$ wt% particles and $1.08 \pm 0.16$ vol% intermetallics (Al <sub>3</sub> Ti).	106
<b>Fig. 4.28</b>	The variation of percentage elongation with porosity content for cast <i>in-situ</i> Mg-Al/Al <sub>3</sub> Ti-Al <sub>2</sub> O <sub>3</sub> composite containing $1.74 \pm 0.24$ wt% particles and $1.08 \pm 0.16$ vol% intermetallics (Al <sub>3</sub> Ti).	106
<b>Fig. 4.29</b>	SEM fractographs showing tensile fracture surfaces at magnification, 1000X; (a) and (b) cast <i>in-situ</i> Mg-Al/Al <sub>3</sub> Ti-Al <sub>2</sub> O <sub>3</sub> composites containing 1.45 and 1.64 wt% of reinforcing particles, and 0.7 and 2.4 vol% porosities respectively, (c) cast Mg-9 wt% Al alloy containing 0.3 vol% porosity and (d) cast commercial magnesium containing 0.1 vol% porosity.	107
<b>Fig. 4.30</b>	Powder X-ray diffraction patterns of (a) cast <i>in-situ</i> Mg-Al/Mg <sub>2</sub> Si composite, synthesized using Al-20 wt% Si master alloy, at processing temperature of 760 °C, designated as MS20/76 and (b) cast Mg-9 wt% Al alloy.	108

<b>Fig. 4.31</b>	Powder X-ray diffraction pattern of cast Al-15 wt% Si master alloy, processed at temperature, 920 °C.	108
<b>Fig. 4.32</b>	Powder X-ray diffraction patterns of cast <i>in-situ</i> Mg-Al/Mg <sub>2</sub> Si composites synthesized, at 760 °C using Al-Si master alloys containing respectively 9, 15 and 20 wt% Si and designated as MS9/76, MS15/76 and MS20/76.	109
<b>Fig. 4.33</b>	SEM/EDS point analysis of <i>in-situ</i> Mg-Al/Mg <sub>2</sub> Si composite synthesized, using Al-20 wt% Si master alloy, at processing temperature of 760 °C at various locations; (a) spot 1, (b) spot 2, (c) spot 3, (d) spot 4.	112
<b>Fig. 4.34</b>	The distributions of magnesium, aluminium and silicon across the matrix alloy and the intermetallics, Mg <sub>2</sub> Si in the cast <i>in-situ</i> Mg-Al/Mg <sub>2</sub> Si composite, synthesized at processing temperature of 760 °C using Al-20 wt% Si master alloy ; the label (1) indicates the intermetallic phase, Mg <sub>2</sub> Si, (2) the β-phase, Al <sub>12</sub> Mg <sub>17</sub> , (3) α-Mg and (4) the spinel, MgAl <sub>2</sub> O <sub>4</sub> .	113
<b>Fig. 4.35</b>	SEM micrograph and EDS X-ray mapping for various elements of <i>in-situ</i> Mg-Al/Mg <sub>2</sub> Si composite synthesized, at processing temperature of 760 °C using Al-20 wt% Si master alloy.	114
<b>Fig. 4.36</b>	Typical optical micrograph of cast Al-15 wt% Si master alloy, processed at 930 °C; the label (1) indicates silicon needles.	115
<b>Fig. 4.37</b>	a) Lower and (b) higher magnification optical micrographs of cast Mg-Al/Mg <sub>2</sub> Si <i>in-situ</i> composite synthesized at 760 °C using Al-15wt%Si master alloy; the label (1) indicates the intermetallics, Mg <sub>2</sub> Si and (2) the β-phase, Al <sub>12</sub> Mg <sub>17</sub> .	115
<b>Fig. 4.38</b>	Lower and higher magnification optical micrographs of cast <i>in-situ</i> Mg-Al/ Mg <sub>2</sub> Si composite synthesized, at 800 °C using cast Al-15wt%Si master alloy; at the bottom (a) & (b), the middle (c) & (d) and the top (e) & (f).	116
<b>Fig. 4.39</b>	Optical micrographs of cast Al-Si master alloys synthesized at 930 °C with different nominal composition of silicon metal particles; (a) 9 wt% Si, (b) 15 wt% Si, and (c) 20 wt% Si.	117

<b>Fig. 4.40</b>	SEM micrographs of cast <i>in-situ</i> Mg-Al/Mg <sub>2</sub> Si composite, synthesized at 760 °C using cast Al-Si master alloy with different amount of silicon content; (a) 9 wt% Si, (c) 15 wt% Si, (e) 20 wt% Si and at lower magnification; (b) 9 wt% Si, (d) 15 wt% Si, and (f) 20 wt% Si at higher magnification.	118
<b>Fig. 4.41</b>	The variation of amount of <i>in-situ</i> generated reinforcement, Mg <sub>2</sub> Si, and porosity content for the middle segments of cast ingots of <i>in-situ</i> Mg-Al/Mg <sub>2</sub> Si composites with amount of silicon added.	119
<b>Fig. 4.42</b>	The variation of amount of porosity with <i>in-situ</i> generated reinforcement, Mg <sub>2</sub> Si, for the middle segments of cast ingots of <i>in-situ</i> Mg-Al/Mg <sub>2</sub> Si composites.	119
<b>Fig. 4.43</b>	SEM micrographs of cast <i>in-situ</i> Mg-Al/Mg <sub>2</sub> Si composites, synthesized using cast Al-15wt%Si master alloy at different processing temperatures; (a) 720 °C, (b) 760 °C and (c) 800 °C.	120
<b>Fig. 4.44</b>	The variation of hardness with normalized location ( <i>h/H</i> ) along the height of cast ingot of <i>in-situ</i> Mg-Al/Mg <sub>2</sub> Si composite, synthesized at 760 °C using cast Al-15 wt% Si master alloy.	123
<b>Fig. 4.45</b>	The variation of hardness with processing temperature for cast <i>in-situ</i> Mg-Al/Mg <sub>2</sub> Si composite, synthesized using cast Al-15 wt% Si master alloy.	123
<b>Fig. 4.46</b>	The variation of hardness with reinforcement, Mg <sub>2</sub> Si for cast <i>in-situ</i> Mg-Al/Mg <sub>2</sub> Si composites, synthesized at 760 °C using different cast Al-Si master alloys.	124
<b>Fig. 4.47</b>	Comparison between average Brinell hardness for cast <i>in-situ</i> Mg-Al/ Mg <sub>2</sub> Si composite containing 6.54 ± 0.76 vol% reinforcement and 1.7 vol% porosity, designated as MS20/76, cast Mg-Al alloy containing 0.6 vol% porosity and cast commercially pure Mg containing 0.2 vol% porosity.	124
<b>Fig. 4.48</b>	The comparison between tensile properties for the three segments of the cast <i>in-situ</i> Mg-Al/Mg <sub>2</sub> Si composite, synthesized at 760 °C using cast Al-9 wt% Si master alloy.	125

<b>Fig. 4.49</b>	The variation of tensile properties with processing temperature for cast <i>in-situ</i> Mg-Al/Mg <sub>2</sub> Si composite, synthesized using cast Al-15 wt% Si master alloy.	125
<b>Fig. 4.50</b>	The variation of ultimate tensile strength with porosity content for cast <i>in-situ</i> Mg-Al/Mg <sub>2</sub> Si composite containing 4.52 ± 0.64 vol% reinforcement, Mg <sub>2</sub> Si.	126
<b>Fig. 4.51</b>	The variation of percentage elongation with porosity content for cast <i>in-situ</i> Mg-Al/Mg <sub>2</sub> Si composite containing 4.52 ± 0.64 vol% reinforcement, Mg <sub>2</sub> Si.	126
<b>Fig. 4.52</b>	Effect of particle content on the ultimate tensile strength at zero porosity of cast <i>in-situ</i> Mg-Al/Mg <sub>2</sub> Si composites.	127
<b>Fig. 4.53</b>	Effect of particle content on the percentage elongation at zero porosity of cast <i>in-situ</i> Mg-Al/ Mg <sub>2</sub> Si composites.	127
<b>Fig. 4.54</b>	SEM fractographs showing tensile fracture surfaces; (a) and (b) cast <i>in-situ</i> Mg-Al/Mg <sub>2</sub> Si composites containing 2.43 and 4.12 wt% of reinforcing particles, and 0.6 and 2.3 vol% porosities respectively and (c) cast Mg-9 wt% Al base alloy containing 0.5 vol% porosity.	130
<b>Fig. 5.1</b>	The variation of cumulative volume loss with sliding distance at different normal loads of 10, 20, 30 and 40 N and sliding speed of 1 m/s for the bottom, middle and top segments of cast ingots of the following <i>in-situ</i> Mg-Al/Al <sub>3</sub> T-Al <sub>2</sub> O <sub>3</sub> composites: (a) MT8/80, (b) MT10/80, (c) MT12/80, (d) MT14/80, (e) MT12/75 and (f) MT12/85.	142
<b>Fig. 5.2</b>	The variation of cumulative volume loss with sliding distance at different normal loads of 10, 20, 30 and 40 N and sliding speed of 1 m/s for the bottom, middle and top segments of cast ingots of (a) commercial magnesium and (b) Mg-9 wt% Al alloy.	145
<b>Fig. 5.3</b>	A comparison of cumulative volume loss after dry sliding for 3000 m for the middle segments of cast ingots of <i>in-situ</i> composite, MT14/85, containing 2.45 wt% reinforcing particles and 1 vol% porosity, cast Mg-9 wt% Al alloy and cast commercial magnesium under similar load and sliding conditions.	148

<b>Fig. 5.4</b>	The variation of wear rate with normal load for the middle segments of cast ingots of <i>in-situ</i> composite, MT14/80, containing 2.45 wt% reinforcing particles and 1 vol% porosity, cast Mg-9 wt% Al alloy and cast commercial magnesium.	148
<b>Fig. 5.5</b>	The variation of wear rate with normal load for the bottom, middle and top segments of cast ingots of different <i>in-situ</i> Mg-Al/Al <sub>3</sub> Ti-Al <sub>2</sub> O <sub>3</sub> composites: (a) MT8/80, (b) MT10/80, (c) MT12/80, (d) MT14/80, (e) MT12/75 and (f) MT12/85.	150
<b>Fig. 5.6</b>	The variation of wear rate with porosity content for cast <i>in-situ</i> Mg-Al/Al <sub>3</sub> Ti-Al <sub>2</sub> O <sub>3</sub> composites containing reinforcing particles varying over a limited range of (a) 1.55 ± 0.2 wt%, (b) 1.98 ± 0.2 wt% and (c) 2.52 ± 0.26 wt%.	151
<b>Fig. 5.7</b>	The variation of wear rate with particle content for cast <i>in-situ</i> Mg-Al/Al <sub>3</sub> Ti-Al <sub>2</sub> O <sub>3</sub> composites containing porosity varying over a limited range of (a) 0.8 ± 0.2 vol%, (b) 1.2 ± 0.2 vol% and (c) 1.6 ± 0.2 vol%.	152
<b>Fig. 5.8</b>	The variation of wear coefficient with porosity content for cast <i>in-situ</i> Mg-Al/Al <sub>3</sub> Ti-Al <sub>2</sub> O <sub>3</sub> composites containing reinforcing particles varying over a limited range of (a) 1.55 ± 0.2 wt%, (b) 1.98 ± 0.2 wt% and (c) 2.52 ± 0.26 wt%.	153
<b>Fig. 5.9</b>	The variation of wear coefficient with particle content for cast <i>in-situ</i> Mg-Al/Al <sub>3</sub> Ti-Al <sub>2</sub> O <sub>3</sub> composites containing porosity varying over a limited range of (a) 0.76 ± 0.15 vol%, (b) 1.15 ± 0.2 vol% and (c) 1.56 ± 0.2 vol%.	154
<b>Fig. 5.10</b>	The variation of cumulative volume loss with sliding distance at different normal loads of 10, 20, 30 and 40 N and sliding speed of 1 m/s for the bottom, middle and top segments of cast ingots of the following <i>in-situ</i> Mg-Al/Mg <sub>2</sub> Si composites: (a) MS9/76, (b) MS15/76, (c) MS20/76, (d) MS15/72 and (e) MS15/80.	159
<b>Fig. 5.11</b>	A comparison of cumulative volume loss after dry sliding for 3000 m for the middle segments of cast ingots of <i>in-situ</i> Mg-Al/Mg <sub>2</sub> Si composite containing 6.54 vol% reinforcement (Mg <sub>2</sub> Si) and 1.685 vol% porosity, cast Mg-9 wt% Al alloy and cast commercial magnesium under similar load and sliding conditions.	159

- Fig. 5.12** The variation of wear rate with normal load for the middle segments of cast ingots of *in-situ* Mg-Al/Mg<sub>2</sub>Si composite, designated as MS20/76, containing 6.54 vol% reinforcement and 1.7 vol% porosity, cast Mg-9 wt% Al alloy and cast commercial magnesium. 160
- Fig. 5.13** The variation of wear rate with normal load for the bottom, middle and top segments of cast ingots of different *in-situ* Mg-Al/Mg<sub>2</sub>Si composites: (a) MS9/76, (b) MS15/76, (c) MS20/76, (d) MS15/72 and (e) MS15/80. 161
- Fig. 5.14** The variation of wear rate with porosity content for cast *in-situ* Mg-Al/Mg<sub>2</sub>Si composites containing reinforcing particles varying over a limited range of (a)  $2.4 \pm 0.04$  wt% and (b)  $4.64 \pm 0.52$  wt%. 162
- Fig. 5.15** The variation of wear rate with particle content for cast *in-situ* Mg-Al/Mg<sub>2</sub>Si composites containing porosity varying over a limited range of (a)  $0.8 \pm 0.3$  vol% and (b)  $1.8 \pm 0.3$  vol%. 162
- Fig. 5.16** The variation of wear coefficient with porosity content for cast *in-situ* Mg-Al/Mg<sub>2</sub>Si composites containing reinforcing particles varying over a limited range of (a)  $2.44 \pm 0.04$  vol% and (b)  $4.64 \pm 0.2$  vol%. 165
- Fig. 5.17** The variation of wear coefficient with particle content for cast *in-situ* Mg-Al/Mg<sub>2</sub>Si composites containing porosity varying over a limited range of (a)  $0.8 \pm 0.3$  vol% and (b)  $1.8 \pm 0.3$  vol%. 165
- Fig. 5.18** The variation of coefficient of friction with sliding distance at different normal loads of 10, 20, 30 and 40 N and sliding speed of 1 m/s for the following *in-situ* Mg-Al/Al<sub>3</sub>T-Al<sub>2</sub>O<sub>3</sub> composites: (a) MT8/80, (b) MT10/80, (c) MT12/80, (d) MT14/80, (e) MT12/75 and (f) MT12/85. 167
- Fig. 5.19** The variation of coefficient of friction loss with sliding distance at different normal loads of 10, 20, 30 and 40 N and sliding speed of 1 m/s for (a) cast commercial magnesium and (b) cast Mg-9 wt% Al alloy. 167

<b>Fig. 5.20</b>	The variation of average coefficient of friction with normal load at sliding speed of 1 m/s for different cast <i>in-situ</i> Mg-Al/Al <sub>3</sub> Ti-Al <sub>2</sub> O <sub>3</sub> composites containing reinforcing particle and porosity contents respectively given in the legend of the figure.	168
<b>Fig. 5.21</b>	The variation of average coefficient of friction with normal load at sliding speed of 1 m/s for cast commercial magnesium and cast Mg-9 wt% Al alloy.	168
<b>Fig. 5.22</b>	The variation of coefficient of friction with sliding distance at different normal loads of 10, 20, 30 and 40 N and sliding speed of 1 m/s for the following <i>in-situ</i> Mg-Al/Mg <sub>2</sub> Si composites: (a) MS9/76, (b) MS15/76, (c) MS20/76, (d) MS15/72 and (e) MS15/80.	172
<b>Fig. 5.23</b>	The variation of average coefficient of friction with normal load at sliding speed of 1 m/s for different cast <i>in-situ</i> Mg-Al/Mg <sub>2</sub> Si composites containing reinforcement, Mg <sub>2</sub> Si, and porosity contents respectively given in the legend of the figure.	172
<b>Fig. 5.24</b>	X-ray diffraction pattern for wear debris generated during dry sliding wear of (a) cast <i>in-situ</i> Mg-Al/Al <sub>3</sub> Ti-Al <sub>2</sub> O <sub>3</sub> composite (b) cast <i>in-situ</i> Mg-Al/Mg <sub>2</sub> Si composite.	173
<b>Fig. 5.25</b>	Optical micrographs of typical samples of wear debris generated during dry sliding of pin samples of (a) cast <i>in-situ</i> Mg-Al/Al <sub>3</sub> Ti-Al <sub>2</sub> O <sub>3</sub> composite (b) cast <i>in-situ</i> Mg-Al/Mg <sub>2</sub> Si composite and (c) Mg-9 wt % Al alloy.	174
<b>Fig. 5.26</b>	SEM micrographs at a magnification, X300, showing the worn surfaces of a cast <i>in-situ</i> Mg-Al/Al <sub>3</sub> Ti-Al <sub>2</sub> O <sub>3</sub> composite designated by MT12/80, containing 1.1 vol% porosity and 2.1 wt% particles, at different normal loads.	175
<b>Fig. 5.27</b>	SEM micrographs at a magnification, X300, showing the worn surfaces of a cast <i>in-situ</i> Mg-Al/Al <sub>3</sub> Ti-Al <sub>2</sub> O <sub>3</sub> composite designated by MT12/80, containing 1.1 vol% porosity and 2.1 wt% particles, at different normal loads.	176



- Fig. 5.28** Typical SEM micrographs at a magnification, X300, showing the worn surfaces of cast *in-situ* Mg-Al/Mg<sub>2</sub>Si composites designated by (a) and (b) MS9/76, containing 0.8 vol% porosity and 2.42 vol % reinforcement, Mg<sub>2</sub>Si, at normal loads 10 and 40 N respectively, and (c) and (d) MS20/76, containing 2.6 vol% porosity and 6.4 vol % reinforcement, Mg<sub>2</sub>Si, at normal loads 10 and 40 N respectively. 177
- Fig. 5.29** Comparison of wear rates with increasing load between cast *in-situ* Mg-Al/Al<sub>3</sub>Ti-Al<sub>2</sub>O<sub>3</sub> composites designated by (c) MT8/80 and (d) MT14/80 and cast *in-situ* Mg-Al/Mg<sub>2</sub>Si composites designated by (e) MS9/76 and (f) MS20/76, along with those of (a) cast commercial Mg and cast Mg-9 wt% Al alloy. 180
- Fig. 5.30** Comparison of coefficient of friction with increasing load between cast *in-situ* Mg-Al/Al<sub>3</sub>Ti-Al<sub>2</sub>O<sub>3</sub> composites, designated by (c) MT8/80 and (d) MT14/80, and cast *in-situ* Mg-Al/Mg<sub>2</sub>Si composites, designated by (e) MS9/76 and (f) MS20/76, along with those of (a) cast commercial Mg and cast Mg-9 wt% Al alloy. 180

# LIST OF TABLES

Table No.	Title	Page No.
Table 2.1	Results of hardness measurement of Mg and Mg/Al <sub>2</sub> O <sub>3</sub> samples.	29
Table 2.2	Hardness values of Mg and Mg/ TiB <sub>2</sub> composites.	30
Table 2.3	Hardness values of AZ91 and <i>in-situ</i> particulate AZ91 composites.	30
Table 2.4	Tensile properties Mg/SiC <sub>p</sub> and Mg alloy/SiC <sub>p</sub> composites.	33
Table 2.5	Tensile properties of Mg and Mg/Al <sub>2</sub> O <sub>3</sub> composites.	34
Table 2.6	Room temperature tensile properties of Mg and Mg/Ti <sub>p</sub> .	35
Table 2.7	Mechanical properties of pure aluminium and TiB <sub>2</sub> /Al composites.	37
Table 2.8	Important properties of magnesium and reinforcement phases.	55
Table 3.1	Chemical compositions of as received commercial magnesium and aluminium ingots.	62
Table 3.2	The constituents, their nominal amounts and processing temperatures used for solidification processing of different cast Al-based composites.	66
Table 3.3	Details of various cast <i>in-situ</i> Mg-Al/Al <sub>3</sub> Ti-Al <sub>2</sub> O <sub>3</sub> composites developed by using aluminium based composites and the processing temperatures.	67
Table 3.4	The constituents and their nominal amounts used for solidification processing of different cast Al-Si master alloys.	68
Table 3.5	Details of various cast <i>in-situ</i> Mg-Al/Mg <sub>2</sub> Si composites synthesized, Al-Si master alloys used for these composites and the processing temperatures.	69
Table 4.1	Optimum processing parameter for solidification processing of cast <i>in-situ</i> Mg-Al/Al <sub>3</sub> Ti-Al <sub>2</sub> O <sub>3</sub> and Mg-Al/Mg <sub>2</sub> Si composites.	137
Table 5.1	TiO <sub>2</sub> particles addition, processing temperature and physical characteristics of different cast <i>in-situ</i> Mg-Al/Al <sub>3</sub> Ti-Al <sub>2</sub> O <sub>3</sub> composites.	143

<b>Table 5.2</b>	Physical characteristics for the bottom, middle and top segments of cast commercial magnesium and cast Mg-9 wt% Al base alloy.	144
<b>Table 5.3</b>	Silicon metal particles addition, processing temperature and physical characteristics of different cast <i>in-situ</i> Mg-Al/Mg <sub>2</sub> Si composites.	155
<b>Table A-1</b>	Mechanical properties, density and porosity content at the bottom, middle and top height segments of cast Mg-9 wt% Al alloy and commercial magnesium.	192
<b>Table A-2</b>	Mechanical properties, density, porosity and reinforcement content at the bottom, middle and top height segments of cast <i>in-situ</i> Mg-Al/Al <sub>3</sub> Ti-Al <sub>2</sub> O <sub>3</sub> composites.	193
<b>Table A-3</b>	Mechanical properties, density, porosity and reinforcement content at the bottom, middle and top height segments of cast <i>in-situ</i> Mg-Al/Mg <sub>2</sub> Si composites.	194

# NOMENCLATURES

<u>Symbol</u>	<u>Definition</u>	<u>Unit</u>
$b$	Burgers vector of the matrix dislocation	m
$d$	Inter-planer spacing	Å
$F$	Frictional force	N
$F_a$	Force required to shear the adhesion bond	N
$F_d$	Force required to deform the obstructing asperities elastically or plastically	N
$H_l$	Heat transfer coefficient of the melt	J/(m <sup>2</sup> °C s)
$H_p$	Heat transfer coefficient of the reinforcement	J/(m <sup>2</sup> °C s)
$H_w$	Hardness of the soft material	MPa
$k$	Wear coefficient	-
$L_w$	Normal load	N
$V_p$	Volume fraction of porosity	vol%
$RA$	Relative accuracy	%
$R_e$	Reynolds number	-
$S_w$	Sliding distance	m
$V_c$	Volume of the composite material	m <sup>3</sup>
$V_f$	Volume fraction of the reinforcement	vol%
$V_h$	Hindered settling velocity	m/s
$V_m$	Volume of the matrix alloy	m <sup>3</sup>
$V_v$	Volume of the porosity	m <sup>3</sup>
$V_w$	Volume loss due to sliding wear	mm <sup>3</sup>
$W_c$	Mass of the composite material	kg
$W_m$	Mass of the matrix alloy	kg
95%CL	95% Confidence Limit	%
$\theta$	Peak intensity angle	degree
$\lambda$	Wave length of CuK <sub>α</sub> radiation	Å
$\mu$	Coefficient of friction	-
$\mu_a$	Coefficient of friction due to adhesion	-
$\mu_d$	Coefficient of friction due to deformation	-

$\nu$	Poisson's ratio of the material	-
$\rho_r$	Density of the reinforcing particles	$\text{g/cm}^3$
$\rho_c$	Density of the composite material	$\text{g/cm}^3$
$\rho_l$	Density of the liquid	$\text{g/cm}^3$
$\rho_m$	Density of the matrix alloy	$\text{g/cm}^3$
$\rho_p$	Density of the reinforcement	$\text{g/cm}^3$
$\sigma_{ut}$	Ultimate tensile strength	MPa
$\sigma_{uto}$	Ultimate tensile strength at zero porosity	MPa
$\alpha$	Weakening factor	-
$\Delta H$	Latent heat of fusion	J/g

Materials as the primary building block for technological development have dictated nearly every design and every useful application that an engineer could devise. In spite of the present level of sophistication in the engineering sciences, it is no longer a question of being satisfied to design with the existing materials. Instead, in the ever changing technology scenario, one requires new materials with better properties to meet new design requirements for specific applications. Composite materials represent a unique category of materials, bringing together often extreme, but desired properties not attainable in conventional materials. Generally, a composite is defined as man made combination of two or more materials, often belonging different categories like polymers, ceramics, metals etc., suitably arranged or distributed with a separating interface. Moreover, the characteristics of the composite are distinctly different from those of the components in isolation. The history of man-made composite materials dates back to ancient materials technologies of early civilizations. They used laminated bows for extra strength, mixtures of straw and mud for building bricks, forged wrought iron and steel together to make sabers, dispersed platinum in gold and silver. These are some of the examples of composite materials, discovered by ingenuity of our ancient forefathers.

Composite materials constitute a continuous matrix phase where the reinforcement phase(s) is distributed. The reinforcement can be in the form of fibers, whiskers, platelets or particles. There could also be composites where both the combining phases are continuous, known as interpenetrating composites. Particle-reinforced metal matrix composites (PMMCs) is a special category of practically isotropic discontinuously reinforced composites (DRCs) which have either hard or soft particles or their mixtures embedded in a ductile metal or alloy matrix. The PMMCs are of particular interest due to their ease of fabrication by conventional methods at lower costs (Ray, 1993). PMMCs combine metallic properties (ductility and toughness) with the special characteristics of particle reinforcements, often leading to greater strength, higher wear resistance and higher elevated temperature properties depending on the nature of particles. The spectrum of properties that one can achieve in a composite material is the result of synergy between the constituents and these properties cannot be achieved in any of its constituents alone. Thus, the composite materials have extended the horizon of engineering materials and significant research effort is directed to develop different types of composites and determine their potential as future engineering material (Rohatgi, 1995).

Stable elevated temperature properties may be achieved if the reinforcement is thermally stable. In PMMC's where reinforcement is added externally, the resulting combination of *ex-situ* composite may not be thermodynamically stable at elevated temperatures. Over the last two decades, considerable research efforts have been directed towards the production of *in-situ* PMMCs, in which the reinforcements are formed *in-situ* in a metallic matrix by chemical reaction between the constituents during the composite fabrication. Compared to conventional *ex-situ* PMMCs, the *in-situ* PMMCs exhibits the following advantages: (a) the *in-situ* reinforcements generated during high temperature processing, are thermodynamically stable and do not dissolve or form reaction larger at higher service temperatures, thereby leading to less degradation during elevated-temperature service; (b) the *in-situ* generated reinforcements are finer in size and their distribution in the matrix is relatively more uniform, which may lead to better mechanical properties; and (c) the reinforcement-matrix interfaces are clean and uncontaminated which may result in good interfacial bonding, leading to higher ductility and toughness and also, improved wettability.

Using *in-situ* approach, PMMCs with a wide range of matrix materials (including aluminium, titanium, copper, nickel and iron), and second-phase particles (including borides, carbides, nitrides, oxides, silicides and their mixtures or intermetallic compounds of reactive metals such as Al, Ti, Mg, Cu, Zn, Si, etc) have been synthesized. Recent efforts have led to the development of PMMCs with magnesium as matrix material, and borides, carbides, nitrides, oxides, silicides and their mixtures as second-phase particles. Usually, green preform/master alloy will be processed through powder metallurgy route and the resulting material will be used in the development of magnesium based *in-situ* PMMCs through various casting techniques.

Magnesium and its alloys, owing to their low density (two third of aluminium and one fifth of iron), good damping characteristics, dimensional stability and excellent machinability, have become potential candidate for light-weight structural materials. Its excellent machinability is characterized by low power requirements (about 80% of aluminium, 25% of cast iron or 15% of low carbon steel), long tool life (four to five times greater than aluminium), excellent surface evenness and small fragmented chips. Further, magnesium is the fourth abundantly available metal, in nature and available at relatively low cost. It is easy to fabricate this metal and its alloys by a number of conventional techniques. The demand for magnesium alloys has been increasing rapidly owing to the pursuit of the automotive industry for light-weight materials for application in components in order to achieve improved fuel economy and

lower emission levels. According to an industrial review in 1998, there are 60 different types of components, from instrument panels to engine components, in which magnesium is either already used or being developed for use. The use of magnesium in automobile parts is predicted to increase globally at an average rate of 15% per year (Lee, 2000).

As the usage of magnesium alloy components in automobiles and other energy saving applications increase, further improvement of some of the material properties, such as high elastic modulus, hardness, wear resistance and lower thermal coefficient of expansion are increasingly desired. In recent years, attempts have been made to synthesize ceramic and metallic particle-reinforced magnesium based composites so as to enhance the hardness, elastic modulus, yield strength, and tribological properties of their monolithic counterparts. By applying cost effective manufacturing techniques considerable expansion of these magnesium matrix composites is expected in the consumer goods, automotive, aerospace and other energy saving applications. Although several manufacturing process can be used to produce such composites, the casting route is especially attractive and gaining more acceptance as a result of their low cost, high production rate, and potential to make near net shape product.

Being a highly reactive metal, magnesium and its alloys require environmental protection to prevent their oxidation and burning during solidification processing. A number of fluxes have been developed to provide protective cover to the melt during processing. However at present,  $SF_6/CO_2$  or argon atmosphere is quite popular to provide protective cover to the melt.

Tribology is crucial to modern machinery which uses sliding and rolling surfaces. Friction between the moving components causes dissipation of energy and wear may limit the life of a component by adversely affecting its performance. The purpose of research in tribology is understandably the minimization and/or elimination of losses resulting from friction and wear at all levels of technology where the rubbing of surfaces is involved. Application of composites in such components requires characterization of their friction and wear behaviour. The mechanical properties of materials are important in determining their tribological behaviour. In PMMCs, mechanical properties depend on the amount, size, shape and distribution of the dispersed phase apart from the mechanical properties of matrix material and the nature of interface. Both hard and soft reinforcing particles have been found to lower friction and improve wear resistance (Rohatgi, Ray and Liu, 1992). Cast metals, alloys and composites often have considerable porosities but its effect on friction and wear behaviour has not been systematically investigated so far.



In the present investigation, the aim is to develop some novel combinations in magnesium based composites using two stage solidification processing. The processing will also try to take advantage of the release of valuable metallic element from low cost metal oxide by reaction with the melt during processing. Aluminium alloy composite has been processed using titanium oxide particles as “Precursors” to generate reinforcing alumina ( $\text{Al}_2\text{O}_3$ ) particles *in-situ* and also, to release titanium for generating reinforcing intermetallic ( $\text{Al}_3\text{Ti}$ ) in aluminium matrix. The resulting composite has been used in the synthesis of magnesium based cast *in-situ* composite to inherit the oxide and intermetallic of aluminium based composite. In the processing of another type of cast *in-situ* magnesium based composite, aluminium-silicon master alloy has been prepared by adding silicon to molten aluminium. The influences of different key processing parameters like processing temperature, the amount of oxide added, on the evolution of microstructure will be investigated and their impact on the mechanical properties and tribological behaviour of the resulting cast *in-situ* composites is to be evaluated, with special attention to interaction between particle content and porosity. The knowledge base generated through this study is expected to lead to an understanding of the relationship between processing parameters, microstructures, mechanical properties and tribological properties and it may contribute to the identification of critical factors for processing in order to control the properties of these cast *in-situ* composites.

### 2.1 Composite Material: Historical Development

The history of man-made composite materials dates back to ancient materials technologies of early civilization. They used laminated bows for extra strength, mixtures of straw and mud for building blocks, dispersed platinum in gold and silver. Iron rods were used to reinforce masonry in the nineteenth century, leading to the development of steel-reinforced concrete. Phenolic resin reinforced with asbestos fibres was introduced in the beginning of the twentieth century. The first fibreglass boat was made in 1942; reinforced plastics were also used in aircraft and electrical components at this time. Filament winding was invented in 1946 and incorporated into missile applications in the 1950s. The first boron and high strength carbon fibres were introduced in early 1960s, with applications of advanced composites to replace aircraft components by 1968.

In conventional metal casting technology, ceramic particles were considered to be undesirable inclusions impairing strength and ductility of the casting. In the mid-sixties, nickel-coated graphite powders were incorporated in aluminium alloys by injecting the powders together with argon gas into a molten bath of the alloy; this marked the beginning of cast metal matrix particulate composites (Badia and Rohatgi, 1969). In 1969, at the Indian Institute of Technology Kanpur, Ray (1969) successfully developed cast aluminium-alumina composites by incorporating alumina particles by stirring the molten alloy with an impeller as the particles were added, and thus, the process of stir-casting emerged. Alloying elements such as magnesium promoted wetting such that mixing of non-wetting particles into liquid alloy was possible without prior coating. In the early seventies, Massachusetts Institute of Technology began the practice of introducing particles to semi-solid alloys between the solidus and the liquidus temperature for the alloy (Mahrabian et al., 1974). The enhanced viscosity of the semi-solid alloy increased the stability of the slurry by delaying particle flotation or settlement. At the University of Roorkee, presently the Indian Institute of Technology Roorkee, an arrangement for the bottom pouring was introduced so that the slurry could be stirred until casting, thereby eliminating the need to withdraw the stirrer before solidification (Prasad et al., 1982).

MMCs such as boron/aluminium were introduced in 1970. Starting from the late 1970s, applications of composites expanded widely to the aircraft, automotive, sporting goods and biomedical industries. In the automotive industry, the major driving forces for developing and implementing new materials and manufacturing technology are fuel economy, reduced vehicle emissions, and increased vehicle safety at competitive cost. The automobile industry has successfully applied Aluminium based particulate composites, chiefly SiC/Al and Al/Al<sub>2</sub>O<sub>3</sub>, in pistons, engine blocks, disc rotor brakes, drums, calipers, connecting rods, drive shafts, snow tire studs and other parts. Most notable example is the development of integrally cast aluminum base MMC engine block reinforced with graphite and Saffil fibres by Honda company in early 1990s (Ebisawa et al.). Some of the proven applications of typical MMCs in the automotive industry include, using of aluminium diesel engine pistons containing Saffil short fibres by Toyota since 1985, Al/SiC<sub>w</sub> connecting rods by Nissan, Al/Al<sub>2</sub>O<sub>3</sub> connecting rods by Dupont and Chrysler, Al/TiC<sub>p</sub> connecting rods and pistons by Martin Marietta, Al/SiC<sub>p</sub> rear brake drum, drive shaft, engine cradle by GM, Al/SiC<sub>p</sub> Brake rotors by Lotus Elise, Volkswagon, Chrysler and Lanxide, Al/SiC<sub>p</sub> brake disc on ICE bogies by Knorr-Bremse and Kobenhavn, and Mg/SiC<sub>p</sub> sprockets, pulleys, covers by Dow Chemical (Prasad et al., 2004).

At present, the emphasis has shifted to the development of newer MMCs such as *in-situ* MMCs in which the reinforcements are formed *in-situ* by promoting chemical reactions among the constituents of the melt during the processing step. Various techniques of preparation of *in-situ* composites are also extended to CMCs including carbon/carbon composites having high strength and high wear resistance over and above their suitability for high temperature applications. The reinforcing phase of *in-situ* MMCs are usually oxides, nitrides, carbides, borides or intermetallics compounds of reactive metals such as Al, Ti, Mg, Cu, Zn, Si, etc (Lewis, 1991).

## 2.2 Light Weight *In-Situ* Metal-Matrix Composites

The word '*in-situ*' is Latin by origin meaning 'in position'. The Merriam-Webster Dictionary gives the English meaning as "in the natural or original position or place". '*In-situ* composite' is the term applied to a relatively small, but fast expanding domain of materials where the reinforcing phase is formed within the parent phase by controlled melt growth, chemical reaction, or transformation and deformation. The *in-situ* concept is not entirely new, as nature provides many examples such as wood, bone etc. But, man-made *in-situ* composite processing is confined to those permitted by thermodynamics and kinetics space, through control of composition and process variables to arrive at the desired duplex structures. But

today, *in-situ* composites consist of metals, intermetallics, ceramics and inorganic compounds whose microstructural control led to new avenues in magnetic, electrical, optical, thermal, chemical and structural applications.

The term '*in-situ*' with reference to composites was first used in reference to directionally solidified alloys where controlled heat flow results in extended directionality of the micro-constituents to give impressive mechanical properties. The first *in-situ* composites that were processed were non-structural (Glasso, 1967; Weiss, 1971), but later the process was proven to be successful in the development of new materials that replaced conventional superalloys (Bradley, 1988; Duhl, 1989).

Production of high-strength *in-situ* composites is based on the principle of dispersion strengthening, in which, the metal matrix is strengthened by a fine dispersion of second phase particles such as oxides, carbides or intermetallics. Dispersions of various particulates can be achieved by a number of ways viz. surface oxidation of ultrafine powder followed by compaction, sintering and extrusion of fine powders, mechanical alloying, co-precipitation, internal oxidation, decomposition of inorganic compounds and electrolytic methods (Hoffman and Mantell, 1966; Grant, 1970; Graham et al., 1970; Kothari, 1984; Cense et al., 1977). The dispersoids create obstacles to the movement of dislocation and the strength enhancement due to interaction between the particles and dislocations was earlier explained by Orowan (1948) and Martin (1980). Additionally, strength arising from grain size refinement (Hall-Petch strengthening) also contributes to the overall strengthening of the material.

Compared to PMMCs produced by conventional method or *ex-situ* PMMCs, the *in-situ* PMMCs exhibit the following advantages: (i) the *in-situ* formed reinforcements are thermodynamically stable and do not dissolve at higher temperature or do not have a reaction layer, thereby leading to less degradation during elevated-temperature services; (ii) the *in-situ* generated reinforcements are finer in size and their distribution in the matrix is relatively more uniform, which may lead to better mechanical properties; and (iii) the reinforcement-matrix interfaces are clean and uncontaminated which may improve wettability and result in excellent interfacial properties.

### **2.2.1 Processing of *In-Situ* Metal-Matrix Composites**

To overcome some of the inherent problems, like residual microporosity, uneven distribution of reinforcement, non-wetting of the reinforcement, control of matrix-reinforcement interface, processing cost, that are associated with conventionally processed MMCs; novel *in-situ* processing techniques have been developed, where the *in-situ* second

phase is formed within the parent phase by controlled reaction. The last couple of decades have seen the birth of new *in-situ* processes which have been developed in an effort to optimize the structure and properties of *in-situ* metal matrix composites. These processing techniques have been reviewed by Koczak and Premkumar (1993), Daniel et al. (1997) and Tjong and Ma (2000). These processes have in common the concept of developing the reinforcing phase by some reaction process between the constituents of the materials to form oxides, carbides, nitrides, silicides, borides, intermetallics or their mixtures within the size range of 0.5-5  $\mu\text{m}$ . This is in contrast to first generation processes which involved the incorporation of a separately formed ceramic or intermetallics particle into the matrix by stirring, blending or injection (*ex-situ* approaches). Many of these *in-situ* processes are still in the development stages in various laboratories and are yet to find commercial application. In this section, processing routes of recently developed *in-situ* composites are reviewed. For better clarity, they have been broadly classified according to state of the metallic matrix and reactants during processing. Accordingly, the processing routes can be classified into four categories: (a) solid-liquid reaction process; (b) vapor-liquid-solid reaction process; (c) solid-solid reaction process, and (d) liquid-liquid reaction process.

#### **(a) Solid-Liquid Reaction Process**

In these processes inorganic compounds react *in-situ* to form reinforcing phases in the presence of a third liquid metallic phase, or alternatively the compounds react with some component in the melt to form *in-situ* reinforcements. In essence, this process is a solvent-assisted reaction wherein the reinforcing particles are generated in the solvent medium (the matrix) via diffusion of the components. This process has been widely adopted to fabricate *in situ* MMCs. Several processes fall under this category and are grouped together below.

##### **(i) Self-Propagating High-Temperature Synthesis (SHS)**

Self-propagating high-temperature synthesis (SHS), developed by Merzhanov and coworkers in the 1970s, refers to a process in which materials with a sufficiently high heat of formation are synthesized in a combustion wave, which after ignition, spontaneously propagates throughout the reactants and converts them into the products. The process has the advantages of sub-micrometer reinforcement size, nascent interfaces, economical processing, thermodynamic stability coupled with rapid reaction kinetics and the ability to produce high volume fractions of carbides, borides, oxides, aluminides, silicides and nitrides. The process is characterised by high combustion temperatures, up to 3000-4000  $^{\circ}\text{C}$  and the front velocities

from 1 to 250 mm/s. The SHS process has been extensively employed for the production of ceramic (Holt and Munir, 1986, 1987), intermetallic (Philpot et al., 1987) and intermetallic matrix composites (IMCs) (Sampath et al., 1993; Miyamoto et al., 1987). Ceramic reinforcements with a high heat of formation are ideally suited for SHS processing of MMCs. Aluminium matrix composite reinforced with 30 vol% TiC, TiB<sub>2</sub> and TiC/TiB<sub>2</sub> particles (Gotman et al., 1994), *in-situ* TiB<sub>2</sub> particles reinforced Mg composite (Wang et al., 2004), Mg-matrix composite reinforced with *in-situ* TiB<sub>2</sub>-TiC particulate (Wang et al., 2004), *in-situ* (TiB<sub>2</sub>-TiC)p/AZ91 magnesium matrix hybrid composite by Ma et al. (2005) are some typical examples of *in-situ* MMCs fabricated by this method.

(ii) *Direct Reaction Synthesis (DRS)*

Direct reaction synthesis (DRS) refers to a process in which reactant powders, or compacts of reactant powders, are directly added into molten metal and the ceramic reinforcing particles are formed *in-situ* through the exothermic reaction between reactants or between reactant and some component of the melt. Maity et al. (1993) have investigated the possibility of fabricating *in-situ* Al<sub>2</sub>O<sub>3</sub> reinforced Al composite by means of the DRS process. Nakata et al. (1995) have processed *in-situ* formed carbide particulate reinforced Al-based *in-situ* composites reinforced with TiC, ZrC and TaC particles. *In-situ* TiB<sub>2</sub> particles reinforced Mg-matrix composite (Wang et al., 2004) and Mg-based composite reinforced with *in-situ* 3.9 vol% (TiB<sub>2</sub> + TiC) ceramic particles (Zhang et al., 2005) have also been synthesized using this method.

During the present decade, the DRS technique has been further developed as a novel *in-situ* process to prepare Al-based MMCs at the Harbin Institute of Technology (HIT), Harbin, PR China (Zhang et al., 1999A and 1999B) and at the Indian Institute of Technology Roorkee (IITR), India (Abdulhaqq, Ghosh, Jain, and Ray, 2005, 2006). Huashun et al. (2006) have synthesized Al-Al<sub>3</sub>Ti composites by a direct reaction method, in which Al<sub>3</sub>Ti was formed by the reaction of Ti and Al in aluminum alloy melt. They reported that the morphology of Al<sub>3</sub>Ti has changed apparently from the fine particle to needle-like to large block with the increase of Al<sub>3</sub>Ti content. The addition of 3 wt% magnesium changed the morphology of Al<sub>3</sub>Ti to short rod-like precipitates distributed homogeneously in the Al matrix.

(iii) *Exothermic Dispersion (XD)*

In the 1980s, an exothermic dispersion (XD) process, termed XD<sup>TM</sup> technology, was developed by Martin Marietta Laboratories, Baltimore, MD, USA (Ray, 1993; Ma et al., 1994). The process is a solvent-assisted reaction wherein the ceramic phase is precipitated in

the solvent medium (the matrix) via diffusion of the components. In the XD process, matrix alloy and reacting constituents are mixed initially in the solid state and ignited to generate a self-propagating reaction throughout the mixture (Ray, 1993), as shown schematically in Fig. 2.1. For the reaction to be self-propagating it has to be exothermic. This process results in stable submicroscopic dispersion of reinforcing particles in a matrix alloy which generally melts at such a high heat as generated by the reaction. Also, high diffusivity of the reacting constituents in the molten alloy helps to bring them together for further reaction and thereby contributes to an increase of the rate of reaction. However, the higher the diffusivities of these constituents, the coarser will be the size of dispersoids; inter-particle distance will also increase resulting in lowering of tensile strength. This is best illustrated by the formation of  $TiB_2$  particles in an aluminium matrix. Titanium, boron and aluminium, both in the form of elemental powders or alloys of Al-Ti and Al-B, are mixed and heated to a sufficiently high temperature to provide a molten aluminium medium in which titanium and boron diffuse and precipitate out  $TiB_2$  in the matrix alloy (Kuruvilla et al., 1990; Mitra et al., 1991; Vyletelet al., 1991 and 1993; Caracostas et al., 1992; Krajewskiet al., 1993).

(iv) *Directed Metal Oxidation (DIMOX)*

Directed metal/melt oxidation (DIMOX) is an innovative technique developed by Lanxide Corporation, USA to produce metal-ceramic composites by exposing molten metal to oxidizing atmosphere at relatively high temperatures, more than 900 °C, (Koczak, Premkumar, 1993). The final product is a three-dimensional, interpenetrating network of oxide and microchannels of metal alloy. The reaction product grows toward the oxidizing atmosphere as shown schematically in Fig. 2.2. The reaction is sustained by wicking of the molten alloy to the surface by capillary forces. The metal is the main component of the alloy, which is oxidized to form *in-situ*  $Al_2O_3$ . Elements such as magnesium and zinc are present in the melt in small quantities, less than 10%, and help to initiate the oxidizing reaction by forming a porous spinel compound and thereby preventing formation of a passive oxide film at the surface as normally occurs in pure aluminium. The alloying elements also alter the surface energies of the melt to facilitate the wetting of the oxide and promote the wicking of the molten alloy. The main advantages of this technique include the ability to form relatively complex, fully dense composites with tailor-made properties to meet the needs of a wide range of applications (Murthy and Rao, 1995).

Matrix and reinforcement precursor materials

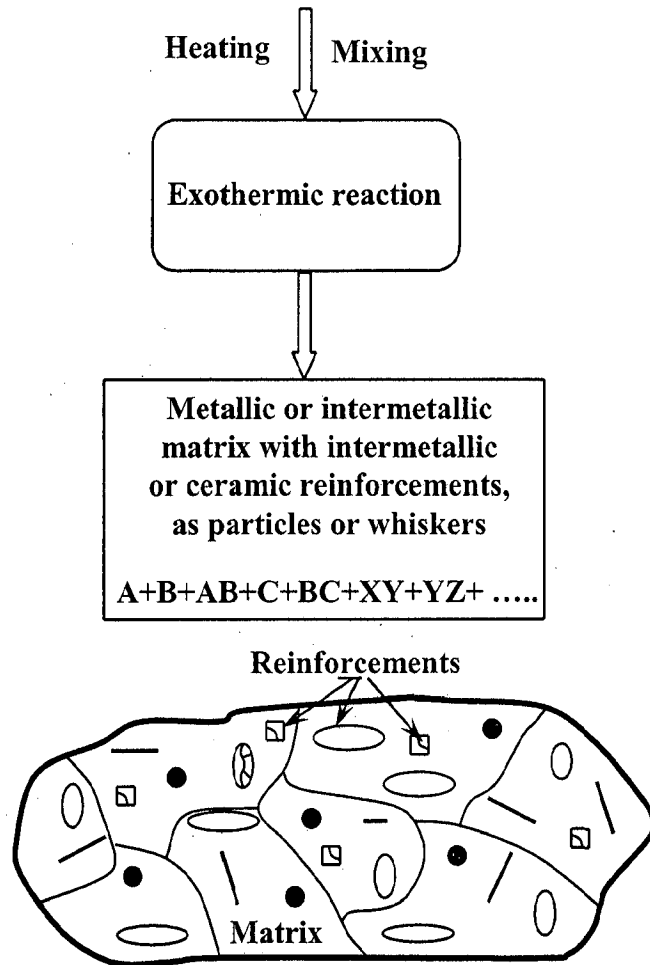


Fig. 2.1: Schematic diagram of XD process for producing *in-situ* composite materials.



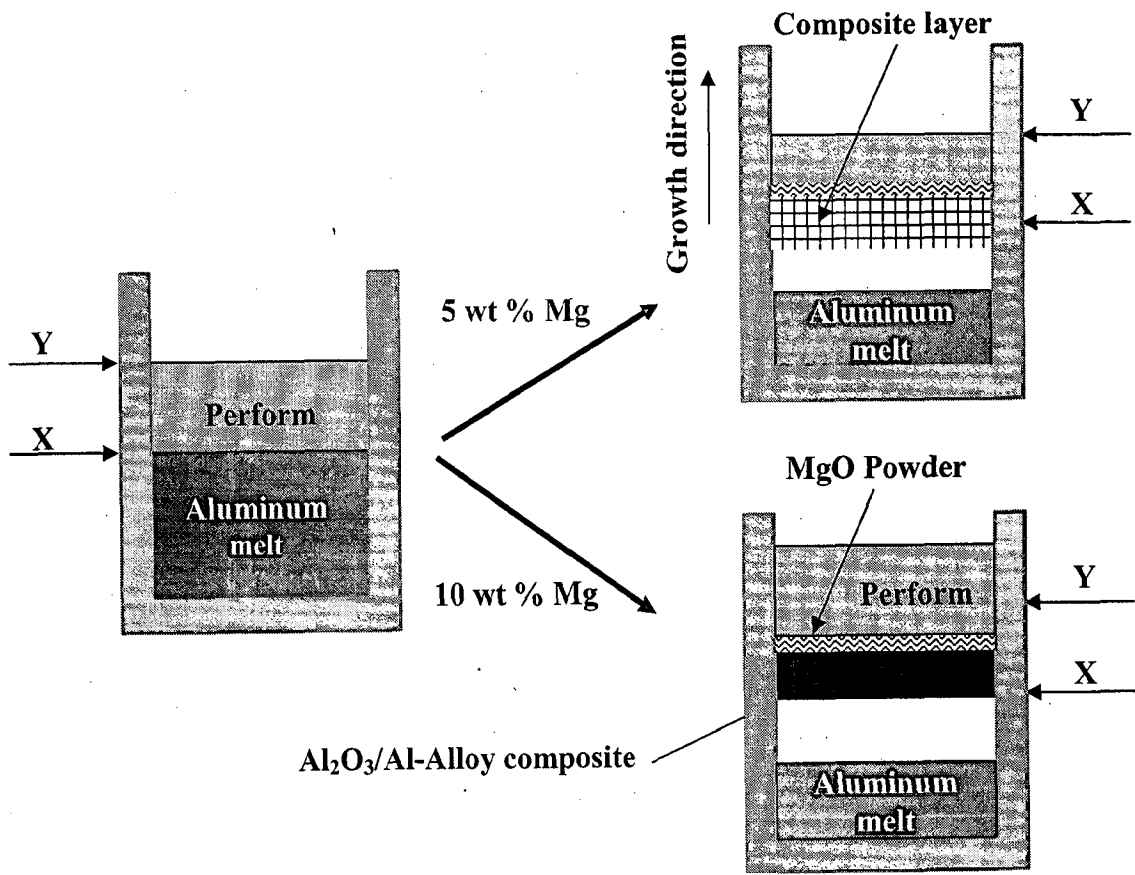


Fig. 2.2: Schematic diagram of the directed metal oxidation process.

(v) *Mixed-Salt Reaction*

The London Scandinavian Metallurgical Company (LSM) has developed a patented process termed mixed-salt reaction process to produce *in-situ* aluminium base MMCs based on their existing technology to produce a range of grain-refining alloys for the aluminium industry (Davies et al., 1987 and 1992). In this process, mixed salts of titanium and boron ( $K_2TiF_6 + KBF_4$ ) are reacted in molten aluminium to form *in-situ* particles of  $TiB_2$ . The  $TiB_2$  particles of 1-2  $\mu m$  in diameter are formed *in-situ* by this process; a 2014 alloy with  $TiB_2$  particles reportedly had yield strength of 500 MPa with 5% elongation and an elastic modulus of 90 GPa. The nature of particle-matrix interface is unclear. Due to the presence of salts in the reaction process, it is conceivable that the  $TiB_2$  formed would be coated with some undesirable reaction products, in which case the effectiveness of the borides in contributing to the *in-situ* composite strengthening of the matrix would be diminished. In a similar way Martin and coworkers (2001) synthesized magnesium reinforced with *in-situ* formed titanium and magnesium boride particles by reacting molten magnesium and mixed salts of  $K_2TiF_6$  and  $KBF_4$ . Pure Al, Al-4 wt% Cu and A356 composites reinforced with *in-situ*  $TiB_2$  particles (Wood et al., 1993, Lu et al., 1997), have also been processed using this technique.

(vi) *Reactive Spontaneous Infiltration (RSI)*

This process involves simultaneous infiltration and reaction of a porous solid preform with the melt to form a very fine, and thermodynamically stable, reinforcing ceramic phase (Dunand et al., 1993). In the process, a powder mixture is placed in an alumina crucible, and the an Al or Al alloy ingot is placed above the loose bed of the powder mixture. The crucible containing ingot-powder pairs are then placed in an induction furnace under nitrogen or argon atmosphere. The specimens are then heated above the melting temperature of the ingot for a specified time to allow infiltration and reaction with the powder. Typical examples include, *in situ* boride ( $TiB_2$ ,  $NbB_2$ ,  $TaB_2$ ,  $HfB_2$ ) reinforced Al-matrix composites by using powder mixture of  $TiN(Ti_xN_{1-x})-B$ ,  $Ti(Nb,Ta,Hf)-B_4C$  (Taheri-Nassaj et al., 1996, 1997) and  $TiC_p$  reinforced Mg-matrix composites (Dong et al., 2004). It offers the advantage of producing composites with a high ceramic content and near-net-shape fabrication (Muscat and Drew, 1994).

(b) *Liquid-Gas Reaction Process*

This process has been developed by Koczak and Kumar (1989), in which the reinforcing phase is the product of a gas-liquid reaction caused by the injection of gas into reactive liquid metal, as shown schematically in Fig. 2.3. The rapid reaction between the solute alloying element(s) and the reacting gas alone or mixed with an inert gas, introduce

into the melt at constant processing temperature produces a fine refractory dispersion in the matrix alloy. A typical example is the injection of CH<sub>4</sub> plus Ar bearing gas into Al-Ti melt at a high temperature and thereby the carbon released from the injected gas reacts with Ti in the melt to form TiC. The processing time can range from 20 min to 2 h and the processing temperature varies between 1200 and 1300 °C (Sahoo and Koczak, 1991).

**(c) Solid-Solid Reaction Process**

*(i) Mechanical alloying (MA)*

Mechanical alloying (MA) is a solid state powder processing method which involves repeated cold deformation and fracture of particles as a result of the high energy ball-sample collisions. This method can be used to produce fine-grained alloyed powder particles in metal-metal and metal-ceramic systems (Tjong and Ma, 2000). Fabrication of *in-situ* Al<sub>4</sub>C<sub>3</sub> particles reinforced Al composites via MA of Al with C (Jangg et al., 1988), Al<sub>4</sub>C<sub>3</sub> dispersoid and SiC particulate mixture-reinforced Al composites via MA of C, Al, and SiC powder mixture (Ma et al., 1994) and TiB<sub>2</sub> particle reinforced aluminium composites via MA of Ti and B powders (Lu et al., 1998), and subsequent annealing of as-milled mixture powders are some of the examples. In recent years, Lu et al. (2003) fabricated Mg-based composite reinforced by Mg<sub>2</sub>Si formed *in-situ* via mechanical alloying process.

*(ii) Reactive Hot Pressing (RHP)*

Reactive hot pressing (RHP) refers to a process in which ceramic reinforcement is *in-situ* formed through chemical reaction between elements or between element and compound during hot pressing of mixture powders. Synthesis of *in-situ* TiB whisker reinforced Ti-Al-4V composites (Lu et al., 1992) and TiB/Ti composites containing high volume contents of TiB whiskers (30-92%) (Sahay et al., 1999) are some typical examples.

**(d) Liquid-Liquid Reaction Process**

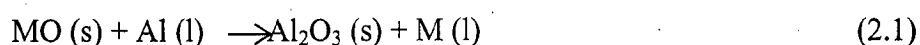
Mix alloy process is an example for liquid-liquid reactions developed by Sutek Corporation (Giessen, 1985). The process involves the reaction between two metal streams to form the ceramic particulates. Two or more high-speed, turbulent molten metal streams are made to impinge upon one another in a mixing chamber, thereby resulting in intimate mixing and reaction to produce the second phase. The resulting mixture can then be cast in a mould or rapidly solidified via melt spinning or atomization. This technology has been successfully used to produce copper alloys reinforced with extremely fine *in-situ* formed TiB<sub>2</sub> particles for electrical applications.

### (e) Plasma Reactive Synthesis

Basically, the process utilizes the high thermal energies of plasma to create reactive chemical species in the presence of heated vapour, liquid and/or solids. Thermal-plasma enhanced processes either with liquid, gaseous, or particulate precursors have been demonstrated to have the potential to synthesize unique composite structures in a wide range of materials and material systems. Typical examples include Al with AlN, Al<sub>2</sub>O<sub>3</sub> and SiC; NiCrTi-based alloys with TiC or TiN; intermetallics such as TiAl, AlTi<sub>3</sub>, MoSi<sub>2</sub> and other ceramics with oxides, nitrides, borides and/or carbides. Fig. 2.4 schematically illustrates the principle of the three innovative plasma-processing routes. Particulates, liquids, gases and solid or liquid surfaces can all be treated with the high temperatures of the plasma jets allowing melting and reaction between most materials, provided the thermodynamics and the kinetics are favourable.

#### 2.2.2 Thermodynamics of *In-Situ* Reaction

During the last two decades, a great variety of processing techniques have been developed to fabricate *in-situ* MMCs. A number of reactive systems have been adopted by various researchers. Furthermore, the thermodynamic feasibility of *in-situ* reactions involved in fabricating *in-situ* composites has been considered by a number of researchers. The obvious attraction of the production of *in-situ* MMCs by reduction of oxides process lies in its ability to convert cheap raw materials directly to MMCs, thus significantly minimizing the number of processing steps involved in production. For synthesizing Al<sub>2</sub>O<sub>3</sub>-AlM/Al composites, the reaction in the process can be represented as follows



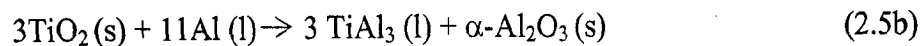
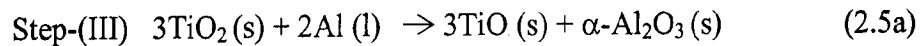
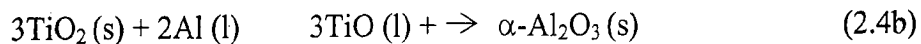
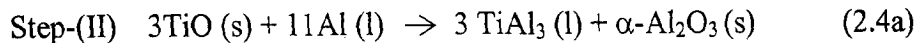
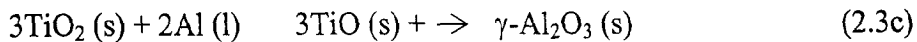
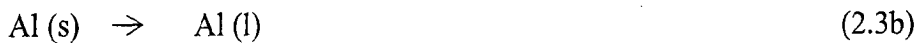
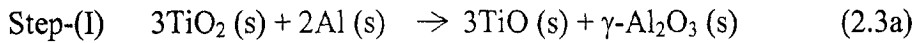
where, Al<sub>2</sub>O<sub>3</sub> is a ceramic reinforcement and M is a metal, which is also produced in the process. M can alloy with aluminium and may even, generate intermetallic reinforcement, depending on their binary phase diagram and the extent of M released.

In view of the above, it is initially important to examine if the desired cast *in-situ* Al<sub>2</sub>O<sub>3</sub>-AlM/Al composite can be produced by reaction synthesis process according to thermodynamic principles. In this regard, all the possible reactions between Al and M should be considered. For example, in case of Al-TiO<sub>2</sub> system, the Gibbs free energy change of formation of Al<sub>2</sub>O<sub>3</sub>, TiAl<sub>3</sub> and TiAl are more negative than those of other phases such as TiO and so on. Thus, it is reasonable to assume that the final products will be Al<sub>2</sub>O<sub>3</sub>, TiAl and TiAl, where the chemical reaction can be described by



The concept of production of cast *in-situ* Al<sub>2</sub>O<sub>3</sub>-Al particulate composite by thermodynamically controlled chemical reactions between aluminium (Al) and metal oxide (MO) has been justified by several workers. Liquid metal infiltration is an established process for production of fibre-reinforced as well as particle reinforced MMCs. This technique was used by Fukunaga and coworkers (1990) to produce *in-situ* composites. The process has been named as “reaction squeeze casting”, where preforms of TiO<sub>2</sub> preheated to 340-500 °C were infiltrated with molten pure aluminium of 800-890 °C. X ray diffraction and electron probe micro analysis identified the presence of α-Al<sub>2</sub>O<sub>3</sub>, TiAl and TiAl<sub>3</sub> in addition to unreacted aluminium and TiO<sub>2</sub> particles in different sections of the infiltrated composites.

Feng and Froyen (2000) have been investigating the reaction mechanism for an Al-TiO<sub>2</sub> system by using thermal analysis, XRD diffraction and microstructural characterization. By heating the starting material 83.33 wt%Al-16.67 wt%TiO<sub>2</sub> up to 1100 °C at 10 °C/min, TiAl<sub>3</sub> and α-Al<sub>2</sub>O<sub>3</sub> are finally formed in the aluminium matrix. TiO and γ-Al<sub>2</sub>O<sub>3</sub> are proved to be the transitional phases during the reactive process. They found that the *in-situ* processing involves three intermediate steps, which are as follows



### 2.2.3 Morphology of *In-Situ* Formed Particles

Compared to the conventional *ex-situ* composites, one of the several advantages of the *in-situ* particulate composites is that finer reinforcing particles are distributed more uniformly in the matrix alloy. Generally, the reinforcing particles in the *in-situ* composites are of the order of 0.1-5.0 μm (Maity and Panigrahi, 1995) and (Aikin, Jr., 1997). Such finer size of the

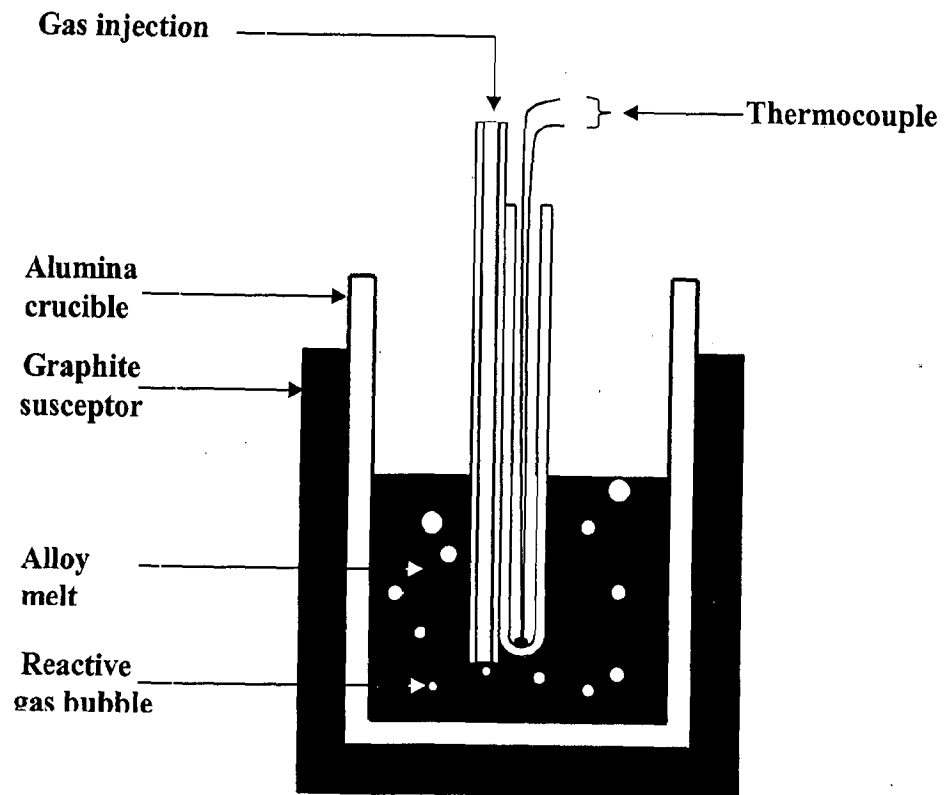


**Fig. 2.3:** Schematic diagram of the liquid-gas *in-situ* reaction process.

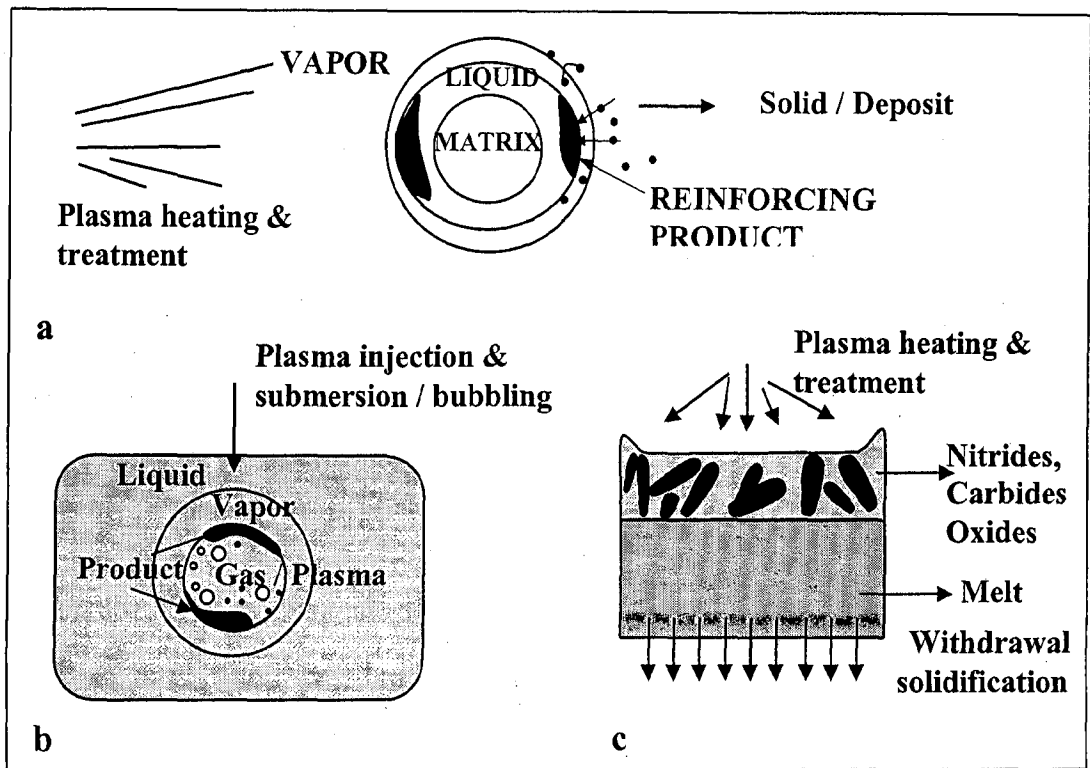


**Fig. 2.4:** Schematic diagram of several reactive plasma processing routes to form *in-situ* composite materials: (a) plasma-particulate reactive synthesis, (b) plasma-injected reactive gas synthesis and (c) plasma-melt interface enhanced materials synthesis.

reinforcing particles is desirable for the improved mechanical and tribological properties of the composites, as it has been established fundamentally and experimentally that finer particles are more effective in reinforcing the composites than relatively coarser particles (Arsenault, 1991). Particles of about 1-2  $\mu\text{m}$  have been proved to be the optimum size for effective reinforcement of the composites, as far as the particle size is concerned. However, distribution of particles of this size range in *ex-situ* composites produced either by powder technology or liquid metallurgy is not uniform, as clustering of particles takes place, resulting in poor mechanical properties. On the other hand, the particles formed *in-situ* is evenly distributed and particle-particle contact is also avoided. Further the interface is thermodynamically stable and compatible with the matrix (Peng Yu et al, 2004).

In case of liquid processed *in-situ* composites, either, the liquid metal and/or its alloying elements are oxidised, carburized, nitrided or boronised. The additions are either solid particles or gases. When solid particles are charged into liquid metal, the *in-situ* formed particles are the size range similar to that of the added particles. This implies that, individual particles added react with the liquid metal to form particles of similar size (Maity et al, 1993 and 1994). The shape of *in-situ* formed particles are equiaxed and polygonal, rounded or irregular under normal processing conditions. In general, starting powders of equiaxed shape produces particles of equiaxed shape in the *in-situ* composites (Maity et al, 1995). However, the influence of size of added particles on the morphology of *in-situ* formed particles is still not fully understood. It is believed that processing temperature, processing time, cooling rate, initial particle size, chemistry of the matrix alloy and reactants and reaction mechanism are possibly contributes the final size and morphology of the *in-situ* formed particles.

#### **2.2.4 Interface in *In-Situ* Metal-Matrix Composites**

For achieving better mechanical properties, cleaner particle-matrix interfaces and free from excessive particle-matrix reaction products are essential in composite materials. Though improved elastic modulus and strength are obtainable in presently *ex-situ* composites, these materials lack in sufficient fracture toughness and ductility for potential applications. Toughness is particularly reduced in case of composites with weak interfaces, where excessive reaction products are distributed at the periphery of the reinforcing particles. For example, brittle  $\text{Al}_4\text{C}_3$  compounds were observed at the interfaces of Al-SiC particle composites (Ibrahim et al., 1991). Cracks are favorably propagated through such weak interfaces and hence toughness is deteriorated.



Ma and coworkers (1996) have investigated the particle-matrix interface in the *in-situ* (Al<sub>2</sub>O<sub>3</sub>-TiB<sub>2</sub>)/Al particulate composites. They show that the interfaces between *in-situ* formed Al<sub>2</sub>O<sub>3</sub> and TiB<sub>2</sub> particles and the aluminium matrix are clean and free from any interfacial compound. Furthermore, no specific orientation relationship is observed between the *in-situ* formed particle and aluminium matrix.

Wear resistance of composites may also be severely affected due to easy pull out of the particles from weak interfaces (Alpas and Embury, 1990). Hence cleaner interfaces would be helpful to have better control over the mechanical properties of the composites. In general, the interfacial reaction is less in powder metallurgy processed composites compared to those processed by liquid metallurgy techniques, as lower processing temperature is used in the former approach. This factor resulted in higher strength levels in powder processed SiC/Al particulate composites in comparison to equivalent material produced by liquid phase process (Ibrahim et al., 1991). The reaction between the reinforcement and matrix may occur during secondary fabrication, e.g. in arc welding process where high temperatures are realised.

The interfaces are clean and stable in most of the *in-situ* particulate composites. Cleaner interfaces has been reported in *in-situ* Al<sub>2</sub>O<sub>3</sub>/Al (Maity et al., 1993), (Al<sub>2</sub>O<sub>3</sub>+TiB<sub>2</sub>)/Al (Ma et al., 1994), MgAl<sub>2</sub>O<sub>3</sub>/Al (Maity et al., 1994), Al<sub>4</sub>C<sub>3</sub>/Al (Ma et al., 1994A) and TiB<sub>2</sub>/Ni/Al (Xing et al., 1994) particulate composites. As thermodynamically stable particles, are only possible to be grown in these composites, the interfacial reaction is minimum or negligible. An additional characteristic of interface is the coherency between the lattices of the matrix and the particles. Coherency at the interface may further enhance strong bonding, since nucleation of voids at coherent interface is expected to be more difficult during deformation.

## 2.3 Solid-Liquid Reaction Processing

### 2.3.1 Mixing of Solid Liquid Slurry

The major problems in mixing of solid particles by a molten metal alloy arise from (i) difficulties in incorporation of non-metallic particles in molten metal, (ii) difficulties to obtain homogeneous distribution of particles in the cast composite and (iii) formation of porosity in the composite.

These difficulties of foundry technique are largely depend upon (i) physical and chemical nature of the particles, (ii) temperature of the melt and (iii) mixing conditions of the vortex method. Ghosh and Ray (1988A) found that the increase of porosity is roughly proportional to the volume fraction of alumina particles in a composite. While mixing non-

wetting particles in molten alloy by stirring, the particles and bubbles are sucked together at the centre of the vortex below the stirrer as it was confirmed by water modeling by Ghosh and Ray (1988B). The air bubble most likely are pulled into the melt in association with the ceramic particles. The introduction of gases during mixing could be minimized by preheating of alumina particles to 800 °C prior to their addition in the melt to remove the adhered moisture from these particles.

The porosity formation in cast composites, produced by foundry technique involving mechanical agitation of the slurry, is one of the most detrimental effects of this process. Caron and Masounave (1990A) have introduced an interesting variation of particle dispersion process which has the potential to synthesis low-porosity composites. In this process, particles form a bed at the bottom of a crucible and liquid metal is poured over it. The bed is then sealed by liquid metal on application of vacuum at the bottom. When vacuum at the bed reaches the desired level, a rotating stirrer is introduced to disperse the bed of particles into the liquid metal. This process is a combination of liquid metal infiltration to exclude air from the particulate bed, and even dispersion of particles in the liquid metal. Ray (1993) show that due to presence of particles at the bottom it requires a high stirring speed to lift up particles for dispersion, where the stirring speed may be high compared to that required to distribute particles added from the top. The advantage gained by exclusion of air envelope formed around particles during infiltration in term of reduced porosity in cast composites, may be offset by requirements of high stirring speed causing a higher rate of suction of bubbles through the vortex, resulting in an increase in porosity content of the cast composites.

#### **(a) Influence of Stirrer Geometry**

Mechanical stirrers of different designs were used to stir particles into molten alloy to produce cast particulate composites. These mechanical stirrers can be primarily classified into two groups depending on the direction of fluid flow such as the radial flow or axial flow stirrer. In radial flow the stirrer pumps the liquid in radial direction, while in axial flow the stirrer pumps the liquid parallel to the shaft of the stirrer. The turbine stirrer is the most popular stirrer used in chemical engineering industry for liquid-liquid, solid-liquid, and gas-liquid mixing. However, in addition to this other type of stirrers like the flat paddle anchor, helical ribbon and helical screw stirrers are also used for these systems Nagata (1975). There are two basic types of turbine stirrer such as the flat-blade or radial flow type and pitched-blade or axial flow type. The flat-blade produces a radial mixing pattern and desirable for high-shear mixing and it is recommended for shallow tanks having liquid of height less than 1.2 part of the turbine diameter. The pitched blade turbine stirrer produces flow in one component parallel to the vertical center line.

Surappa and Rohatgi (1978) used clay coated marine stirrer to incorporate and distribute graphite particles into molten aluminium alloy. Ghosh and Ray (1988C) used flat blade stirrer in order to incorporate alumina particles into the semi-solid aluminium alloy. A fluted stirrer was designed by Duralcan, (Ray, 1995), and it is claimed that the stirrer leaves the top of the melt relatively quite and thus reduces exposure of fresh liquid alloy to the environment resulting into less dissolution of gases in the melt.

### **(b) Influence of Process Variables**

In a mixing process of solid particles in molten or semi-solid alloy the main parameters considered are (i) position of the stirrer inside the melt, (ii) size of the stirrer, (iii) speed of the stirrer and (iv) melt temperature. The position and the size of the stirrer are often represented by dimension less parameters as  $h/H$  and  $d/D$  respectively, where  $h$  is the height of the stirrer from the bottom of the crucible,  $H$  is the height of the melt inside the crucible,  $d$  is the stirrer diameter and  $D$  is the diameter of the melt surface. The stirrer diameter affects fluidization of solid particles by a liquid. Use of too small diameter of stirrer keeps the solid particles suspended at the periphery of the vessel with no deposits at the center and when too large a diameter of stirrer is used the solid particles remain suspended at the center of the vessel bottom. Therefore, the optimum diameter of the stirrer should be such that solid particles are fluidized at both the central and peripheral parts at a given speed of stirring (Nagata, 1975). Ghosh and coworkers (1984A) in their extensive investigation on particle incorporation through vortex created by a flat blade stirrer have recommended an optimum stirring condition of particle incorporation as  $d/D = 0.62$  and  $h/H = 0.81$  at stirring speed of 16 rps. In the chemical engineering practices of mixing (Nagata 1975) it is recommend that the stirrer diameter larger than 60% of the vessel diameter is useful for mixing of solid particles in liquids having viscosity lying in the range of 3800 to 92000 cp. However, it was observed (Ghosh and Ray, 1988D) that porosity content in cast composite increases almost proportionately with the particle incorporation, which indicates that possibly there exists a similar mechanism for the incorporation of particle and porosity and particle incorporation plays a positive role in enhancement of porosity.

The main objectives of agitation of molten alloy are to help the incorporation of solid particles along with their uniform suspension in the molten alloy and to enhance the wettability of non wettable solid particles in the molten alloy (Caron and Maounave, 1990B). The state of suspension of solid particles in a melt is not usually homogeneous since non-uniformity is observed due to the unevenness of melt velocities. Therefore, one should find an optimum stirrer speed at which the solid particles are suspended. When one stirs molten

alloy by the turbine stirrer it creates a swirling motion in the liquid resulting in a vortex which is found helpful for incorporating poorly wetting particles added to the surface of the melt. The inner and outer surface of the rotating liquid experiences a pressure difference and the radial velocity distribution of the liquid at the surface may be determined by applying Bernoulli's equation as stated below.

$$V_t r_c = C \quad (2.6)$$

where,  $V$  is the tangential velocity at a radial position  $r_c$  from the centerline of the crucible and  $C$  is a constant. The particles added to the surface of the liquid undergo rotary motion and are drawn towards centerline due to movement of the liquid. The regions of higher  $V_t$  help the particle to attain a higher kinetic energy barrier in the process of immersion.

In an analysis of particle dispersion and fluid particle interaction affecting the incorporation of alumina particles in molten aluminium-magnesium alloy, Ghosh and coworkers (1984B) optimized the stirrer speed at the optimum size and position of the flat-blade stirrer and recommended that a stirring speed of 16 rps gives maximum particle incorporation at  $d/D = 0.62$  and  $h/H = 0.81$ . However, during stirring an initiation of exposure of stirrer, helping the particle incorporation, was found to occur at different stirring speed with a change in  $d/D$  ratio of stirrer. In the cold model experiment, Ghosh and Ray (1988D) also observed that at certain stirring speed a sudden incorporation of non-wettable beads in water takes place. It was noted that the exposure of the stirrer starts at higher speed of stirring for the stirrer having a lower  $d/D$  ratio.

### 2.3.2 Settling and Distribution of Particles in Molten Slurry

The homogeneous distribution of reinforced particles in the cast ingot largely depends upon distribution of the particles in the molten slurry inside the crucible followed by their redistribution in the mould during solidification. The distribution of particles in molten slurry depends on many factors such as the relative density between the particles and the melt, which decides the settling, or floating of particles and the secondary flow resulting from the transition of a fluid flow from lower to higher momentum layer inside the melt. But, in absence of stirring the redistribution of particles inside the mould is largely governed by the relative density of the particles to that of the melt, especially when the time of solidification is relatively long enough to allow the particles to settle or float depending on their densities. However, the difference in thermal diffusivity between the particles and the melt also affect the particle redistribution.

### (a) Particle Settling in the Crucible

Transportation of homogeneous slurry, prepared by stirring of particles into molten alloy, for casting at different place is performed either by using a slurry pump or holding it in a ladle. During holding, the slurry is required to be continuously stirred if the holding time is long enough to avoid considerable settling leading to inhomogeneous particle distribution in cast components (Yarandi et al., 1992). Stokes derived an expression for internal settling velocity,  $V_s$ , of single rigid sphere through unbounded quiescent Newtonian fluid at zero Reynolds number,  $Re$ , by equating viscous drag and the gravitational force modified by buoyancy (Ray, 1995) as follows

$$V_s = 2 (\rho_p - \rho_l) g r^2 / \eta \quad (2.7)$$

where,  $\rho_p$  and  $\rho_l$  are the densities of the particle and liquid respectively,  $g$  is the acceleration due to gravity,  $r$  is the radius of the particle, and  $\eta$  is the liquid viscosity. This simple picture of settling based on hydrodynamic forces and gravity does not hold for slurries because of interaction between particles. In addition the non-hydrodynamic forces like thermal forces, electrical forces, and weekly London-Van-der-wall forces may sometimes become equally important in a given system. Even if one ignores non-hydrodynamic forces, taking into account the interaction between polysized particles in slurry during settling is quit complicated. The settling of particles during holding and transportation of melt-particles slurries the settling of particles in a ladle is hindered due to presence of other particles in the slurry. The hindered setting velocity,  $V_h$ , is expressed by Richardson and Zaki, (1954) as follows

$$V_h = V_s (1 - V_f)^n \quad (2.8)$$

where,  $V_s$  is the Stokes settling velocity,  $V_f$  is the volume fraction of the particles,  $n$  is a constant as a function of Reynolds number,  $Re$ . For  $Re < 0.2$ ,  $n = 4.65 + 19.5 D/D_c$ , and for  $0.2 < Re < 1.0$ ,  $n = (4.35 + 17.5D/D_c) Re - 0.35$ , where,  $D_c$  is the diameter of the container, and  $D$  is the particle diameter.

Hanumath and coworkers (1992) have developed a resistance probe to measure the passage of the boundary between particle free and particle containing regions in an alloy. The results indicate that settling rate is a strong function of volume fraction of particles as described by Eq. (2.16). Yarandi et al (1992) have investigated particle settling in slurry

containing 10, 15, and 20 vol% of SiC particles of average sizes 9 and 15  $\mu\text{m}$  respectively, dispersed in A354 aluminium alloy. As a consequence of settling, a particle denuded zone appears at the top of the melt and variation of length of this zone is measured with settling time by rapid quenching of the slurry. They have also proposed an expression to calculate the length of the denuded zone, at any time,  $X_t$ , and it depends on the depth of the slurry  $H$ , as a function of geometry of the crucible as follows

$$X_t = \frac{H(1-f_0)}{V(f_0)f_0(n+1)} \left[ 1 - \left( 1 - \frac{3f_0}{(1-f_0)H} \right)^{n+1} \right] \quad (2.9)$$

where,  $f_0$  is the overall volume fraction and  $V(f_0)$  is the initial hindered settling speed. They have also shown that the composite containing 10 vol%, of 9  $\mu\text{m}$  size particles develops particle free zone at the top of the ingot with much faster rate than in the composite containing 15 vol% particles of the same size due to additional hindrance to particle settling because of the presence of higher volume fraction of particles.

Ray (1995) was reported that the use of fine particles reduces the settling rate in spite of their large volume. Moreover, if one use a mixture of fine and coarse particles in slurry, the coarse particles settles faster compared to fine particles and leave the top region of the slurry soon after they start settling. The volume fraction of particles, therefore, reduces at the top, enhancing the hindrance of settling velocity or rate of settling of the fine particles. If the size of the fine and coarse particles matches so, as given by the following equation, the fine particles come in a position to catch up with the coarse particles.

$$\frac{r_1}{r_2} < \left[ \frac{1-V_{fs}}{1-V_f} \right] \quad (2.10)$$

where, the slurry of  $V_f$  volume fraction of solid particles, contains  $V_{fs}$  volume fraction of fine particles of radius  $r_2$  and  $(V_f - V_{fs})$ , volume fraction of coarse particles of radius  $r_1$ . However, the same investigator has also shown that in slurries containing coarse and fine particles of volume fraction 0.11 and 0.15 violating the condition given by Eq. (2.10) does not show significant segregation of coarse and fine particles. It leads to believe that the comparatively slow movement of the finer particles acts as screen and slows down the coarser particles by physically obstructing their passage during settling.

## **(b) Particle Settling and Distribution in the Mould**

In a cast particulate metal matrix composite the distribution of particles is an important factor which influences the properties of the composite material. In the molten metal processing route, the particle distribution in solidified material is primarily affected by three different physical processes; (i) particle settling (or floating), (ii) particle agglomeration and (iii) particle rejection. The settling and agglomeration occur in liquid state, whereas the particle rejection occurs during solidification. When a solid-liquid interface approaches a particle suspended in liquid metal, the particles are either captured or rejected by the interface. If the particles are captured the redistribution of the particles in the solid remains same as it was in the liquid. However, if the particles are rejected by the interface, they segregate to the inter-dendritic region which solidifies last. From the experimental results and theoretical investigations, it is learned that the interaction between the particles and the moving solid-liquid interfaces (particles captured or rejected) is governed by the materials properties and solidification condition, such as the interfacial energies, interface shape, interface velocity, thermal conductivity, the type and size of particles, and the properties of the liquid (Rohatgi, 1995).

Jin and Lloyd (1990) have examined the interaction between SiC particles and a growing solid-liquid interface and reported that during solidification of particle reinforced hypoeutectic Al-Si alloy, the particles are rejected or captured by the growing aluminium dendrites depending on the cooling rate during solidification. At low cooling rate where the dendrite arm spacing is larger than the particle size, the particles segregate into the inter-dendritic region. While at higher cooling rates, where the dendritic arm spacing smaller than the particle size, particles become virtually immobile and no solidification induced segregation results. The particle capture condition is the same as the heterogeneous nucleation condition, i.e. particles which act as heterogeneous nucleation catalysts are not rejected by the solid/liquid interface.

During solidification of a melt containing dispersion of second phase particles, the initial distribution of particles can change due to three phenomena, (i) buoyant motion of the particles (ii) pushing of the particles by the moving solidification front, and (iii) by convection currents in the melt. It is shown that for any heat extraction rate there is an optimum particle size which gives maximum uniformity of distribution of particles in solidified material. Theories of particle pushing (Stefanescu et al, 1988) predict that there is a critical velocity of the solidification front, below which the front pushes the particles with it. Above the critical velocity, the front grows around the particles and engulfs them. The critical velocity is a function of the particle size, the temperature gradients at the solidification front and a number

of material properties such as the ratio of thermal conductivity of the particles and the melt, the coefficient of molecular surface forces between the particle and the solidification front, etc. Analysis of experimental results produced by Stefanescu (1988) showed that the critical velocity depends on particle radius  $r$  according to the following equation.

$$V_{cr} r^n = C \quad (2.11)$$

Where, the exponent  $n$  ranges from 0.28 to 0.9

There are two basic theoretical approaches to study the particle behaviour at solid-liquid interface i.e., thermodynamic and kinetic approaches. The thermodynamic model suggested by Omenyi and Neumann predict the engulfment, when the change in free energy due to engulfment is negative. Whereas the kinetic approach is based on the simple idea, that so a finite layer of liquid exists between the particle and the solid the particle will not be engulfed (Stefanescu, 1988). The critical velocity,  $V_{cr}$ , below which the particles are pushed and above which particles are engulfed, for a solid-liquid interface to engulf a solid particle with radius  $r$  is expressed as

$$V_{cr} = \frac{\Delta\sigma_o d_o}{6(n-1)\eta r} \left(2 - \frac{k_p}{k_l}\right) \quad (2.12)$$

where,  $\Delta\sigma_o$  is the difference in surface tension between liquid and solid,  $d_o$  is the inter-atomic distance,  $n$  is a constant varies in the range from 2 to 7,  $\eta$  is the viscosity of the melt,  $k_p$  is the thermal conductivity of the particle, and  $k_l$  is the melt thermal conductivity. In fact, the practical process is more complicated than predicted by a simple  $V_{cr}$  equation (Eq. 2.12). It is obvious that the particle destabilizes the interface. In a particular case when  $k_p < k_l$  a bump may form, roll off and remelt when another bump may form adjacent to the new position of the particle. Thus, the interface ceases to be flat and the particle may be pushed before entrapment.

For each type of particle-liquid combination a critical velocity exists below which the particles are pushed by the moving solid-liquid interface and above which they are trapped. It was suggested by Rohatgi and coworkers (1986) that this driving force, which tends to keep finite separation between the growing solid and a particle and pushes the particle, arises from the increase in specific energy as the separation between the particle and the surface of the primary solid tend toward zero. In order to maintain this separation, fluid must reach the region of solid-liquid interface underneath the particle by the process of diffusion and flow. The theoretical critical velocity  $V_{cr}$  is given by the following equation



$$V_{cr} = \left[ \frac{n+1}{2} \right] \left[ \frac{\Delta H \rho_l a_o V_o D_l}{K_c T r^2} \right] \quad (2.13)$$

where  $n$  is a constant nearly equal to 5,  $\Delta H$  is the latent heat of fusion,  $a_o$  is the lattice constant,  $V_o = a_o^3$ ,  $D_l$  is the diffusion coefficient of the liquid, and  $r$  is the radius of the particle. Rohatgi (1986) shows that all graphite particles including some very small ones, are pushed by  $\alpha$ -Al dendrites into the last freezing liquid, even though the actual rate of solidification is much higher than the theoretical velocity predicted by Eq. (2.13) for particle capture. It is reported that when the ratio of the thermal conductivity of particle and liquid is less than unity the rate of growth of the front situated under the particle increases and the particle can not be captured by the growing crystal (Rohatgi 1986). However, they proposed an alternative empirical and fairly general criterion, which is best explained by the experimental results, called the heat diffusivity criterion, according to which the ratio of diffusivity of the particle to that of the liquid should be greater than unity for the capture of particles as stated below

$$\left( \frac{H_p C_p \rho_p}{H_l C_l \rho_l} \right)^{1/2} > 1 \quad (2.14)$$

where,  $H$ ,  $C$  and  $\rho$  are respectively the heat coefficient, specific heat and density and the subscript  $l$  and  $p$  is referred to the liquid and particle respectively.

## 2.4 Mechanical Properties of Light Weight PMMCs

The mechanical properties of the particulate metal-matrix composites (PMMCs) depend upon the type, the size, shape, the volume fraction and the distribution of particles inside the composites. The characteristics of particle-matrix interface also play an important role in controlling mechanical properties of the composites, which is governed by the wettability of reinforced particles in a melt and affinity of the particles to be attached to the gas bubbles either sucked into the melt during mixing by stirring or being available on release of dissolved gases by the molten metal during its solidification from a high processing temperature.

### 2.4.1 Hardness Behaviour

The hardness value of a material is a measure of its resistance to permanent deformation by indentation. Investigation of hardness for a material is very important especially, when it is subjected to wear. Many researchers have investigated hardness

behaviour of number of particulate metal-matrix composites. Saravanan and Surappa (2000) measured hardness values of pure Mg-30 vol% SiC<sub>p</sub> composite and reported higher hardness value for the composite (55 VHN) than compared to pure magnesium (45 VHN).

Hassan and Gupta (2005) have investigated micro-hardness and macro-hardness in their studies on nano-Al<sub>2</sub>O<sub>3</sub> reinforced magnesium nano-composites produced by powder metallurgy technique (PM) followed by hot extrusion. The results are as reported in Table 2.1. There is an increase in matrix hardness with an increase in percentage of nano-Al<sub>2</sub>O<sub>3</sub>. This could be attributed primarily to (a) the presence of relatively harder ceramic particles in the matrix, (b) a higher constraint to the localized matrix deformation during indentation due to their presence, and (c) reduced grain size. Hassan and Gupta (2006) have also examined hardness behaviour of cast magnesium and magnesium/2.5 wt% Al<sub>2</sub>O<sub>3</sub> nanocomposites synthesized by using disintegrated melt deposition technique (DMD) followed by hot extrusion. They reported that the presence of nano-Al<sub>2</sub>O<sub>3</sub> reinforcement has led to a significant increase in macro-hardness of Mg in the case of DMD processed material (65 15HRT) compared with PM processed material (60 15HRT). Relatively non-uniform distribution of reinforcement and their marginal effect on grain refinement limited the increase in hardness of PM processed material (~40%) when compared with DMD processed material (~76%).

**Table 2.1** Results of hardness measurements of Mg and Mg/Al<sub>2</sub>O<sub>3</sub> samples (from Hassan and Gupta, 2005; Srikanth et al., 2005).

Materials	Mg/0.00 vol%Al <sub>2</sub> O <sub>3</sub>	Mg/0.22 vol%Al <sub>2</sub> O <sub>3</sub>	Mg/0.66 vol%Al <sub>2</sub> O <sub>3</sub>	Mg/1.11 vol%Al <sub>2</sub> O <sub>3</sub>	Mg/1.00 vol%Al <sub>2</sub> O <sub>3</sub>
Macro-hardness (15HRT)	43 ± 0	51 ± 0	56 ± 0	60 ± 1	--
Micro-hardness (HV)	37 ± 0	44 ± 0	50 ± 1	70 ± 0	52 ± 3

Wang and coworkers (2004) investigated the hardness values of TiB<sub>2</sub>/Mg particulate composites processed by powder metallurgy technique with different volume fractions of TiB<sub>2</sub> particulates. They reported that as compared with as-cast pure Mg (32 HB), the hardness values of the composites reinforced with 10, 20 and 30 vol% TiB<sub>2</sub> particulates were increased by 41% (45 HB), 106% (66 HB) and 181% (90 HB), respectively. This could be attributed primarily to (a) the presence of harder TiB<sub>2</sub> particulates in the magnesium matrix and (b) a higher constraint to the localized matrix deformation during indentation due to the presence of TiB<sub>2</sub>.

Wang et al. (2006) have studied the hardness behaviour of magnesium alloy matrix composites reinforced with 2, 5 and 7.5 wt% fine TiB<sub>2</sub> (~7 µm) particulates fabricated by adding a TiB<sub>2</sub>-Al compact mixed with fine TiB<sub>2</sub> and Al powders to magnesium melt and using a semi-solid slurry stirring technique. They have mentioned that, the hardness of Mg alloy composite was higher and increases with increasing TiB<sub>2</sub> content as compared to as-cast AZ91 as shown in Table 2.2.

**Table 2.2** Hardness values of Mg and Mg/ TiB<sub>2</sub> composites.

Materials	As-cast AZ91	2wt%TiB <sub>2</sub> /AZ91	5wt%TiB <sub>2</sub> /AZ91	7.5wt%TiB <sub>2</sub> /AZ91
Hardness (HB)	62	74	80	82

Comparison of hardness values of typical *in-situ* particulate AZ91 composites and their matrix alloys is given in Table 2.3. Jiang et al. (2003) have reported highest hardness value (83 HB) in their *in-situ* 10 vol% TiC<sub>p</sub>/AZ91 composite. They have used powder metallurgy route in the preparation of master alloy which was used in the fabrication of *in-situ* composite. Wang et al. (2004) and Ma et al. (2005) have also used similar technique in the preparation of master alloy/green perform for their *in-situ* composites.

**Table 2.3** Hardness values of AZ91 and *in-situ* particulate AZ91 composites.

Sl. No.	Primary processing	Materials	Hardness (HB)	Investigator
1	Semisolid slurry stirring technique	As-cast AZ91	60	Jiang et al. (2003)
		<i>In-situ</i> 10 vol% TiC <sub>p</sub> /AZ91	83	
2	Stir casting technique	AZ91D alloy	60	Wang et al. (2004)
		<i>In-situ</i> 5 wt% TiC <sub>p</sub> /AZ91D	80	
3	Remelting and dilution stir casting technique	AZ91 alloy	56	Ma et al. (2005)
		<i>In-situ</i> 5 wt% (TiB <sub>2</sub> -TiC) <sub>p</sub> /AZ91	79	

Abdulhaqq and coworkers (2005) have investigated hardness behaviour of cast *in-situ* Al(Mg, Mn)-Al<sub>2</sub>O<sub>3</sub> (MnO<sub>2</sub>) composite with different processing variables (processing temperature 670-850 °C and processing time 3-15 Min.). The findings of their investigations are as follows

- For cast *in-situ* composite resulted from Al(5% Mg)-3% MnO<sub>2</sub>, the hardness has increased with increased processing temperature until 780 °C, but decreased with further increased temperature beyond 780 °C.
- At a fixed processing temperature of 780 °C, for cast *in-situ* composite resulted from Al(5% Mg)-3% MnO<sub>2</sub>, as the processing time increased from 3 to 10 minutes, the hardness increased, but beyond 10 minutes, the hardness has decreased.

Abdulhaqq et al. (2006) have also investigated hardness behaviour of cast *in-situ* Al(Mg, Ti)-Al<sub>2</sub>O<sub>3</sub> (TiO<sub>2</sub>) composite along the height from the bottom of the cast ingot synthesized at 780 °C. They observed that, the hardness was relatively constant within a band of values until the middle of the ingot, but decreased rapidly at the top, inspite of the increased particle content. The variation in Brinell hardness in the middle segment of the ingot with processing temperature of cast *in-situ* Al(Mg, Ti)-Al<sub>2</sub>O<sub>3</sub> (TiO<sub>2</sub>) composite also has been examined. They reported that the hardness increased linearly with increased processing temperature upto 850 °C, the maximum temperature investigated.

## 2.4.2 Tensile Properties

Tensile properties, except the ductility, show increasing values by reinforcing magnesium and aluminium alloys with particles. Following four different mechanisms are thought to be responsible for increasing strength and elastic modulus (Friedrich and Mordike, 2006).

- Orowan mechanism: interdependence between particles and dislocations.
- Strengthening by stabilizing or reducing grain size.
- Increasing the amount of dislocation around the particles and the development of internal stress due to misfit during thermal expansion.
- Strengthening of matrix due to different strain properties of both matrix and particles.

SiC particulates (SiC<sub>p</sub>) are extensively used to synthesis particulate reinforced metal matrix composites because of their high strength, high stiffness and stable chemical activity. For example, Laurent et al. (1992) investigated the tensile properties of extruded AZ91D-15 vol% SiC<sub>p</sub> composites processed in the semi-solid temperature range between 581 to 587 °C

prior to extrusion. The tensile properties were compared with the room-temperature tensile test results published by the Dow chemical company for AZ91D alloys. They found that in composites containing 15 vol% SiC<sub>p</sub> of size 54 μm, the room-temperature yield strength (YS) was 257 MPa, a value 20% higher than the yield strength of 215 MPa observed in unreinforced AZ91D alloy. The ultimate tensile strength (UTS) in the same composite was 289 MPa, a value close to 296 MPa, observed in the unreinforced alloys. A significant improvement in elastic modulus of up to 46% was observed compared to elastic modulus of 45 GPa observed in the AZ91D alloy but the total elongation of the composite decreased drastically to 0.7% compared to 10.2% measured in the unreinforced alloy for die cast AZ91-15 vol% SiC<sub>p</sub> reinforced composites.

Lloyd (1994) reported typical properties of some of the commercially available magnesium alloy based composites and unreinforced base alloys as provided by Dow co. For AZ91 alloy reinforced with 9.4 vol% and 15.1 vol% SiC<sub>p</sub>, the yield strengths were observed to be 191 and 208 MPa respectively but the ultimate tensile strengths were 236 MPa for both these composites. In these composites, the elastic modulus were 47.5 to 54 GPa in the composites containing 9.4 vol% and 15.1 vol% SiC<sub>p</sub> respectively but the elongation observed were 2 and 1% respectively. When the base alloy has been changed to AZ61 containing lower amount of aluminium but reinforced with 20 vol% of SiC<sub>p</sub>, it was observed that the yield strength of the unreinforced alloy, 157 MPa, increased to 260 MPa in the composite. The tensile strength of the unreinforced alloy, 198 MPa also increased to 328 MPa in the composite. There was very little reduction of percentage elongation with reinforcement from 3.0 to 2.5 %. The elastic modulus increased considerably from 38 GPa to 80 GPa on reinforcement. Thus, it appears that one may get relatively better tensile strength, elastic modulus and percentage elongation in lower aluminium alloys.

Lee and coworkers (1997) have investigated the tensile properties of AZ91 and AZ91/ SiC<sub>p</sub> composites produced by powder metallurgy technique, using 8, 30, 50 μm size SiC particles. They reported that the yield strength and tensile strength of extruded composites were higher than that of magnesium alloy, and the yield strength of magnesium alloy/SiC<sub>p</sub> (8 μm) composites was superior to that of magnesium alloy/SiC<sub>p</sub> (50 μm) composites, mainly because of grain refinement in the matrix.

Chua et al. (1999) investigated influence of size (15, 20, 25, 38, 50 μm) SiC particles on mechanical properties of Mg/SiC<sub>p</sub> composites. Authors have reported that, there are only little differences in the 0.2% YS and tensile strength of the 15-25 μm SiC<sub>p</sub> reinforced composites but that with 50 μm particulate possesses a much lower 0.2% YS and tensile

strength. It could also be seen that an increase in particle size gave an increase in the Young's modulus. The ductility was however severely reduced. As compared to the matrix, the composites exhibit an overall lower 0.2% YS and tensile strength. Tensile properties of some of the SiC<sub>p</sub> reinforced magnesium composites are summarized in Table 2.4.

**Table 2.4:** Tensile properties Mg/SiC<sub>p</sub> and Mg alloy/SiC<sub>p</sub> composites.

Sl. No.	Material	0.2% YS (MPa)	UTS (MPa)	E (GPa)	Ductility (%)	Investigators
1	AZ91/15 vol% SiC <sub>p</sub>	257	289	–	0.7	Laurent et al. (1992)
2	Mg/10 vol% SiC <sub>p</sub>	120	160	45	2.0	Krishnadev et al. (1993)
3	AZ91/16.1 wt% SiC <sub>p</sub>	191	236	47.5	2.0	Lloyd (1994)
4	Mg/10 vol% SiC <sub>p</sub>	135	152	44.7	0.8	Luo (1995)
5	Mg/15.1 vol% SiC <sub>p</sub>	100	150	–	1.0	Vijaymohan and Gopalkrishna (1996)
6	Mg/30 vol% SiC <sub>p</sub>	229	258	59	2	Saravanan and Surappa (2000)
7	Mg/9.3 vol% SiC <sub>p</sub>	120 ± 5	181 ± 6	44 ± 2	4.7 ± 1.3	Gupta et al. (2000)

After SiC particulate reinforcement, extensive work has been taken place in Al<sub>2</sub>O<sub>3</sub> particulate reinforced aluminium based composites, however, very few researchers have tried to synthesize Al<sub>2</sub>O<sub>3</sub> particulate reinforced magnesium based composites. Hassan and Gupta (2005) studied tensile properties of elemental magnesium nano-Al<sub>2</sub>O<sub>3</sub> reinforced magnesium nano-composites produced by powder metallurgy technique (PM) followed by hot extrusion. They reported that, ambient temperature tensile tests revealed significant improvement in 0.2% YS, UTS and ductility of magnesium with the progressive addition of nano-sized Al<sub>2</sub>O<sub>3</sub> particles as shown in Table 2.5. Simultaneous increase in 0.2% YS, UTS and ductility of Mg/Al<sub>2</sub>O<sub>3</sub> composites when compared to pure magnesium can primarily be attributed to the

coupled effect of: (a) heavily built multi-directional thermal stress due to the generation of dislocation at the  $\text{Al}_2\text{O}_3/\text{Mg}$  interface and (b) the effective transfer of applied tensile load to the uniformly distributed enormous number of well-bonded strong nano- $\text{Al}_2\text{O}_3$ . Hassan and Gupta (2006) have also examined tensile behaviour of cast magnesium and magnesium/2.5 wt%  $\text{Al}_2\text{O}_3$  nano-composites synthesized by using disintegrated melt deposition technique (DMD) followed by hot extrusion. They reported that the presence of nano- $\text{Al}_2\text{O}_3$  reinforcement has led to a significant increase in 0.2% YS, UTS and ductility of Mg in the case of DMD processed material compared with PM processed material as shown in Table 2.5. The 0.2% YS, UTS and ductility combination of the magnesium nano-composites containing 0.66 and 1.11 vol% of alumina remained higher when compared to high strength magnesium alloy AZ91 reinforced with much higher amount of micrometer size  $\text{SiC}$  particles. Fractography studies revealed that the typical brittle fracture of pure Mg changed to ductile due to the incorporation of nano- $\text{Al}_2\text{O}_3$  particles.

**Table 2.5:** Tensile properties of Mg and Mg/ $\text{Al}_2\text{O}_3$  composites.

Sl. No.	Material	0.2% YS (MPa)	UTS (MPa)	E (GPa)	Ductility (%)
1	Pure Mg*	69-105	165-205	40-44	5-8
2	Mg (Cast) **	135	196	38	12
3	Mg (PM)	132 ± 7	193 ± 2	41.2	4.2 ± 0.1
4	Mg (DMD)	97 ± 2	173 ± 1	42.8	7.4 ± 0.2
5	Mg/0.22 vol% $\text{Al}_2\text{O}_3$ (PM)	169 ± 4	232 ± 4	42.5	6.5 ± 2.0
6	Mg/0.66 vol% $\text{Al}_2\text{O}_3$ (PM)	191 ± 2	247 ± 2	43.4	8.8 ± 1.6
7	Mg/1.11 vol% $\text{Al}_2\text{O}_3$ (PM)	194 ± 5	250 ± 3	44.5	6.9 ± 1.0
8	Mg/1.11 vol% $\text{Al}_2\text{O}_3$ (DMD)	175 ± 3	246 ± 3	52.7	14.0 ± 2.4
9	AZ91/16.1 vol% $\text{SiC}_p$ ***	191	236	47.5	2

\* ASM Handbook (1990)

\*\* Saravanan and Surappa (2000)

\*\*\* Lloyd (1994)

Even though  $\text{SiC}_p$  reinforcement has been extensively used to fabricate particulate metal matrix composites, many relevant results show that the addition of  $\text{SiC}_p$  often badly reduces the ductility of magnesium, despite increasing its yield strength and elastic modulus, and therefore unfavorably affects the use of these composites in structural applications. The limited success of  $\text{SiC}_p$  reinforced magnesium matrix composites, may be chiefly ascribed to

the difference in crystal structure, and the large mismatches of coefficient of thermal expansion (CTE) and elastic modulus between SiC and Mg. Alternatively, some of the metallic particulates and intermetallics with higher strength and similar physical characteristics to magnesium can be more promising for strengthening Mg and Mg alloys. A few studies have been conducted to investigate the reinforcing effects of intermetallics, titanium, copper and nickel particulates.

Lu et al. (2003) investigated mechanical properties of magnesium-based composite reinforced by Mg<sub>2</sub>Si *in-situ* formed via mechanical milling process and observed improved yield and ultimate tensile strengths compared with magnesium alloy. Further they observed the yield strength increased with the increase in the amount of Mg<sub>2</sub>Si from 201 to 245 as Mg<sub>2</sub>Si reinforcement increased from 5 to 15%. They reported that the increase in the mechanical properties was associated with the formation of Mg<sub>2</sub>Si and refinement of microstructure. Mg-Si alloys with addition of Al exhibited a higher tensile strength than Mg-Si alloys due to the solution strengthening effect of the aluminium in magnesium.

Hassan and Gupta (2002) measured tensile properties of magnesium reinforced with fine elemental titanium particles and reported that the presence of titanium reinforcement led to an improvement of 0.2% YS and ductility while the UTS was marginally lowered as shown in Table 2.6. Perez et al. (2004) determined the mechanical properties in the temperature range of 25 to 300 °C of a Mg-10(vol%)Ti<sub>p</sub> composite. They have reported that the composite has shown a high strength (160 MPa), with a high elongation at room temperature (8%), higher than most of ceramic reinforced magnesium composites. They also observed a decrease of strength from 160 MPa at room temperature to 70 MPa at 100 °C and a high ductility at temperatures above 100 °C. Ho et al. (2004) have reported improvement in stiffness, 0.2% YS and UTS with marginal degradation in ductility of AZ91 reinforced with fine copper particles.

**Table 2.6:** Room temperature tensile properties of Mg and Mg/Ti<sub>p</sub>.

Materials	Reinforcement (vol%)	0.2% YS (MPa)	UTS (MPa)	Ductility (%)
Mg	–	100 ± 4	258 ± 16	7.7 ± 1.2
Mg/5.6 Ti	2.2	163 ± 12	248 ± 9	11.1 ± 1.4
Mg/9.6 Ti	4.0	154 ± 10	239 ± 5	9.5 ± 0.3



Xi and coworkers (2006) measured tensile properties of titanium alloy (Ti-6Al-4V) reinforced magnesium matrix composite. They have reported that the UTS, 0.2% YS and elastic modulus of magnesium alloy (ZK51) were markedly increased by the introduction of Ti-6Al-4V particles, while the ductility was decreased to some extent. They have also reported that, the addition of Ti-6Al-4V particles seems to be more beneficial for the ductility of magnesium matrix composites than the addition of SiC particles.

Lu et al. (2004) examined mechanical properties of magnesium-based composites reinforced respectively with four types of particles such as SiC, TiC, TiB<sub>2</sub> and ZrB<sub>2</sub> at different volume fractions synthesized through powder metallurgy route. They reported that the strengths of the ZrB<sub>2</sub>, TiC and SiC MMCs reinforced with 5 vol% are respectively 246, 245 and 235 MPa. The strengths of the ZrB<sub>2</sub> and SiC composites continuously increased with increased volume fraction of reinforcement while TiC composite has shown less dependent on its volume fraction. The optimal volume fraction is about 8%. Among all four composites, ZrB<sub>2</sub> reinforced composite has shown the highest yield strength and TiB<sub>2</sub> reinforced composite the lowest one. Although TiB<sub>2</sub> is an effective reinforcement used widely in Al MMCs, it did not show any strengthening effect but even weakened its matrix. The yield strength of the composite reinforced with 5 vol% TiB<sub>2</sub> has shown a dramatic reduction to 207 MPa. At 8 vol% TiB<sub>2</sub>, the strength of the MMC has approached to pure matrix.. Ductility of all the four MMCs has decreased with increased volume fraction of reinforcements. Among the four MMCs, SiC MMC has possessed the highest ductility while the ZrB<sub>2</sub> the second. TiB<sub>2</sub> MMC has shown less dependence on its volume fraction.

The mechanical properties of *in-situ* particulate composites have been evaluated by several workers. Fine *in-situ* formed reinforcing particles are dispersed more uniformly in the matrices of *in-situ* composites, leading to significant improvements in the strength, stiffness, creep and wear resistance of the composites. The superior mechanical properties of *in-situ* composites were first reported by Westwood and Winzer (1987). They showed that *in-situ* TiB<sub>2</sub>/Al particulate composites produced by XD process, exhibit moduli up to 40% higher than that of pure aluminium and improved strength retention at elevated temperatures. Kuruvilla and coworkers (1990) compared the tensile properties of *in-situ* TiB<sub>2</sub>/Al composites synthesized by XD process with those of the *ex-situ* composites containing similar amount of reinforcing phase (20 vol%). Their results are summarized in Table 2.7. Apparently, the modulus, tensile strength and hardness of the *in-situ* composite are found comparatively higher than those of *ex-situ* composite, although the *ex-situ* composite exhibits considerably improved properties compared to those of unreinforced pure aluminium. Such higher properties in *in-situ* composites were primarily attributed to fine dispersion of the high-modulus TiB<sub>2</sub> particles and cleaner interfaces leading to strong bonding with the matrix.

**Table 2.7:** Mechanical properties of pure aluminium and TiB<sub>2</sub>/Al composites.

Materials	YS (MPa)	UTS (MPa)	E (GPa)	Elong. (%)	Hardness (VHN)
Pure aluminium	64	90	70	21	37
<i>Ex-situ</i> 20 vol% TiB <sub>2</sub> /Al composite	121	166	96	16	85
<i>In-situ</i> 20 vol% TiB <sub>2</sub> /Al composite	235	334	131	7	110

Ma and coworkers (1996 and 1997) have examined the tensile properties of *in-situ* (Al<sub>2</sub>O<sub>3</sub>+TiB<sub>2</sub>)/Al particulate composites prepared by reactive hot pressing (RHP) route. They showed that increasing the amount of boron in the Al-TiO<sub>2</sub>-B system, the amount and size of intermetallic phase TiAl<sub>3</sub> are apparently reduced and more TiB<sub>2</sub> particles are *in-situ* formed, leading to a significant increase in the strength of the *in-situ* particulate composites. They reported that the yield and ultimate tensile values were 109.53 MPa and 144.76 MPa respectively in *in-situ* (10.5 vol%Al<sub>2</sub>O<sub>3</sub>)/Al composite, whereas those properties were improved to 339.74 MPa and 381.16 MPa respectively in *in-situ* (10.5 vol%Al<sub>2</sub>O<sub>3</sub>+9.5 vol%TiB<sub>2</sub>)/Al composite.

In the above studies it is observed that, modulus of elasticity, YS, UTS and hardness, have shown better properties both at room temperature as well as at higher temperatures by reinforcing magnesium alloys with particles.

## 2.5 Tribological Behaviour of Light Weight PMMCs

Friction and wear processes are inevitable when two surfaces undergo sliding or rolling under load. Friction is a serious cause of energy dissipation, and wear is the cause of material wastage. Considerable savings can be made by reducing the friction and controlling the wear. An understanding of various friction and wear mechanisms is necessary for one to make the right selection of materials, coatings, surface treatments and operating conditions for a given application.

### 2.5.1 Friction Behaviour

Friction is the resisting force tangential to the common boundary between two bodies when, under the action of an external force, one body moves or tends to move relative to the surface of the other (Suh, 1973). Friction experienced during a sliding condition is known as *sliding friction*, and friction experienced during a rolling condition is known as *rolling friction*. Despite the considerable amount of work has been devoted to the study of friction

since the early investigations of Leonardo da Vinci (15<sup>th</sup> century), Amontons (17<sup>th</sup> century), Coulomb (18<sup>th</sup> century), Suh, Archard, Rohatgi, Ray and so on (20<sup>th</sup> century) there is no much information on friction behaviour of many engineering materials. The frictional behaviour of materials is important in tribology not only because the frictional force between sliding surfaces is of interest, but also because it generally affects the wear behaviour (Rabinowicz, 1977; Suh and Sin, 1981). Frictional force is generated as a consequence of three basic mechanisms of asperity deformation, ploughing, and adhesion, are responsible for the generation of the friction force in materials.

The asperity deformation determines the static coefficient of friction and also affects the dynamic coefficient of friction, as the asperities are continuously generated due to delamination of the sliding surface (Suh, 1973). The contribution of the asperity deformation to friction is expected to be the largest when two identical metals slide against each other since the surface always remains rough. In a dynamic situation where the surfaces become smooth, most of the normal load is carried by the entrapped wear particles and the flat contacts. A frictional force can arise also due to the adhesion of two nearly flat surfaces. Bengisue and Akay (1997) focused on the friction force resulting from elastic and plastic deformation of the asperities and local friction due to adhesion between asperities of sliding pair in absence of lubricants. The force required to overcome friction will consist of the force required to shear the adhesion bond  $F_a$  and the force,  $F_d$ , required to deform elastically or plastically the obstructing asperities of the relatively softer material in the path of the asperities of the relatively harder material. If,  $L_w$ , is the applied normal load on the contacting surface, the coefficient of friction  $\mu_o$  is expressed as

$$\mu_o = \frac{F_a + F_d}{L_w} = \mu_a + \mu_d \quad (2.15)$$

where  $\mu_a$  and  $\mu_d$  are the friction coefficient due to adhesion and deformation respectively.

The ploughing component of the frictional force can be due to the penetration of hard asperities or due to the penetration of wear particles. When two surfaces are of equal hardness, the particle can penetrate both surfaces. As the surfaces move with respect to each other, grooves will be formed in one or both of the surfaces. When one of the surfaces is very hard and smooth, the wear particle will simply slide along the hard surface and no ploughing can

occur. However, when the hard surface is very rough wear particles can anchor in the hard surface and plow the soft surface. The friction due to ploughing was investigated by Sin and coworkers (1979); they showed that the contribution of ploughing to the friction coefficient is very sensitive to the ratio of the radius of curvature of the particle to the depth of penetration.

The friction of two rubbing bodies is not independent of velocity as first suggested by Coulomb. It has been shown by many researchers that friction is a function of velocity and not dependent on load alone. In general, at low velocities, friction increases with velocity and it decreases with velocity at high velocities. Friction has also been shown to depend on surface roughness. Whitehead and Archard both indicated that the effect of surface roughness is largest at light loads. For hard materials, e.g. steels, friction increases with roughness and for soft materials such as rubber, fibres and nylon friction decreases with roughness. Many research workers have indicated that, friction depends on material properties such as hardness, surface energy, strain, density, shear strength, modulus of elasticity, recrystallization temperature, yield and tensile strength. Bowden and Tabor have indicated that friction is inversely proportional to hardness, and from deformation energy considerations Tsuya has showed that the friction force is proportional to density. Friction has also been reported to depend significantly on temperature and environment. In vacuum, friction can be increased by up to 12 times, probably because of an increase in the area of contact and therefore the adhesion component of friction (Peter, 1983).

The effect of sliding distance on friction depends on the nature of initial deformation of the rubbing surfaces which is governed by surface finish, load, velocity, material properties and environment. During sliding, friction may undergo up to three distinct stages: (1) an initial stage which depends on surface finish and the nature and breakdown of oxide films; (2) a second stage consisting of plastic deformation and work hardening the near-surface layers; (3) a third stage which may involve constant microstructure or equilibrium of sliding processes, resulting from temperature stability and equilibrium of oxide formation and breakdown. Rigney and Hirth believe the steady state stage of friction to be due to the attainment of a steady state microstructure. Blau suggested that this is probably achieved by crystallographic reorientation of near-surface microstructure, giving rise to preferred crystal texture (Peter, 1983).

The coefficient of friction of various composites containing hard particles show higher coefficient of friction which may be attributed to higher deformation during asperity-asperity interaction despite reduced contribution of adhesion (Rohatgi, Liu and Ray, 1992). Rana and Stefanescu (1989) have observed a substantial decrease in coefficient of friction with increasing

volume fraction of SiC particles. However, they observed that increasing the size of SiC particles for a given volume fraction, has hardly much effect on coefficient of friction of aluminium base composites. Similarly, Roy and coworkers (1992) have observed lowering of coefficient of friction in the aluminium base composite reinforced by hard particles but particle size does not affect the coefficient of friction. But Jokinen and Andresson (1990) observed that coefficient of friction depend moderately on particle size. Sato and Mehrabian (1976) have observed that by reinforcing Al-4Cu-0.75Mg alloy by a wide range of particles like Al<sub>2</sub>O<sub>3</sub>, TiC, SiC, and silica, results in higher coefficient of friction in the composites.

Leonard and coworkers (1997) observed that the steady state coefficient of friction in SiC/A357 particulate composite is significantly higher at a load of 6 N (0.12 for alloy and 0.25 for composite). However, at load range of 28 N to 189 N, the coefficient of friction of both the alloy and composite lies in a narrow range (0.06 to 0.08 for alloy and 0.08 to 0.1 for composite). Their results thus clearly indicate that at higher applied load coefficient of friction varies marginally with applied load. Higher coefficient of friction in composite than in the alloy is expected to be due to differences in surface roughness of these two materials where, composite is having comparatively higher surface roughness because of the presence of hard particles.

Straffelini (1997) also examined almost similar kind of variation of coefficient of friction with applied load in Al<sub>2</sub>O<sub>3</sub> particle reinforced 6061 Al alloy matrix composite. On contrary to these earlier studies, Venkataraman and Sundararajan (1996) observed in SiC/Al composite, that the coefficient of friction of the composites and unreinforced alloy initially increases sharply with the applied load and reaching to a stable value at a critical applied load of 50 N. In the same way, coefficient of friction initially increases with sliding distance and reaching to a stable value after a sliding distance of 0.5 km. However, they again reported that the unreinforced alloy exhibit less coefficient of friction than that of the composite irrespective of applied load. At higher applied load, the variation in coefficient of friction in the unreinforced alloy and composite is marginal. They have not given any explanation for such kind of behaviour. One of the reasons may be the entrapment of the fine debris deformed, material at the surface and subsurface gets softer and counter subsurface adhered with each other, which lead to higher frictional force for delamination of the adhered layer. As a result, with the increase in applied load, coefficient of friction increases. But after a critical applied load, both the surfaces reach to an optimum surface conditions and the mechanism of wear may not change. This leads to a stable value of coefficient of friction.

## 2.5.2 Dry Sliding Wear

Dry sliding wear is defined by a wear process in which there is no intentional lubricant or moisture introduced into the contact area. Wear is defined by the American Society for Testing of materials (ASTM, 1993) as 'damage to a solid surface, generally involving the progressive loss of material, due to relative motion between that surface and a contacting substance or substances.' Wear has been a concern to users of metals for thousands of years. One need to consider the importance of maintaining sharp hunting knives, axes and swords to realize that the search for more wear-resistant metals dates back to metal-age. After many years of research, it has been shown that the presence of hard phases has beneficial effects on wear resistance. Wear studies are generally conducted for one or more of the following reasons:

- To understand the wear behaviour of a particular family of materials.
- To optimize or select materials for a particular application (i.e. simulation and screening).
- To understand the effects of certain variables on a particular type of wear mode or process.
- To support the development of predictive or descriptive models for wear in specific tribosystems.

Based on the nature of movement or the media involved in an interaction under load, different types of wear have been classified as follows (Sarkar, 1980): (1) adhesive wear, (2) abrasive wear, (3) corrosive wear, (4) erosive wear and (5) fatigue wear. Adhesion is the phenomenon resulting in attractive force between two surfaces in close contact. The adhesive wear of metals and alloys occurs through the formation and destruction of adhesive junctions followed by transfer, oxidation and diffusion between sliding surfaces. Adhesive wear is associated with low sliding velocity, small load and smooth surfaces. This is a universal type of wear that can occur with every machine and is hard to be eliminated but can only be reduced. To prevent adhesive wear of metals, the sliding metal couples should be chosen to have minimum tendency to form solid solutions, and this could be achieved by metals having different crystal structures and chemical properties (Rabinowicz, 1980, 1984). A critical evaluation of the assumptions of the adhesion theory of wear lead to following (Suh, 1977):

- The adhesion theory of wear assumes that the material removal due to shearing of junctions is only possible when the strength of the junction is more than the shear strength of the softer material.
- Adhesion theory does not make any concrete predictions on how the fracture occurs in any of the surfaces.
- The theory also ignores the controlling effect of friction force on the wear rate.
- Adhesion theory does not consider the structure and the mechanical properties of the materials.

The wear resulting from adhesive wear process has been described phenomenologically by the well-known Archard's equation (Archard, 1980):

$$V_w = k \frac{L_w S_w}{H_w} \quad (2.16)$$

where  $S_w$  is the sliding distance,  $L_w$  is the normal load,  $H_w$  is the hardness of the soft material and  $k$  is the wear coefficient. The wear coefficient represents the properties of the friction couple and only has real meaning provided the wear mechanisms does not change, i.e. there is no change from mild to sever wear (Eyre, 1976). In spite of the different mechanisms proposed to explain wear during dry sliding; the proposed behaviour for wear by Archard is obeyed under a variety of situation although the mechanism assumed by him may not always holds good.

Abrasive wear occurs when two surfaces, one of which is harder and rougher than the other in sliding contact. In this process, asperities of the harder surface press into the softer surface, with plastic flow of the softer surface occurring around the asperities from the harder surface. When a tangential motion is imposed, the harder surface removes the softer material by combined effects of microploughing, microcutting and microcracking. This type of wear is dangerous because it can occur suddenly with introduction of a contaminant and leads to high wear rates and extensive damage to the surfaces. Khrushchov (1974) has studied the influence of material properties on abrasive wear and has shown that in case of pure metals and nonmetallic hard materials, a direct proportionality exists between the relative wear resistance and the hardness. In addition to the hardness, the toughness (ductility) of mating materials is also important. Hard-facing processes are widely used to provide abrasive wear-resistant surfaces (Bhushan and Gupta, 1991).

In corrosive wear, the dynamic interaction between environment and mating material surfaces plays a significant role. This interaction gives rise to a cyclic stepwise process:

- In the first step, the contacting surfaces react with environment, and reaction products are formed on the surface.
- In the second step, attrition of the reaction products occurs as a result of crack formation and/or abrasion in the contact interactions of the materials.

Razavizadeh and Eyre (1982) investigated the oxidation behaviour of aluminium alloys and concluded that corrosive wear occurs by combined process of oxidation and deformation, and fracture to produce layers that are compacted into grooves in the metal surface. Oxidative surfaces become smoother with time as the troughs become filled with oxide, and oxidative wear then occurs by the fracture of platelike debris.

Erosive wear of materials and components caused by the impingement of solid particles or small drops of liquid or gas can be a life-limiting phenomenon for systems in erosive environments. The response of engineering materials to the impingement of solid particles or liquid drops varies greatly depending on the class of material, the state of materials to which those materials have been exposed and the environmental parameters associated with the erosion process, such as impact velocity, impact angle, and particle type and size. When two sliding surfaces come into contact, asperities on the softer surface are deformed by repeated loading to generate a relatively smooth surface. Eventually, asperity-plane contacts, the softer surface experiences cyclic loading as the asperities of the harder surface plough through it and finally leading to fatigue wear (Suh, 1977). For fatigue wear control all that is necessary is to design the microstructure of the materials with high hardness and toughness.

The wear resistance of the composite materials is of great interest because of their potential tribological use in automobiles, such as pistons, pistons rings, valve seats, disc rotor brakes, drums and other parts, and as a solution to many other problems like of die wear during the extrusion etc. Liu and coworkers (1992) show that in elastic-plastic materials, like composites, wear particles are generated by the following mechanisms (i) adhesion, deformation and fracture of asperities resulting from repeated single or multi asperities interaction during sliding, (ii) ploughing hard entrapped particles or hard asperities at the sliding surface and (iii) delamination caused by subsurface crack nucleation and propagation. The wear debris generated by these mechanisms forms loose particles or sometimes transfers to the counterface by mechanical interlocking or by adhesion on it. It is observed that the wear of the composites is different from the monolithic materials. Hosking et al (1982) have shown that the wear mechanism of the composite material changes from purely adhesive to mixed mode of oxidative-abrasive wear.



Surappa and coworkers (1982) reported that the wear resistance of the Al-Si alloy matrix increases linearly with hardness, while the same of Al-Si alloy reinforced by alumina particles deviates from linearity within similar range of hardness. The composite shows higher wear resistance than the Al-Si alloy due to change in wear mechanism from purely adhesive in case of aluminium alloy to oxidative abrasive in case of particulate metal matrix composite. Pan and coworkers (1990) show that chemical reaction occurs between  $\text{Al}_2\text{O}_3$  particles and steel giving rise to formation of a layer of oxides at the mating surface, which results in no weight loss after the run-in stage for the  $\text{Al}_2\text{O}_3$ -metal matrix composite. It is also reported that the presence of hard particles like  $\text{Al}_2\text{O}_3$  or SiC on the surface preferentially abrades disc material and thus promote formation of iron-rich layer on the surface. The formation of such layers and their stability was reported by Yen and Ishihara (1996) to control the wear process. Pramila et al (1992) have investigated the worn surface and subsurface under scanning electron microscope (SEM) and shown that the presence of dispersed SiC particles helps in reducing the propensity of material flow at the surface and at the same time leads to the formation of iron-rich layer on the surface.

Alpas and Zhang (1994) present the ideal wear scenario of the composite, for well bonded particles with matrix during dry sliding. They have shown that the aluminium matrix around the particles worn away and essentially all the contacts established between the reinforcement particles and the counterface material developed a contact shear stress at the particle-matrix interface causing particle decohesion. This situation have explained that the increase in area fraction or volume fraction of particles decreases the wear of the composite due to the increase of contact area between the hard particles and the counterface, where the particles act as primary load bearing component of the composite. However, as the size of the particles increased the particles are found to carry the applied load more effectively protecting the aluminium matrix efficiently. Further Alpas and Zhang (1994) have also shown in their wear experiment carried out on Al-SiC composite at low normal loads that, the SiC particles in Al-SiC composite act as main load bearing component in wear test and in respect to wear of the composite the presence of SiC particles of 15.8  $\mu\text{m}$  size is superior to SiC particles of 2.4  $\mu\text{m}$  in size at a given volume fraction of particles. However, it was observed that in presence of the comparatively smaller size particles the particles are unable to resist the loads and include in the load zone, which is called the mechanically affected zone.

Saravanan and Surappa (2000) have conducted tribological studies on pure magnesium-30 vol% SiC particle composite and reported a wear rate lower by two orders of magnitude compared to pure Mg, when tested against steel disc using pin-on disc machine.

Sanjay Kumar Thakur and Brij Kumar Dhindwa (2001) have observed strong influence of interparticle distance in cast infiltrated composites on the tribological properties of SiC<sub>p</sub> reinforced Al and Mg metal matrix composites. The unlubricated sliding wear behavior of magnesium alloy AZ91 composites reinforced with feldspar particles of size 30-50 μm have been evaluated by Sharma et al (2000). Results have indicated that the wear rates of the composites are lower than that of the matrix alloy and further decreased with the increase in feldspar content. Increase in the applied load has increased the wear severity by changing the wear mechanism from abrasion to particle cracking induced delamination wear.

Lim et al. (2003) investigated the wear behaviour of magnesium-based MMCs reinforced with SiC<sub>p</sub> during dry sliding (velocity range of 0.2-5.0 m/s) under loads of 10 and 30 N. The composites have exhibited slightly superior wear resistance under the lower load, but the effects of the SiC particle reinforcements on wear resistance are not as conclusive under the higher load. SEM examinations of the worn composites have identified the following wear mechanisms: abrasion, oxidation, delamination, adhesion, thermal softening and melting. Wang et al. (2004) tested the sliding abrasive wear rates of the unreinforced AZ91D alloy and *in-situ* TiC (5 wt%)/AZ91D composite tested under a load of 5N using a pin-on-disc apparatus. They reported that the wear resistance of the TiC (5 wt%)/AZ91D composite are higher than those of the unreinforced AZ91D alloy and improvement of wear resistance of the composite might be from the presence of TiC particulates.

Lim and coworkers (2005) studied the wear characteristics of Mg composites containing various amounts (up to 1.11 vol%) of nano-sized alumina particulates using a range of sliding speeds from 1 to 10 m/s, under a constant load of 10 N. They reported that the wear resistance of the composites improved with increasing amounts of reinforcement, which were particularly effective under the higher sliding speeds. FESEM examination identified the dominant wear mechanisms as abrasion, adhesion and thermal softening. Wear by delamination, which had been common in earlier work on Mg and Al MMCs with micron-sized reinforcements, was not evident.

### **2.5.3 Influence of Variables on Dry Sliding Wear**

The dry sliding wear of composite materials depends primarily upon microstructure of the composites which includes the particle-matrix interface, type of particles, size and distribution of particles in the matrix, volume fraction of reinforced particles and wear parameters like load, sliding distance, sliding speed, counterface material and environment. The

effect of these parameters on the wear and friction of the composites has been studied by many investigators. Under this section, a due emphasis have been given to realize the effect of experimental variables such as sliding distance, applied load, sliding speed, reinforcement volume fraction, size and type, humidity and porosity content on the dry sliding wear behaviour particulate metal-matrix composites.

#### **(a) Sliding Distance**

Wang and Rack (1991) observed the mixed behaviour of wear rate of aluminium alloy-based composites with sliding distance depending on speed, type and orientation of reinforcement. According to this investigation, composites exhibit steady state wear rate within the entire range of sliding distance (up to 3 km) when the sliding speed is less than 0.36 m/s. At higher sliding speed they examined unsteady state wear rate up to sliding distance of 1 km.

How and Baker (1997 and 1999) reported steady state wear rate decreases with sliding distance in 10 vol% saffil fibre/Al-6061 composites irrespective of applied load. Sannino and Rack (1995A) also reported similar behaviour in 20 vol% SiC/2001-Al particulate composite. This is attributed to the fact that delamination of subsurface layers generating loose debris which gives turbulent friction at the interfaces and this may be the dominating wear mechanism. However, after prolonged duration transferred layer may be discontinued and locally fused to cause adhesion kind of wear.

#### **(b) Applied Load**

Pramila Bai and coworkers (1992) reported addition of 20 vol% SiC<sub>p</sub> to a Al356 alloy improves the wear resistance due to decrease in the tendency of material flow at the surface. The increased wear resistance of composite is attributed to strain energy dissipation (due to fracture and fragmentation of reinforcement), formation of hardened layer (due to fracture and realignment of reinforcement in the matrix) and more load bearing capability of the reinforcement. The hardened layer in the alloy reported to be deeper than that in composite. As the hardened layer is plastically constrained, more surface crack may be generated at the substrate/mixed layer interface and in the alloy a greater depth of delamination may take place. Additionally, the hardened layer of the composite is harder than that of the alloy, which also increases the load bearing capacity of the composite.

Alpas and Zhang (1992A, 1992B and 1993) noted three regime of wear when considering the effect of load on the wear resistance of the alloy and composites. They reported at least two folds increase in wear resistance of the composite with respect to its base alloy at a load of less than 15 N. However, at higher load regime, alloy and composite exhibit almost similar wear performance. This is attributed to fracture of silicon carbide particle ( $\text{SiC}_p$ ), which leads to decrease in load bearing capacity of these particles under high load conditions. Higher wear resistance of composite may be attributed to the fact that addition of alumina improves elevated temperature strength and thermal stability of the alloy and thus restrict adhesive wear. Increase in transition load of aluminium due to addition of 10 to 40 vol% SiC particles was reported by Venkatanaman and Sundararajan (1996). They also reported that the transition load could not be correlated with the bulk hardness of material.

Jiang et al. (2003) reported wear rate of the unreinforced AZ91 twice as large as that of *in-situ* 10 vol% TiC/AZ91 composite at all loads tested under loads ranging from 5 to 35 N. Improvement of wear resistance of the composite might be resulted from the presence of TiC particles. Ma et al. (2005) studied the sliding abrasive wear rates of *in-situ* 5 wt% ( $\text{TiB}_2$  - TiC)<sub>p</sub>/AZ91 composite under contact loads of 5N and 35N at a constant sliding using a pin-on-disc apparatus. They reported that the presence of  $\text{TiB}_2$  and TiC particulates in AZ91 has a significant improvement in wear resistance of the composite.

### (c) **Sliding Speed**

Wang and Rack (1991A) observed that initial wear rate, at a distance of 0.3 km, of the unreinforced alloy and  $\text{SiC}_p$  (particles) or  $\text{SiC}_w$  (whiskers) /Al composite are almost same. But, at higher sliding speed, the wear rate of composite is significantly less than that of the unreinforced alloy. They also observed that the steady state wear rate of unreinforced alloy increases monotonically with the sliding speed. On the other hand, steady state wear rate of composite decreases with increase in sliding speed. Roy and coworkers (1992) also made similar observation. With the increase in sliding speed, the steady state temperature of both the unreinforced alloy and composite increases linearly. At relatively higher sliding speed of 3.9 m/s, the surface temperature rise in the composite is almost half of that of the unreinforced alloy. Wilson and Alpas (1997) constructed a wear mechanism map for temperature rise, wear rate and wear mechanism. The maps clearly demonstrate that all these facts are the results of interaction of load and sliding speed. With the increase in sliding speed, the transition load decreases and surface temperature increases.

Wilson and Alpas (1997) reported that the 20 vol% SiC/Al356 particulate composites exhibit less wear rate than that of unreinforced alloy and the transition load of both the unreinforced alloy and composite is a strong function of sliding speed. The wear rate of the unreinforced alloy increases monotonically with sliding speed. But the composites exhibit almost a steady state wear rate up to a sliding speed of 1 m/s. These investigators reported that the transition load for severe wear decreases with the increase in sliding speed and the transition load of the composite, which is significantly higher than that of the unreinforced alloy. Depending on the applied load and speed, the wear mechanism varies. According to this investigation, unreinforced alloy exhibits higher wear due to localized melting, brazing and delamination at relatively slow speed and lower applied load. But the ceramic reinforcement enhances the high temperature strength and produced harder and thermally stable mixed layer over the specimen surface. Thus, these particles increase the transition speed to sever wear.

However, other investigators Alpas and Zhang (1994) have reported that for each load there is a critical sliding speed, where the wear rate changes from moderate wear rate to severe wear rate. They have also found that for each sliding speed there is a critical load, where the wear rate changes from mild wear rate to severe one and in general the wear rate and friction increases with the increase of the sliding speed.

#### **(d) Reinforcement Volume Fraction**

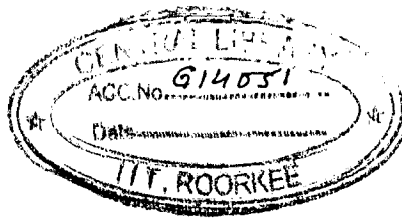
Many researchers have demonstrated that the wear rate of PMMCs decreases significantly with increase in volume fraction of reinforcement. However, there are cases in which wear properties deteriorate with increase in volume fraction of reinforcement after certain limits. Sato and Mehrabian (1976) have observed that there is reduction of wear rate by a factor of four when Al-4%Cu-0.75%Mg alloy is reinforced by a wide range of particles like Al<sub>2</sub>O<sub>3</sub>, TiC, SiC and SiO<sub>2</sub>. Surappa and coworkers (1982) have observed that when reinforced with 5 wt% of Al<sub>2</sub>O<sub>3</sub>, both Al and Al-Si alloy show improved wear resistance. Anand and Kishore (1983) have also observed a similar effect of continuous decrease in wear rate with increasing corundum content in Al-Zn alloy up to 30 wt% of corundum. Zam Zam (1989) has observed that there is an improved wear resistance in composites reinforced by hard particle of SiC only up to a critical volume fraction and beyond it the wear resistance deteriorates. This critical volume fraction depends on the applied load. But Alpas and Embury (1990) observed a marginal decrease in wear rate when 2024 Al alloy was reinforced by 20 wt% of 14 μm SiC particles although the hardness was almost double. Jokinen and Andresson (1990) have observed that in 6061 Al alloy reinforced with 20 wt% of SiC particles, the wear rates reduced in the composites at low loads resulting in contact stress of 3.2 MPa but not under heavy loads

corresponding to contact stress of 12.7 MPa. Roy and coworkers (1992) have observed that the wear rate in composites reinforced with hard particles decreases but it depends only on volume fraction but not on the type and size of particles.

Venkataraman and Sundararajan (1996) observed that the transition load as well as wear or seizure resistance of pure aluminium could be increased significantly with the increase in SiC particle content. They reported that the transition load for Al, 10 vol% SiC/Al and 4 vol% SiC/Al are 45, 120 and 1200 N respectively. They also tried to correlate transition load with the hardness. It is observed by these investigators that even the hardness of other aluminium alloy is higher than that of composite; the transition load is noted to be less than that of the composites. They explained on the basis of different nature of mechanically mixed layer in alloy and composites, subsurface cracking and microstructural change. It is reported that the transition load increases with increase in hardness and thickness of mechanically mixed layer.

Laden and coworkers (2000) observed that addition of 4 vol% SiC particles improves considerably the wear resistance of SiC/Al-390 brake disc and it is further improved by increasing SiC content from 4 vol% to 8 vol% SiC. It is interestingly noted by these investigators that in case of 8 vol% SiC brake disc, a blackish transformed layer of a hardness value of 700 HV entirely covers the surface after several braking cycles. But at lower particle contents this layer was noted to be discontinuous and thus leads to higher wear rate. Hutchings and coworkers (2000) also made an attempt for predicting the effect of Al<sub>2</sub>O<sub>3</sub> particle content on the steady state wear rate of Al6061 alloy through the use of rule of mixture. After experimental verification, they suggested that if the reinforcing particles are strongly bonded with the matrix, wear resistance of the composite would improve linearly with the increase in particle volume fraction. At the same time they concluded that the counterface would be subjected to more wear with the increases in particle content.

Wang et al. (2004) evaluated the abrasive wear rates of magnesium metal matrix composites reinforced with 10, 20 and 30 vol% TiB<sub>2</sub> particulates fabricated by powder metallurgy. They reported that the wear resistance of Mg MMCs has increased with the increasing of the reinforcement volume fraction. This was due to the strong particulate-matrix bonding and high hardness of the TiB<sub>2</sub> particulate. Further reported that the addition of only 10 vol% TiB<sub>2</sub> to magnesium matrix has lead to a sharp reduction in volume wear rate. But the volume wear rates of the composites appear to decrease slightly with the increasing of TiB<sub>2</sub> volume fraction from 10% to 30%. Wang et al. (2006) investigated the wear behaviour of AZ91 matrix composites containing various amounts (2, 5 and 7.5 wt%) of fine TiB<sub>2</sub> (~7 µm) particulates and reported that as compared with as-cast AZ91, wear resistance TiB<sub>2</sub>/AZ91 composite was higher and increased with increasing of TiB<sub>2</sub> content.



**(e) Reinforcement Size**

Jokinen and Anderson (1990) observed that for low load condition, the composite with SiC particles having a size of 13  $\mu\text{m}$ , leads to promising improvement in wear resistance as compared to the unreinforced alloy. But when the size of the particle is reduced to 5  $\mu\text{m}$ , composite suffers from inferior wear resistance. Rana and Stefanescu (1989), however, examined no such improvement in wear performance when particle size is increased from 50 to 100  $\mu\text{m}$ . Straffelini and coworkers (1997) reported that finer particle size resulted in significant improvement in wear resistance especially at higher applied load (200 N). They observed decohesion between coarse SiC particle and the matrix. The plastic constraint effect exerted by coarse and non-deformable SiC particles leads to higher localized stress concentration that facilitates such decohesion. These SiC particles damaged the surface oxide layer and produces naked material surface resulting in higher wear rate.

Alpas and Zhang (1992A and 1992B) reported that at a sliding speed of 0.16 m/s and lower applied load of 17.2 N, the wear resistance of SiC/A356 particulate composite could be improved significantly by increasing the size of SiC particle from 9  $\mu\text{m}$  to 18  $\mu\text{m}$ . However, at harsh wear condition, no significant improvement is noticed because of coarser SiC particle. But the transition load is reported to be improved to a great extent. At mild wear condition, coarser particles provide greater protection as these are less stressed and also more effective to form a transferred or mixed layer over the specimen. But after a critical applied load, these particles may fracture and cause delamination of oxide layer or mixed layer. Sannino and Rack (1995B) observed that wear resistance of the SiC/Al2009 composite decreases with an increase in size of SiC particle. They conferred that adhesion and micro-ploughing were predominant for smaller SiC particles, but degree of particle fracturing, subsurface delamination and flake removal increases with the increase in particle size. On contrary to aforementioned, Roy and coworkers (1992) reported that the wear rate in their composite which is reinforced with hard particles does not depend on the type and size of particles.

**(f) Type of Reinforcement**

Wang and Rack (1991) observed that at slower speed, less than 1 m/s, SiC particle provide better wear resistance as compared to SiC whisker reinforced composite. But at higher speed SiC whisker proved to be superior to that of SiC particle reinforced one. Abrasion and delamination of oxidative wear surface may characterize the mild wear of the alloy. As the stress concentration could be higher in SiC whisker composite, there would be greater possibility of fracturing of these whiskers, which facilitates abrasion and delamination of

oxidative layer from the specimen surface. But at higher speed, the temperature increases to a level where a more stable mechanically mixed layer is produced in which the whiskers are embedded and align themselves in sliding direction and thus protecting removal of wear debris. In case of particle, the SiC may help in delaminating the mixed layer by their abrading action.

Roy and coworkers (1992) made systematic study to examine the effect of different kinds of reinforcement on the dry sliding wear of particulate composites. B<sub>4</sub>C reinforcement leads to maximum improvement in wear resistance and reduction in coefficient of friction irrespective of applied load. They further reported that at lower applied load SiC, TiB<sub>2</sub> and B<sub>4</sub>C particles provide almost same performance. They also stated that reinforcement having higher wear resistance would lead to more improvement in wear resistance of the composite. Whereas, Roy and coworkers (1992) have shown that there is no effect of the type of particle on the wear rate under dry sliding, while they have observed that with an increase of the applied load, at constant sliding speed, Al<sub>2</sub>O<sub>3</sub> particles fracture and the wear rates of the composites increase to levels comparable to those of the unreinforced alloy. The transition to this region was delayed at higher loads in composite with a higher volume fraction of particles.

Straffelini and coworkers (1997) reported that Al<sub>2</sub>O<sub>3</sub> particle reinforced Al composite leads to better wear resistance as compared to SiC reinforced one even though the hardness and fracture toughness of the later one is greater than the former one. The probable reason may be Al<sub>4</sub>C<sub>3</sub> carbide formation between SiC and matrix, which makes the interface brittle and results in pull out of SiC particles during sliding process. On the other hand swelling of fine Al<sub>2</sub>O<sub>3</sub> may help in forming a stable transferred layer. On the contrary, Hosking and coworkers (1982) reported that SiC reinforced composite is superior to Al<sub>2</sub>O<sub>3</sub> reinforced one for improving the wear resistance of the alloy because of the former one possess superior hardness and toughness than the later one. Wilson and Alpas (1997) reported that wear rate of 20% SiC/A356 particulate composite is almost invariant to the type of reinforcement and heat treatment.

Laden and coworkers (2000) reported that composite reinforcing with spherical morphology of SiC particle exhibits significantly higher wear resistance as compared to that with angular one. In the former one, friction may be sliding rather than ploughing which was observed in the later one. The sharp corners of the SiC particle result in abrasive friction mechanism and resulting in pull out of the SiC particle from composite. Fracturing tendency of SiC particle increases due to large stress concentration in and around the angular particles. Additionally, a broken angular particle also reduces the toughness of mixed layer or oxide layer.

### **(g) Humidity Content**

A relatively little works are available in the open literature for the influence of humidity on the tribological behaviour of the materials. Yen (1997) has reported some



interesting observations over the effect of humidity on the friction and wear of Al-Si eutectic alloy. It has been shown that the moisture content has a significant effect on the friction and wear of Al-Si alloy. The wear rates decrease by two orders of magnitude as the relative humidity increases from 3% to 100%, while the friction coefficient has a higher value at those humidity.

#### **(h) Porosity Content**

The effect of porosity on the wear and friction coefficient of metals has been studied by Vardavoulias and coworkers (1993) and reported that the pores enhance the surface roughness of the material, decrease the real contact area between two sliding parts and consequently increase the contact pressure and promote particles detachment during sliding. Suh (1977) has observed that the increase in porosity content of the composites reduces the required length of crack propagation to link-up with other cracks to cause delamination.

From the detailed discussions on wear rates of different PMMCs, it is apparent that there are divergences. It may be due to processing which may decide the state of interfacial bonding. If the hard particles are not well bonded, there might be easy de-bonding of the particles resulting in increased contribution to wear rate more than compensating the decrease in the real area of contact due to increased hardness.

## **2.6 Problem Formulation**

Critical review of the published literature reveals the art of incorporation of ceramic, intermetallic or metallic particulate reinforcement into a ductile matrix has led to a promising class of material called particulate metal-matrix composites (PMMC). Magnesium MMCs have demonstrated mechanical properties similar to those of aluminum MMCs, and they can be used for similar lightweight structural and functional components for automotive and aerospace applications to further decrease cost of transportation, environmental pollution by lowering fuel consumption. The advantage of magnesium based MMCs compared with aluminium based MMCs is that the former allow a weight saving of approximately 20-25% for the same structural application. Magnesium based MMCs also provide similar tribological performances, better castability and dimensional stability, and superior machinability compared with aluminum alloys and aluminium based MMCs (Kevorkijan et al., 2003). Among the various ceramic reinforcements, SiC is most widely used as particle reinforcement in magnesium based composites because of its relatively better wettability and stability in magnesium melt.

However, SiC particles drastically decrease ductility of magnesium matrix. Additionally, there is a large mismatch of coefficient of thermal expansion and elastic modulus between SiC and magnesium. In recent years, the particles of TiC, TiB<sub>2</sub>, B<sub>4</sub>C and Al<sub>2</sub>O<sub>3</sub> have also received attention as particle reinforcement for magnesium based composites. The present study explores the possibility of reinforcing Mg-Al alloy by Mg<sub>2</sub>Si and Al<sub>3</sub>Ti, possessing outstanding features as mentioned in the following paragraphs. Compared with other manufacturing techniques of producing particle reinforced magnesium based metal matrix composites (MMCs), stir casting costs as little as one-third to one-tenth for mass production (Surappa et al., 1997) and therefore the stir casting route of synthesis of MMCs has been extensively explored. In addition, magnesium based composites fabricated by this method may lead to near net shape manufacture by using conventional foundry techniques.

Increasing demand for lightweight materials in automotive and aerospace applications, magnesium and its alloys are increasing attention of the scientific community and the industry (Jambor and Beyer, 1997; Friedrich and Schumann, 2001). Typical examples of the components made out of magnesium and its alloys for automotive application include valve covers, intake manifolds, cog tooth sprockets, automotive pulley, oil pump cover, transmission castings, engine castings and cylinder liner (Friedrich and Schumann, 2001; Mordike and Ebert, 2001). According to an industry review in 1998, there are 60 different types of components, from instrument panel to engine components, in which magnesium is used or is being developed for use. The use of magnesium in automobile parts is predicted to increase globally at an average rate of 15 % per year (Lee et al., 2000).

A light-grey coloured alkaline-earth metal, magnesium (Mg), has a density (1.74 g/cm<sup>3</sup>) approximately two-thirds that of aluminium and one-fifth that of iron, and a melting point (650 ± 2 °C) very close to that of aluminium. It has a hexagonal crystal structure with lattice parameters  $a = 0.32092$  nm and  $c = 0.52105$  nm (Polmear, 1995). Besides ultra lightness, magnesium possesses a relatively high thermal conductivity (155 W/(kg K) at 25 °C), relatively low CTE (25.2 x 10<sup>-6</sup> K at 20 °C) high damping capacity, excellent castability and superior machinability. Its excellent machinability is characterized by low power requirements (about 80% of Al, 25% of CI or 15% of MS) long tool life (four to five times greater than aluminium), excellent surface evenness and small fragmented chips (Metal Handbook, 1990; Friedrich and Mordike, 2006; Videm et al. 1994).

Aluminium is a preferred alloying element for magnesium alloys. It improves strength and hardness and widens freezing range and improves the castability. When present in amount

in excess of 6 wt%, the alloy becomes heat treatable, but commercial magnesium alloys rarely exceeds 10 wt% of aluminium. An aluminium content of 6 wt% yields the optimum combination of strength and ductility. The solubility limit of aluminium at the eutectic temperature is 11.5 at% (12 wt%) and falls to about 1% at room temperature. Above the solubility limit  $Mg_{17}Al_{12}$ , a brittle intermetallic, precipitates out and consequently plays a dominant role in determining the properties. The creep resistance is limited in these alloys due to the poor thermal stability of the  $Mg_{17}Al_{12}$  phase. The commercial alloys based on Mg-Al involve further alloying additions of zinc, e.g., AZ91, AZ81 and AZ63 (Davis, 2003; Friedrich and Mordike, 2006). In the present work, Mg-Al alloy with Al content similar to commercial magnesium alloy, AZ91 (contains 8.5-9.5 wt% Al), has been selected as matrix material.

A wide range of materials such as oxides, carbides, borides or nitrides in the form of particles, short fibres, long fibres, whiskers or hybrids (particles + short fibres/whisker) can be used as reinforcements for magnesium MMCs (Friedrich and Mordike, 2006). Intermetallics ( $Mg_2Si$ ,  $Al_3Ti$ , etc.) or fine metallic particles (Cu, Ti, Ni particulates) can also be used as reinforcement for Mg-MMCs (Hassan and Gupta, 2002; Lu et al., 2003; Lu et al., 2003; Tsuzuki, 2004; Perez et al., 2004; Ho et al., 2004; Wang et al., 2004; Jiang et al., 2005; Huashun, 2006). The chemical reaction between particles and matrix alloy has to be taken in to consideration while choosing the particles for tailoring a MMC. Magnesium alloy melt generally shows chemical reactivity with most other materials. As a result, the particles are often chemically attacked or even totally converted into a different phase. However, this problem may not be there in *in-situ* magnesium MMCs, because reinforcing particles are formed *in-situ* in the melt during synthesis of the composites. The particle reinforced MMCs always show isotropic behaviour due to the symmetry of nearly spherical shape. In the case of magnesium MMCs, the low density also plays an important role in the homogenous particles distribution.

Considering the different factors, the choice of reinforcement in our current investigation has been narrowed down to *in-situ* formed ceramic particle,  $Al_2O_3$  and intermetallics,  $Al_3Ti$  and  $Mg_2Si$ , which are expected to remain stable in magnesium alloy matrix at elevated service temperatures. These reinforcement phases are expected to serve the interest of automobile industries in the contest of their need for new materials to be employed in various structural and tribological applications. The important properties of magnesium and reinforcement phases are given in Table 2.8.

**Table 2.8:** Important properties of magnesium and reinforcement phases.

Material	Density, $\rho$ (kg/mm <sup>3</sup> )	Melting point, (°C)	Young's modulus, E, (GPa)	CTE (K <sup>-1</sup> )	Crystal structure	Colour
Mg	1740	649	40	$25.2 \times 10^{-6}$	hcp	light-grey
$\alpha$ -Al <sub>2</sub> O <sub>3</sub>	3400	2050	---	---	hexagonal	white
Al <sub>3</sub> Ti	3300	1350	220	---	tetragonal	---
Mg <sub>2</sub> Si	1990	1085	120	$7.5 \times 10^{-6}$	cubic CaF <sub>2</sub> type	bluish- grey

Aluminium oxide commonly referred to as alumina, Al<sub>2</sub>O<sub>3</sub>, possesses strong ionic bonding giving rise an excellent combinations of properties. Alumina is chemically inert and has a high melting point, high electrical resistance and high hardness (Foltz and Blackmon, 1997). It can exist in several crystalline phases which all revert to the most stable hexagonal alpha phase at elevated temperatures. This is the phase of particular interest for structural and tribological applications.

Al<sub>3</sub>Ti is an ordered intermetallic compound offering lighter weight, high strength and hardness. It has a tetragonal crystal structure with lattice parameters  $a = 0.3848$  nm and  $c = 0.8596$  nm. Al<sub>3</sub>Ti has low density (3.3 g/cm<sup>3</sup>), high melting point (1350 °C), high elastic modulus (~220 GPa). Al<sub>3</sub>Ti also has an excellent resistance to oxidation and corrosion in fluoride atmosphere (Nakamura and Kimura, 1991; Wang et al., 2004; Tjong et al., 2003; Nayak and Murty, 2004). At present, this is the phase of particular interest for many researchers to use as a good candidate of *in-situ* reinforcement for MMCs for structural and tribological applications. It has strong interfacial bonding with many metal and alloy matrices.

Wang et al. (2004) reported production of Al<sub>3</sub>Ti particulates in two different morphologies in the *in-situ* Al-Al<sub>3</sub>Ti MMCs, both nominally equiaxed (blocky) and plate or needle-like (flaky). The blocky particulates have a small aspect ratio, whilst the aspect ratio of the flaky Al<sub>3</sub>Ti particulates is large. The flaky Al<sub>3</sub>Ti forms by growing along its  $\langle 1\ 1\ 0 \rangle$  direction of dendrite arms at high temperature and moderate cooling rate, whilst the blocky particulates grow in both  $\langle 1\ 1\ 0 \rangle$  and  $\langle 0\ 0\ 1 \rangle$  directions under super saturation of titanium in the melt of the system. The size of Al<sub>3</sub>Ti apparently increases with increasing Al<sub>3</sub>Ti content. Huashun et al. (2006) have also reported changing of morphology apparently from fine particle, needle-like to large block with increasing Al<sub>3</sub>Ti content, as observed in Al-Al<sub>3</sub>Ti

composites prepared by the direct reaction of Ti and Al in aluminum alloy melt. Further they claimed that the addition of magnesium can markedly change the morphology of  $\text{Al}_3\text{Ti}$  and reduce their size. Short rod-like  $\text{Al}_3\text{Ti}$  was formed and homogeneous distribution was obtained with the addition of 3 wt% Mg.

Magnesium forms only one compound with silicon,  $\text{Mg}_2\text{Si}$  (36.6 wt%), which crystallizes in a cubic  $\text{CaF}_2$  type lattice with a lattice constant  $a = 0.635$  nm. The atom centers of this structure form a lattice analogous to that of the diamond. Bonding in this compound is essentially covalent, the ionic component representing not more than 25% (Dvorina et al., 1969).  $\text{Mg}_2\text{Si}$ , intermetallic compound, is a bluish-gray powder. The  $\text{Mg}_2\text{Si}$  exhibits a high melting temperature (1085 °C), light weight, high strength, high hardness ( $4.5 \times 10^9$  N/m<sup>2</sup>) and low coefficient of thermal expansion ( $7.5 \times 10^{-6}$  K<sup>-1</sup>).  $\text{Mg}_2\text{Si}$  also has got a low density of  $1.99 \times 10^3$  kg/m<sup>3</sup> and a reasonably high elastic modulus of 120 GPa.  $\text{Mg}_2\text{Si}$  has high corrosion-resistance in addition to excellent mechanical properties (Dvorina et al., 1969; Jiang et al., 2005; Serikawa et al., 2006). With these properties,  $\text{Mg}_2\text{Si}$  has attracted much interest as a potential reinforcement candidate for the metal matrix composites for aerospace, automotive, and other applications (Lu et al., 2003; Tsuzuki, 2004; Jiang et al., 2005).  $\text{Mg}_2\text{Si}$  reinforcement forms stable interface with the metal matrices especially with aluminium alloy and magnesium alloys and has the potential for cost reduction of the metal matrix composites (Zhao et al., 2004).

The present study aims to develop magnesium based composite containing reinforcements of intermetallic compounds like  $\text{Al}_3\text{Ti}$ ,  $\text{Mg}_2\text{Si}$  and alumina. To generate these reinforcements *in-situ* the base alloy should contain aluminium, which may ensure thermodynamic stability of the reinforcing phases containing aluminium. The commercial Mg-Al alloy is AZ91 which has around 9 wt% of aluminium apart from about 1 wt% zinc and so, Mg-9 wt% Al alloy has been chosen as the matrix. Earlier *in-situ* composites containing alumina and  $\text{Al}_3\text{Ti}$  have been synthesized by displacement reaction between relatively cheaper oxides and molten aluminium. But a direct displacement reaction with the melt of Mg-Al alloy may not result in the desired phases and the undesirable hygroscopic oxide like MgO may form in considerable quantity. Thus, the idea of a two stage solidification processing emerged. In the first stage aluminium based composite will be synthesized following the known route of reaction between  $\text{TiO}_2$  particles with molten aluminium. The composite that results by solidification of the slurry containing alumina particles generated by reaction, in the molten alloy containing aluminium and titanium released from  $\text{TiO}_2$ , may be added to magnesium melt in the second stage of processing so as

to adjust the composition of the alloy to the desired Mg-9 wt% Al. It is hoped that the intermetallic and the alumina of aluminium based composite added to molten magnesium will be inherited by the magnesium based composite. If this idea succeeds then detailed investigation on the processing and the effect of varying amount of  $\text{TiO}_2$  in aluminium based composite on the mechanical and tribological properties may be carried to explore possibilities of application of such composites.

The other system that will be attempted is the magnesium based composite containing  $\text{Mg}_2\text{Si}$  as reinforcement in the same matrix of Mg-9 wt% Al alloy. For this purpose, Al-Si alloy will be prepared containing different amounts of silicon in both hypo-eutectic and hyper-eutectic range in the first stage and this alloy will be added to molten magnesium to the extent that the resulting matrix alloy reaches the desired composition. The eutectic and pro-eutectic silicon is expected to react with magnesium to result in  $\text{Mg}_2\text{Si}$  and aluminium will get alloyed with magnesium to provide the matrix of the resulting composite, where  $\text{Mg}_2\text{Si}$  will be distributed. If the processing leads to the desired composite, the processing and the composition of Al-Si alloy added on the mechanical and tribological behaviour will be investigated.

The present investigation is aimed to develop two systems of *in-situ* composites as described above following processing routes conceived for the purpose of the present study. The properties of the resulting composites will be explored in order to find their suitability for various applications.

This chapter describes design and fabrication of experimental set-up followed by the experimental procedures used in the present investigation for solidification processing of cast *in-situ* composite materials and their characterization in respect of mechanical and tribological properties. Unreinforced base alloy has also been processed in the similar way for comparison with the cast *in-situ* composites.

### 3.1 Design and Fabrication of Experimental Set-up

A batch type stircasting furnace cum pouring set-up has been designed and fabricated for solidification processing of magnesium based composites with a maximum melting capacity of 1 kg (Ray, 1993; Carreño-Morelli et al., 1998; Matin et al., 2001). The schematic diagram of the experimental set-up is as shown in Fig. 3.1 and the photographic view of the same is as shown in Fig. 3.2.

The experimental set-up mainly consists of the following parts:

1. Melting unit
2. Stirring arrangement
3. Mould chamber
4. Power supply unit
5. Argon gas supply system.

#### 1. *Melting Unit*

The melting unit consists of an electrical resistance heating vertical muffle furnace designed for a maximum input power of 2.5 kW and a maximum temperature of 1100 °C. The furnace was constructed by winding a electrical resistance heating element, Kanthal A-1 wire of gauge 16 SWG over an alumina muffle of size 150 mm × 150 mm × 300 mm, having a total resistance of 21 ohms (Cherepin and Mallik, 1967; Kanthal Handbook). One end of the muffle was kept open and the other end was closed with a hole at its centre. A suitable steel structure was designed and fabricated to assemble the furnace. Thermal insulating materials, such as ceramic wool, aulundum powder, fire-clay bricks, asbestos sheets and asbestos powder has been used in the fabrication of the furnace. For melting magnesium, a

cylindrical low carbon steel crucible (ASM Handbook, Vol. 15, 1992) having a diameter of 90 mm and 220 mm height with conical bottom with hole of 20 mm diameter was fabricated as shown in Fig. 3.1 and Fig. 3.2. The hole was closed by inserting a graphite plug in it. A lever arrangement was made for unplugging the crucible to pour the composite slurry into the mould, which is kept in the mould chamber.

## **2. *Stirring arrangement***

A stirring arrangement was made for stirring the melt in the crucible. A ½ HP electric motor, having a maximum rated speed of 4000 rpm was used to drive the stirrer. The motor was mounted centrally above the furnace by a fixture arrangement as shown in Fig. 3.1 and Fig. 3.2. The stirrer was fixed to the shaft of the motor by a screw coupling arrangement. A provision was also made for the stirrer height adjustment by moving the fixture up and down. A non-contact type speed sensor was used to measure the rotational speed of the stirrer.

## **3. *Mould chamber***

The mould chamber was mounted vertically below the furnace and inline with the muffle. It was a two-piece low carbon steel cylindrical part [Carreño-Morelli et al., 1998] of diameter 150 mm and a total height 500 mm with an easy accessibility to keep in and to take out the low carbon steel mould of size 30×30×300 mm. Two ports were provided in the mould chamber; one was for in letting the argon into the mould chamber and the other was for out letting the air.

## **4. *Power supply unit***

A power supply unit consisting of an ammeter, voltmeter, temperature controller and an autotransformer was connected to supply voltage of 240 V. A calibrated chromel-alumel thermocouple was used to measure the temperature of the furnace by placing it close to the muffle wall. A digital temperature controller in the range of 0-1550°C with a controller accuracy of ±5°C was used for maintaining the furnace temperature.

## **4. *Argon supply system***

An argon supply system was made by connecting the hose pipe to a regulator mounted on an argon cylinder and to the inlet port of the mould chamber and a ceramic tube linking to the low carbon steel crucible inside the muffle. Along with the regulator, two more valves were connected to control the flow of argon supply either to crucible or to mould chamber.



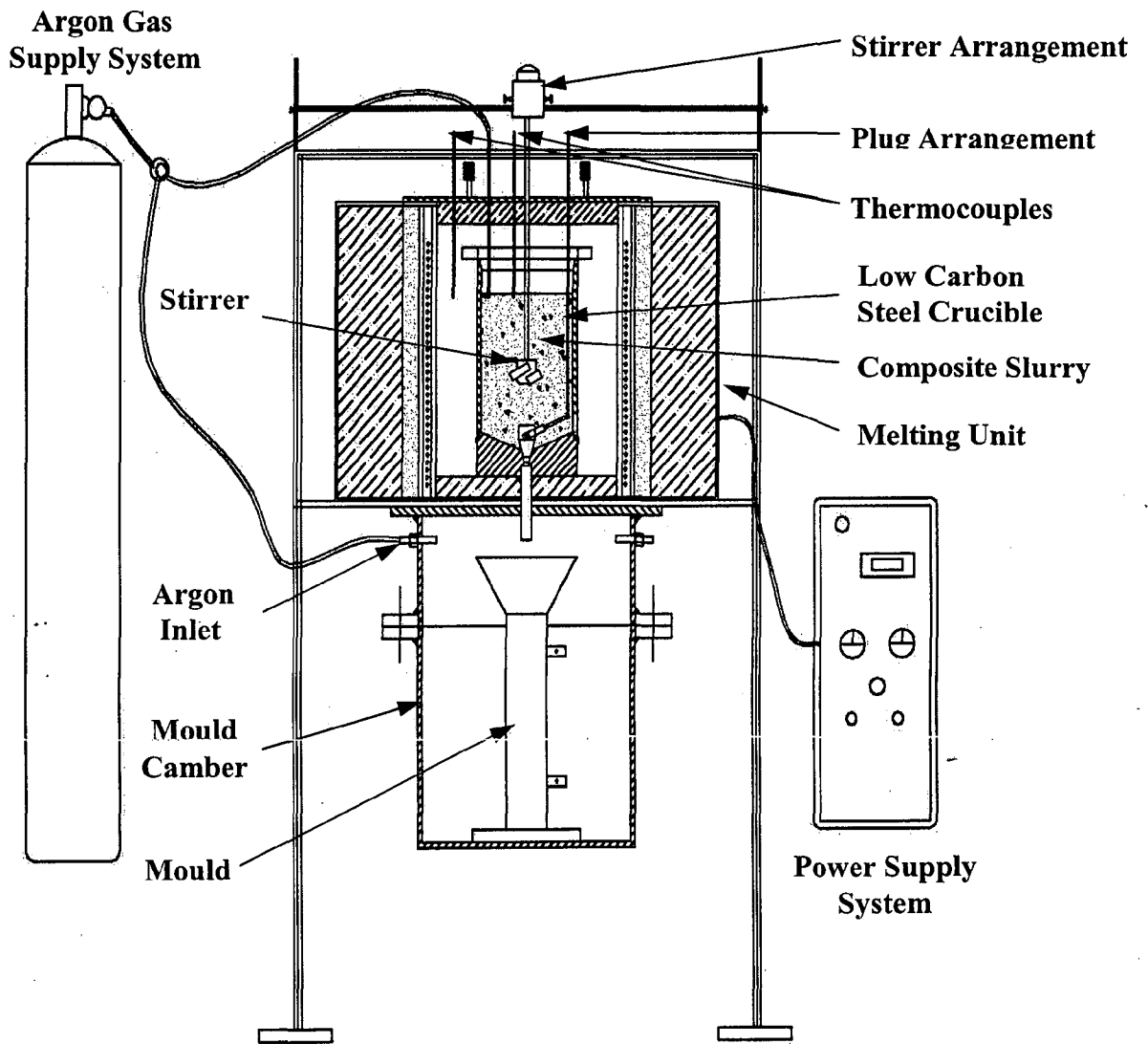


**Fig. 3.1:** Schematic diagram showing experimental set-up for stir casting used for solidification processing of cast *in-situ* composites and unreinforced base alloys.

## 3.2 Selection of Stirrer

The use of axial stirrer for agitating the molten metal or alloy would result in both axial and radial flows and their relative magnitudes could be controlled by the design of stirrer to suit a desired condition of mixing. Further, the viscosity of the mixing system, the melt-particle slurry was important. Three types of stirrer such as flat blade stirrer, turbine blade stirrer and pitched blade stirrer were commonly used for the solidification processing of composites by stircasting. In present investigation two types of pitched blade stirrers were chosen and fabricated from graphite blocks. A graphite stirrer having four pitched blades (45° pitch angle), as shown in Fig. 3.3 (a), was used in an effort to retain maximum amount of oxide particles and to result in uniform distribution of particles in the melt-particle slurry to be casted. Another type of stirrer having two pitched blades (45° pitch angle), as shown in Fig. 3.3 (b), was used in an effort to result in uniform distribution of *in-situ* generated particles in the magnesium melt-particle slurry to be casted as final *in-situ* composite.

## 3.3 Solidification Processing of *In-Situ* Composites

### 3.3.1 Materials for Processing of *In-Situ* Composites

#### (a) Matrix Alloy

Magnesium and its alloys were chosen as the matrix alloy for studies on current cast *in-situ* composites. Aluminium was chosen as the main alloying element. The chemical compositions of the commercial magnesium and aluminium, in weight percent, as determined by optical emission spectrometer (Thermo Jarrell Ash, Atom Comp 181, Franklin, USA), used in solidification processing of different cast *in-situ* composites and unreinforced alloys are given in Table 3.1.

**Table 3.1:** Chemical compositions of as received commercial magnesium and aluminium ingots.

Material	Chemical composition (wt%)								
	Si	Fe	Zn	Cr	Ni	Mn	Cu	Al	Mg
Mg-Ingot	0.040	0.026	0.028	0.000	0.017	0.013	0.061	0.031	99.784
Al-Ingot	0.103	0.192	0.091	0.043	0.032	0.009	0.023	99.479	0.028

#### (b) Reinforcement Materials

Titanium dioxide (TiO<sub>2</sub>) powder was selected as precursor oxide for generating fine *in-situ* reinforcing alumina particles and intermetallics, Al<sub>3</sub>Ti, in aluminium based composites

on the basis of reasonably fast kinetics of reduction by molten aluminium and this composite is used in the synthesis of one type of magnesium based *in-situ* composite investigated here. Low cost and easy availability of titanium oxide powder were also important considerations. TiO<sub>2</sub> powder supplied by S.D. Fine-Chem Pvt. Ltd., Mumbai, India, was having a purity and density of 99% and 3.3 g/cm<sup>3</sup> respectively. The average particle size of the TiO<sub>2</sub> powder is  $d_{50\%} = 0.9 \mu\text{m}$ , as determined in a MALVERN particle size analyzer and the result of particle size analysis is shown in Fig. 3.4. Silicon metal powder alloyed with aluminium was opted in the synthesis of another type of magnesium based *in-situ* composite, where silicon of aluminium alloy will react with magnesium to form intermetallics, Mg<sub>2</sub>Si. Silicon powder supplied by Loba Chemie Pvt. Ltd, Mumbai, India, was having a purity, density and particle size of 98.5%, 2.33 g/cm<sup>3</sup> and 74  $\mu\text{m}$  respectively.

### 3.3.2 Cast Mg-Al/Al<sub>3</sub>Ti-Al<sub>2</sub>O<sub>3</sub> *In-Situ* Composite

Solidification processing of cast magnesium alloy based composite inheriting *in-situ* generated reinforcing intermetallics, Al<sub>3</sub>Ti, and Al<sub>2</sub>O<sub>3</sub> particles has been carried out in two stages; (a) processing of cast Al-based composite for generating *in-situ* Al<sub>3</sub>Ti, and Al<sub>2</sub>O<sub>3</sub> and (b) processing of cast *in-situ* Mg-alloy based composite by addition of aluminium based composite synthesized in the first stage.

#### (a) Cast Al-based Composite Processing

About 700 g of commercially pure aluminium was melted and superheated to a desired processing temperature in a clay-graphite crucible inside the muffle furnace. Before any addition, the surface of the melt was cleaned by skimming. Prior to addition, the weighed amounts of TiO<sub>2</sub> particles were preheated to about 300 °C and the rate of addition of oxide particles was controlled at an approximate rate of 0.2-0.3 g/s. A graphite pitched blade stirrer with four pitched blades (45° pitch angle) was used to disperse the TiO<sub>2</sub> particles in the melt. The speed of the stirrer was kept constant at 600 rpm. A non-contact type speed sensor was used to measure the stirring speed. The temperature of the melt was measured by using a digital temperature indicator connected to a chromel-alumel thermocouple placed at a depth of 15-20 mm inside the melt. During stirring, the temperature of the slurry was maintained within  $\pm 10$  °C of the processing temperature. A magnesium lump of 5 wt% was wrapped in aluminium foil and plunged into the melt-particle slurry after the addition of TiO<sub>2</sub> particles. When the desired time of the stirring elapsed, the stirrer was stopped and taken out from the

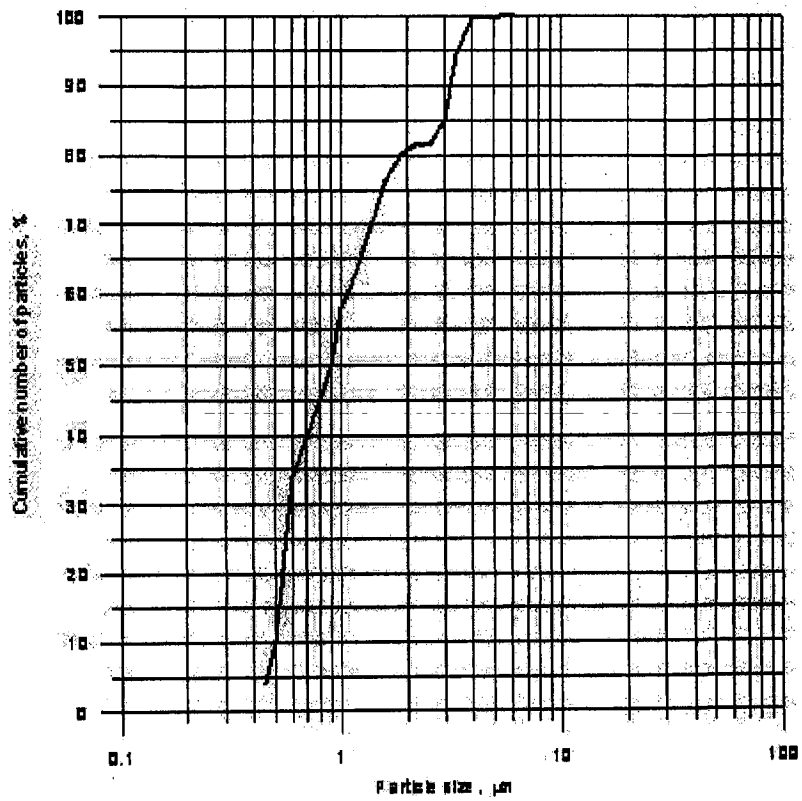


**Fig. 3.4:** Particle size analysis for as-received titanium dioxide (TiO<sub>2</sub>) particles.

crucible. Then, the crucible was taken out from the furnace and the melt-particle slurry was poured into a split type, graphite coated and preheated permanent steel mould of size 50×50×120 mm. No degassing practice of the melt or the slurry was carried out at any stage of processing. The cast Al-based composite ingot was cooled immediately by immersing in a water bath. The composite has been designated on the basis of its constituents. The first letter indicates the base metal, A in the present case for aluminium followed by T to indicate the amount of TiO<sub>2</sub> added to the aluminium based composite along with its amount in wt% separated by / and two digits of processing temperature. The scheme of variation of the constituents, their nominal amounts and processing temperatures used for solidification processing of different cast Al-based composites are shown in Tables 3.2.

**Table 3.2:** The constituents, their nominal amounts and processing temperatures used for solidification processing of different cast Al-based composites.

Cast Al-based composites with designation	Aluminium (wt%)	Magnesium (wt%)	TiO <sub>2</sub> (wt%)	Processing temperature (°C)
AT8/94	87	5	8	940
AT10/94	85	5	10	940
AT12/94	83	5	12	940
AT14/94	81	5	14	940
AT10/104	85	5	10	1040
AT10/80	85	5	10	800

### (b) Cast Mg-alloy based In-situ Composite Processing

The solidification processing of Mg-alloy based *in-situ* composites had been carried out by melting magnesium and dissolving aluminium based composite in it. About 450 g of commercially pure magnesium along with weighed amounts of different Al-based composites, both in the form of small pieces were put into the graphite coated steel crucible in the furnace. The weight percentages of different Al-based composites were chosen in such a way that to achieve aluminium content in the Mg-alloy based *in-situ* composites similar to aluminium composition in AZ91 (8.5-9.5 wt%) alloy. Earlier to putting the raw materials, the circular hole at the bottom centre of the steel crucible was plugged properly with a graphite

plug. The charge was melted and super heated to a desired temperature under argon inert atmosphere. A graphite pitched blade stirrer with two pitched blades (45° pitch angle) was used to disperse in the melt uniformly the Al<sub>2</sub>O<sub>3</sub> particles and Al<sub>3</sub>Ti intermetallics contained in aluminium based composite. The speed of the stirrer was kept constant at 700 rpm. A non-contact type speed sensor was used to measure the stirring speed. The temperature of the melt was measured by using a digital temperature indicator connected to a chromel-alumel thermocouple placed inside the melt. During stirring, the temperature of the slurry was maintained within ±10 °C of the processing temperature. After stirring for about 4 minutes, the stirrer was raised and the graphite plug was removed by operating lever arrangement so as to pour the melt-particle slurry into the split type, graphite coated and preheated permanent steel mould of size 30 ×30×300 mm, kept in the mould chamber right below the graphite stopper under argon inert atmosphere. The cast *in-situ* composite ingot was taken out immediately from the mould chamber and cooled by immersing in a water bath. The composite has been designated on the basis of its constituents. The first letter indicates the base alloy, M in the present case for magnesium followed by T to indicate the amount of TiO<sub>2</sub> added to the aluminium based composite along with its amount in wt% separated by / and two digits of processing temperature. The list of various cast Mg-Al/Al<sub>3</sub>Ti-Al<sub>2</sub>O<sub>3</sub> *in-situ* composites synthesized, Al-based composites used for these Mg-Al composites and the processing temperatures are shown in table 3.3.

**Table 3.3:** Details of various cast *in-situ* Mg-Al/Al<sub>3</sub>Ti-Al<sub>2</sub>O<sub>3</sub> composites developed by using aluminium based composites and the processing temperatures.

Designation of Cast <i>in-situ</i> Mg-Al/Al <sub>3</sub> Ti-Al <sub>2</sub> O <sub>3</sub> composites	Al-based composites used for synthesis of Mg-based composites	Processing temperature (°C)
MT8/80	AT8/94	800
MT10/80	AT10/94	800
MT12/80	AT12/94	800
MT14/80	AT14/94	800
MT12/75	AT12/94	750
MT12/85	AT12/94	850

### 3.3.3 Cast Mg-Al/Mg<sub>2</sub>Si *In-Situ* Composite

Solidification processing of magnesium alloy based composite containing *in-situ* generated Mg<sub>2</sub>Si intermetallics has been carried out in two stages; (a) processing of cast aluminium-silicon master alloy and (b) processing of cast *in-situ* Mg-based composite using the Al-Si alloy developed in the first stage.

#### (a) Al-Si Master Alloy Processing

Aluminium-silicon master alloy was processed in the same manner as that of cast Al-based *in-situ* composite discussed earlier. After melting, aluminium melt was superheated to a processing temperature of 920 °C and the elemental silicon particles were added while stirring. The master alloy is designated on the basis of constituents. The base metal is designated by A followed by the major alloying element indicated by S for silicon and its amount in the alloy in wt%, separated by / followed by first two digits of the processing temperature. The scheme of variation of the constituents and their nominal amounts used for solidification processing of different cast master alloys are shown in Tables 3.4.

**Table 3.4:** The constituents and their nominal amounts used for solidification processing of different cast Al-Si master alloys.

Al-Si master alloys with designation	Aluminium (wt%)	Magnesium (wt%)	Silicon (wt%)
AS9/92	86	5	09
AS15/92	80	5	15
AS20/92	74	5	20

#### (b) Cast Mg-alloy based *In-situ* Composite Processing

Mg-Al/Mg<sub>2</sub>Si *in-situ* composite was processed in the same manner as that of cast Mg-Al/Al<sub>3</sub>Ti-Al<sub>2</sub>O<sub>3</sub> *in-situ* composite discussed in the previous section except the stirring time and processing temperatures. The stirring time used was 3 minutes. The composite is designated on the basis of constituents. The base alloy is designated by M followed by the major alloying element of the aluminium alloy indicated by S for silicon and its amount in the alloy in wt%, separated by / followed by first two digits of the processing temperature. Details of various cast *in-situ* Mg-Al/Mg<sub>2</sub>Si composites synthesized, Al-Si master alloys used for processing of Mg-Al composites and the temperatures are shown in table 3.5.

**Table 3.5:** Details of various cast *in-situ* Mg-Al/Mg<sub>2</sub>Si composites synthesized, Al-Si master alloys used for these composites and the processing temperatures.

Designation of cast Mg-Al/Mg <sub>2</sub> Si <i>in-situ</i> composites	Al-Si master alloys used for synthesis of Mg-Al composite	Processing temperature (°C)
MS9/76	AS9/92	760
MS15/76	AS15/92	760
MS20/76	AS20/92	760
MS15/72	AS15/92	720
MS15/80	AS15/92	800

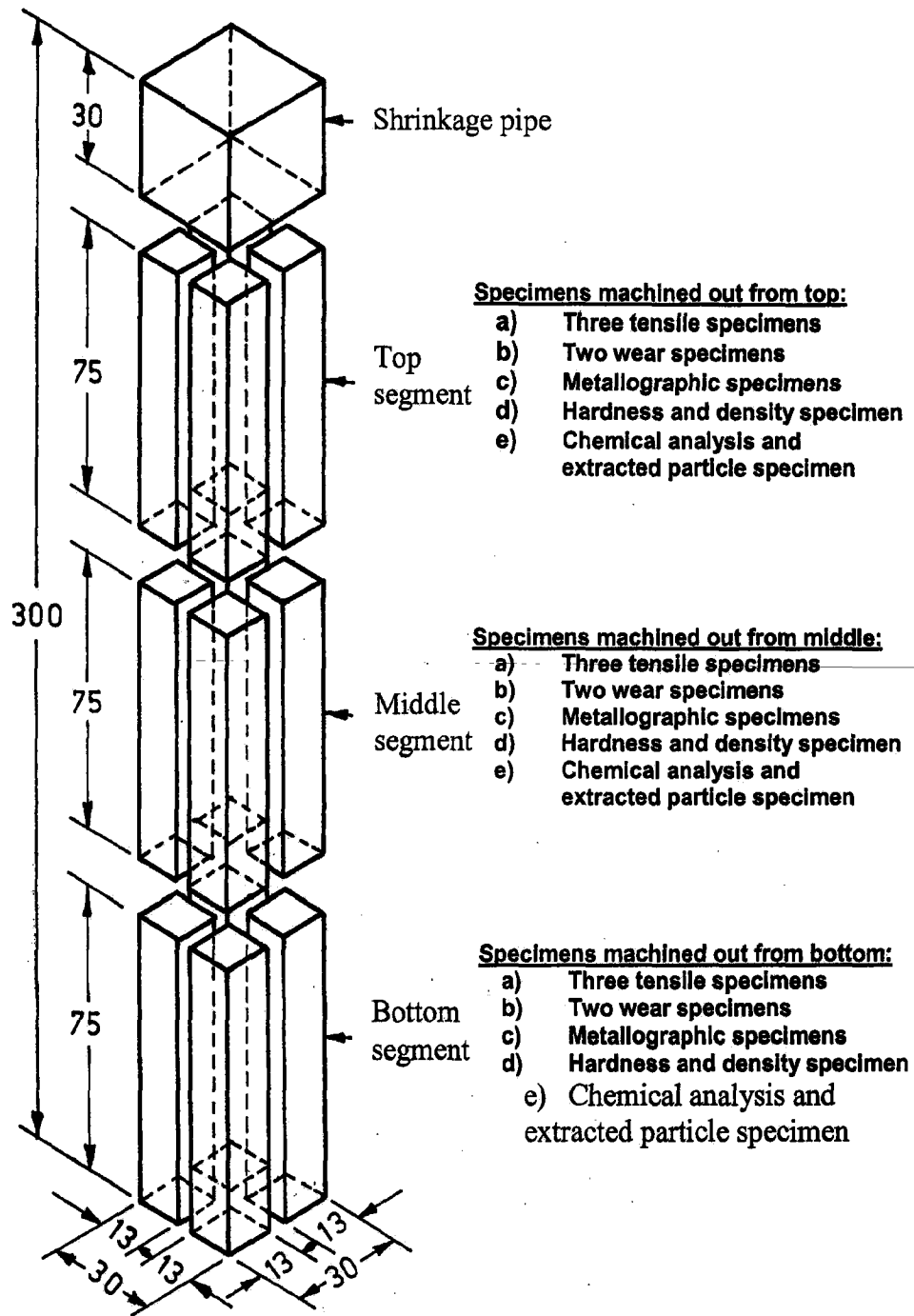
### 3.3.4 Cast Mg-Al base alloy and commercial Mg

Cast unreinforced Mg-Al alloy containing 9 wt% aluminium, similar to the aluminium content in cast *in-situ* magnesium composites, and cast unreinforced commercial magnesium were prepared using the same experimental set-up and procedures stated above. These castings were used for comparison of microstructures, mechanical and tribological properties with those obtained in the different cast *in-situ* magnesium composites.

## 3.4 Specimens Location

In order to investigate the microstructure, the distribution of reinforcing particles, the porosity and the resulting mechanical and tribological properties, the height of the cast ingot below the shrinkage pipe was divided into three equal segments designated as the bottom, the middle and the top as shown schematically in Fig. 3.5. At least three tensile specimens, two wear specimens, and one metallographic specimen were machined out from each segment. All the microstructures, porosity content, particle content, hardness and tensile properties reported in the present study relate to those observed in the middle height segment of the cast ingot unless mentioned otherwise.





All dimensions are in mm.

**Fig. 3.5:** Location of the test specimens machined out from the bottom, the middle and the top segments of the cast ingot of *in-situ* composite.

### 3.5 Chemical Analysis

The chemical composition of the matrix alloy of cast *in-situ* composites was analysed by GBC AVANTA-M Atomic Absorption Spectrometers (AAS), Victoria, Australia. A known mass (about 10.0 g) of cast *in-situ* composite was dissolved in a suitable chemical reagent, 1.5M hydrochloric acid, for selective dissolution of the magnesium alloy matrix (Handbook of Chemistry and Physics, 1981). The filtered solution was further diluted 1000 times by using ultra pure distilled water. For calibration purpose a standard solution of each element was prepared by dissolving pure metallic elements and then analysed by AAS to determine the amount of titanium/silicon and other elements in the matrix alloy of cast *in-situ* composite. For each cast *in-situ* composite the chemical analysis was carried out by collecting samples from their bottom, the middle and the top to arrive at the reported average chemical composition of the matrix.

### 3.6 X-Ray Diffraction Analysis

The residue (insoluble oxides) obtained from the above procedure of particle extraction, were filtered out using ashless filter paper, which is completely burnt by heating at about 700 °C for 2 hours. The oxide particles left were cooled and subjected to X-ray diffraction study with a D8 Advance, Bruker axs, Karlsruhe, Germany, X-ray diffractometer in the two theta range of 20°-100° using CuK<sub>α</sub> radiation target and nickel filter. The Goniometer speed was 2°/Min. In the same way, X-ray diffraction analysis was carried out for powder samples of the cast *in-situ* composites prepared by grinding the composites with the help of a hard jeweller's file in order to determine the constituent phases present in the *in-situ* composites. For all the intensity peaks and corresponding values of  $2\theta$ , the interplanar spacing,  $d$ , was estimated using Bragg's law

$$\lambda = 2d \sin\theta \quad (3.1)$$

where,  $\lambda$  is the wavelength of CuK<sub>α</sub> radiation used for diffraction and was taken as 1.5413 Å for estimating the  $d$  values, which was used for identification of various phases with the help of inorganic JCPDS X-ray diffraction data cards.

## 3.7 Microstructural Studies

### 3.7.1 Optical Microscopy and Scanning Electron Microscopy (SEM)

The scheme of sectioning the cast ingot of *in-situ* composite, as shown in Fig. 3.4, was used to prepare specimens for metallographic studies. Three sections collected from the bottom, middle and top segments of each cast ingots of the *in-situ* composite were prepared by standard metallographic procedure for metallographic examination under optical microscope, Olympus, PME3, Tokyo, Japan, scanning electron microscope (SEM), LEO, Cambridge and field emission scanning electron microscope (FE-SEM), FEI QUANTA 200 FEG, Czech Republic. The SEM studies were carried out with an electron beam accelerating potential of 15 kV/20 kV. The final polishing of the specimens was carried out on a fine velvet polishing cloth using polishing grade II alumina suspension. The polished specimens of different cast *in-situ* composites and cast unreinforced alloys were examined under optical and scanning electron microscopes to study the presence of particles and porosity in the matrix. The typical distribution of incorporated particles and various micro-structural features of the matrix in cast *in-situ* composite and cast unreinforced alloys were photographed and reported.

### 3.7.2 Electron Probe Micro-Analysis (EPMA) and Energy Dispersive X-Ray Spectroscopy (EDS)

The metallographic samples of different cast *in-situ* composites and cast unreinforced base alloys already prepared for optical microscopy and SEM were also examined under electron probe micro analyzer (EPMA), JEOL JXA-8600 M, with a beam diameter of 2  $\mu\text{m}$  at an accelerating potential of 25 kV and field emission scanning electron microscope (FE-SEM) with EDS attachment, FEI QUANTA 200 FEG, Czech Republic at an accelerating potential of 20 kV. The intermetallic phases in the microstructure of the cast *in-situ* composites and of the unreinforced base alloys were identified and quantitative chemical analysis was carried out by EPMA and EDS. During EPMA/EDS analysis, the beam was selectively focused on the phase constituents of relatively larger size in order to obtain reliable results by avoiding any significant influence of matrix alloy. A quantitative chemical analysis (point and line scanning) of the cast *in-situ* composites was carried out by EPMA and EDS. An elemental mapping of the cast *in-situ* composites was also carried out by EPMA and EDS.

## 3.8 Estimation of Reinforcement Content

### 3.8.1 Estimation of Oxide Particles

The particle volume fraction of the cast *in-situ* composites was estimated with a specific attention to identify the presence of particles at the bottom, the middle and the top segment of each cast ingot of *in-situ* composite. To estimate the particle content of these segments of each cast ingot, three samples of known mass of around 10.0 g were taken from each ingot and dissolved in a suitable chemical reagent of 1.5 M hydrochloric acid for selective dissolution of the magnesium alloy matrix without any appreciable attack on oxide particles (Handbook of Chemistry and Physics, 1981). The insoluble oxides were filtered out using ashless filter paper, which was completely burnt in pre-weighed ceramic crucible by heating at about 700 °C for 2 hours to obtain the particles as residue in the crucible. The crucible containing the residual particles was cooled and weighed in an electronic balance having a least count of 0.01 mg. The amount of residual particles was estimated by deducting the known weight of the crucible from the measured weight of the crucible containing residual particles. The particle content of the cast *in-situ* composite was determined with respect to the known weight of the cast *in-situ* composite dissolved in each test. The tests were repeated twice and average particle content at each segment were determined.

### 3.8.2 Estimation of Intermetallics

Determination of the volume fraction of a particular phase or constituent in a microstructure is one of the most important and common stereological measurements. The simplest procedure for estimating the volume fraction of a particular phase is to survey the microstructure and estimate, or guess, the area fraction. However, in the present study, the intermetallic phases, Mg<sub>2</sub>Si formed due to limited solubility of silicon in magnesium and Al<sub>3</sub>Ti formed due to limited solubility of titanium in aluminium (master composite), were observed as grayish areas under optical microscope. The volume fractions of the intermetallic phases in the microstructure of the different cast *in-situ* composites were estimated by point counting method. The magnification in the microscope was so adjusted that a maximum resolution could be obtained and at the same time the condition of not more than one grid-point in one counting intermetallic phase could be satisfied. For each result, at least 25 measurements were performed at random locations for each specimen, until a less than 10 percent relative accuracy was attained. The percent relative accuracy (% RA) is determined by dividing the 95% confidence limit (95% CL) by the data mean value ( $X_m$ ) and expressing it as a percentage, i.e.

$$\%RA = \frac{95\%CL}{X_m} \times 100 \quad (3.2)$$

The 95% CL was calculated using the following relationship

$$95\%CL = \frac{t \times s}{\sqrt{(N-1)}} \times 100 \quad (3.3)$$

where, the statistical values of  $t$  varies with the number of measurements ( $N$ ) and  $s$  is the standard deviation of the data. However, some researchers standardize on a single value of  $t$  for calculating the 95% CL, using either 1.96 or 2 irrespective of the value of  $N$  (Voort, 1984).

### 3.9 Estimation of Porosity Content

The porosity content in the cast ingot of the *in-situ* composite was estimated as follows. The volume of the cast *in-situ* composite,  $V_c$ , is given by

$$V_c = V_m + V_r + V_p \quad (3.4)$$

where,  $V_m$  is the total volume of the matrix alloy,  $V_r$  is the volume of reinforcing particles and  $V_p$  is the volume of voids leading to porosity. However, the mass of the cast *in-situ* composite,  $W_c$ , is expressed as

$$W_c = W_m + W_r \quad (3.5)$$

where,  $W_m$  is the mass of the matrix alloy and  $W_r$  is the mass of ceramic particles. Therefore, the density of the cast *in-situ* composite  $\rho_c$  may be written as

$$\rho_c = \frac{W_c}{V_c} = \frac{(W_m + W_r)}{(V_m + V_r + V_p)} \quad (3.6)$$

The terms in Eq. [3.6] may be rearranged to find the volume of porosity in the cast *in-situ* composite as follow

$$V_p = \frac{(W_m + W_r)}{\rho_c} - \left( \frac{W_m}{\rho_m} + \frac{W_r}{\rho_r} \right) \quad (3.7)$$

where,  $\rho_c$  is the density of the cast *in-situ* composite,  $\rho_m$  is the density of the matrix alloy and  $\rho_r$  is the density of the ceramic particles. The density was determined by weight loss method.

## 3.10 Studies on Mechanical Properties

### 3.10.1 Hardness Testing

The Brinell hardness test is a simple indentation test for determining the hardness of a wide variety of materials and it is particularly preferred for particle reinforced composites as it could provide a better average hardness over a larger area containing several fine particles in the matrix. The Brinell hardness of the cast *in-situ* composites and unreinforced base alloys were studied on the samples prepared from the bottom, middle and top segments of the cast ingots according to ASTM-E10 standards. The testing was carried out at a load of 153.3 N by using a steel ball of diameter 2.5 mm. The load was applied for 30 seconds on a sample and then the diameter of indentation was measured from a projection of the indentation on a screen with the help of an optical lens provided in the hardness tester type Dia Tester 2RC, Democratic Republic of Germany. For each indentation, an average of two diameters measured perpendicular to each other was used to find the corresponding hardness. On each sample at least eight indentations for hardness measurement were made at different locations and the average of these readings is reported as the hardness value of the material.

The effect of distribution of particle and porosity contents on hardness of cast *in-situ* composite was studied by measuring Brinell hardness along the entire height of the cast ingot containing different extent of particles and porosities in each region. On each region (15 mm in height) at least three indentations for hardness measurement were made at different locations and the average of these readings is reported as the hardness value of that region.

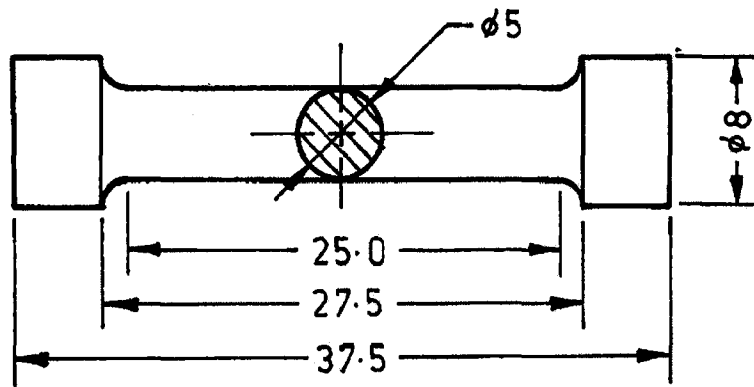
### 3.10.2 Tensile Testing

The tensile tests were carried out at ambient temperature for the cast *in-situ* composites and cast unreinforced alloy. The specimens were machined from the bottom, middle and top segments of each cast ingot as shown in Fig. 3.5. The shape and dimension of the tensile specimens, conforming to ASTM-E8M specification, is shown schematically in Fig. 3.6. At least three tensile specimens of 5.0 mm gauge diameter and 25 mm gauge length, machined out from each segment of each cast *in-situ* composite and unreinforced alloy, were tested under uniaxial tension in a Hounsfield, Monsanto, H25KS/05, Surrey, England, tensile testing machine at a strain rate of  $6.67 \times 10^{-4} \text{ s}^{-1}$  and the average of ultimate tensile strength, yield strength and percentage elongation is reported as the tensile property of the material. After fracture of the specimens, the fracture surfaces were examined under scanning electron microscope and characteristic features of all the fracture surfaces were photographed.

### 3.11 Wear and Friction Testing

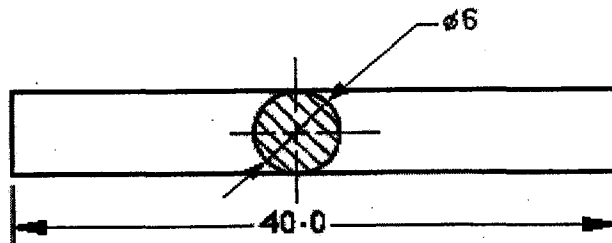
Dry sliding wear tests were carried out as per ASTM-G99, by sliding a cylindrical pin with a flat polished end against a counterface of hardened steel disc under ambient condition (Relative Humidity = 35-60% and Temperature = 21-24 °C) using a pin-on-disc machine, model TR-201C manufactured by M/S. DUCOM, Bangalore, India. The test pin has a diameter of 6 mm and length of 40 mm as shown schematically in Fig. 3.7. The counterface disc is made of EN-32 steel hardened to 62-65 HRC. Different loads of 10 N, 20 N, 30 N, and 40 N were applied on the pin normal to the sliding contact during wear test of each cast *in-situ* composite. The track radius was kept constant at 40 mm and the rotating speed of the disc was maintained at 239 rpm, corresponding to a linear speed of 1.0 m/s. The wear tests were carried out for a total sliding distance of about 3000 m. The cumulative weight loss was measured by interrupting a wear test at regular intervals of five minutes. An electronic balance (Mettler AJ 100, Cambridge, England) having least count of 0.01 mg, was used to measure the weight loss of the material specimen due to sliding process. The cumulative volume loss after a given sliding distance was determined by dividing the cumulative weight loss by the density of the test pin. The density of the cast *in-situ* composite was determined by weight loss method. The tangential (frictional) force was monitored continuously during the wear tests for the determination of coefficient of friction of the cast *in-situ* composites. Prior to wear testing, all the test pin surfaces were polished up to 4/0 grade emery paper, so that the surface roughness of the test pin is approximately  $R_a = 0.4 \mu\text{m}$ . Both the counterface disc and the test pin were cleaned well by acetone followed by drying under ambient condition. In order to check the reproducibility, the wear tests were replicated thrice and the mean results of cumulative volume loss with sliding distance were used for further calculations of wear rates and wear coefficients. For comparison of tribological behaviour of cast *in-situ* composites with those of the base material alone, wear tests were carried out also on cast commercial magnesium and unreinforced base alloys processed similarly as cast *in-situ* composites.

After wear testing the tips of the test pins were cut along a plane parallel to their worn surfaces. The characteristic features of all the worn surfaces samples were examined under scanning electron microscope (SEM). The wear debris generated during the wear tests of the cast *in-situ* composites and the unreinforced alloys were carefully collected and examined under optical microscope.



All dimensions are in mm.

**Fig. 3.6:** Shape and size of the tensile test specimen.



All dimensions are in mm.

**Fig. 3.7:** Shape and size of the wear and friction test specimen.



## RESULTS AND DISCUSSION

### Processing, Microstructure and Mechanical Properties of Cast *In-Situ* Composites

---

---

Cast *in-situ* Mg-Al/Al<sub>3</sub>Ti-Al<sub>2</sub>O<sub>3</sub> and Mg-Al/Mg<sub>2</sub>Si composites have been synthesized by melting magnesium and adding to it the cast Al-based composites developed earlier by adding TiO<sub>2</sub> to molten Al-Mg alloy, and Al-Si master alloy respectively. This chapter contains the results of processing and structural characterization through X-ray diffraction analysis and microstructural studies. The influence of the amount of TiO<sub>2</sub>/Si particles added and processing temperature on the microstructure and their impact on the mechanical properties observed in the composites have been examined in the context of the morphology of reinforcing particles, density and porosity of the cast *in-situ* composites.

#### 4.1 Structural Characterization of Cast *In-Situ* Mg-Al/Al<sub>3</sub>Ti-Al<sub>2</sub>O<sub>3</sub> Composites

##### 4.1.1 X-ray Diffraction Analysis

Cast *in-situ* Mg-Al/Al<sub>3</sub>Ti-Al<sub>2</sub>O<sub>3</sub> composite has been synthesized by addition of cast Al-based composite to molten magnesium at a given processing temperature so that the matrix may consist of Mg-9 wt% Al alloy. The composite has been designated on the basis of its constituents. The first letter indicates the base alloy, M in the present case for magnesium followed by T to indicate the amount of TiO<sub>2</sub> added to the aluminium based composite along with its amount in wt% separated by / and two digits of processing temperature. Thus, MT14/80 represents magnesium based composite developed by addition of aluminium based composite developed by addition of 14 wt% of TiO<sub>2</sub>, to molten magnesium at 800°C. The characterization of the composites has started with the identification of different phases through X-ray diffraction analysis. Typical powder X-ray diffraction (XRD) patterns of the powder of cast *in-situ* composite MT14/80 is shown in Fig. 4.1(a) to represent Mg-Al/Al<sub>3</sub>Ti-Al<sub>2</sub>O<sub>3</sub> composites synthesized. The XRD patterns of the residue extracted by dissolving the matrix of the same composite partially and of those extracted by dissolving the matrix

completely are shown respectively in Figs. 4.1 (b) and (c). The indexing of the patterns has been done by manual searching procedure with the help of JCPDS-Data Cards, on the basis of profiled phases expected in the context of chemical content. The peaks in the pattern of the composite powder, as shown in Fig. 4.1(a) belong to primary solid solution of Mg,  $\beta$ - $\text{Al}_{12}\text{Mg}_{17}$  and intermetallics,  $\text{Al}_3\text{Ti}$ . As the strong peaks of majority phase of primary solid solution of magnesium has overshadowed the peaks of the *in-situ* composite, the peaks of  $\text{Al}_3\text{Ti}$  are weak and the peaks of oxides are not at all detected. For detection of various oxides present in the *in-situ* composite, the particles are extracted by dissolving the soluble constituents of the same composite in 1.5M HCl and the extracted particles are subjected to XRD. The peaks in the pattern of the extracted particles, as shown in Fig. 4.1(c), belong to,  $\alpha$ - $\text{Al}_2\text{O}_3$ , MgO,  $\text{MgAl}_2\text{O}_4$  and  $\text{Al}_2\text{TiO}_5$ . The intermetallics phase  $\text{Al}_3\text{Ti}$  appears to have been dissolved in the solution during the particle extraction. So, for further confirmation of presence of  $\text{Al}_3\text{Ti}$  in the cast *in-situ* composite, the matrix alloy is partially dissolved in further diluted HCl (0.8M) and the residue obtained after filtration is subjected to XRD. The XRD pattern is shown in Fig. 4.1(b). Strong peaks of  $\text{Al}_3\text{Ti}$  in the pattern clearly show its existence in the cast *in-situ* composite. Thus, on the basis of XRD analysis, the composites developed by addition of Al(Mg)- $\text{TiO}_2$  to magnesium contains, apart from majority phase of primary solid solution of magnesium in the matrix, other phases distributed in the matrix such as  $\text{Al}_3\text{Ti}$ ,  $\alpha$ - $\text{Al}_2\text{O}_3$ , MgO,  $\text{MgAl}_2\text{O}_4$  and  $\text{Al}_2\text{TiO}_5$ .

#### 4.1.2 Microstructural Studies

EDS and EPMA studies have been carried out for the phase identification and their compositional analysis of cast *in-situ* Mg-Al/ $\text{Al}_3\text{Ti}$ - $\text{Al}_2\text{O}_3$  composite. A SEM micrograph and EDS spectrums with chemical composition of constituents present at various locations of cast *in-situ* composite, MT14/80, are shown in Fig. 4.2. EDS spectrums and chemical composition of different elements present at spot 1 and spot 3 corresponds to primary solid solution of aluminium in magnesium in EDS spectrum and chemical composition at spot 2 corresponds to the oxide particle,  $\text{Al}_2\text{O}_3$ . Results of compositional analysis of spot 4 and spot 5 are displayed in Figs. 4.2(d) and 4.2(e), both of these corresponds to  $\text{Al}_3\text{Ti}$ . It is noticed from the EDS spectrums that there is no evidence of presence of iron in the matrix alloy of *in-situ* composite due to iron pick up from the crucible.

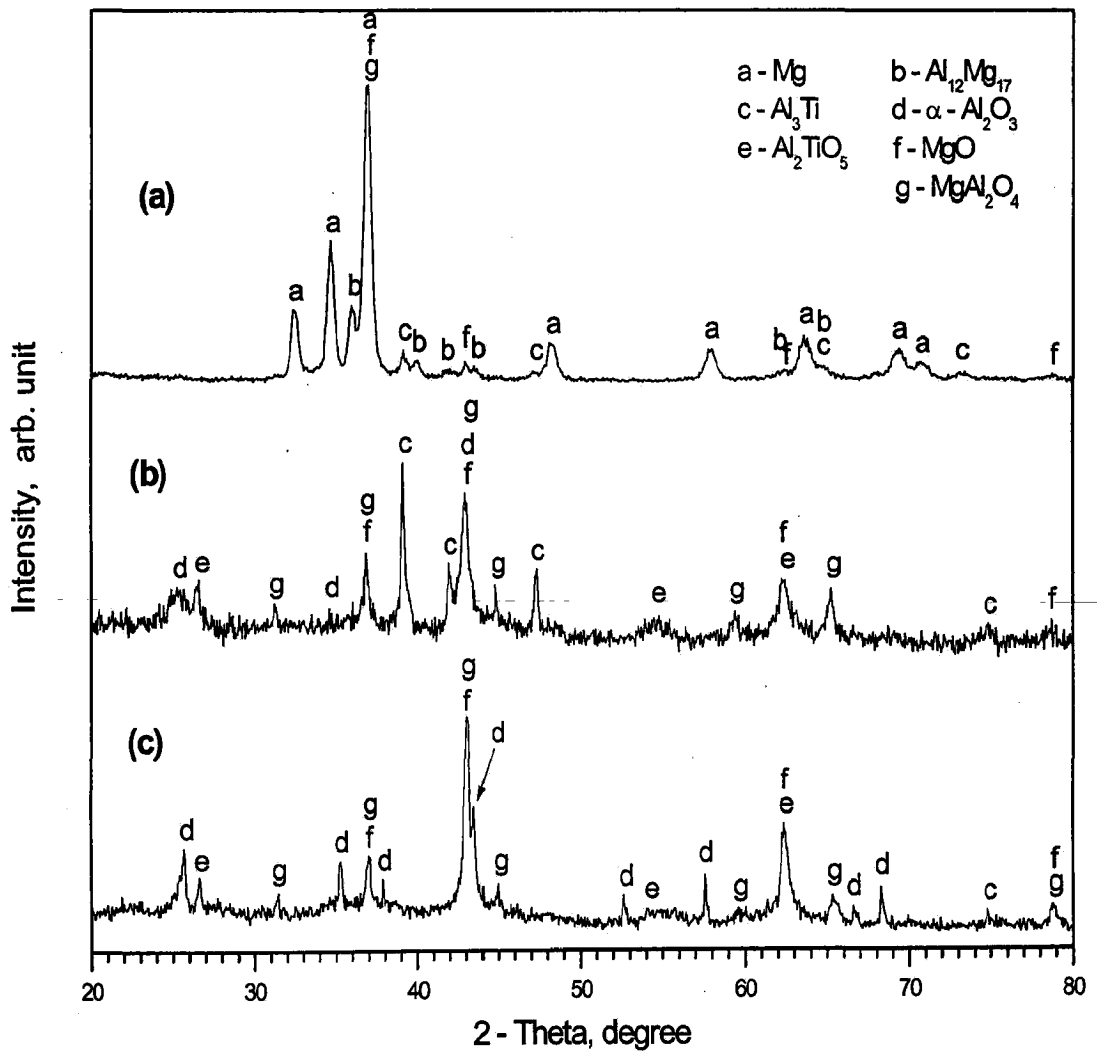


**Fig. 4.1:** Powder X-ray diffraction patterns of (a) powder of a cast *in-situ* Mg-Al/ $\text{Al}_3\text{Ti}$ - $\text{Al}_2\text{O}_3$  composite designated as MT14/80, (b) residue extracted by partially dissolving the matrix of the same composite and (c) particles extracted by completely dissolving the matrix of the same composite.

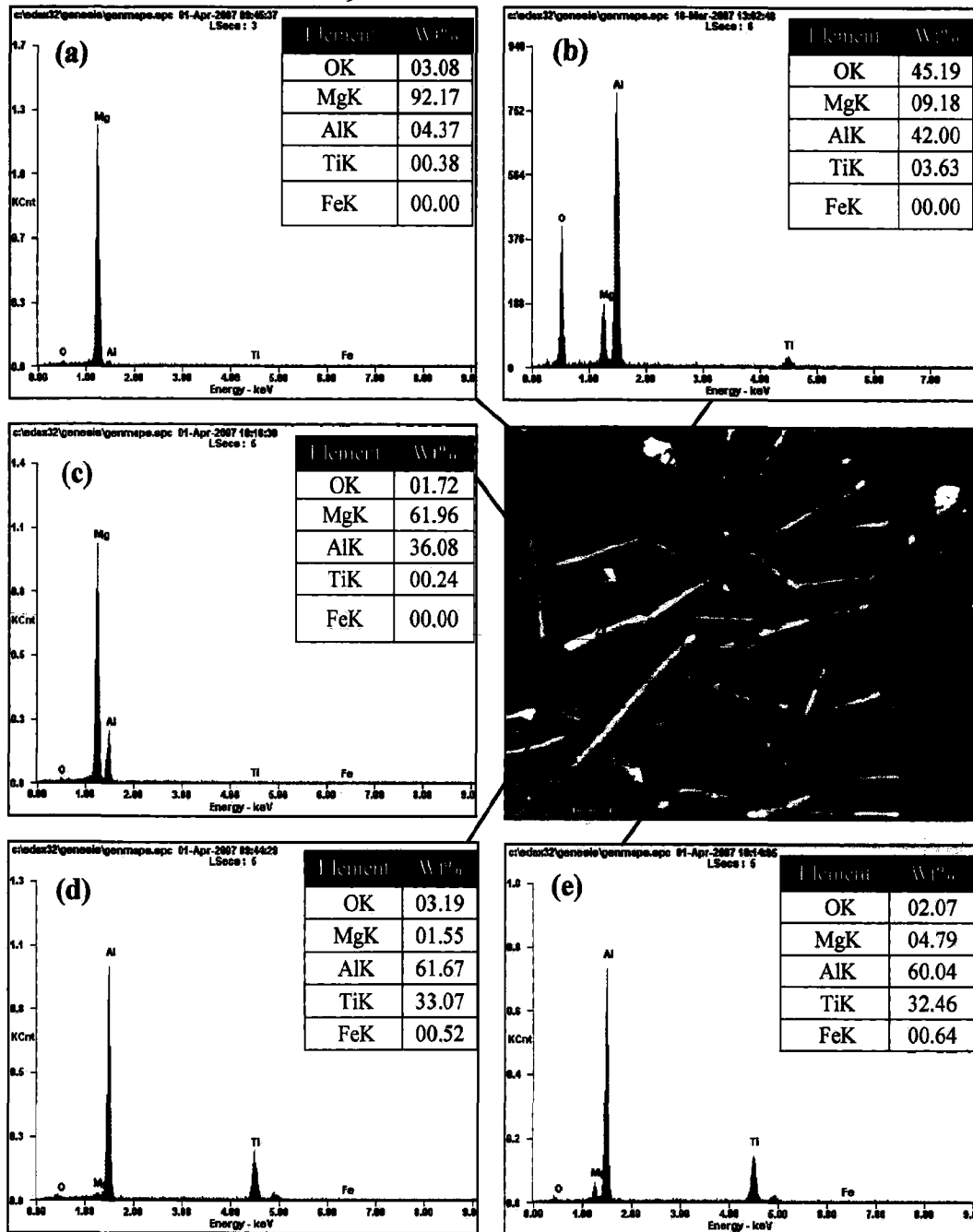


Fig. 4.2: SEM/EDS point analysis of a cast *in-situ* Mg-Al/Al<sub>3</sub>Ti-Al<sub>2</sub>O<sub>3</sub> composite designated as MT14/80 at various locations; (a) spot 1, (b) spot 2, (c) spot 3, (d) spot 4 and (e) spot 5.

The distributions of magnesium, aluminium, titanium, oxygen and iron across the matrix alloy, the *in-situ* generated alumina particle,  $\text{Al}_3\text{Ti}$  and  $\beta\text{-Al}_{12}\text{Mg}_{17}$  (as obtained through EDS line scan analysis) in a cast *in-situ* Mg-Al/ $\text{Al}_3\text{Ti}$ - $\text{Al}_2\text{O}_3$  composite, designated as MT12/85, are shown in Fig. 4.3. The distribution of aluminium is approximately constant through the entire matrix of the cast *in-situ* composite. Drastic increase of aluminium can be seen in the region of alumina particle and  $\text{Al}_3\text{Ti}$ , while drastic decrease of magnesium can be seen in these regions. Increase of aluminium and decrease of magnesium can be noticed in the region of  $\beta\text{-Al}_{12}\text{Mg}_{17}$ . Highest intensity of oxygen in the region of alumina particle and highest intensity of titanium in the region of  $\text{Al}_3\text{Ti}$  is observed. Very small peaks of iron indicating traces of it present at one of the interfaces of  $\text{Al}_3\text{Ti}$ .

A SEM micrograph and EDS X-ray maps of various elements of a cast *in-situ* Mg-Al/ $\text{Al}_3\text{Ti}$ - $\text{Al}_2\text{O}_3$  composite, designated as MT14/80, are shown in Fig. 4.4. There is a strong evidence of presence of densely distributed intermetallics,  $\text{Al}_3\text{Ti}$  in different shapes and sizes from the elemental distribution of aluminium and titanium, and depletion of magnesium at the corresponding places. From the distribution of oxygen and the availability of aluminium at the corresponding locations, presence of alumina particle could be expected. This is also confirmed by phase identification in X-ray diffraction pattern as discussed earlier in this chapter.

A typical optical micrograph of cast aluminium based composite, AT10/94, developed with 10 wt%  $\text{TiO}_2$ , at a processing temperature of 940 °C, is shown in Fig. 4.5. It shows the intermetallics, titanium aluminide ( $\text{Al}_3\text{Ti}$ ) forming due to release of titanium to the matrix alloy beyond the limit of solid solubility, by reduction of titanium dioxide by molten aluminium.  $\text{Al}_3\text{Ti}$  display needlelike or platelike shapes with an average aspect ratio of about 12. Similar microstructures containing  $\text{Al}_3\text{Ti}$  with different shapes and aspect ratio were observed by Feng and Froyen (2000), Wang et al. (2004) and Abdulhaqq et al. (2006).

Optical micrographs of a cast *in-situ* Mg-Al/ $\text{Al}_3\text{Ti}$ - $\text{Al}_2\text{O}_3$  composite, synthesized at processing temperature of 800 °C using Al-based composite developed with 12 wt%  $\text{TiO}_2$ , designated as MT12/80, are shown in Fig. 4.6 and fairly good distribution of the intermetallics,  $\text{Al}_3\text{Ti}$  is observed. The average aspect ratio of  $\text{Al}_3\text{Ti}$  is about 9. Some amount of oxide is also seen in the micrographs as shown in Figs. 4.6(a) and (b), while  $\beta$ -phase,  $\text{Mg}_{17}\text{Al}_{12}$  is clearly visible in Fig. 4.6(b). A comparison of Figs. 4.5 and 4.6 shows that the intermetallics,  $\text{Al}_3\text{Ti}$  observed in the cast *in-situ* Mg-Al/ $\text{Al}_3\text{Ti}$ - $\text{Al}_2\text{O}_3$  composite are similar to those in the Al-based composite, except few of the needlelike shape  $\text{Al}_3\text{Ti}$  intermetallics have broken into smaller pieces. Additionally,  $\beta$ -phase,  $\text{Al}_{12}\text{Mg}_{17}$  is also present in the *in-situ* composite. The optical microstructures of the specimens sectioned from the bottom, middle and top segments

along the height of the cast *in-situ* Mg-Al/Al<sub>3</sub>Ti-Al<sub>2</sub>O<sub>3</sub> composite ingot, synthesized using Al-based composite containing 12 wt% TiO<sub>2</sub> particles, at processing temperature of 800 °C, designated as MT12/80, are shown in Fig. 4.7. A comparison of the microstructures reveals that there are some differences at the top segment of the ingot from that at the bottom segment. Distribution of the intermetallics, Al<sub>3</sub>Ti is almost similar, but the size of Al<sub>3</sub>Ti appears to be comparatively little bigger at the bottom segment than at the top.

#### **(a) Influence of Amount of TiO<sub>2</sub> Particles Addition**

It is required to increase the reinforcement content in cast Al-based composite to increase the reinforcement fraction in the Mg-based cast *in-situ* composites. Different Al-based composites have been developed by dispersing increasing amounts of TiO<sub>2</sub> particles, in the range 8-14 wt%, in molten aluminium at processing temperature of 940 °C while maintaining the other processing parameters constant. The optical micrographs of cast Al-based composites synthesized with 8 wt%, 10 wt%, 12 wt% and 14 wt% of TiO<sub>2</sub> particles additions are shown respectively in Figs. 4.8(a), (b), (c) and (d). A comparison among these four micrographs shows that the intermetallics, Al<sub>3</sub>Ti number remains almost the same but the size of Al<sub>3</sub>Ti has increased with increased amount of TiO<sub>2</sub> particles addition.

The volume fractions of Al<sub>3</sub>Ti and Al<sub>2</sub>O<sub>3</sub> in cast *in-situ* Mg-Al/Al<sub>3</sub>Ti-Al<sub>2</sub>O<sub>3</sub> composites are varied by synthesizing the composites using Al-based composites developed with addition of different amounts of TiO<sub>2</sub> particles. SEM micrographs of cast *in-situ* Mg-Al/Al<sub>3</sub>Ti-Al<sub>2</sub>O<sub>3</sub> composites synthesized using Al-based composites developed by increasing amounts of TiO<sub>2</sub> particles, respectively 10, 12 and 14 wt%, designated as MT10/80, MT12/80 and MT14/80, are shown at lower and higher magnification in Fig. 4.9. A comparison of these micrographs shows that, as observed in Al-based composites, the size of Al<sub>3</sub>Ti has increased in cast Mg-Al/Al<sub>3</sub>Ti-Al<sub>2</sub>O<sub>3</sub> *in-situ* composites, synthesized using Al-based composites with increased amount of TiO<sub>2</sub> particles addition.

The effect of the addition of different amounts of TiO<sub>2</sub> particles in the development of cast *in-situ* Mg-Al/Al<sub>3</sub>Ti-Al<sub>2</sub>O<sub>3</sub> composites on the *in-situ* reinforcing particles generated is shown in the Fig. 4.10. The figure shows that the variation of amount of reinforcing particles extracted from the bottom, the middle and the top of cast ingots of *in-situ* composites is more or less a linear function of addition of TiO<sub>2</sub> particles, having a co-efficient of correlation of least square fit lying in the range of 0.98 to 0.99. However, higher amounts of reinforcing particles are found at the bottom of cast ingots of *in-situ* composites. The variation of porosity at the bottom, the middle and the top of cast ingots of cast *in-situ* Mg-Al/Al<sub>3</sub>Ti-

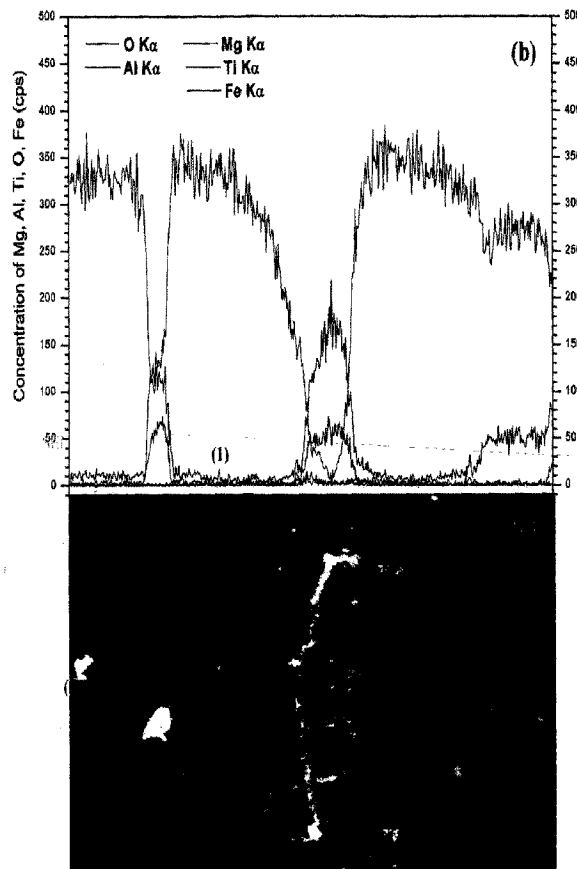


**Fig. 4.3** (a) SEM micrograph and (b) distribution of various elements of a cast *in-situ* Mg-Al/Al<sub>3</sub>Ti-Al<sub>2</sub>O<sub>3</sub> composite designated as MT12/85; the label (1) indicates the intermetallic phase, Al<sub>3</sub>Ti, (2) the oxide particle, Al<sub>2</sub>O<sub>3</sub> and (3) the  $\beta$ -phase, Al<sub>12</sub>Mg<sub>17</sub>.

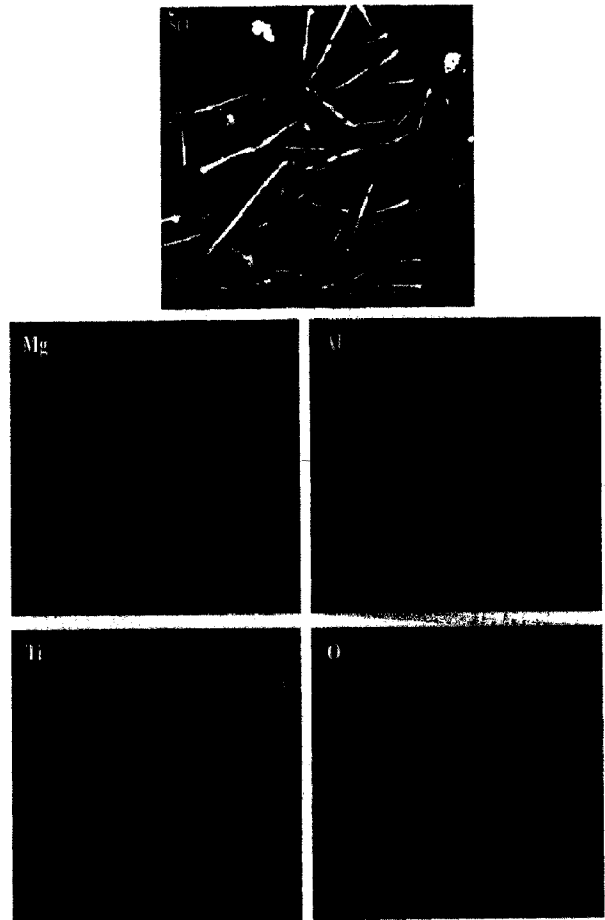
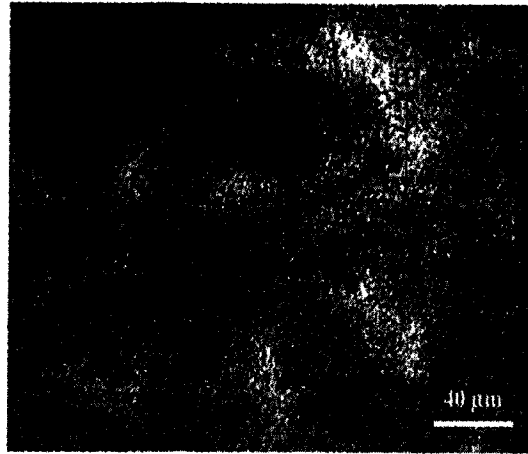
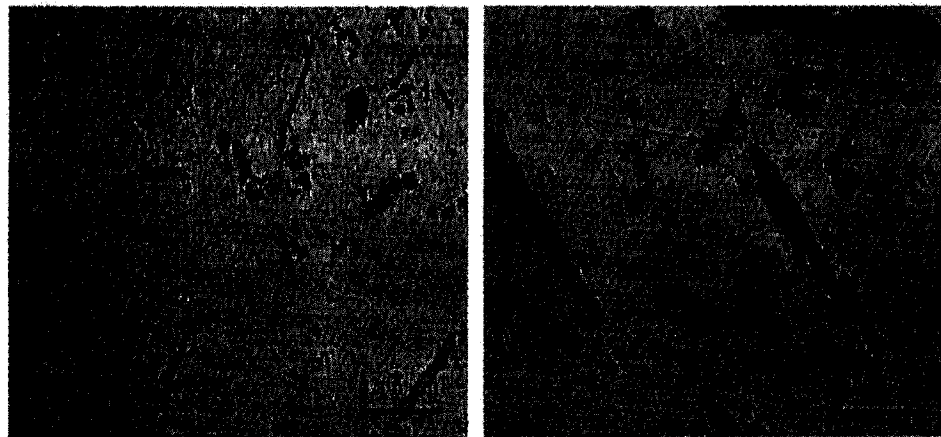


Fig. 4.4: SEM micrograph and EDS X-ray mapping for various elements of a cast *in-situ* Mg-Al/Al<sub>3</sub>Ti-Al<sub>2</sub>O<sub>3</sub> composite designated as MT14/80.





**Fig. 4.5:** Typical optical micrograph of cast Al-based composite of nominal composition of Al(5%Mg)-10%TiO<sub>2</sub> processed at 940 °C; the label (1) indicates the intermetallics, Al<sub>3</sub>Ti and (2) the oxide.



**Fig. 4.6:** a) Lower and (b) higher magnification optical micrographs of a cast *in-situ* Mg-Al/Al<sub>3</sub>Ti-Al<sub>2</sub>O<sub>3</sub> composite designated as MT12/80; the label (1) indicates the intermetallics, Al<sub>3</sub>Ti, (2) the oxide and (3) the β-phase, Al<sub>12</sub>Mg<sub>17</sub>.

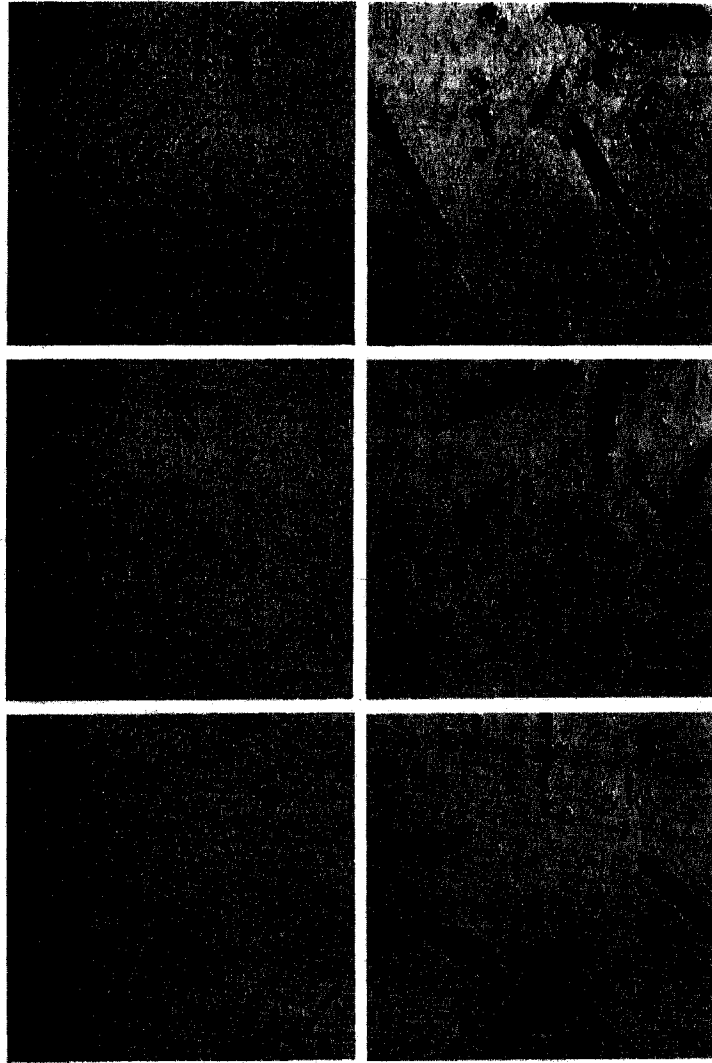
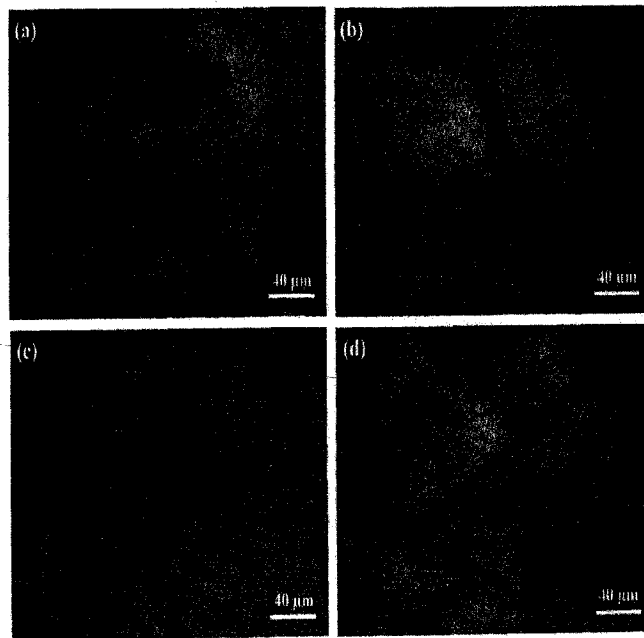
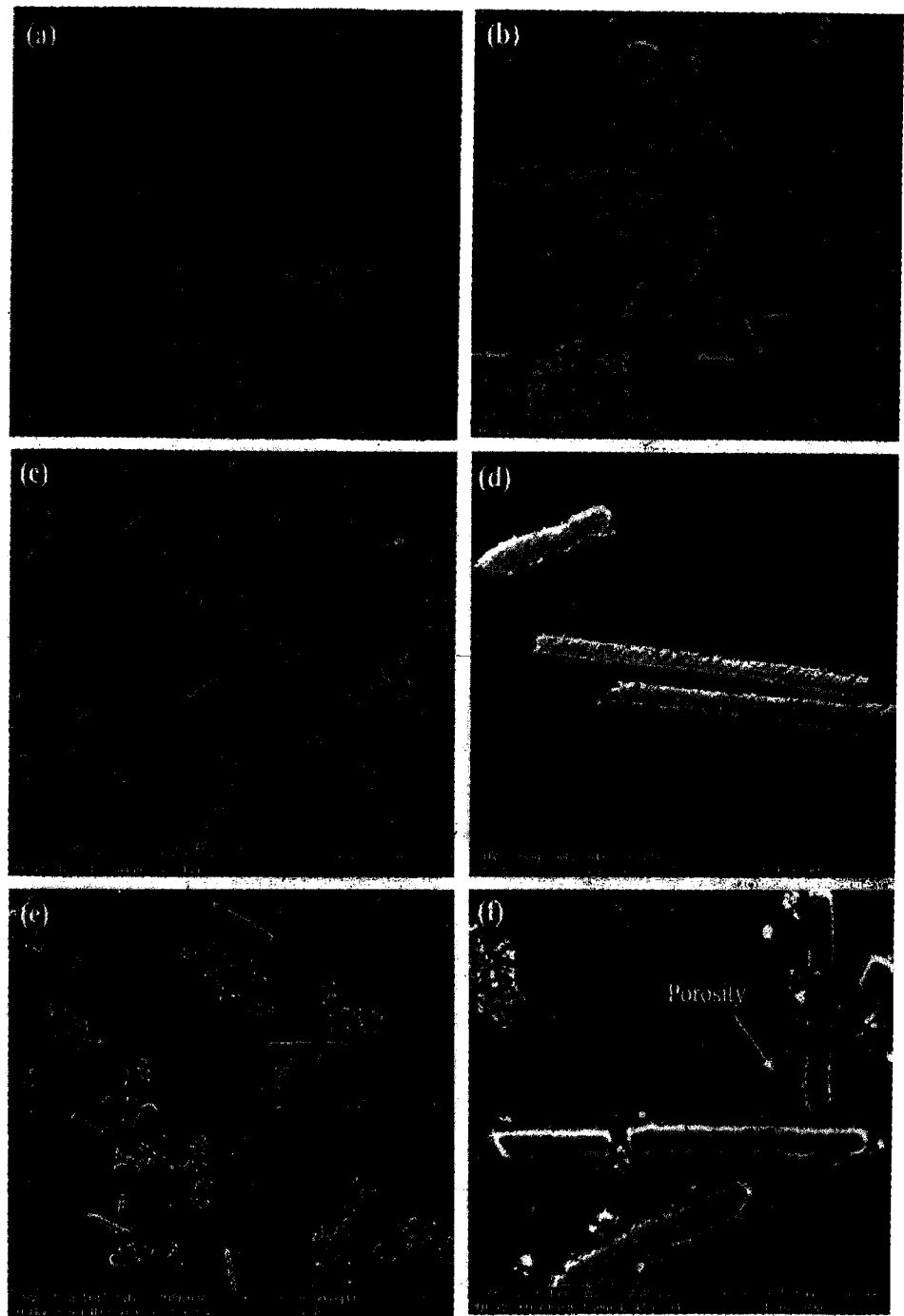


Fig. 4.7: Lower and higher magnification optical micrographs of a cast *in-situ* Mg-Al/Al<sub>3</sub>Ti-Al<sub>2</sub>O<sub>3</sub> composite designated as MT12/80; at the bottom (a) & (b), the middle (c) & (d) and the top (e) & (f).



**Fig. 4.8:** Optical micrographs of cast Al-based composites synthesized at 940 °C with different nominal composition of TiO<sub>2</sub> particles; (a) 8 wt% (b) 10 wt% (c) 12 wt% and (d) 14 wt%.



**Fig. 4.9:** SEM micrographs of different cast *in-situ* Mg-Al/Al<sub>3</sub>Ti-Al<sub>2</sub>O<sub>3</sub> composites developed by increasing amounts of TiO<sub>2</sub> particles, respectively 10, 12 and 14 wt% and designated as; (a) & (b) MT10/80, (c) & (d) MT12/80 and (e) & (f) MT14/80; at lower and higher magnification.

$\text{Al}_2\text{O}_3$  composites with amount of  $\text{TiO}_2$  particles added is shown in Fig. 4.11. The influence of increasing amount of  $\text{TiO}_2$  particles from 8 wt% to 14 wt% on porosity is not so conclusive, however, the porosity increases with increasing addition of  $\text{TiO}_2$  particles from 8 wt% to 10 wt%. Higher porosities are observed at the top segments than at bottom segments of cast ingots. The variation of difference in weight fraction of extracted particles at the top and bottom segment of cast ingot of *in-situ* Mg-Al/ $\text{Al}_3\text{Ti}$ - $\text{Al}_2\text{O}_3$  composites with amount of  $\text{TiO}_2$  particles is shown in Fig. 4.12. Even though, the difference in extracted particles is the lowest at  $\text{TiO}_2$  particles addition of 10 wt% and the highest at 12 wt%, the increasing difference in extracted particles is observed with increasing addition of  $\text{TiO}_2$  particles. The variation of porosity with amount of particles extracted at the bottom, the middle and the top of cast ingots of *in-situ* Mg-Al/ $\text{Al}_3\text{Ti}$ - $\text{Al}_2\text{O}_3$  composites is shown in Fig. 4.13. Irrespective of particle content, the higher porosities are observed at the top and the lower porosities are observed at the bottom segments of cast ingots of *in-situ* composites.

#### **(b) Influence of Processing Temperature**

Cast Al-based composites have been developed using 10 wt%  $\text{TiO}_2$  particles, at different processing temperatures of 800 °C, 940 °C and 1040 °C while maintaining the other remaining process parameters constant. It is observed that the extent of reaction of  $\text{TiO}_2$  particles with molten aluminium increases with increasing processing temperature during processing, as indicated by the increased size of intermetallics,  $\text{Al}_3\text{Ti}$ , in the microstructures shown in Figs. 4.14(a), 4.8(b) and 4.14(b). SEM micrographs of cast *in-situ* Mg-Al/ $\text{Al}_3\text{Ti}$ - $\text{Al}_2\text{O}_3$  composites, synthesized at processing temperatures of 750 °C, 800 °C and 850 °C using Al-based composite developed with 12 wt%  $\text{TiO}_2$ , are shown in Fig. 4.15. A comparison of these micrographs reveals the degradation/dissolution of the intermetallics,  $\text{Al}_3\text{Ti}$ , at the processing temperature of 850 °C showing discontinuities in the middle and irregular boundary. Thus, it appears that a processing temperature lower than 850 °C may lead to superior mechanical properties.

### **4.1.3 Mechanical Properties of Cast *In-Situ* Mg-Al/ $\text{Al}_3\text{Ti}$ - $\text{Al}_2\text{O}_3$ Composites**

The presence of porosity deteriorates the mechanical properties of the cast particulate composites similarly as it happens in cast metals and alloys. The volume fraction of porosity and the reinforcing particles along with their shape, size, and distribution, has considerable

effect on the observed mechanical properties. The nature of the particles and the particle-matrix interface also influences the mechanical properties of the cast composites. An understanding of the mechanical behaviour is extremely important for exploring the possibility of application in structural components as well as in the context of wear, which involves the process of mechanical deformation and fracture apart from other aspects. Further, the contact area in a sliding contact is also determined by its hardness. For comparison, cast unreinforced Mg-9 wt% Al alloy have been processed similarly as that of the cast *in-situ* composites but without incorporating any reinforcement.

### (a) Hardness Measurement

The Brinell hardness in the cast *in-situ* composites have been measured and correlated with their processing parameters. Typical variations in Brinell hardness measured along the height from the bottom of cast ingot of *in-situ* Mg-Al/Al<sub>3</sub>Ti-Al<sub>2</sub>O<sub>3</sub> composites, MT12/80, has been plotted in terms of normalized height ( $h/H$ ) as shown in Fig. 4.16, where  $h$  is the height of the location from the bottom of the cast ingot where hardness is measured and  $H$  is the total height of the cast ingot. Error bars indicate the standard deviation around the average value. The hardness remains relatively constant within a limited band of values and decreases slightly as one moves from the bottom to the top of the cast ingot.

The Brinell hardness has been measured in the middle segment of the cast ingot for the cast *in-situ* composites synthesized at different processing temperatures. The effect of different processing temperatures on the Brinell hardness of cast *in-situ* Mg-Al/Al<sub>3</sub>Ti-Al<sub>2</sub>O<sub>3</sub> composites, MT12/75, MT12/80 and MT12/85, is shown in Fig. 4.17. The hardness remains almost constant with variation in processing temperature, however, the average value appears to decrease with increasing processing temperature till 850 °C, the maximum temperature investigated here.

The Brinell hardness has been measured for the cast *in-situ* Mg-Al/Al<sub>3</sub>Ti-Al<sub>2</sub>O<sub>3</sub> composites, MT8/80, MT10/80, MT12/80 and MT14/80, synthesized at processing temperature of 800 °C using Al-based composites processed with different amounts of TiO<sub>2</sub> particles. The plot marked (a) in Fig. 4.18 shows the variation of Brinell hardness with extracted particles from the cast *in-situ* composites. The particle content of these cast *in-situ* composites has been determined by the dissolution of the matrix. As the particle content increases, the hardness increases significantly within the investigated range of TiO<sub>2</sub> particles added here. The plot marked (b) in Fig. 4.18 shows the variation of Brinell hardness with

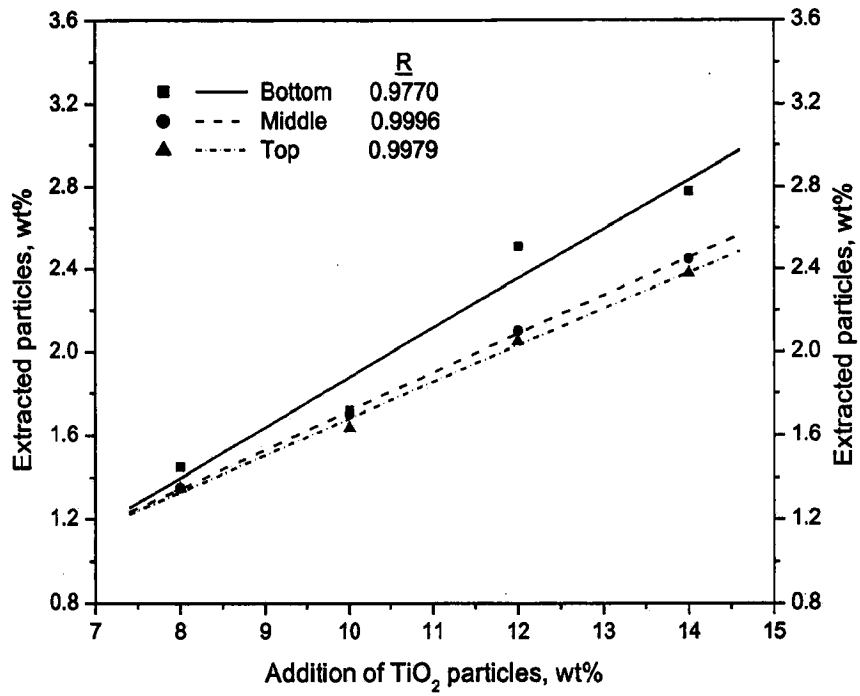


**Fig. 4.10** The variation of amount of reinforcing particles extracted at the bottom, the middle and the top of cast ingots of cast *in-situ* Mg-Al/Al<sub>3</sub>Ti-Al<sub>2</sub>O<sub>3</sub> composites with amount of TiO<sub>2</sub> particles added.

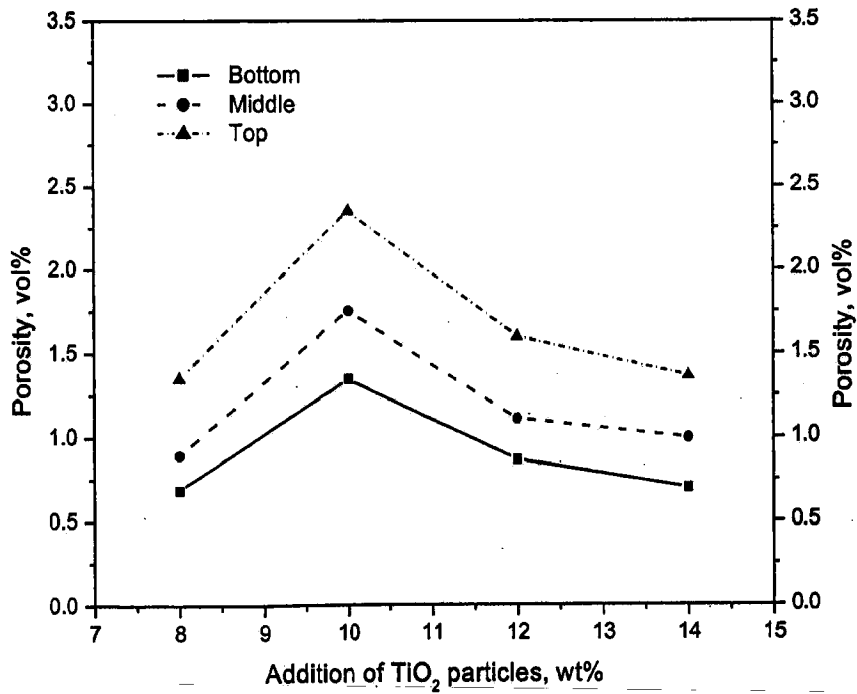


**Fig. 4.11** The variation of porosity at the bottom, the middle and the top of cast ingots of cast *in-situ* Mg-Al/Al<sub>3</sub>Ti-Al<sub>2</sub>O<sub>3</sub> composites with amount of TiO<sub>2</sub> particles added.

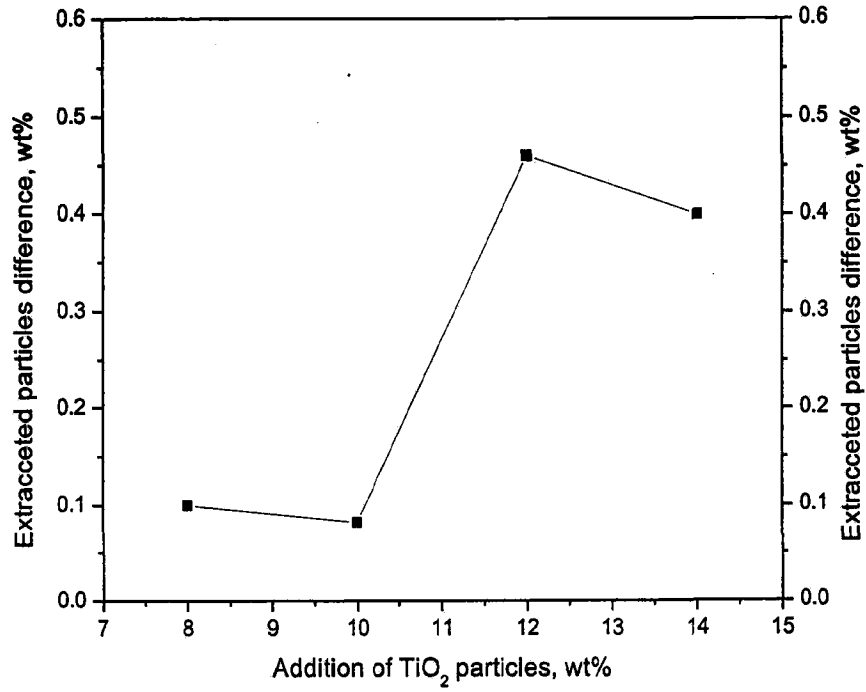


**Fig. 4.12** The variation of difference in weight fraction extracted particles at the top and bottom of cast ingot of *in-situ* Mg-Al/Al<sub>3</sub>Ti-Al<sub>2</sub>O<sub>3</sub> composites with varying amounts of TiO<sub>2</sub> particles.

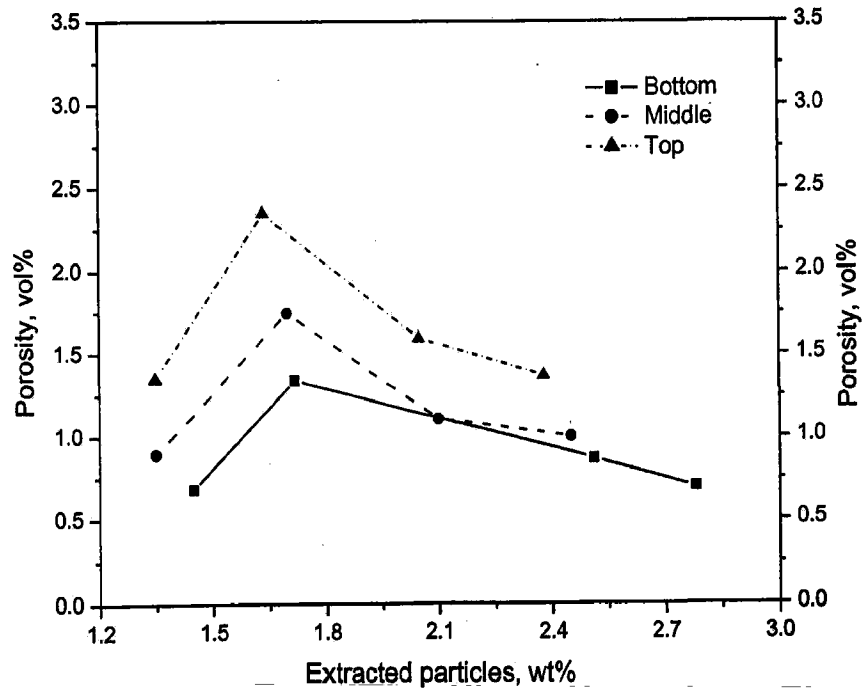


**Fig. 4.13** The variation of porosity with amount of particles extracted at the bottom, the middle and the top of cast ingot of *in-situ* Mg-Al/Al<sub>3</sub>Ti-Al<sub>2</sub>O<sub>3</sub> composites.



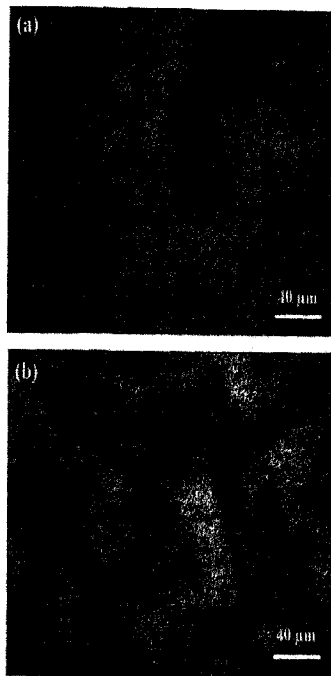


**Fig. 4.14:** Optical micrographs of cast Al-based composites developed using 10 wt% TiC particles at different processing temperatures; (a) 800 °C and (b) 1040 °C.

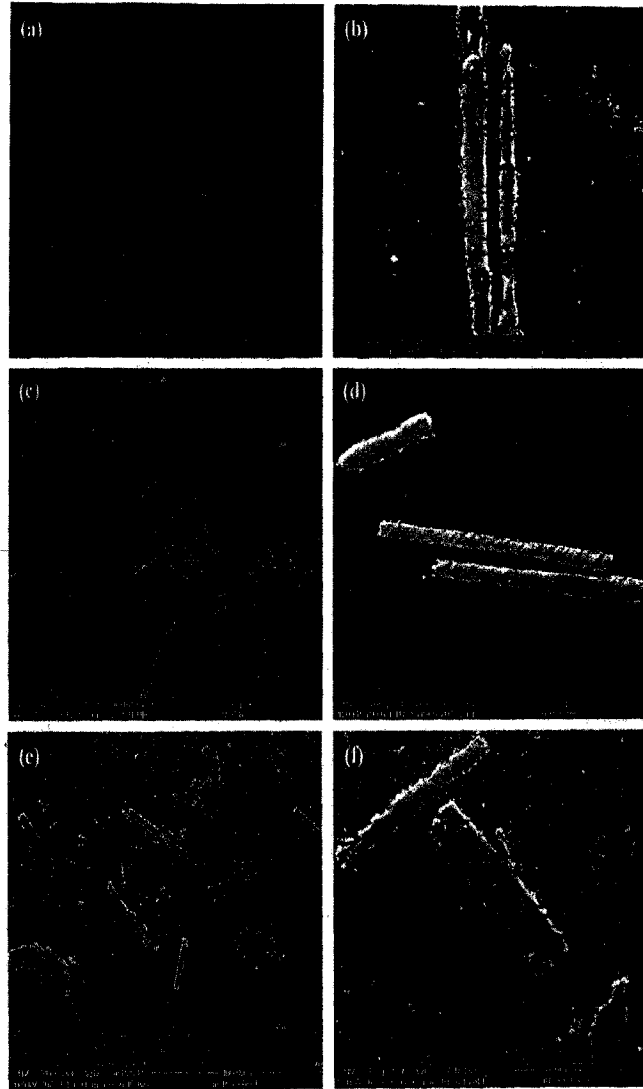


**Fig. 4.15:** SEM micrographs of different cast *in-situ* Mg-Al/Al<sub>3</sub>Ti-Al<sub>2</sub>O<sub>3</sub> composites developed by varying the processing temperature, respectively, 750, 800 and 850 °C and designated as; (a) & (b) MT12/75, (c) & (d) MT12/80 and (e) & (f) MT12/85; at lower and higher magnification.

intermetallics in the cast *in-situ* composites. The volume fraction of intermetallics in the cast *in-situ* composites has been determined by point count method. As the volume fraction of intermetallics increases, there is significant improvement in hardness.

For comparison, the Brinell hardness values of cast commercial magnesium, Mg-9 wt% Al alloy and a cast *in-situ* Mg-Al/Al<sub>3</sub>Ti-Al<sub>2</sub>O<sub>3</sub> composite, designated as MT14/80, are shown in Fig. 4.19. The hardness of cast *in-situ* composite is higher by a factor about 1.4 than that observed in cast Mg-9 wt% Al alloy and about twice that of cast commercial magnesium.

## (b) Tensile Properties

A typical comparison between average tensile properties, ultimate tensile strength and percentage elongation, measured at the bottom, middle and top height segments of ingot of a cast *in-situ* Mg-Al/Al<sub>3</sub>Ti-Al<sub>2</sub>O<sub>3</sub> composite, MT8/80, is shown in Fig. 4.20. Higher tensile properties, ultimate tensile strength and percentage elongation, are obtained at the bottom which contains relatively lower porosity content and higher particle content. It is observed that porosity content increases from 0.7 vol% to 1.4 vol% as one moves from bottom to the top of cast ingot while intermetallic content decreases from 1.45 wt% to 1.36 wt%.

The variations in ultimate tensile strength and percentage elongation for the middle height segment of cast ingot of cast *in-situ* Mg-Al/Al<sub>3</sub>Ti-Al<sub>2</sub>O<sub>3</sub> composites, MT12/75, MT12/80 and MT12/85, are shown in Fig. 4.21. The ultimate tensile strength increases with increasing processing temperature from 750 °C to 850 °C while the percentage elongation is almost constant with increasing processing temperature from 750 °C to 850 °C as shown in Fig. 4.21.

It is a common practice to correlate the mechanical properties of castings directly to the volume fraction of total porosity. Besides reduction in effective cross sectional area, the weakening of a material containing pores essentially happens by the damage caused to the local load bearing capacity of the material due to stress concentration near the pores. Sprigg's equation, a phenomenological model proposed earlier (Sprigg's, 1961) has been used to examine the role of such weakened zones around the pores in determining the strength of cast *in-situ* Mg-Al/Al<sub>3</sub>Ti-Al<sub>2</sub>O<sub>3</sub> composites. The equation relates the property of a composite containing a given amount of particle, P, at a porosity level, V<sub>P</sub> (in volume %) as

$$(P/P_0) = \exp(-\alpha V_P) \quad (4.1)$$

where, P<sub>0</sub> is the property at zero porosity and α is the weakening factor due to pore.

To examine the experimental data obtained for various cast *in-situ* Mg-Al/Al<sub>3</sub>Ti-Al<sub>2</sub>O<sub>3</sub> composites having different particle content in the context of the model equation (4.1), natural logarithmic values of ultimate tensile strength and percentage elongation have been plotted against volume percent of porosity,  $V_p$ , and extrapolated to zero porosity level to get the values of the property at zero porosity, i.e.  $\sigma_{ut0}$  or (percentage elongation)<sub>0</sub>, for each particle content. The typical nature of natural logarithmic values of ultimate tensile strength  $\{\ln(\sigma_{ut})\}$  versus porosity ( $V_p$ ) plots for composites containing 0, 1.45, 1.88 and 2.38 weight percent of particles are depicted in Fig. 4.22. The figure shows that  $\ln(\sigma_{ut})$  is a linear function of porosity content having a co-efficient of correlation (R) in the range of 0.92 to 0.99. The slopes of these curves give the values of  $\alpha$  contained in equation (4.1) and it is a measure of the weakening effect of the pore. The variation of  $\alpha$  with a change in particle content of composite has been estimated following the procedure mentioned above and the results are plotted as shown in Fig. 4.23. It has been observed that the value of  $\alpha$  decreases significantly with an increase in particle content in a composite. In cast composites there is the presence of porosity affecting the tensile properties and, therefore, to isolate the effect of particles alone, it is necessary to eliminate the contribution of porosity in the observed tensile properties to arrive at an estimate of tensile properties at zero porosity. The relationship between the particle content and the ultimate tensile strength at zero porosity,  $\sigma_{ut0}$ , for different composites has been shown in Fig. 4.24. The value of  $\sigma_{ut0}$  has been found to decrease with increasing amount of particle content in the composite.

The natural logarithmic values of percentage elongation,  $\ln(\text{percentage elongation})$ , versus porosity plots for composites containing 0, 1.45, 1.88 and 2.38 wt% particles are depicted in Fig. 4.25. The figure shows that  $\ln(\text{percentage elongation})$ , if fitted as a linear function of porosity content, the co-efficient of correlation may sometimes be as low as 0.78 and it varies in a range between 0.78 to 0.98. The relationship between the particle content and the percentage elongation at zero porosity, (percentage elongation)<sub>0</sub>, for different composites is shown in Fig. 4.26 and the value of (percent elongation)<sub>0</sub> has found to decrease with the increase in the amount of particle content.

The variation in ultimate tensile strength with porosity content for cast *in-situ* Mg-Al/Al<sub>3</sub>Ti-Al<sub>2</sub>O<sub>3</sub> composite containing  $1.74 \pm 0.24$  wt% particles and  $1.08 \pm 0.16$  vol% intermetallics (Al<sub>3</sub>Ti) is shown in Fig. 4.27. The figure shows that the tensile strength of the composite is decreasing with increasing porosity and it is a linear function of porosity content

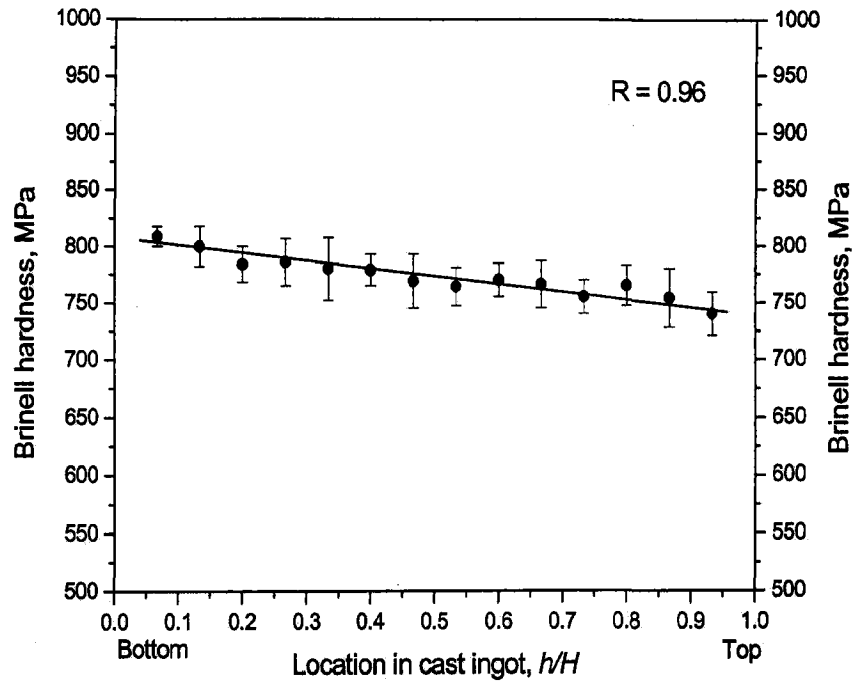


**Fig.4.16** Brinell hardness measurement along the height from the bottom to top of cast ingot of a *in-situ* Mg-Al/Al<sub>3</sub>Ti-Al<sub>2</sub>O<sub>3</sub> composite designated as MT12/80.

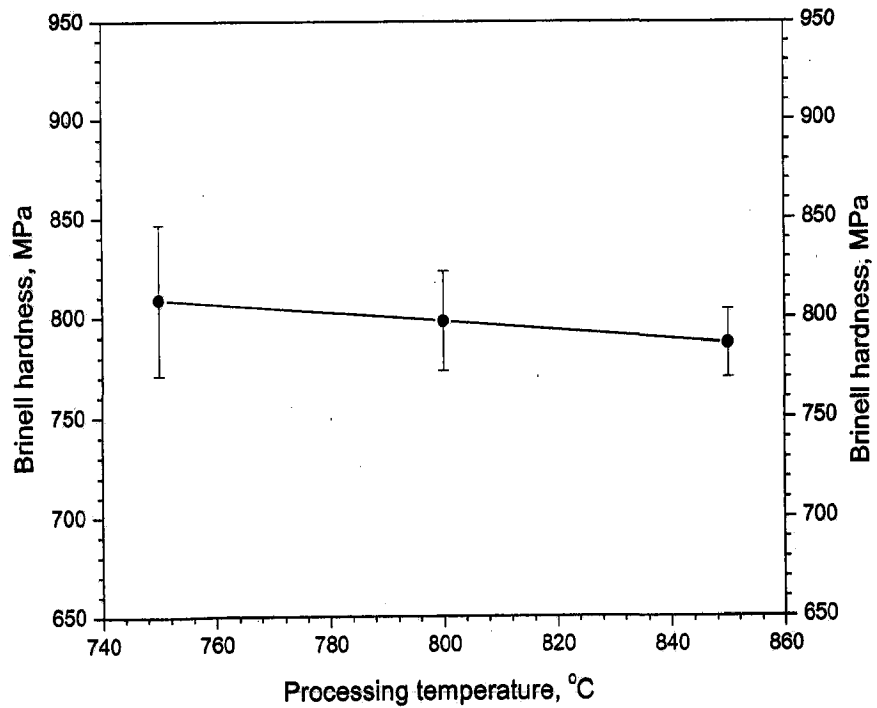


**Fig.4.17** The variation in hardness with processing temperature for cast *in-situ* Mg-Al/Al<sub>3</sub>Ti-Al<sub>2</sub>O<sub>3</sub> composite, synthesized using cast Al-based composite developed with 12 wt% TiO<sub>2</sub>.

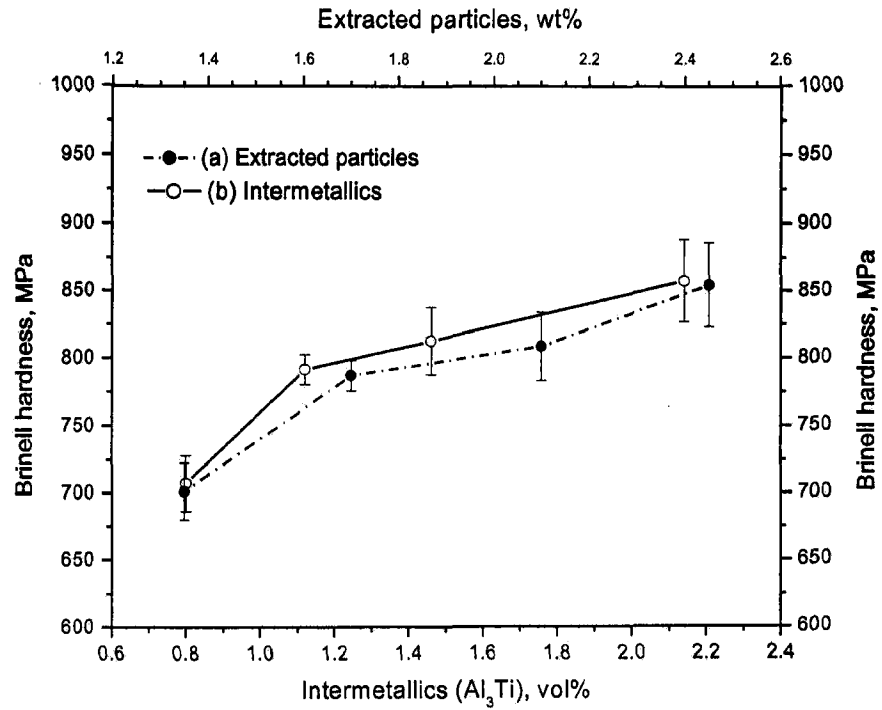


**Fig. 4.18**

The variations of hardness with (a) amount of extracted particles and (b) amount of intermetallics, Al<sub>3</sub>Ti, for cast *in-situ* Mg-Al/Al<sub>3</sub>Ti-Al<sub>2</sub>O<sub>3</sub> composites, synthesized at 800 °C using cast Al-based composites processed with different amounts of TiO<sub>2</sub> particles.

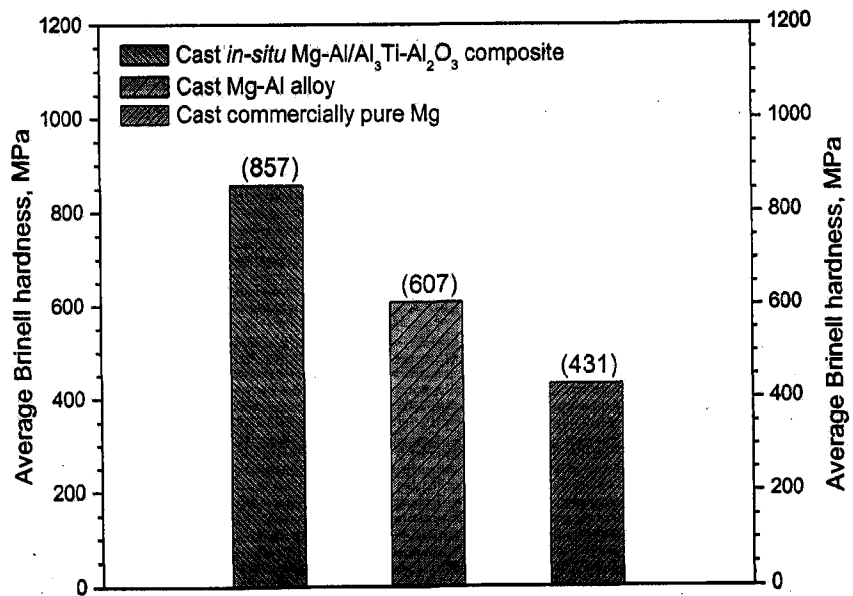


**Fig. 4.19**

Comparison between average Brinell hardness for cast *in-situ* Mg-Al/ Al<sub>3</sub>Ti Al<sub>2</sub>O<sub>3</sub> composite containing 2.14 ± 0.43 wt% extracted particles and 1 vol% porosity, cast Mg-Al alloy containing 0.6 vol% porosity and cast commercially pure Mg containing 0.2 vol% porosity.

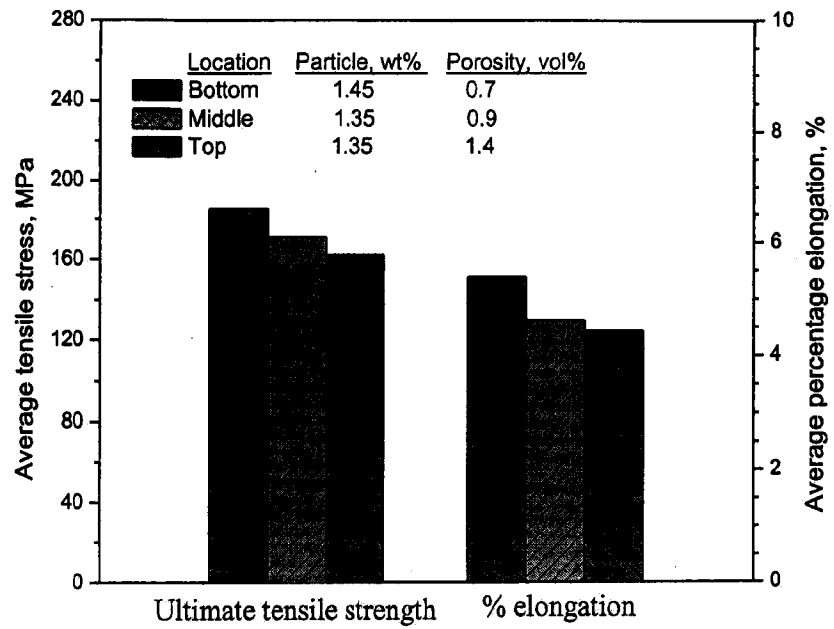


**Fig. 4.20** The comparison between tensile properties for the three segments, the bottom middle and top, of a cast *in-situ* Mg-Al/Al<sub>3</sub>Ti-Al<sub>2</sub>O<sub>3</sub> composite designated as MT8/80.

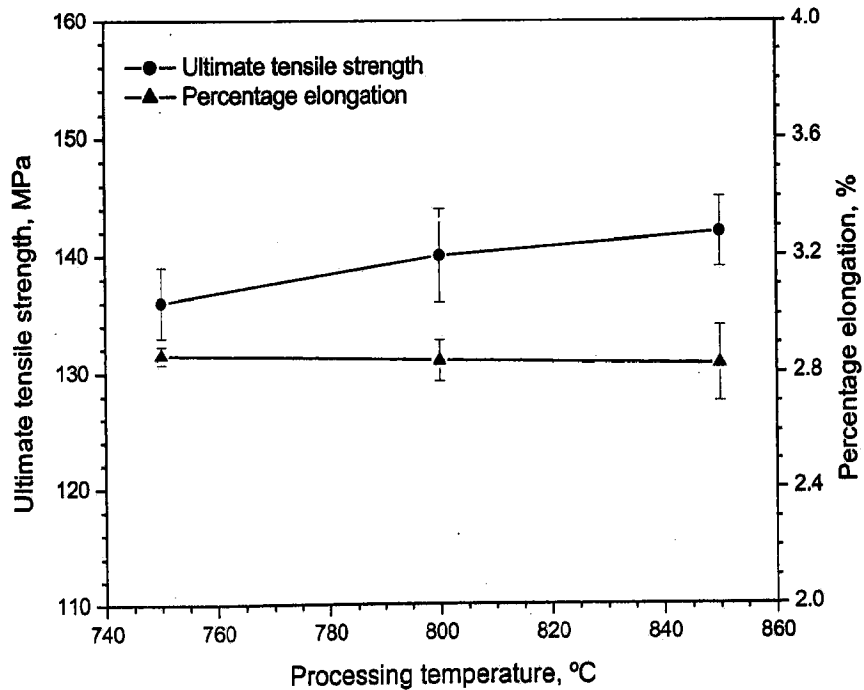


**Fig. 4.21** The variation of tensile properties with processing temperature for cast *in-sit* Mg-Al/Al<sub>3</sub>Ti-Al<sub>2</sub>O<sub>3</sub> composite, synthesized using cast Al-based composit developed with 12 wt%TiO<sub>2</sub> particles.

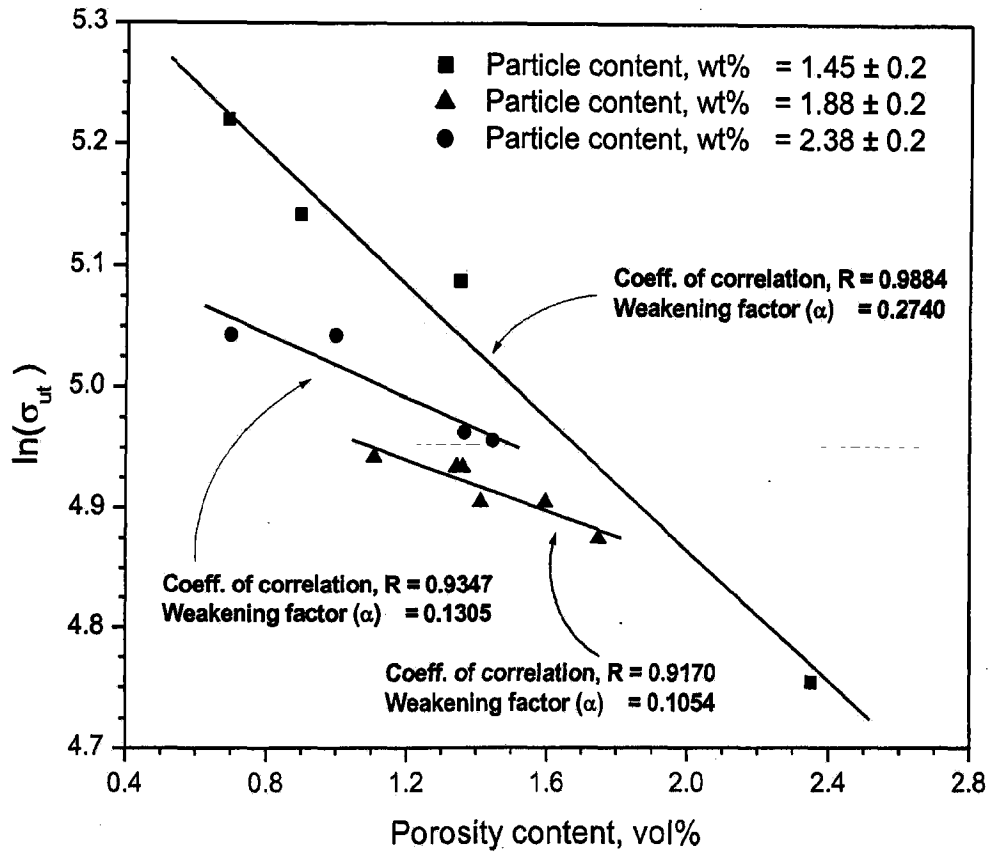


**Fig. 4.22** Effect of porosity content on  $\ln(\sigma_{ut})$  for cast *in-situ* Mg-Al/Al<sub>3</sub>Ti-Al<sub>2</sub>O<sub>3</sub> composites.



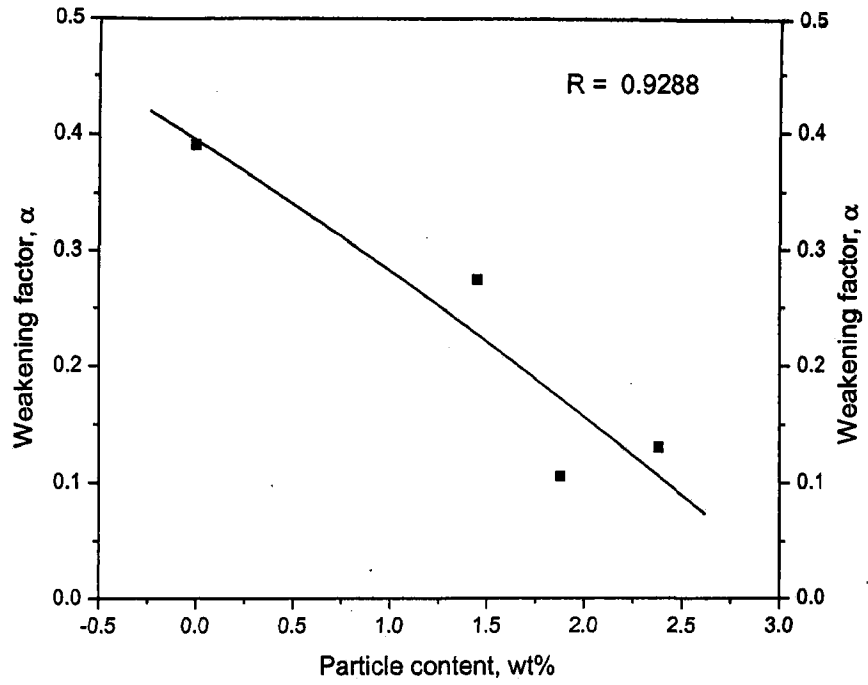


**Fig. 4.23:** Variation of weakening factor,  $\alpha$ , with particle content for the cast *in-situ* Mg-Al/ $\text{Al}_3\text{Ti}$ - $\text{Al}_2\text{O}_3$  composites.

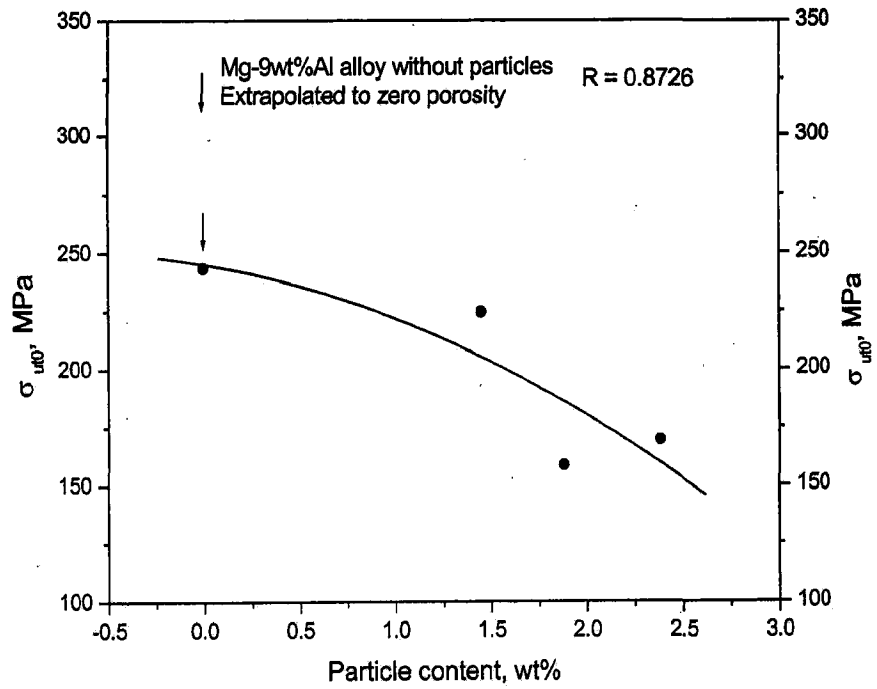


**Fig. 4.24** Effect of particle content on the tensile strength at zero porosity for cast *in-situ* Mg-Al/ $\text{Al}_3\text{Ti}$ - $\text{Al}_2\text{O}_3$  composites.

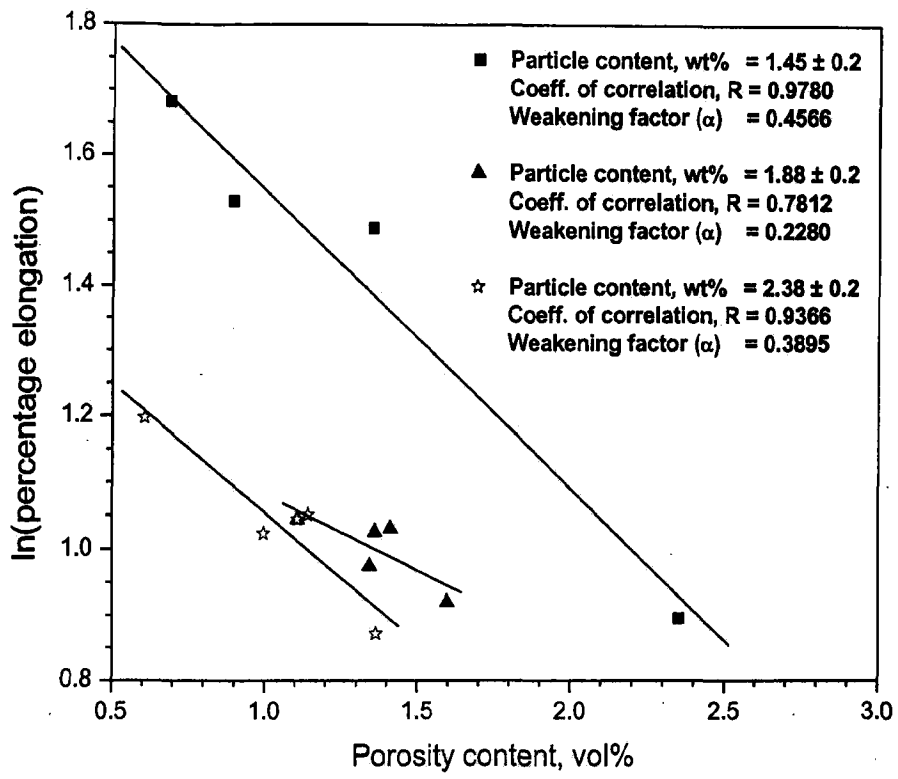


**Fig. 4.25** Effect of porosity content on  $\ln(\text{percentage elongation})$  for cast *in-situ* Mg-Al/ $\text{Al}_3\text{Ti}-\text{Al}_2\text{O}_3$  composites.

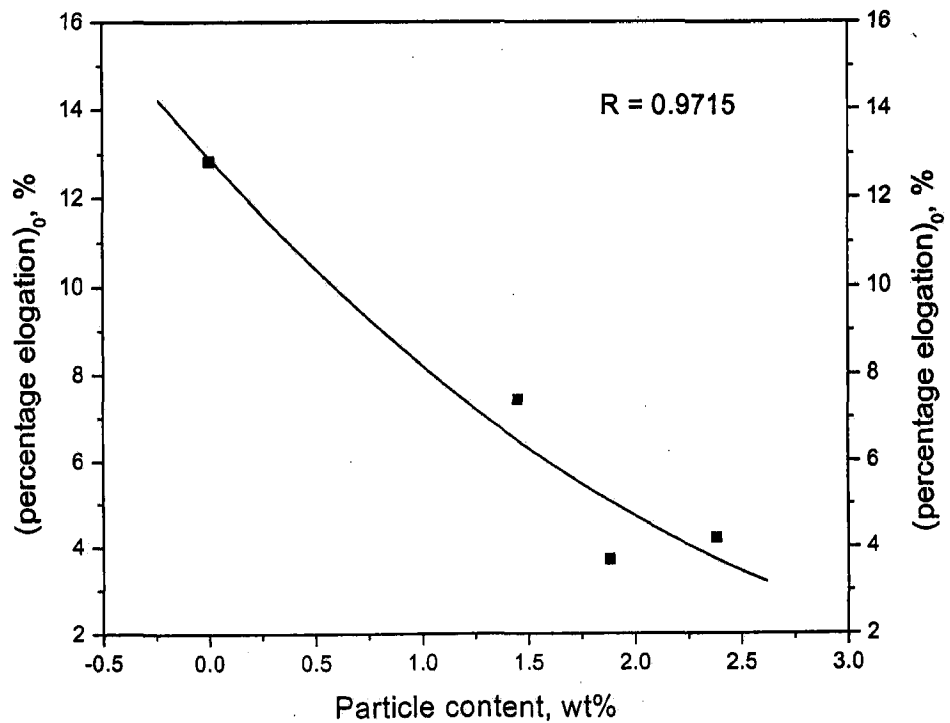


**Fig. 4.26** Effect of particle content on the percentage elongation at zero porosity for cast *in-situ* Mg-Al/ $\text{Al}_3\text{Ti}-\text{Al}_2\text{O}_3$  composites.

having a co-efficient of correlation 0.93. The variation in percentage elongation with porosity content for cast *in-situ* Mg-Al/Al<sub>3</sub>Ti-Al<sub>2</sub>O<sub>3</sub> composite containing  $1.74 \pm 0.24$  wt% particles and  $1.08 \pm 0.16$  vol% intermetallics (Al<sub>3</sub>Ti) is shown in Fig. 4.28. The figure shows that the percentage elongation of the composite is decreasing with increasing porosity and it is a linear function of porosity content having a co-efficient of correlation 0.9.

#### 4.1.4 Fractography

The tensile fractured surfaces of the specimens subjected to tensile test have been studied under scanning electron microscope (SEM) for cast *in-situ* Mg-Al/Al<sub>3</sub>Ti-Al<sub>2</sub>O<sub>3</sub> composites, cast Mg-9 wt% Al alloy and cast commercial magnesium and the results obtained are presented in this section.

The fractured surface of the specimen shown in Fig. 4.29(a) belongs to the best performing specimen ( $\sigma_{ut} = 200$  MPa and elongation = 6.22%) machined from cast *in-situ* Mg-Al/Al<sub>3</sub>Ti-Al<sub>2</sub>O<sub>3</sub> composite containing 1.45 wt% reinforcing particles and 0.7 vol% porosity, as observed under SEM at a higher magnification. The tensile fractured surface revealed the evidence of mixed-mode failure, primarily brittle cleavage and partially ductile fracture. While the Fig. 4.29(b) shows the tensile fracture surface for the worst performing specimen ( $\sigma_{ut} = 112$  MPa and elongation = 2.29%) machined from cast *in-situ* Mg-Al/Al<sub>3</sub>Ti-Al<sub>2</sub>O<sub>3</sub> composite containing 1.64 wt% reinforcing particles and 2.4 vol% porosity, as observed under SEM. The tensile fractured surface shows the mixed-mode fracture, primarily brittle fracture resulting in an overall elongation of 2.29%. Propagation of cracks and fracturing of reinforcement is seen in the figures.

The typical tensile fractured surface of the cast unreinforced Mg-9 wt% Al alloy containing 0.3 vol% porosity has been studied under SEM at higher magnification as shown in Fig. 4.29(c). The fractured surface shows the intergranular cleavages and dimples of ductile fracture resulting in 11.67% elongation. Typical SEM fractograph of fractured surface of cast commercial magnesium containing 0.1 vol% porosity is shown in Fig. 4.29(d). The fractured surface shows the transgranular cleavages and dimples of ductile fracture resulting in overall elongation of 17.53%.

## 4.2 Structural Characterization of Cast Mg-Al/Mg<sub>2</sub>Si *In-Situ* Composites

### 4.2.1 X-ray Diffraction Analysis

Cast *in-situ* Mg-Al/Mg<sub>2</sub>Si composite has been synthesized by adding cast Al-Si master alloy to molten magnesium. The composite is designated on the basis of constituents. The base alloy is designated by M followed by the major alloying element of the aluminium alloy indicated by S for silicon and its amount in the alloy in wt%, separated by / followed by first two digits of the processing temperature. Thus, MS20/76 stands for the composite synthesized by addition of Al-20 wt% Si master alloy to magnesium, at processing temperature, 760 °C. Typical XRD pattern of the powders of cast *in-situ* composite, MS20/76, representing Mg-Al/Mg<sub>2</sub>Si composites and Mg-9 wt% Al alloy processed following the same processing route as that of composite, are shown in Fig. 4.30. The peaks in the XRD pattern of the composite powder belong to intermetallics, Mg<sub>2</sub>Si, primary solid solution of magnesium and  $\beta$ -Al<sub>12</sub>Mg<sub>17</sub> as shown in Fig. 4.30(a). Even though Mg peaks are strong, peaks corresponding Mg<sub>2</sub>Si are clearly seen. The peaks in the XRD pattern of Mg-9 wt% Al alloy powder belong to primary solid solution of magnesium and  $\beta$ -Al<sub>12</sub>Mg<sub>17</sub> as shown in Fig. 4.30(b). A comparison of these two XRD patterns clearly shows the existence of Mg<sub>2</sub>Si in the *in-situ* composite. Fig. 4.31 shows the powder XRD pattern of cast Al-15 wt% Si master alloy, processed at 920 °C. The peaks in the pattern correspond to primary solid solution of silicon in aluminium and silicon. It is understood from the XRD patterns of *in-situ* composite as shown in Fig. 4.30(a) and master alloy as shown in Fig. 4.31 that, the silicon is completely consumed by magnesium to form Mg<sub>2</sub>Si.

Fig. 4.32 shows the XRD patterns of the powders of cast *in-situ* Mg-Al/Mg<sub>2</sub>Si composite synthesized, at processing temperature of 760 °C, using Al-Si master alloys containing respectively 9, 15 and 20 wt% Si and designated as MS9/76, MS15/76 and MS20/76. It is observed in the XRD patterns that the peaks of Mg<sub>2</sub>Si are relatively getting stronger as the silicon content in the master alloy increases from 9 to 20 wt% in Figs. 4.32 (a), (b) and (c). A comparison reveals that, as expected, the formation of increased volume fraction of Mg<sub>2</sub>Si with increased silicon is observed.

### 4.2.2 Microstructural Studies

EDS and EPMA studies have been carried out for the phase identification and their compositional analysis on the microstructure of cast *in-situ* Mg-Al/Mg<sub>2</sub>Si composite. A SEM

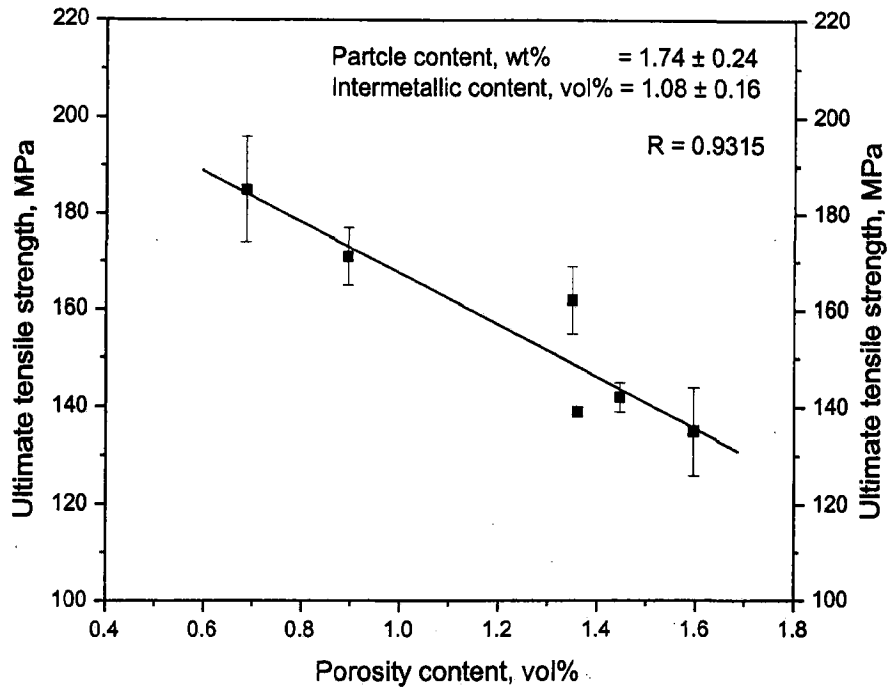


**Fig. 4.27** The variation of ultimate tensile strength with porosity content for cast *in-situ* Mg-Al/Al<sub>3</sub>Ti-Al<sub>2</sub>O<sub>3</sub> composite containing  $1.74 \pm 0.24$  wt% particles and  $1.08 \pm 0.16$  vol% intermetallics (Al<sub>3</sub>Ti).

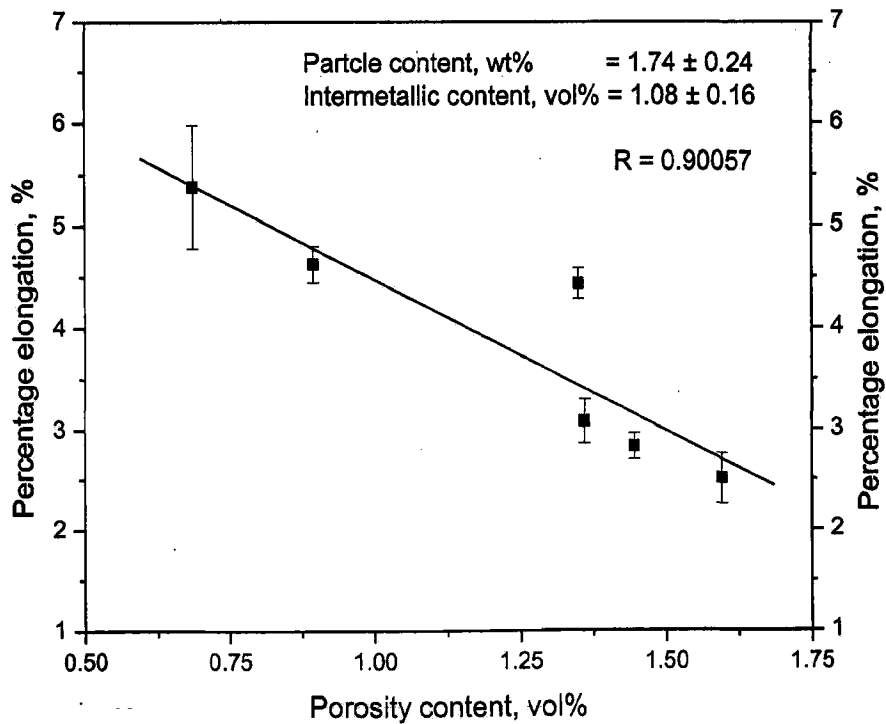


**Fig. 4.28** The variation of percentage elongation with porosity content for cast *in-situ* Mg-Al/Al<sub>3</sub>Ti-Al<sub>2</sub>O<sub>3</sub> composite containing  $1.74 \pm 0.24$  wt% particles and  $1.08 \pm 0.16$  vol% intermetallics (Al<sub>3</sub>Ti).

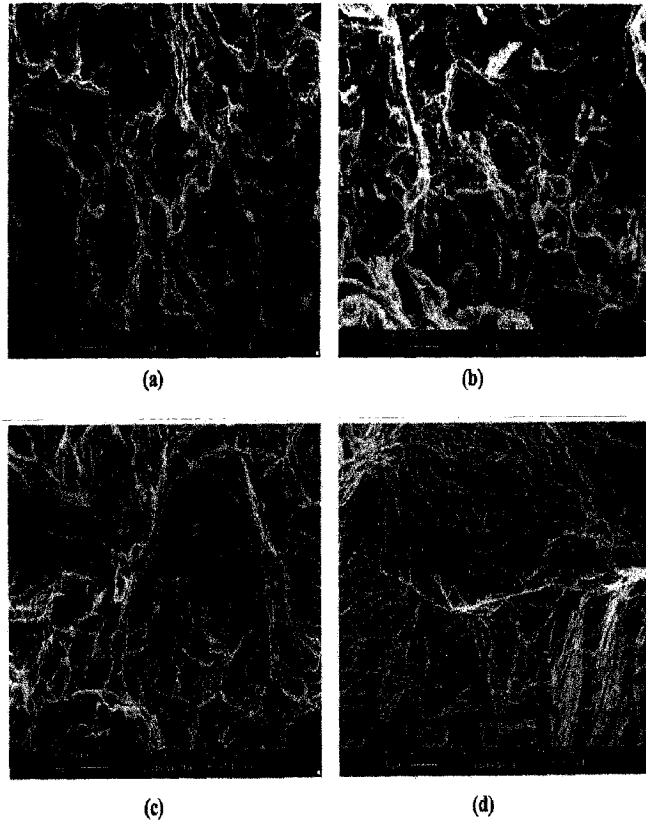


**Fig. 4.29** SEM fractographs showing tensile fracture surfaces at magnification, 1000X; (a) and (b) cast *in-situ* Mg-Al/Al<sub>3</sub>Ti-Al<sub>2</sub>O<sub>3</sub> composites containing 1.45 and 1.64 wt% of reinforcing particles, and 0.7 and 2.4 vol% porosities respectively, (c) cast Mg-9 wt% Al base alloy containing 0.3 vol% porosity and (d) cast commercial magnesium containing 0.1 vol% porosity.

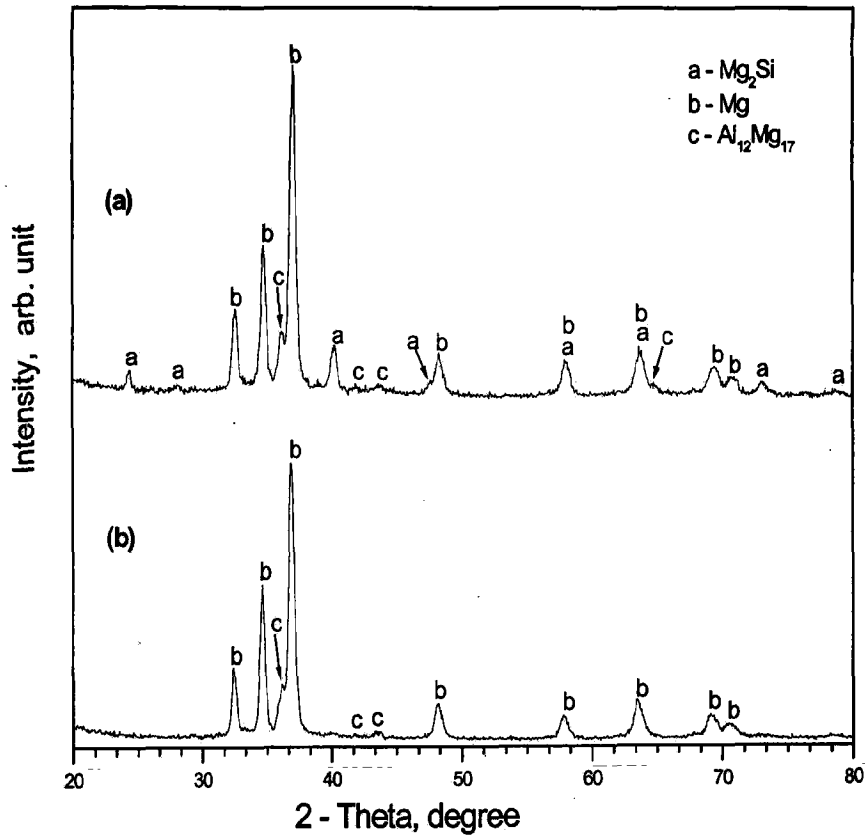


**Fig. 4.30:** Powder X-ray diffraction patterns of (a) cast *in-situ* Mg-Al/ $Mg_2Si$  composite, synthesized using Al-20 wt% Si master alloy, at processing temperature of 760 °C, designated as MS20/76 and (b) cast Mg-9 wt% Al base alloy.

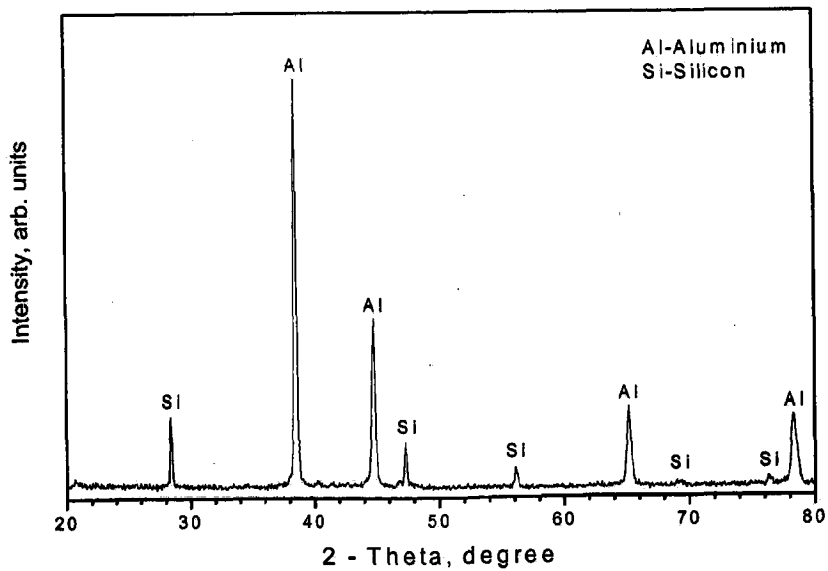


**Fig. 4.31:** Powder X-ray diffraction pattern of cast Al-15 wt% Si master alloy, processed at temperature, 920 °C.

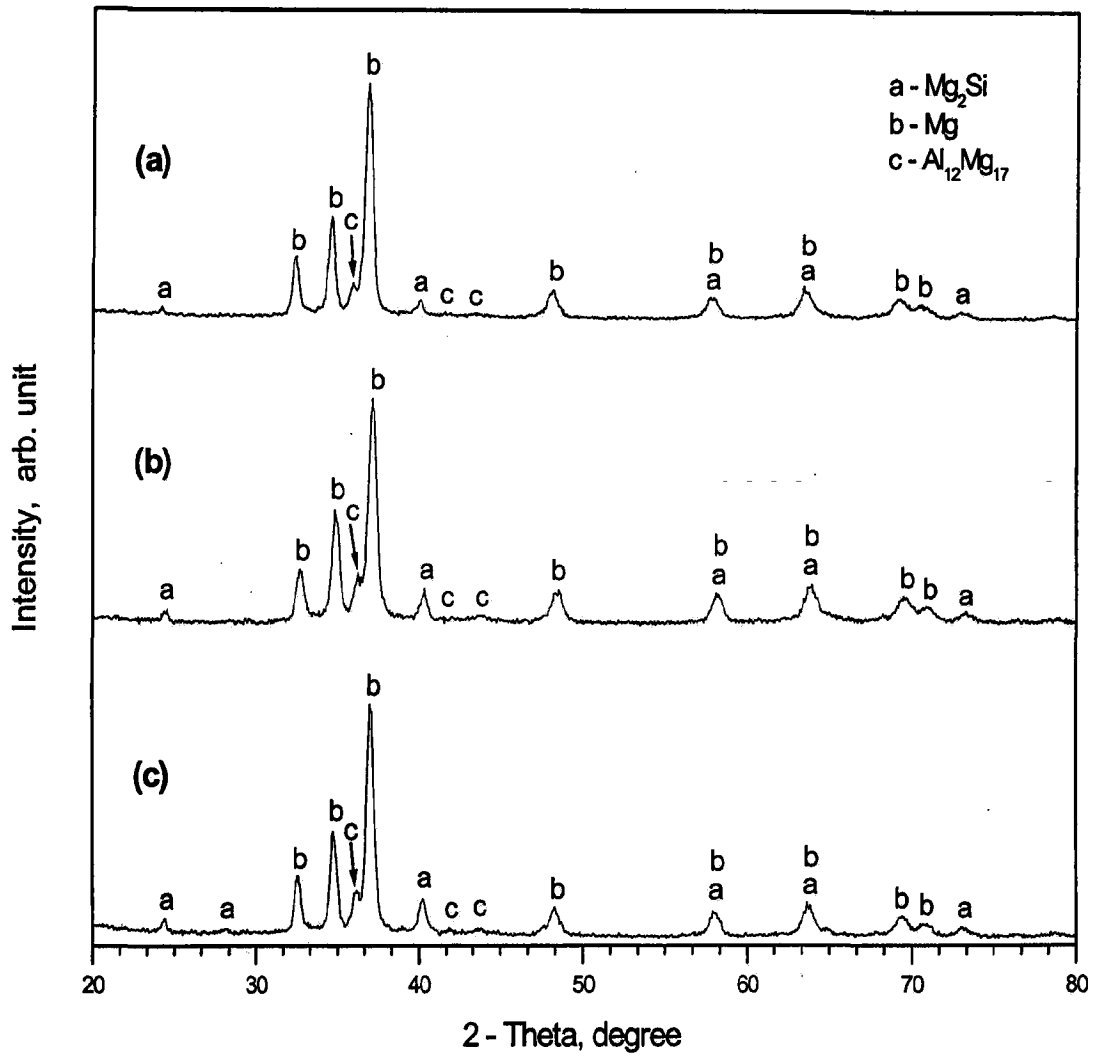


**Fig. 4.32:** Powder X-ray diffraction patterns of cast *in-situ* Mg-Al/ $Mg_2Si$  composites synthesized, at 760 °C using Al-Si master alloys containing respectively 9, 15 and 20 wt% Si and designated as MS9/76, MS15/76 and MS20/76.



micrograph and EDS spectrums with chemical composition of the constituents present at various locations of *in-situ* composite are shown in Fig. 4.33. Results of compositional analysis of spot 1 and spot 4 are displayed in Figs. 4.33(a) and (d), and both these spots correspond to intermetallic,  $Mg_2Si$ , which are blocky in nature. EDS spectrums and chemical composition of various elements present at spot 2 and spot 3 corresponds to  $\beta-Al_{12}Mg_{17}$  and  $\alpha-Mg$  solid solution in the matrix alloy of *in-situ* composite. The distributions of magnesium, aluminium and silicon across the matrix alloy, the *in-situ* generated intermetallics,  $Mg_2Si$  and  $\beta-Al_{12}Mg_{17}$  in the cast Mg-Al/ $Mg_2Si$  *in-situ* composite, as obtained through EDS line scan analysis are shown in Fig. 4.34. The distribution of aluminium is approximately constant through the entire matrix of the cast *in-situ* composite. Increase of aluminium and decrease of magnesium concentration can be noticed in the region of  $\beta-Al_{12}Mg_{17}$ . A SEM micrograph and EDS X-ray mappings for various elements of cast *in-situ* Mg-Al/ $Mg_2Si$  composite are shown in Fig. 4.35. Presence of intermetallics,  $Mg_2Si$ , in the *in-situ* composite, in different shapes and sizes is evident from the elemental distribution of silicon, and depletion of magnesium and aluminium at the corresponding regions. The shape of intermetallics,  $Mg_2Si$ , and at some places,  $\beta-Al_{12}Mg_{17}$  phase can also be observed by the overlay of magnesium, aluminium and silicon maps. There are also some oxide particles which could have been inherited from the raw materials or cast Al-Si alloy.

In the development of cast *in-situ* Mg-Al/ $Mg_2Si$  composite, Al-Si master alloy has been used. A typical optical micrograph of cast Al-15 wt% Si master alloy, processed at 930 °C is shown in Fig. 4.36 and silicon needles are clearly observed in the micrographs. A lower and a higher magnification optical micrographs of cast *in-situ* Mg-Al/ $Mg_2Si$  composite, synthesized at processing temperature of 760 °C using cast Al-15 wt% Si master alloy, designated as MS15/76, are shown in Fig. 4.37. A good distribution of the intermetallics,  $Mg_2Si$ , is observed in the microstructures.  $Mg_{17}Al_{12}$ ,  $\beta$ -phase in Mg-Si phase diagram, is clearly visible as marked by label 2. The average size of  $Mg_2Si$  observed is about 20  $\mu m$  and also, continuous interfaces between  $Mg_2Si$  and matrix alloy could be observed as shown in Figs. 4.37(b) and 4.40(f).

Optical micrographs at lower and higher magnifications, of the specimens sectioned from the bottom, the middle and the top segments along height of the cast *in-situ* Mg-Al/ $Mg_2Si$  composite ingot, synthesized at processing temperature of 800 °C using Al-15 wt% Si master alloy, designated as MS15/80, are shown in Fig. 4.38. A comparison of the microstructures reveals the distribution of  $Mg_2Si$  appears to be more or less similar at all the three segments of the cast ingot of the *in-situ* composite.

### (a) Influence of Amount of Si Particles Addition

In order to increase vol% of  $Mg_2Si$  in cast *in-situ* Mg-Al/ $Mg_2Si$  composites, Al-Si master alloys with increased silicon content are used in the synthesis of different cast *in-situ* Mg-Al/ $Mg_2Si$  composites. Optical micrographs of cast Al-Si master alloys synthesized with 9 wt%, 15 wt% and 20 wt% of Si particles additions are shown respectively in Figs. 4.39(a), (b) and (c). A comparison among these three micrographs shows the increasing vol% of silicon results in it being present in different shapes and sizes. Eutectic silicon needles are observed in micrograph of hypoeutectic alloy as shown in Fig. 4.39(a), while hypereutectic alloy shows blocky silicon precipitates and thick silicon needles as observed in micrographs given in Figs. 4.39(b) and (c). SEM micrographs of cast *in-situ* Mg-Al/ $Mg_2Si$  composites, synthesized at a processing temperature of 760 °C using Al-Si master alloys containing respectively 9, 15 and 20 wt% Si, designated as MS9/76, MS15/76 and MS20/76, are shown respectively in Figs. 4.40(a) and (b), (c) and (d), and (e) and (f). A comparison of these micrographs, shown in Figs. 4.40(a), (b), (c) and (d), reveals that increasing silicon content of the alloy results in increasing volume fraction of  $Mg_2Si$ . But the comparison of the micrographs shown in Figs. 4.40(c), (d), (e) and (f) reveals that blocky silicon precipitate in Al-Si alloy results in coarser  $Mg_2Si$  in Mg-Al/ $Mg_2Si$  composite synthesized with it.

The effect of different amounts of silicon in the Al-Si alloy on the *in-situ* generated reinforcement,  $Mg_2Si$ , and porosity in the cast *in-situ* Mg-Al/ $Mg_2Si$  composites are shown in Fig. 4.41. The Fig. shows that the amount of reinforcement,  $Mg_2Si$ , for the middle segments of cast ingots of *in-situ* composites is increasing almost linearly with the increasing amount of silicon in the Al-Si alloy, while the porosity is increasing gradually with silicon addition from 9 wt% to 15 wt%, but beyond 15 wt% and up to 20 wt%, there is drastic increase in porosity. The variation of porosity with amount of reinforcement,  $Mg_2Si$ , for the middle segments of cast ingots of *in-situ* Mg-Al/ $Mg_2Si$  composites is shown in Fig. 4.42. The Fig. shows that the porosity is increasing gradually with the amount of reinforcement generated from 2.42 vol% to 4.8 vol%, but beyond 4.8 vol% and up to 6.54 vol%, there is relatively sharper increase in porosity.

### (b) Influence of Processing Temperature

Cast *in-situ* Mg-Al/ $Mg_2Si$  composites are synthesized using Al-15wt% Si master alloy at processing temperatures of 720 °C, 760 °C and 800 °C. SEM micrographs of these cast *in-situ* composites, designated as MS15/72, MS15/76 and MS15/80, are shown respectively in Figs. 4.43(a), (b), and (c). From the comparison of these micrographs, it is observed that the intermetallic  $Mg_2Si$  is more clustered at lower processing temperature of 720 °C.

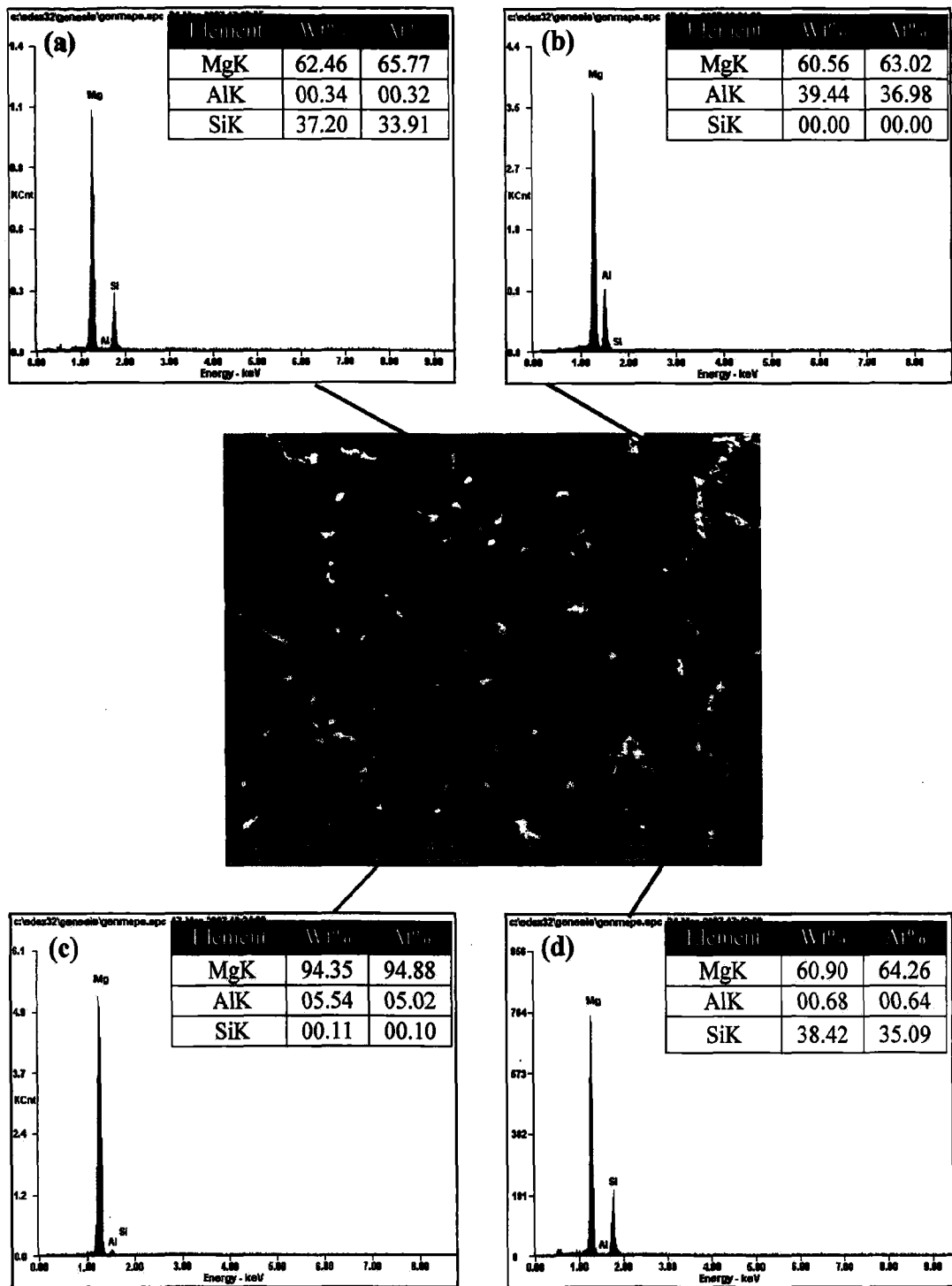


**Fig. 4.33:** SEM/EDS point analysis of *in-situ* Mg-Al/Mg<sub>2</sub>Si composite synthesized, using Al-20 wt% Si master alloy, at processing temperature of 760 °C at various locations; (a) spot 1, (b) spot 2, (c) spot 3, (d) spot 4.

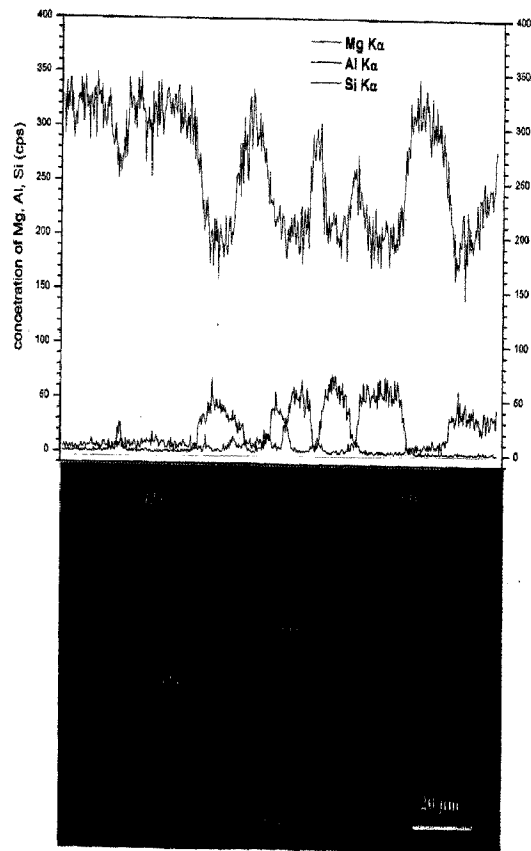


Fig. 4.34: The distributions of magnesium, aluminium and silicon across the matrix alloy and the intermetallics,  $Mg_2Si$  in the cast *in-situ* Mg-Al/ $Mg_2Si$  composite, synthesized at processing temperature of 760 °C using Al-20 wt% Si master alloy ; the label (1) indicates the intermetallic phase,  $Mg_2Si$ , (2) the  $\beta$ -phase,  $Al_{12}Mg_{17}$ , (3)  $\alpha$ -Mg and (4) the oxides

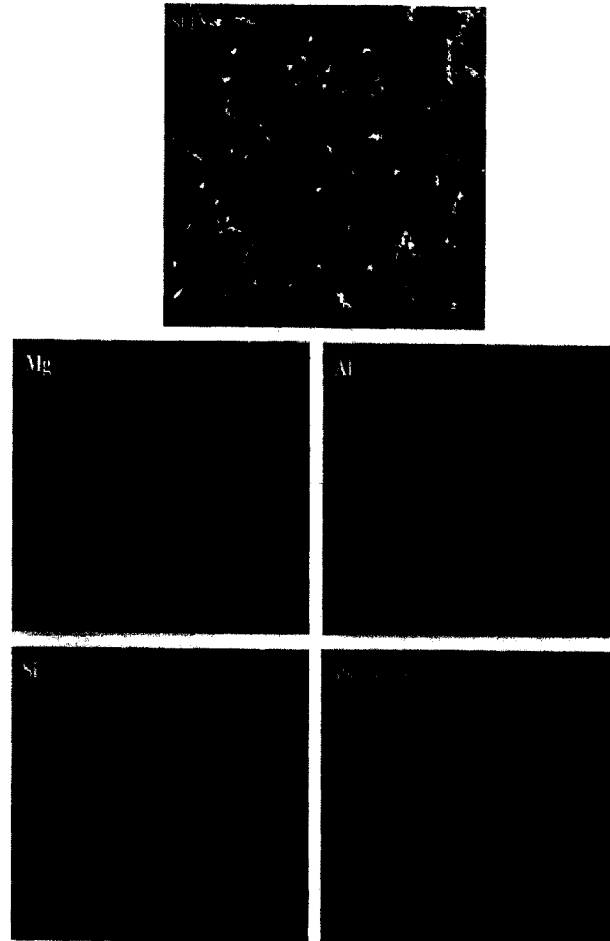


Fig. 4.35: SEM micrograph and EDS X-ray mapping for various elements of *in-situ* Mg-Al/Mg<sub>2</sub>Si composite synthesized, at processing temperature of 760 °C using Al-20 wt% Si master alloy.

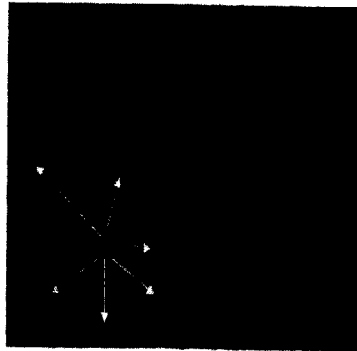


Fig. 4.36: Typical optical micrograph of cast Al-15wt%Si master alloy, processed at 930 °C; the label (1) indicates silicon needles.

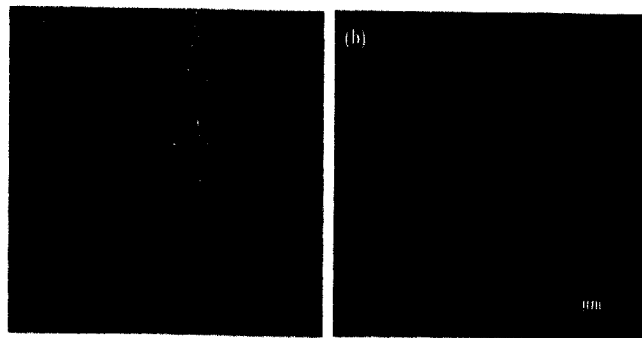
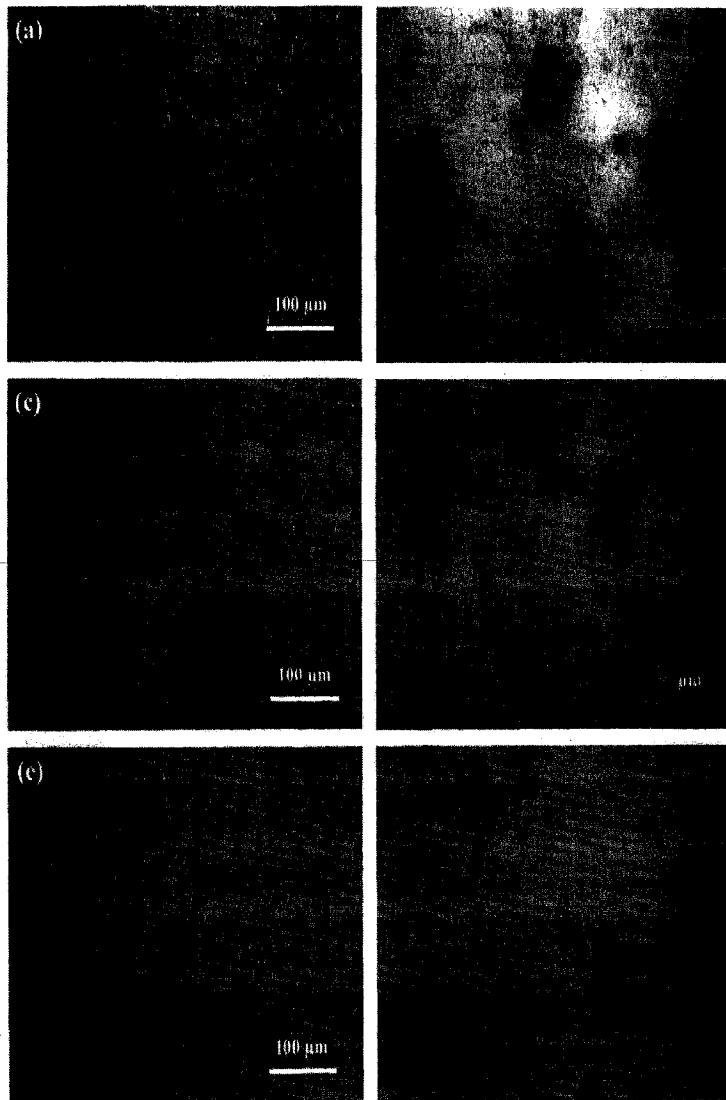
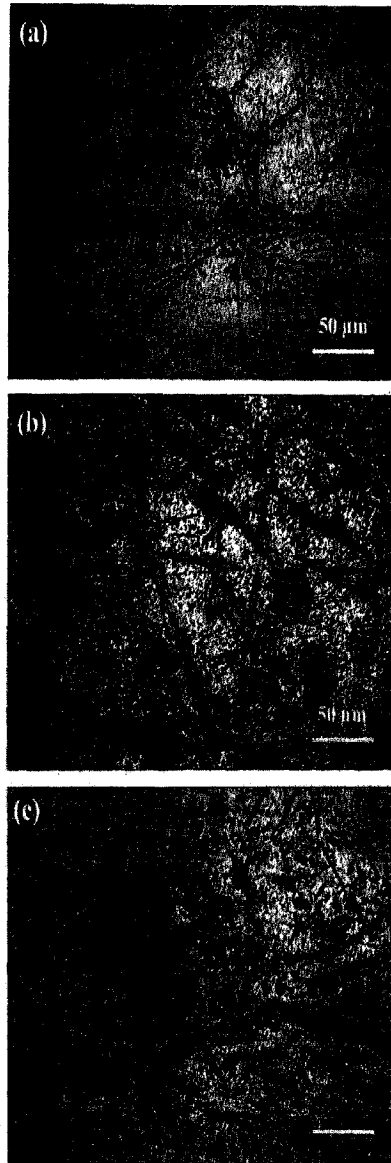


Fig. 4.37: a) Lower and (b) higher magnification optical micrographs of cast Mg-Al/Mg<sub>2</sub>Si *in-situ* composite synthesized at 760 °C using Al-15 wt% Si master alloy; the label (1) indicates the intermetallics, Mg<sub>2</sub>Si and (2) the β-phase, Al<sub>12</sub>Mg<sub>17</sub>.



**Fig. 4.38:** Lower and higher magnification optical micrographs of cast *in-situ* Mg-Al/ $Mg_2Si$  composite synthesized, at 800 °C using cast Al-15 wt% Si master alloy; at the bottom (a) & (b), the middle (c) & (d) and the top (e) & (f).



**Fig. 4.39** Optical micrographs of cast Al-Si master alloys synthesized at 930 °C with different nominal composition of silicon metal particles; (a) 9 wt% Si, (b) 15 wt% Si, and (c) 20 wt% Si.



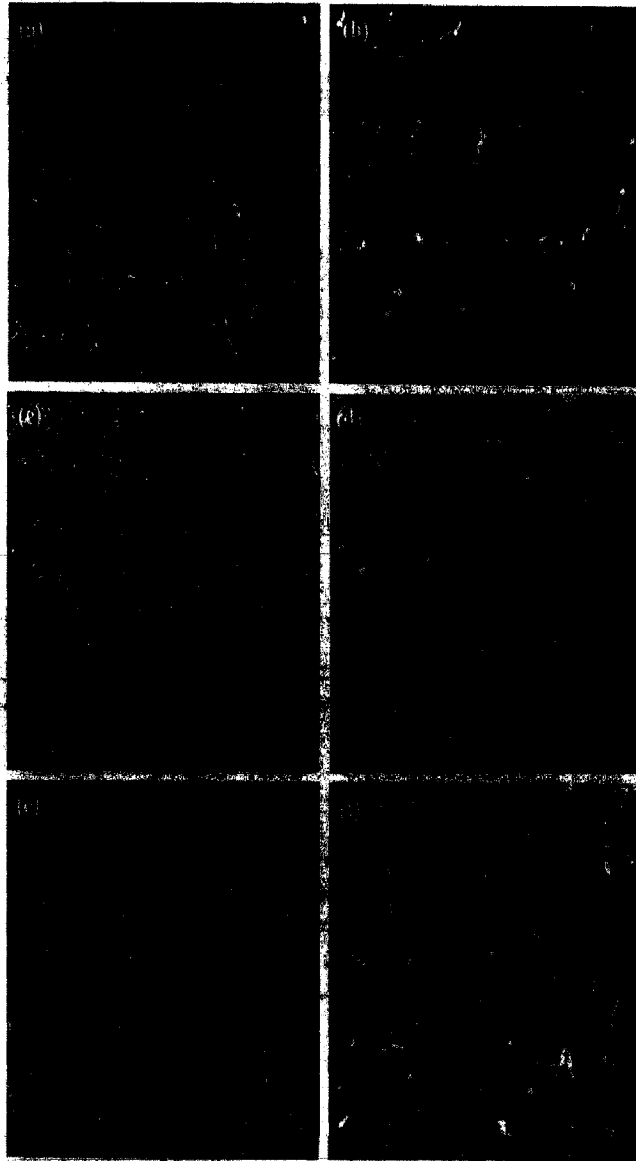


**Fig. 4.40:** SEM micrographs of cast *in-situ* Mg-Al/Mg<sub>2</sub>Si composite, synthesized at 760 °C using cast Al-Si master alloy with different amount of silicon content; (a) 9 wt% Si, (c) 15 wt% Si, (e) 20 wt% Si and at lower magnification; (b) 9 wt% Si, (d) 15 wt% Si, and (f) 20 wt% Si at higher magnification.

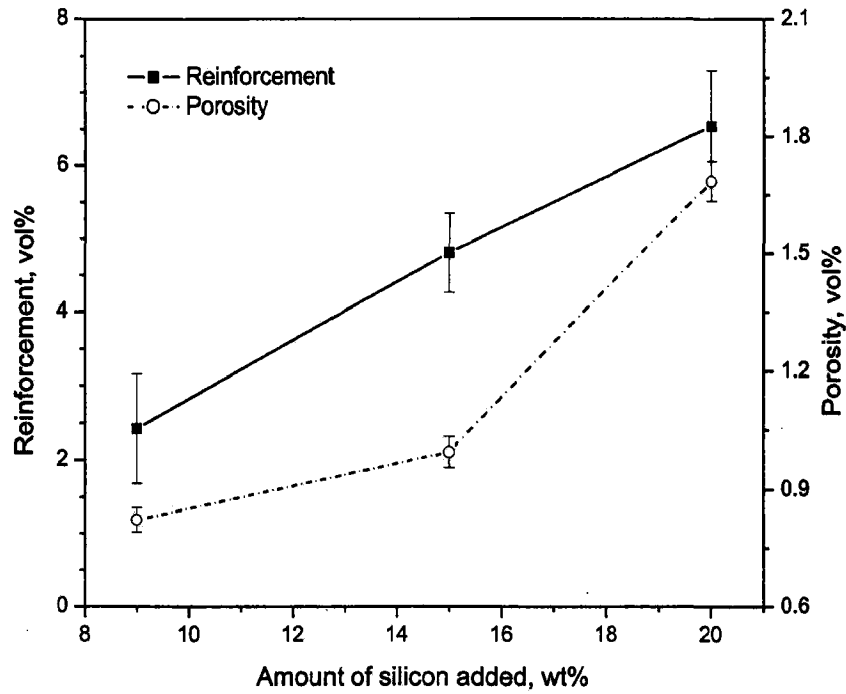


**Fig. 4.41:** The variation of amount of *in-situ* generated reinforcement,  $Mg_2Si$ , and porosity content for the middle segments of cast ingots of *in-situ* Mg-Al/ $Mg_2Si$  composites with amount of silicon added.

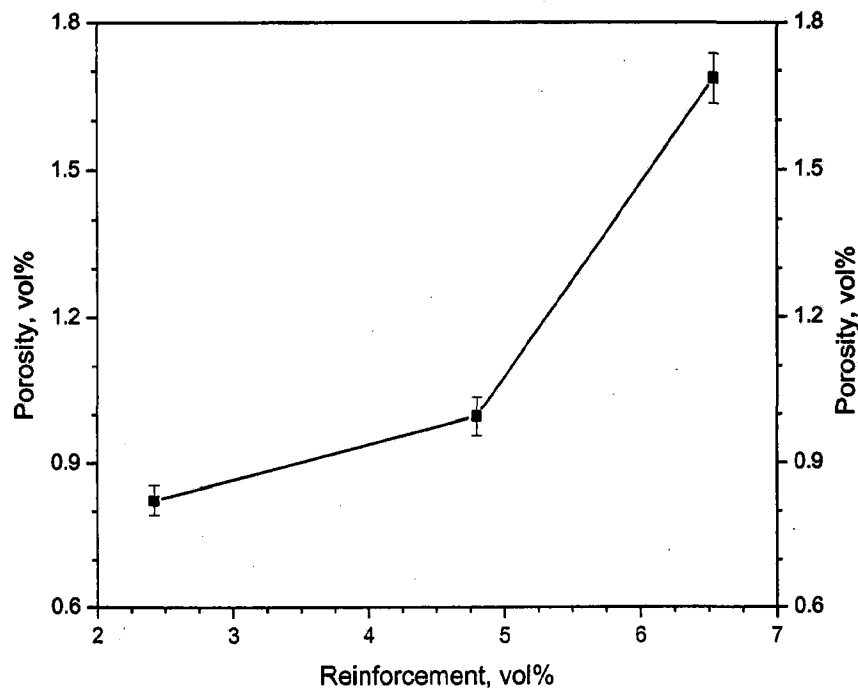


**Fig. 4.42:** The variation of amount of porosity with *in-situ* generated reinforcement,  $Mg_2Si$ , for the middle segments of cast ingots of *in-situ* Mg-Al/ $Mg_2Si$  composites.

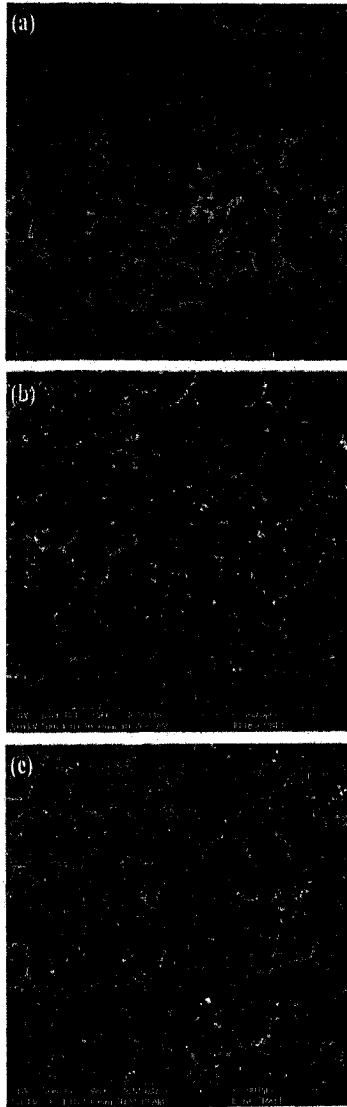


**Fig. 4.43:** SEM micrographs of cast *in-situ* Mg-Al/Mg<sub>2</sub>Si composites, synthesized using cast Al-15 wt% Si master alloy at different processing temperatures; (a) 720 °C, (b) 760 °C and (c) 800 °C.

### 4.2.3 Studies on Mechanical Properties of Cast Mg-Al/Mg<sub>2</sub>Si *In-Situ* Composites

#### (a) Hardness Measurement

Typical variation of Brinell hardness measured along the height from the bottom of ingot of cast *in-situ* Mg-Al/Mg<sub>2</sub>Si composites, synthesized at 760 °C using cast Al-15wt% Si alloy, designated as MS15/76, has been plotted in terms of normalized height ( $h/H$ ) as shown in Fig. 4.44, where,  $h$  is the height of the location from the bottom of the cast ingot where hardness is measured and  $H$  is the total height of the cast ingot. The hardness remained within a limited band of values and decreased slightly as one moves from bottom to top of cast ingot.

The Brinell hardness has been measured for the cast *in-situ* composites synthesized at different processing temperatures. The variation in Brinell hardness in the middle segment of the ingot with processing temperature is shown in Fig. 4.45, for cast *in-situ* Mg-Al/Mg<sub>2</sub>Si composites synthesized using Al-15 wt% Si alloy. The hardness almost remains constant up to a processing temperature of 760 °C, however, it appears to decrease as the processing temperature increased beyond 760 °C upto 800 °C, the maximum processing temperature investigated here.

The Brinell hardness has been measured for the cast *in-situ* Mg-Al/Mg<sub>2</sub>Si composites synthesized at processing temperature of 760 °C using Al-Si master alloys containing different amounts of Si (9, 15 and 20 wt%). The variation of Brinell hardness with amount of reinforcement in the cast *in-situ* composites is shown in Fig. 4.46. The volume fraction of reinforcement in the cast *in-situ* composites has been determined by point count method. As the volume fraction of reinforcement increases, there is a significant improvement in the hardness.

For comparison, the Brinell hardness values of cast commercial magnesium, Mg-9 wt% Al alloy and cast *in-situ* Mg-Al/Mg<sub>2</sub>Si composite synthesized at a processing temperature of 760 °C using Al-20 wt% Si master alloy, designated as MS20/76, are shown in Fig. 4.47. The Brinell hardness of cast *in-situ* composite is higher by a factor about 1.4 than that observed in cast Mg-9 wt% Al alloy and about twice that of cast commercial magnesium.

#### (b) Tensile Properties

A typical comparison between average tensile properties, ultimate tensile strength and percentage elongation, measured at the bottom, middle and top height segments of the ingot of cast *in-situ* Mg-Al/Mg<sub>2</sub>Si composite synthesized at a processing temperature of 760 °C using Al-9 wt% Si master alloy, designated as MS9/76, is shown in Fig. 4.48. The tensile properties observed at the bottom, which contains relatively lower porosity and higher particle content, are slightly higher compared to those observed at the top of the cast ingot. It is observed that

porosity content increases from 0.6 vol% to 1.1 vol% as one moves from bottom to the top of cast ingot while intermetallic content decreases from 2.43 vol% to 2.36 vol%.

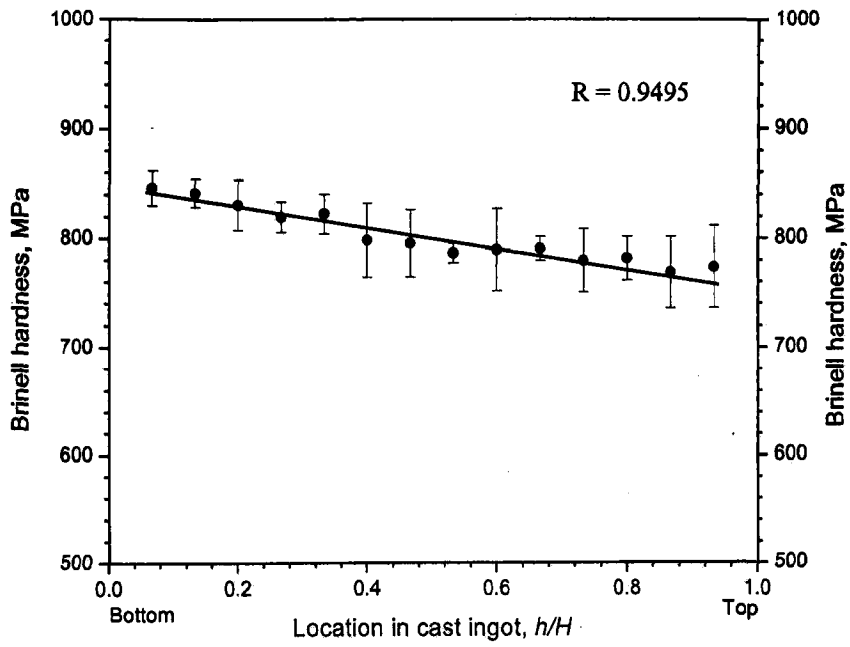
The variations in ultimate tensile strength and percentage elongation for the middle height segment of cast ingot of the cast *in-situ* Mg-Al/Mg<sub>2</sub>Si composite, synthesized at different processing temperatures using the same amount of Al-15 wt% Si master alloy, are shown in Fig. 4.49. The ultimate tensile strength is increasing significantly with increasing processing temperature till 760 °C and thereafter, it is decreasing with further increase in processing temperature beyond 760 °C. The percentage elongation is gradually increasing with increasing processing temperature from 720 °C to 760 °C but decreases significantly with further increase in processing temperature beyond 760 °C.

The variation in ultimate tensile strength with porosity content for cast *in-situ* Mg-Al/Mg<sub>2</sub>Si composite containing  $4.52 \pm 0.64$  volume percent of Mg<sub>2</sub>Si is shown in Fig. 4.50. As expected, the Fig. shows that the tensile strength of the composite is decreasing with increasing porosity and the variation appears to be linear with porosity content in spite of scatter. The linear least square fit has a co-efficient of correlation 0.9. Similarly, the variation in percentage elongation with porosity content for cast *in-situ* Mg-Al/Mg<sub>2</sub>Si composite containing  $4.52 \pm 0.64$  volume percent of Mg<sub>2</sub>Si is shown in Fig. 4.51. The Fig. shows that the percentage elongation of the composite is decreasing with increasing porosity more or less linearly in spite of scatter and the linear least square fit has a co-efficient of correlation 0.85.

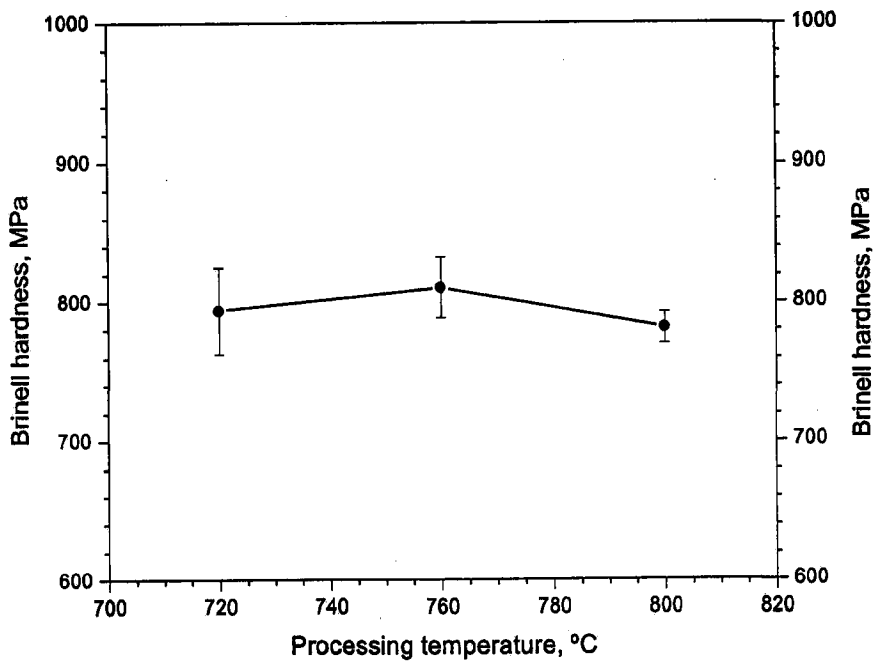
In cast composites there is the presence of porosity affecting the tensile properties and, therefore, to isolate the effect of particles alone, it is necessary to eliminate the contribution of porosity in the observed tensile properties to arrive at an estimate of tensile properties at zero porosity. The relationship between the particle content and the ultimate tensile strength at zero porosity,  $\sigma_{ut0}$ , for different composites has been shown in Fig. 4.52. The ultimate tensile strength at zero porosity,  $\sigma_{ut0}$ , decreases with increasing particle content. The relationship between the particle content and the percentage elongation at zero porosity, (percentage elongation)<sub>0</sub>, for different composites has been shown in Fig. 4.53. The percentage elongation at zero porosity decreases with increasing particle content.

#### 4.2.4 Fractography

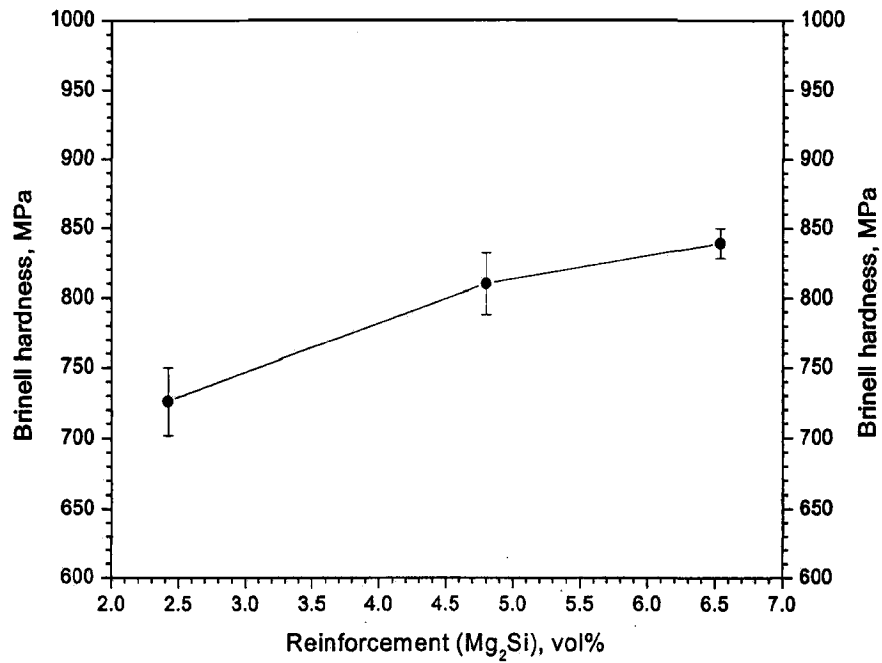
The tensile fractured surfaces of the specimens subjected to tensile test have been studied under scanning electron microscopy (SEM) for the cast *in-situ* Mg-Al/Mg<sub>2</sub>Si composites and the results obtained are presented in this section.



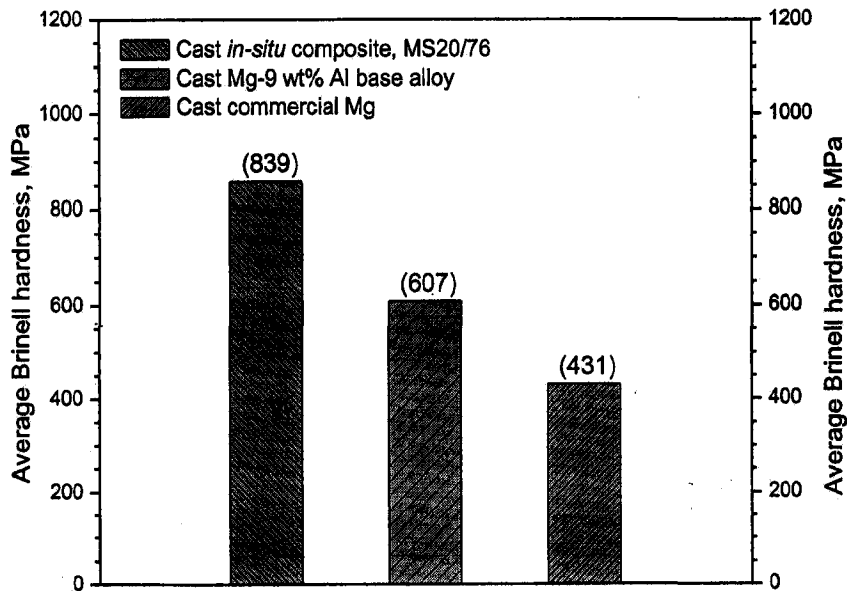
**Fig. 4.44** The variation of hardness with normalized location ( $h/H$ ) along the height of cast ingot of *in-situ* Mg-Al/Mg<sub>2</sub>Si composite, synthesized at 760 °C using cast Al-15 wt% Si master alloy.



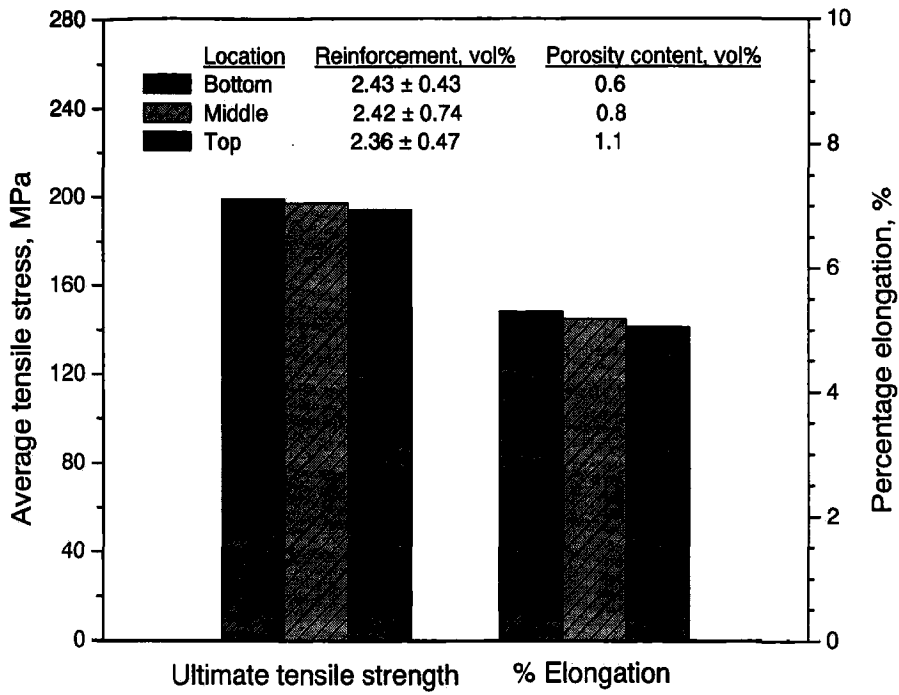
**Fig. 4.45** The variation of hardness with processing temperature for cast *in-situ* Mg-Al/Mg<sub>2</sub>Si composite, synthesized using cast Al-15 wt% Si master alloy.



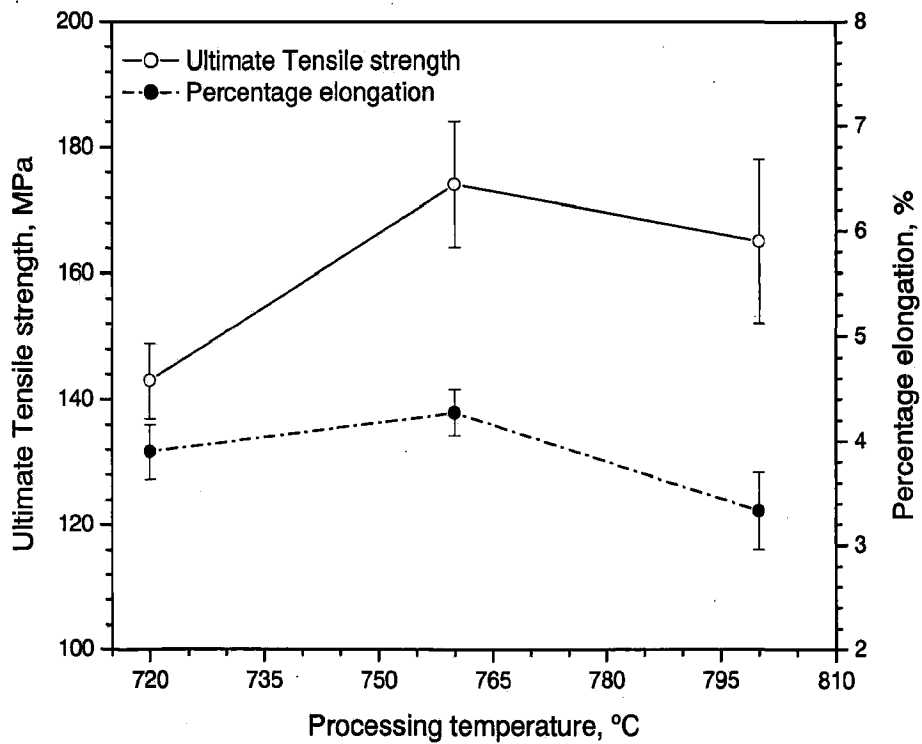
**Fig. 4.46** The variation of hardness with reinforcement, Mg<sub>2</sub>Si for cast *in-situ* Mg-Al/Mg<sub>2</sub>Si composites, synthesized at 760 °C using different cast Al-Si master alloys.



**Fig. 4.47** Comparison between average Brinell hardness for cast *in-situ* Mg-Al/ Mg<sub>2</sub>Si composite containing 6.54 ± 0.76 vol% reinforcement and 1.7 vol% porosity, designated as MS20/76, cast Mg-Al alloy containing 0.6 vol% porosity and cast commercially pure Mg containing 0.2 vol% porosity.

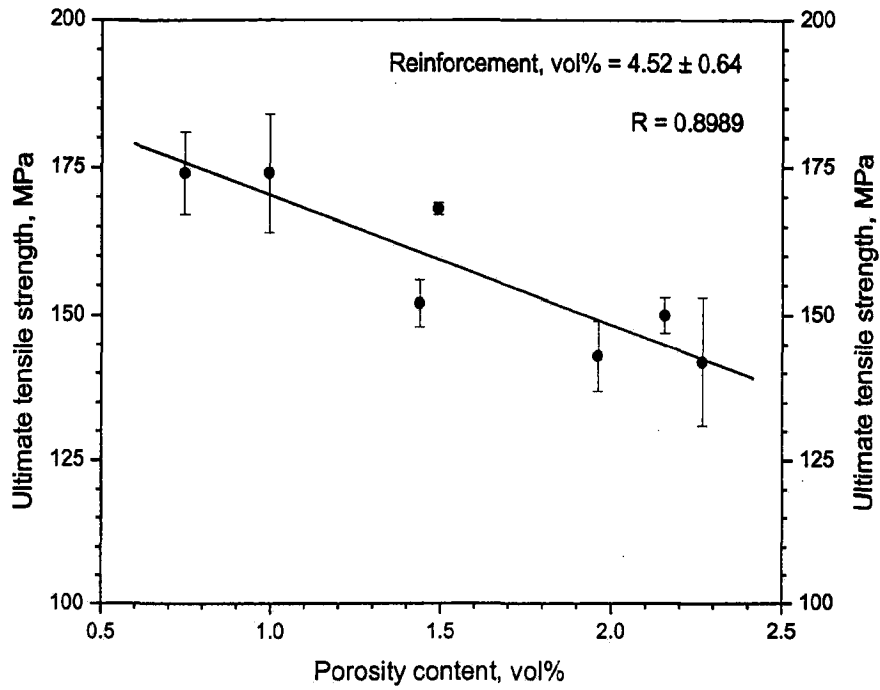


**Fig. 4.48** The comparison between tensile properties for the three segments of the cast *in-situ* Mg-Al/Mg<sub>2</sub>Si composite, synthesized at 760 °C using cast Al-9 wt% Si master alloy.

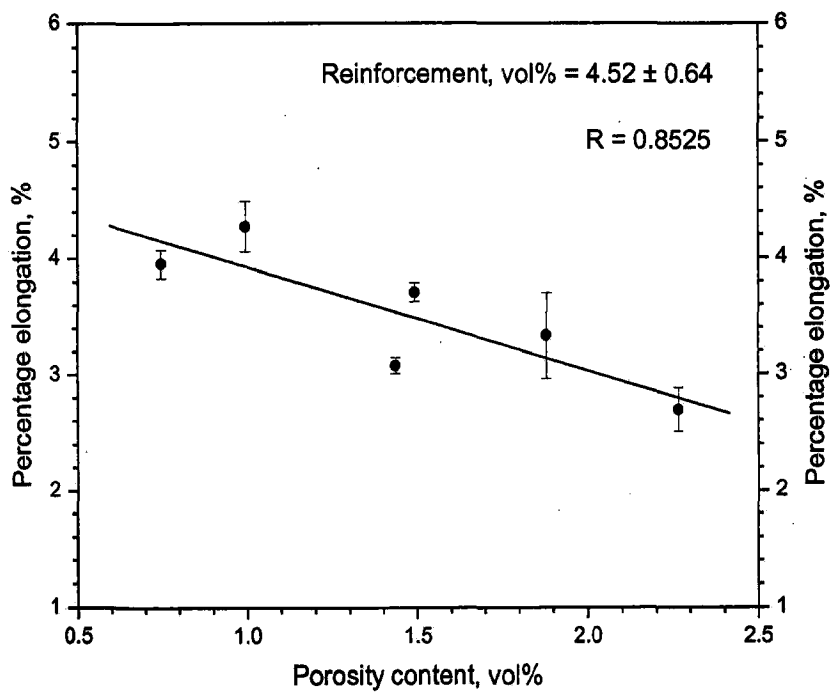


**Fig. 4.49** The variation of tensile properties with processing temperature for cast *in-situ* Mg-Al/Mg<sub>2</sub>Si composite, synthesized using cast Al-15 wt% Si master alloy.

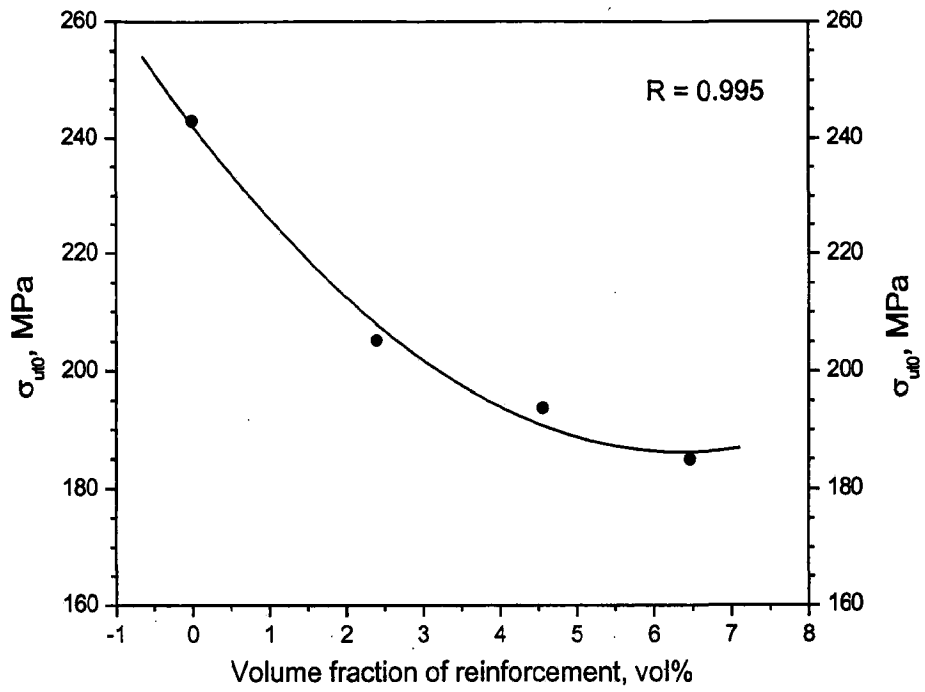




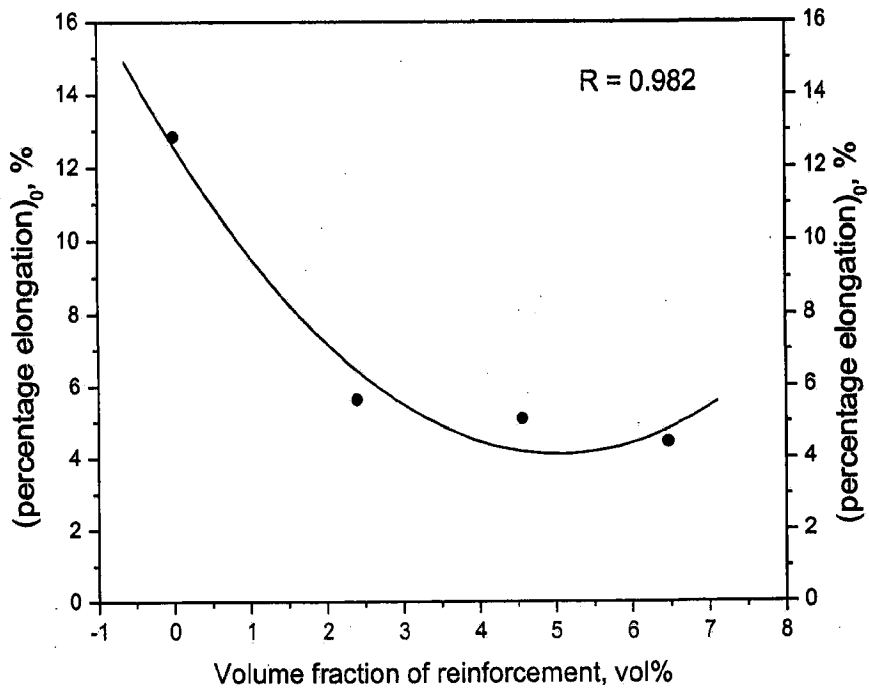
**Fig. 4.50** The variation of ultimate tensile strength with porosity content for cast *in-situ* Mg-Al/Mg<sub>2</sub>Si composite containing  $4.52 \pm 0.64$  vol% reinforcement, Mg<sub>2</sub>Si.



**Fig. 4.51** The variation of percentage elongation with porosity content for cast *in-situ* Mg-Al/Mg<sub>2</sub>Si composite containing  $4.52 \pm 0.64$  vol% reinforcement, Mg<sub>2</sub>Si.



**Fig. 4.52** Effect of particle content on the ultimate tensile strength at zero porosity of cast *in-situ* Mg-Al/Mg<sub>2</sub>Si composites.



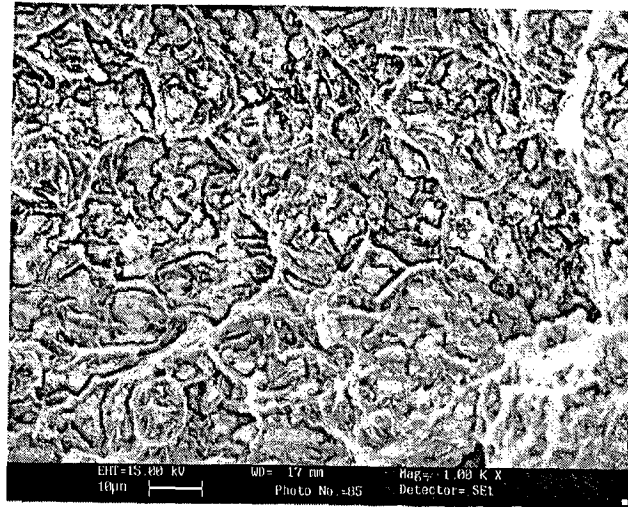
**Fig. 4.53** Effect of particle content on the percentage elongation at zero porosity of cast *in-situ* Mg-Al/ Mg<sub>2</sub>Si composites.

Fig. 4.54(a) shows the typical tensile fractured surface, at higher magnification, as observed under scanning electron microscope for the specimen having better tensile properties, ultimate tensile strength of 207 MPa and elongation of 6.2 %, machined out of cast *in-situ* Mg-Al/Mg<sub>2</sub>Si composite containing 2.43 vol% reinforcement and 0.6 vol% porosity. The tensile fractured surface revealed the evidence of mixed-mode fracture. Primarily brittle sheared regions and some ductile dimples are seen on the fractured surface. While the Fig. 4.54(b) shows the tensile fractured surface as observed under SEM for the worst performing specimen,  $\sigma_{ut} = 112$  MPa, machined out of cast *in-situ* Mg-Al/Mg<sub>2</sub>Si composite containing 4.12 vol% reinforcement and 2.3 vol% porosity. The tensile fractured surface shows the brittle cleavage fracture with relatively larger shrinkage cavity showing dendrites, resulting in an overall elongation of 1.67%. The typical tensile fractured surface of the cast unreinforced Mg-9 wt% Al alloy containing 0.3 vol% porosity has been studied under SEM at different magnifications as shown in Fig. 4.54(c). The fractured surface shows the intergranular cleavages and dimples of ductile fracture resulting in 11.67% elongation.

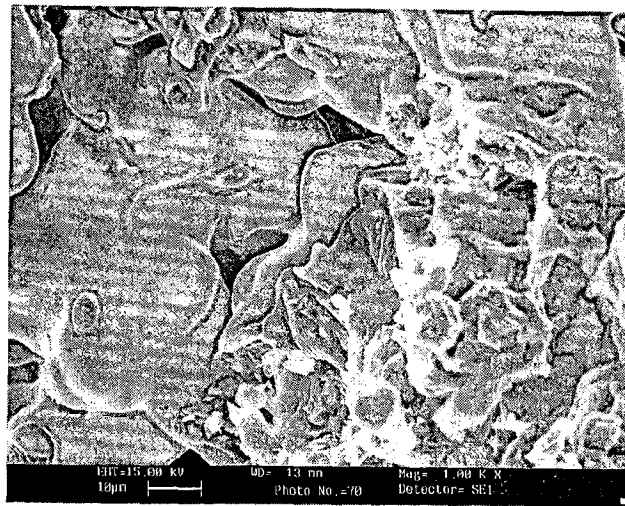
### 4.3 Discussion

Cast *in-situ* magnesium based composites synthesized by addition of cast aluminium based composites, processed earlier by dispersion of TiO<sub>2</sub> particles in molten aluminium, have inherited intermetallic, Al<sub>3</sub>Ti, and alumina particles from the aluminium based composite. The aluminum from the matrix of aluminium based composite has alloyed with molten magnesium and the addition has been controlled to obtain a matrix of Mg-9 wt% Al alloy in all the composites synthesized for this study. Thus, these composites have Al<sub>3</sub>Ti and alumina particles distributed in the matrix of Mg-Al alloy as identified from XRD, EDS and EPMA analysis. The intensity of X-ray diffraction peaks of alumina are so small that they could not be clearly detected from XRD pattern of cast *in-situ* magnesium based composite powder as shown in Fig. 4.1(a) and hence, the particles have been extracted by dissolving the composite in dilute HCl. The XRD pattern of extracted particles from the same *in-situ* composite is as shown in Fig. 4.1(c) and it shows, along with the peaks of alumina, the peaks corresponding to MgO, MgAl<sub>2</sub>O<sub>4</sub> and Al<sub>2</sub>TiO<sub>5</sub>, which generally forms at the interfaces of particles and are helpful in promoting wettability with metallic melts. High intensity peaks of intermetallics, Al<sub>3</sub>Ti, have been identified in the XRD pattern of residue of partially dissolved cast *in-situ* magnesium based composite in relatively highly diluted HCl, as shown in Fig. 4.1(b). Presence of intermetallics, Al<sub>3</sub>Ti and alumina have been further confirmed and identified in the microstructures of *in-situ* composites through EDS point analysis as shown in Fig. 4.2, line scan as shown in Fig. 4.3 and X-ray mapping as shown in Fig. 4.4.

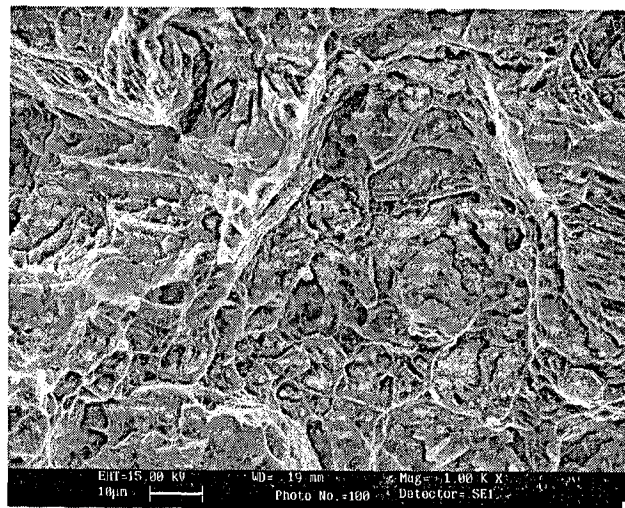
Typical microstructure of cast Al-based composite used in the development of cast *in-situ* Mg-Al/Al<sub>3</sub>Ti-Al<sub>2</sub>O<sub>3</sub> composite is shown in Fig. 4.5 and the microstructure of the resulting magnesium based composite are shown in Fig. 4.6 at lower and higher magnifications. The phases, Al<sub>3</sub>Ti, oxide particles and Al<sub>12</sub>Mg<sub>17</sub> are clearly visible in Figs. 4.6(a), (b), and 4.7 but in aluminium based composite the phases Al<sub>3</sub>Ti and oxide particles are only observed in Fig. 4.5 as Al<sub>12</sub>Mg<sub>17</sub> forms at magnesium rich corner of Mg-Al phase diagram. Increasing addition of TiO<sub>2</sub> particles increases the amount of reinforcement, Al<sub>3</sub>Ti and oxide particles in cast Al-based composite as shown in the Fig. 4.8 and its addition to magnesium to get Mg-9 wt% alloy matrix, in the same way increases the Al<sub>3</sub>Ti content in the cast magnesium based composite as shown in Fig. 4.9. Increasing amount of reinforcing oxide particles as determined by extracted particles, with increasing addition of TiO<sub>2</sub> particles in aluminium based composite is shown in Fig. 4.10. The variation of porosity in cast magnesium based composite with increasing addition of TiO<sub>2</sub> particles in aluminium based composite added is shown in Fig. 4.11 and that with increasing extracted particles is shown Fig. 4.13. The porosity in cast composite increases with increasing particle content in it and it is, thus, expected that increasing TiO<sub>2</sub> addition should result in increasing porosity in aluminium based composite but its addition to magnesium increases porosity only up to 10 wt% TiO<sub>2</sub> but beyond 10 wt% TiO<sub>2</sub>, the higher porosity in aluminum based composite in aluminum based composite is not inherited by magnesium based composite as shown in Fig. 4.11 The argon environment during magnesium melt processing is able to overcome the higher porosity in aluminium based composite but the observed lowering of porosity in magnesium based composite with increasing TiO<sub>2</sub> in aluminium based composite is really surprising. The trend of variation of porosity with extracted particles as shown in Fig. 4.13 is similar to that with increasing TiO<sub>2</sub> addition in aluminium based composite because the amount of extracted particle is proportional to TiO<sub>2</sub> addition in aluminium based composite as shown in Fig.4.10. It has been observed that the bottom of the cast ingot of magnesium based composite has more particles of Al<sub>3</sub>Ti and oxides as shown in Fig. 4.7 and it is indicative of particles not being associated with pores. The variation in difference in weight fraction of extracted particles at the top and bottom of cast ingot of *in-situ* Mg-based composite with amount of TiO<sub>2</sub> particles added to aluminium based composite is shown in Fig. 4.12 and it is observed that there is a jump in the difference beyond 10 wt% TiO<sub>2</sub> and it may be attributed to lower porosity leading to enhanced settling to the bottom. Increasing processing temperature of Al-based composites is expected to result in faster kinetics of chemical reduction of TiO<sub>2</sub> particles by molten aluminium and it results in increasing thickness of Al<sub>3</sub>Ti rods in cast *in-situ* Mg-based composites as shown in Fig. 4.14, but higher temperature for processing of magnesium based composite beyond 800 °C results in degradation of Al<sub>3</sub>Ti rods as shown in Figs. 4.15(e) and (f).



(a)



(b)



(c)

**Fig. 4.54** SEM fractographs showing tensile fracture surfaces; (a) and (b) cast *in-situ* Mg-Al/Mg<sub>2</sub>Si composites containing 2.43 and 4.12 wt% of reinforcing particles, and 0.6 and 2.3 vol% porosities respectively and (c) cast Mg-9 wt% Al base alloy containing 0.5 vol% porosity.

The variation in hardness with location ( $h/H$ ) along the height of cast ingot as given in Fig. 4.16 shows that the hardness of the composite is decreasing slowly within a limited band from the bottom to the top of the ingot as a linear function of distance measured from the bottom having a co-efficient of correlation 0.96. The reason for this may be due to decreasing of intermetallics and particle content and increasing of porosity from the bottom towards the top of the ingot. The hardness decreases with increasing processing temperature of magnesium based composite as shown in Fig. 4.17 and it may be attributed to degradation of  $\text{Al}_3\text{Ti}$  rods. Fig. 4.18 shows increasing hardness with increasing amount of extracted particles and intermetallic contents in *in-situ* composites as expected and the extent of extracted particle and intermetallic content depend on the amounts of  $\text{TiO}_2$  particles added in the processing of Al-based composites. The Brinell hardness for cast *in-situ* Mg-Al/ $\text{Al}_3\text{Ti}$ - $\text{Al}_2\text{O}_3$  composite containing 2.14 wt% of extracted particles and 1 vol% of porosity, shows significant improvement by a factor of 1.4 compared to that observed in either unreinforced cast Mg-9 wt% Al alloy containing 0.6 vol% porosity and a factor of about 2 compared to that in cast unreinforced commercial magnesium containing 0.2 vol% porosity as shown in Fig. 4.19. The Brinell hardness of cast *in-situ* composite, cast Mg-9 wt% Al alloy and cast commercial Mg are respectively, 857, 607 and 431 MPa. The hardness values observed in the investigation for cast commercial Mg and cast Mg-9 wt% Al alloy, which contains the Al similar to AZ91 magnesium alloy, are comparable to those observed by the other investigators. Wang et al. (2004) have reported the Brinell hardness value of 314 MPa for cast pure Mg, while Saravanan and Surappa (2000) have observed the Vicker's hardness value of 441 MPa for cast extruded pure Mg. Jiang et al. (2003) have reported the Brinell hardness value of 589 MPa on for magnesium alloy, AZ91, which mainly contains about 9 wt% Al and 1 wt% Zn, processed through semi-solid slurry stir casting technique. Ma et al. (2005) have reported the Brinell hardness value of 550 MPa for magnesium alloy AZ91 processed through stir casting technique. Wang et al. (2006) have reported the Brinell hardness value of 608 MPa for as cast AZ91.

Wang et al. (2004) have reported the Brinell hardness values respectively, 441, 648 and 883 MPa for Mg based composites reinforced with 10, 20 and 30 vol%  $\text{TiB}_2$  particles, processed through powder metallurgy route. Wang et al. (2006) have observed the Brinell hardness values respectively, 726, 785 and 804 MPa for Mg-Al alloy based composites reinforced with 2, 5 and 7.5 wt%  $\text{TiB}_2$  particles, fabricated by adding a  $\text{TiB}_2$ -Al compact mixed with fine  $\text{TiB}_2$  and Al powders to magnesium melt and using a semi-solid slurry stirring technique. The investigator, Jiang et al. (2003) and Wang et al. (2004) have reported

Brinell hardness values, respectively, 814 and 785 MPa in *in-situ* 10 vol% TiC<sub>p</sub>/AZ91 composite and *in-situ* 5 wt% TiC<sub>p</sub>/AZ91D composite. They have used powder metallurgy route for the preparation of master alloy/green perform which has been used for the fabrication of *in-situ* composite.

The values of UTS and percentage elongation at the middle height segment of cast ingot of *in-situ* Mg-Al/Al<sub>3</sub>Ti-Al<sub>2</sub>O<sub>3</sub> composites are respectively, 171 ± 6 MPa and 4.62 ± 0.18%. The UTS and percentage elongation observed at the middle height segment of cast ingots of Mg-9 wt% Al alloy and commercial magnesium are respectively, 192 ± 10 MPa and 9.32 ± 0.87%, and 149 ± 1 MPa and 17.16 ± 0.04%. Saravanan and Surappa (2000) have reported the values of UTS and percentage elongation, respectively 196 MPa and 12% for extruded pure Mg and 258 MPa and 2% for extruded Mg/30 vol% SiC<sub>p</sub> composite. It is interesting that cast commercial magnesium has shown higher percentage elongation compared to that observed in extruded magnesium by Saravanan and Surappa (2000). Lim et al. (2005) have reported the values of UTS and percentage elongation, respectively 173 MPa and 7.36% for cast extruded pure Mg. Lim et al (2003) in another study have reported UTS and percentage elongation for Mg-Al alloy having composition similar to AZ91, 329 MPa and 5% respectively, but in Mg-Al/8 vol% SiC<sub>p</sub> composite the corresponding values are 268 MPa and 1.2%. Both of these materials have been processed through powder metallurgy route followed by hot extrusion. Luo (1995) have reported the values of UTS and percentage elongation, respectively 152 MPa and 0.8%, for Mg/10 vol% SiC<sub>p</sub> composite, lower than those observed in commercial magnesium. Gupta et al. (2000) have reported the values of UTS and percentage elongation, respectively 181 ± 6 MPa and 4.7 ± 1.3% for extruded Mg/9.3 vol% SiC<sub>p</sub> composite. The UTS is significantly lower than that observed by Lim et al (2003) due to difference in matrix although the extent of reinforcement is similar. Lloyd (1994) has reported the values of UTS and percentage elongation, respectively 236 MPa and 2% for Mg/16.1 wt% SiC<sub>p</sub> composite. Here one observes a lower UTS compared to that observed by Lim et al (2003) using about half of the reinforcement of SiC<sub>p</sub> but using Mg-Al alloy matrix.

The variation in tensile properties at different height segments of cast *in-situ* Mg-Al/Al<sub>3</sub>Ti-Al<sub>2</sub>O<sub>3</sub> composites, synthesized at 800 °C using cast Al-based composite developed with addition of 8 wt% TiO<sub>2</sub>, designated as MT8/80, shows that the higher tensile properties are obtained at the bottom of the cast ingot where there is larger intermetallic and particle content, as shown in Fig. 4.20. It is observed that the porosity increases while the particle and intermetallic content decreases from the bottom towards the top of the cast ingot. The variations in tensile properties like ultimate tensile strength and percentage elongation with processing

temperature show that the ultimate tensile strength is increasing slightly while the percentage elongation is almost constant with increasing processing temperature, as shown in Fig. 4.21. The degradation of intermetallic at higher processing temperature does not appear to impair the tensile properties significantly in the range of processing temperature investigated.

The tensile properties (UTS and percentage elongation) of cast *in-situ* Mg-Al/Al<sub>3</sub>Ti-Al<sub>2</sub>O<sub>3</sub> composite have been extrapolated to zero porosity so as to compare the results without the influence of porosity. It has been observed that with increasing particle content the tensile properties decrease as shown in Figs. 4.24 and 4.26 and better tensile properties are observed at relatively lower particle content. Addition of increasing amount of TiO<sub>2</sub> particles in Al-based composite is observed to release increasing amount of titanium in molten aluminum. The titanium, thus released, is increasing the thickness of the rods of intermetallics, Al<sub>3</sub>Ti, than increasing the number. For transferring higher share of load to these rods, the number or length of the rod should increase or else there may be no enhancement of load in this constituent, which may be responsible for the observed lowering of tensile properties with increasing particle content. However, as discussed earlier, reverse is the case with hardness, it increases with increasing addition of TiO<sub>2</sub> particles as the volume fraction of both intermetallic and the oxide particles increases. Both of the tensile properties, ultimate tensile strength and percentage elongation are decreasing linearly with increasing porosity, having a linear function of porosity content having coefficients of correlation 0.93 and 0.9 respectively, as shown in Figs. 4.27 and 4.28.

The tensile fractured surfaces of the specimens subjected to tensile test have been examined under scanning electron microscope (SEM) for cast *in-situ* Mg-Al/Al<sub>3</sub>Ti-Al<sub>2</sub>O<sub>3</sub> composites, cast Mg-9 wt% Al base alloy and cast commercial magnesium, as shown in Fig. 4.29. The fractured surfaces of the specimens of cast *in-situ* Mg-Al/Al<sub>3</sub>Ti-Al<sub>2</sub>O<sub>3</sub> composites reveal mixed-mode failure consisting of primarily brittle and partially ductile fracture as shown respectively in Figs. 4.29(a) and (b). The typical tensile fractured surface of the cast unreinforced Mg-9 wt% Al alloy containing 0.3 vol% porosity has been studied under SEM as shown in Fig. 4.29(c). The fractured surface shows the intergranular cleavages and dimples of ductile fracture resulting in 11.67% elongation. Typical fractured surface of cast commercial magnesium containing 0.1 vol% porosity shows transgranular cleavages and dimples of ductile fracture resulting in overall elongation of 17.53 % as shown in Fig. 4.29(d).



The present study clearly reveals the potential of cast *in-situ* Mg-Al/Al<sub>3</sub>Ti-Al<sub>2</sub>O<sub>3</sub> composite, synthesized by using cast Al-based composite which has been processed earlier by *in-situ* reduction of TiO<sub>2</sub> by molten aluminium during solidification processing. Although higher porosity levels are common in the materials processed through casting route, it has been possible to limit porosity levels to within about 2 vol% in cast *in-situ* Mg-Al/Al<sub>3</sub>Ti-Al<sub>2</sub>O<sub>3</sub> composites by processing the composite under inert environment. Even though tensile properties are lower, better hardness is observed, which is very essential from tribological point of view.

Cast *in-situ* composite synthesized by using cast Al-Si master alloy, which was processed earlier by dissolving silicon in molten aluminium, has intermetallics, Mg<sub>2</sub>Si, distributed in a matrix of Mg-Al alloy as identified by XRD, EDS and EPMA analysis. A comparison of XRD patterns of cast *in-situ* composite as shown in Fig. 4.30(a) and Mg-9 wt% Al base alloy as shown in Fig. 4.31(b), clearly reveals the presence of Mg<sub>2</sub>Si in *in-situ* Mg-Al/Mg<sub>2</sub>Si composite powder. Along with the peaks of Mg<sub>2</sub>Si, there are peaks corresponding to primary solid solution of aluminium in magnesium and Al<sub>12</sub>Mg<sub>17</sub> as observed in the XRD pattern. Presence of intermetallics, Mg<sub>2</sub>Si, has been further confirmed and identified in the microstructures of *in-situ* composites through EDS point analysis as shown in Fig. 4.34, line scan as shown in Fig. 4.35 and X-ray mapping as shown in Fig. 4.36. The powder XRD pattern of cast Al-15 wt% Si master alloy is shown in Fig. 4.31 and the peaks correspond to primary solid solution of silicon in aluminium and silicon. It is understood from the XRD pattern of *in-situ* composite as shown in Fig. 4.30(a) and master alloy as shown in Fig. 4.31 that, the silicon reacts completely with magnesium forming Mg<sub>2</sub>Si.

As discussed earlier, cast Al-Si master alloy has been used for the development of cast *in-situ* Mg-Al/Mg<sub>2</sub>Si composite and a typical optical micrograph of one such cast Al-Si master alloy showing silicon needles is as shown in Fig. 4.36. A typical microstructure of cast magnesium based composite developed by addition of Al-Si alloy at lower and higher magnifications are shown in Fig. 4.37. The phases, Mg<sub>2</sub>Si and Al<sub>12</sub>Mg<sub>17</sub> are clearly observed in Figs. 4.37(a), (b) and 4.38, as identified and confirmed by XRD and EDS analysis. The reinforcing intermetallics, Mg<sub>2</sub>Si, in cast *in-situ* Mg-Al/Mg<sub>2</sub>Si composites are formed *in-situ* by chemical reaction between magnesium and silicon. The volume fraction of Mg<sub>2</sub>Si generated in cast *in-situ* composites depends on the amount of Si present in the Al-Si master alloys as evident from XRD patterns shown in Fig. 4.32 and micrographs shown in Fig. 4.40. The microstructure of Al-Si alloy show presence of silicon as needles and blocky type shown in Fig. 4.39. Blocky silicon appears in hypereutectic alloy when Si exceeds about 12 wt% in

Al-Si master alloys as shown in Figs. 4.39(b) and (c). As the amount of Si increases, the volume fraction of Mg<sub>2</sub>Si also increases both in size and number as evident from Figs. 4.40 and 4.41 and there is increased intensity of XRD peaks corresponding to Mg<sub>2</sub>Si as shown in Fig. 4.32. As the volume fraction of reinforcement, Mg<sub>2</sub>Si, increases, the volume fraction of porosity also increases in the cast *in-situ* composites as observed in Fig. 4.42. The processing temperature has negligible effect on synthesis of cast *in-situ* Mg-Al/Mg<sub>2</sub>Si composites as observed in Fig. 4.43.

The variation in hardness with location ( $h/H$ ) along the height of cast ingot shows that the hardness of the composite is decreasing slowly within a limited band of variation from the bottom to the top of the ingot and it is a linear function of distance measured from the bottom having a co-efficient of correlation 0.95 as shown in Fig. 4.44. The reason for this may be due to decreasing of intermetallics from the bottom to the top of cast ingot. The variation in hardness with processing temperature shows that the hardness is increasing slightly with increasing processing temperature upto 760 °C; beyond this temperature hardness is decreasing, as shown in Fig. 4.45. Hardness of cast *in-situ* composites increases with increasing volume fraction of Mg<sub>2</sub>Si, as shown in Fig. 4.46. The Brinell hardness for cast *in-situ* Mg-Al/Mg<sub>2</sub>Si composite containing 6.54 vol% reinforcement and 1.7 vol% porosity, is significantly more compared to that of unreinforced cast Mg-9 wt% Al alloy containing 0.6 vol% porosity and cast unreinforced commercial magnesium containing 0.2 vol% porosity by factors of about 1.4 and 2 respectively as shown in Fig. 4.47. The Brinell hardness values of cast *in-situ* composite, cast Mg-9 wt% Al alloy and cast commercial Mg are respectively, 839, 607 and 431 MPa.

The values of UTS and percentage elongation observed at the middle height segment of cast ingot of *in-situ* Mg-Al/Mg<sub>2</sub>Si composites are respectively,  $174 \pm 10$  MPa and  $4.27 \pm 0.22\%$ . The variation in tensile properties in different height segments of cast *in-situ* Mg-Al/Mg<sub>2</sub>Si, synthesized at 760 °C using cast Al-9 wt% Si master alloy, shows that the bottom segment of the cast ingot has slightly higher tensile properties as shown in Fig. 4.48. It is observed that the porosity increases while Mg<sub>2</sub>Si content decreases from the bottom towards the top of the cast ingot. The variations in tensile properties, like ultimate tensile strength and percentage elongation with processing temperature shows that the ultimate tensile strength increases significantly up to 760 °C but beyond 760 °C, it decreases, The percentage elongation increases slightly up to 760 °C but beyond 760 °C, it decreases as shown in Fig. 4.49.

Both the tensile properties - ultimate tensile strength and percentage elongation, decreases linearly with increasing porosity linearly, having coefficients of correlation of 0.9 and 0.85

respectively, as shown in Figs. 4.50 and 4.51. The variation in tensile properties extrapolated to zero porosity, with different volume fraction of reinforcement,  $Mg_2Si$ , shows that higher tensile properties could be obtained at relatively lower volume fraction of  $Mg_2Si$ , as shown in Fig. 4.52 and 4.53. Increasing amount of silicon in Al-Si master alloy results in increasing the size of intermetallics,  $Mg_2Si$ , more than increasing the number of intermetallic blocks and this could be the reason for lowering of tensile properties. However, as discussed earlier, reverse is the case with hardness, it increases with increasing silicon addition in Al-Si master alloy.

The tensile fractured surfaces of the specimens subjected to tensile test have been studied under scanning electron microscope (SEM) for cast *in-situ* Mg-Al/ $Mg_2Si$  composites and cast Mg-9 wt% Al alloy are shown in Fig. 4.29. The fractured surfaces of the specimens of cast *in-situ* Mg-Al/ $Mg_2Si$  composite reveal the evidence of mixed-mode failure, primarily brittle and partially ductile fracture as shown respectively in Figs. 4.54(a) and (b). The typical tensile fractured surface of the cast unreinforced Mg-9 wt% Al alloy containing 0.3 vol% porosity has been studied under SEM as shown in Fig. 4.54(c). The fractured surface shows the intergranular cleavages and dimples of ductile fracture resulting in 11.67% elongation.

The present study clearly reveals the potential of cast *in-situ* Mg-Al/ $Mg_2Si$  composite, synthesized by using cast Al-Si master alloy which was processed earlier by dispersion of silicon particles to molten aluminium during solidification processing. Although the higher porosity levels are common in the materials processed through casting route, it is managed in achieving porosity levels, within about 2.5 vol% in cast *in-situ* Mg-Al/ $Mg_2Si$  composites. Even though tensile properties are lower, better hardness properties are achieved, which is very essential from tribological point of view.

Both the classes of composites are entirely different, because cast *in-situ* Mg-Al/ $Al_3Ti$ - $Al_2O_3$  composite contains both oxide particles (in the range of 1.35-2.45 wt%) as well as intermetallics,  $Al_3Ti$  (in the range of 0.8-2.14 vol%), as reinforcement, where as cast *in-situ* Mg-Al/ $Mg_2Si$  composite contains only intermetallics,  $Mg_2Si$ , but relatively higher volume fraction (in the range of 2.42-6.54 vol%), as reinforcement. Comparatively lower porosities are observed in cast *in-situ* Mg-Al/ $Al_3Ti$ - $Al_2O_3$  composite than cast *in-situ* Mg-Al/ $Mg_2Si$  composites. Higher porosities observed in cast *in-situ* Mg-Al/ $Mg_2Si$  composites could be due to relatively higher volume fraction of  $Mg_2Si$  formed *in-situ* in molten magnesium. But the reinforcing particles and intermetallics in cast *in-situ* Mg-Al/ $Al_3Ti$ - $Al_2O_3$  composite form *in-situ* in molten aluminium during development of Al-based composite. However, in the range of reinforcement and porosity investigated here, cast *in-situ* Mg-Al/ $Al_3Ti$ - $Al_2O_3$  composites show slightly higher values of hardness and slightly lower values

of tensile properties than cast *in-situ* Mg-Al/Mg<sub>2</sub>Si composites. In the end, the optimum processing parameters for solidification processing of cast *in-situ* Mg-Al/Al<sub>3</sub>Ti-Al<sub>2</sub>O<sub>3</sub> and Mg-Al/Mg<sub>2</sub>Si composites in order to attain better mechanical properties are as given in Table 4.1.

**Table 4.1:** Optimum processing parameter for solidification processing of cast *in-situ* Mg-Al/Al<sub>3</sub>Ti-Al<sub>2</sub>O<sub>3</sub> and Mg-Al/Mg<sub>2</sub>Si composites.

Process parameters	Optimum level of process parameters
Processing temperature	750-800 °C.
Processing time	3-5 minutes.
Stirring speed	500-600 rpm.

The results and discussion as described above, shows that it is possible to inherit the constituents of another composite like aluminium based composite developed by addition of TiO<sub>2</sub> here, to create novel combination of phases and reinforcements in another composite, with another base alloy, magnesium in the present case, in order to modify the properties (Ray et al., 2007). It is also possible to cause reaction during solidification processing with the minor phase of another alloy added in order to create the desired constituent as observed in Mg-Al/Mg<sub>2</sub>Si composites (Ray et al., 2007).

# RESULTS AND DISCUSSION

## Tribological Behaviour of Cast *In-Situ* Composites

---

---

The tribological behaviour of different cast *in-situ* Mg-Al/Al<sub>3</sub>Ti-Al<sub>2</sub>O<sub>3</sub> and Mg-Al/Mg<sub>2</sub>Si composites synthesized by addition of aluminium based composite and Al-Si alloy respectively to magnesium have been investigated in terms of friction and dry sliding wear against the counterface of hardened EN-32 steel. Since the formation of porosity in the cast *in-situ* composites prepared by stircasting is observed, the primary focus of this phase of study is to understand the role of *in-situ* generated reinforcing particles/intermetallics and porosity individually on the overall tribological behaviour of the resulting cast *in-situ* magnesium based composites. For the purpose of comparison, the friction and dry sliding wear of the cast unreinforced commercial magnesium and cast unreinforced Mg-9 wt% Al alloy synthesized similarly as the cast *in-situ* magnesium based composites but without any reinforcements, have also been investigated under similar loading and sliding conditions. This chapter presents the results of these investigations followed by a discussion in the context of existing knowledge in open literatures as given in Chapter 2.

### 5.1 Dry Sliding Wear

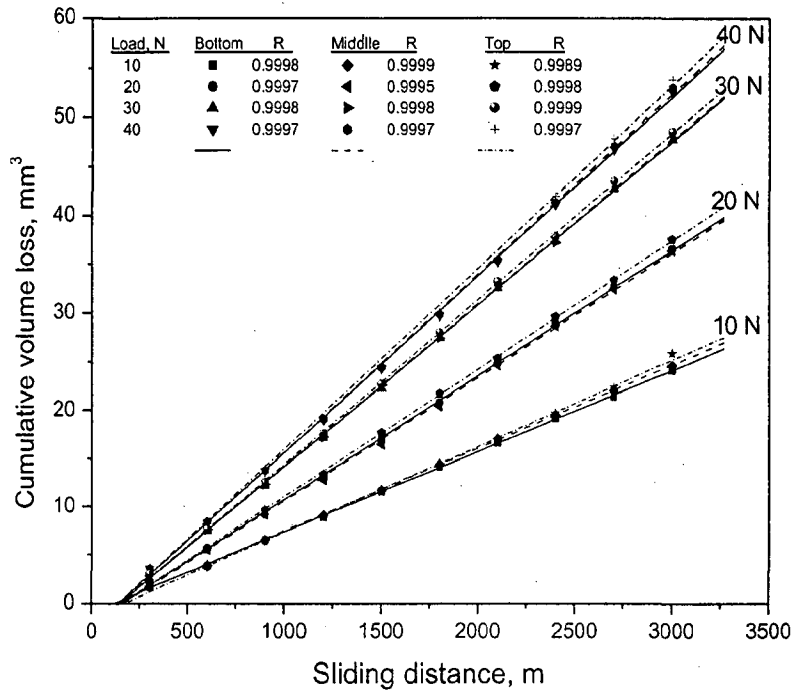
Dry sliding wear tests have been carried out by sliding a cylindrical pin with a flat polished end against a counterface of EN-32 hardened steel disc under ambient condition using a pin-on-disc machine following the procedures as described in Chapter 3, section 3.11. Different loads of 10, 20, 30 and 40 N have been applied on the pin normal to the sliding contact during wear test of each cast *in-situ* composite. The cumulative weight loss with increasing sliding distance have been measured and converted into cumulative volume loss on the basis of density of a test specimen. Three replication tests have been carried out and the average cumulative volume loss ( $V_w$ ) as a function of sliding distance ( $S_w$ ) have been used as the basic results under a given condition of dry sliding. The cumulative volume loss increases linearly with increasing sliding distance and the wear rate ( $V_w/S_w$ ), in units of mm<sup>3</sup>/m, for a given specimen under a given condition of sliding, has been determined from the slope of the linear variation of cumulative volume loss with sliding distance as estimated by the linear least square fit. When the variation of wear rate with normal load is linear, the

wear coefficient ( $V_w H/S_w L_w$ ) has been calculated by multiplying the slope of the variation of wear rate with normal load by the hardness ( $H$ ) of the specimen. The slope of variation of wear rate with normal load has been estimated by linear least square fit. When the variation of wear rate with normal load is non-linear, the variation of wear rate has been taken as piecewise linear in different normal load ranges for the purpose of estimating the slope to calculate the wear coefficients. For comparison of tribological behaviour of cast *in-situ* composites with those of the base material alone, wear tests have been carried out also on cast unreinforced alloy processed similarly as cast *in-situ* composites.

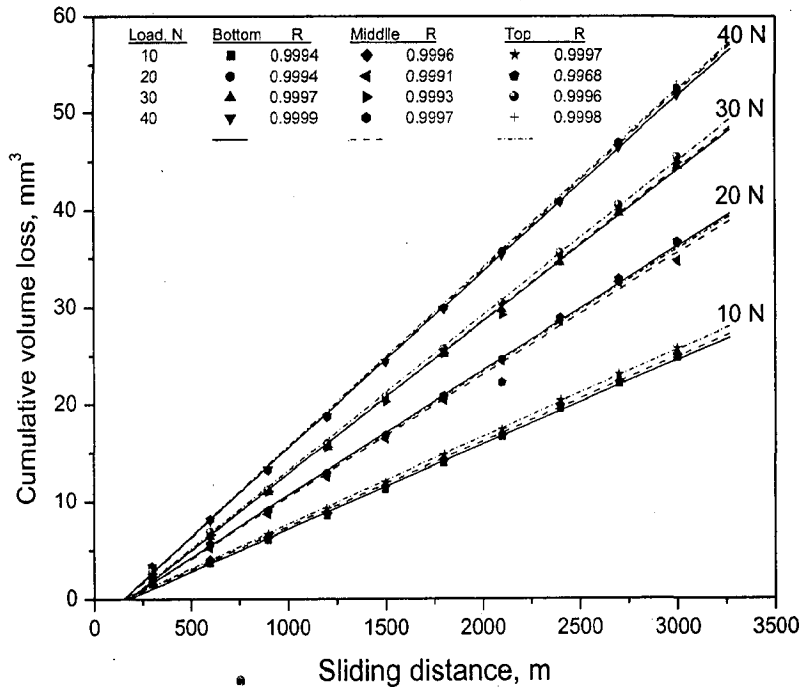
### 5.1.1 Cast *In-Situ* Mg-Al/Al<sub>3</sub>Ti-Al<sub>2</sub>O<sub>3</sub> Composites

Different cast *in-situ* magnesium based composites containing reinforcing particles ranging from 1.35 wt% to 2.78 wt%, intermetallics ranging from 0.73 vol% to 2.22 vol% and porosity ranging from 0.6 vol% to 2.4 vol% are summarized in Table 5.1. This table also contains the processing temperature and wt% of TiO<sub>2</sub> particles added in the development of *in-situ* composites. The designation given to cast *in-situ* composites is based on the addition of TiO<sub>2</sub> particles and processing temperature as mentioned in Chapter 3. Cast unreinforced commercial magnesium and cast unreinforced Mg-9 wt% Al alloy have been tested for wear and friction for comparison with the cast *in-situ* composites. The porosity content of cast unreinforced commercial magnesium and cast unreinforced Mg-9 wt% Al alloy are summarized in Table 5.2. The methods for determination of chemical composition of the matrix alloy, particle content and porosity content of cast *in-situ* composites are given in detail in the experimental procedure, given in Chapter 3.

The variation of cumulative volume loss with sliding distance at different normal loads of 10, 20, 30 and 40 N at a constant sliding speed of 1 m/s for the bottom, middle and top segments of cast ingots of following *in-situ* composites are shown respectively in Figs. 5.1(a) to (f): (a) MT8/80, (b) MT10/80, (c) MT12/80, (d) MT14/80, (e) MT12/75 and (f) MT12/85. For a given normal load, the cumulative volume loss increases linearly with increasing sliding distance and the lines obtained by linear least square fit for different loads are indicated in the figures. For each normal load, a very small difference in cumulative volume loss variation is observed among three segments of cast ingots of *in-situ* composites and relatively higher cumulative volume loss is observed for the top segments than that of the bottom segments, which may be due to relatively higher porosities at the top segments, as given in the Table 5.1. There is no significant load-induced wear transition in the load range investigated. However, the lines at different normal loads sometimes converge at low sliding distance where the differences in wear volumes at different loads are relatively small.

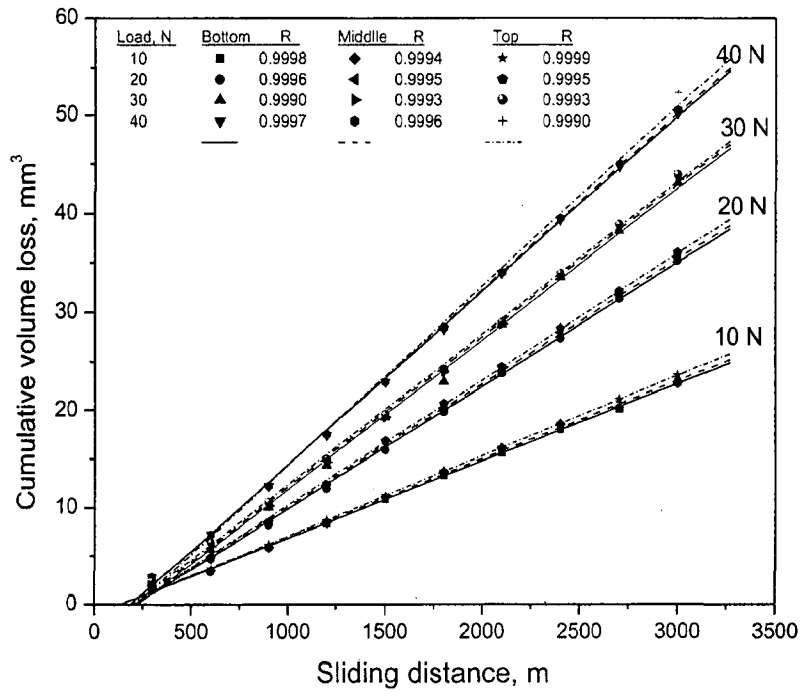


(a) The composite, MT8/80

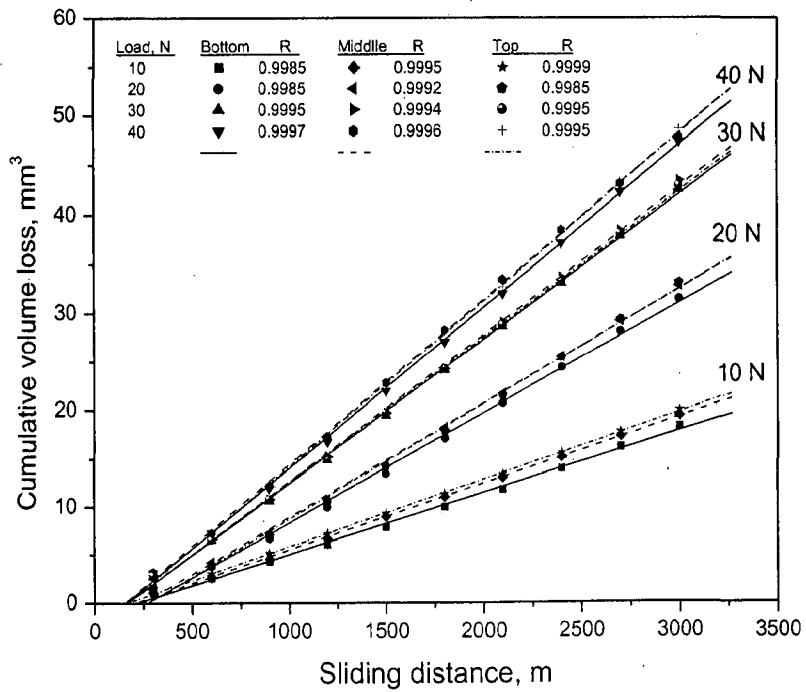


(b) The composite, MT10/80

Continued/-



(c) The composite, MT12/80



(d) The composite, MT14/80

Continued/-



**Table 5.1:** TiO<sub>2</sub> particles addition, processing temperature and physical characteristics of different cast *in-situ* Mg-Al/Al<sub>3</sub>Ti-Al<sub>2</sub>O<sub>3</sub> composites.

<i>In-situ</i> composite designation	TiO <sub>2</sub> particles addition (wt%)	Processing temperature (°C)	Location in ingot	Porosity (vol%)	Reinforcement		Brinell hardness (MPa)
					Intermetallics (vol%)	Particles (wt%)	
MT8/80	8	800	Bottom	0.7	0.84	1.45	718
			Middle	0.9	0.80	1.35	707
			Top	1.4	0.73	1.35	686
MT10/80	10	800	Bottom	1.3	1.18	1.72	796
			Middle	1.8	1.12	1.7	781
			Top	2.4	1.10	1.64	774
MT12/80	12	800	Bottom	0.9	1.94	2.51	824
			Middle	1.1	1.46	2.1	798
			Top	1.6	1.30	2.05	782
MT14/80	14	800	Bottom	0.7	2.22	2.78	892
			Middle	1.0	2.14	2.45	857
			Top	1.4	1.82	2.38	833
MT12/75	12	750	Bottom	0.7	1.74	2.51	837
			Middle	1.1	1.26	2.18	803
			Top	1.4	1.22	1.88	789
MT12/85	12	850	Bottom	0.6	1.50	2.50	817
			Middle	0.9	1.44	2.26	787
			Top	1.4	1.34	1.98	774

One may also observe that most of these linear least square fit lines do not pass through the origin and a few of them, particularly at higher normal loads, have even negative intercepts. The negative intercepts are common at higher humidity when the surface layer containing oxides from the counterface readily form on the sliding surface of the test specimen and effectively protect it from wear particularly at lower normal loads. These transfer layers on the sliding surface of the test pins are visible with naked eye because of red to black oxides of iron from the counterface when test pins sliding under low normal loads are examined. At higher normal loads these transfer layers are not visible possibly because the transfer layers are continuously removed as they form.

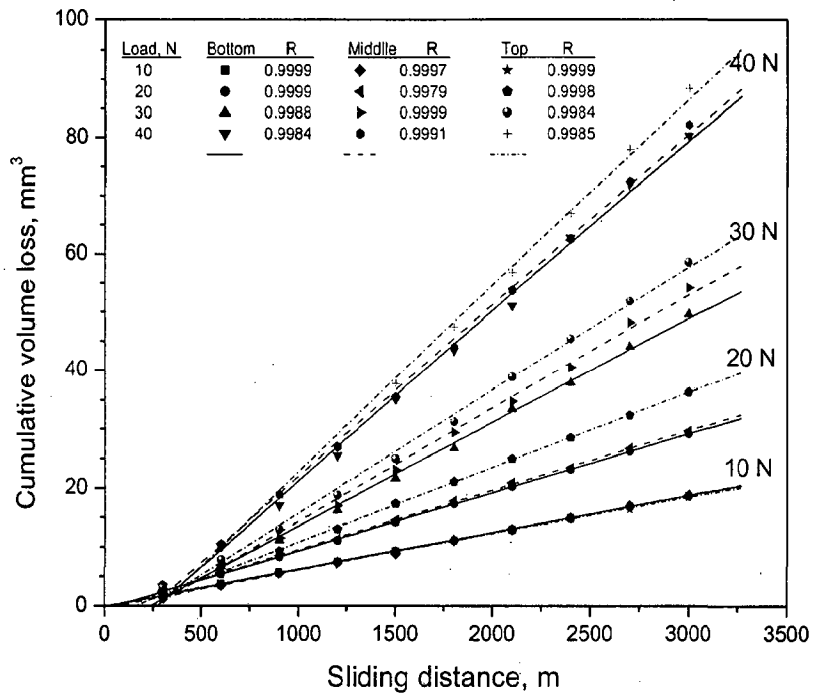
In order to identify the role of reinforcing particles and intermetallics on the wear behaviour, the wear behaviour of the present cast *in-situ* magnesium based composites has been compared with those observed in cast unreinforced commercial magnesium and cast unreinforced Mg-9 wt% Al alloy processed similarly as the cast *in-situ* composites. Results of

typical wear behaviour for cast unreinforced commercial magnesium and cast unreinforced Mg-9 wt% Al alloy are shown in Figs. 5.2(a) and (b) respectively. It is observed that the cumulative volume loss increases linearly with increasing sliding distance and normal load similarly as observed in cast *in-situ* composites, indicating that Archard's adhesive wear equation (Eq. 2.16) for single phase material is being followed. For all normal loads other than 10 N, comparatively higher cumulative volume loss is observed for the top segment than the middle and bottom segments of cast ingot of unreinforced commercial magnesium. But in case of cast unreinforced Mg-9 wt% Al alloy, for all normal loads, little higher cumulative volume loss is observed for the top segment than the middle and bottom segments of cast ingot. This might be due to comparatively higher porosity, as given in the Table 5.1, at the top segment than at other two segments.

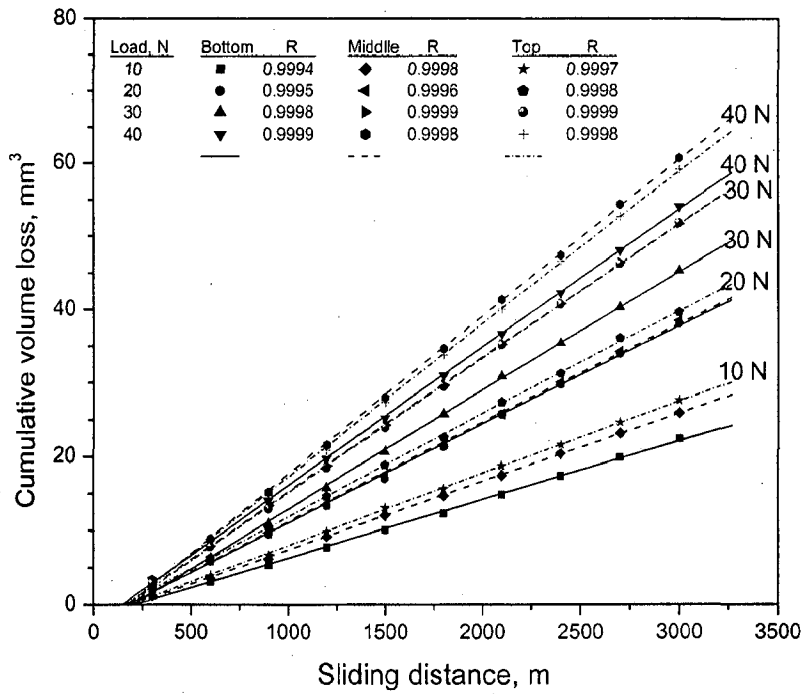
**Table 5.2:** Physical characteristics for the bottom, middle and top segments of cast commercial magnesium and cast Mg-9 wt% Al base alloy.

Material	Location in ingot	Porosity (vol%)	Brinell hardness (MPa)
Cast commercial Mg	Bottom	0.1	439
	Middle	0.2	431
	Top	0.3	423
Cast Mg-9 wt% Al alloy	Bottom	0.3	615
	Middle	0.6	607
	Top	0.7	594

Fig. 5.3 shows the comparison of cumulative volume loss for middle segments of cast ingots of cast *in-situ* magnesium based composite, MT14/80, containing 2.45 wt% of reinforcing particles, 2.14 vol% intermetallics and 1 vol% of porosity, unreinforced commercial magnesium and Mg-9 wt% Al alloy at the highest normal load of 40 N and sliding distance of 3000 m. The cumulative volume loss in cast *in-situ* composite is significantly lower than those observed in the cast unreinforced commercial magnesium and Mg-9 wt% Al alloy, by about 42 % and 21 % respectively. The porosity content of the cast unreinforced Mg-9 wt% Al alloy is lower than that of the cast *in-situ* composite and the porosity in cast commercial magnesium is significantly lower than that in cast *in-situ* composite and cast unreinforced Mg-9 wt% Al base alloy. Thus, the reduced volume loss of the cast *in-situ* based composite over that of cast unreinforced commercial



(a) Cast commercial magnesium



(b) Cast Mg-9 wt% Al alloy

**Fig. 5.2:** The variation of cumulative volume loss with sliding distance at different normal loads of 10, 20, 30 and 40 N and sliding speed of 1 m/s for the bottom, middle and top segments of cast ingots of (a) commercial magnesium and (b) Mg-9 wt% Al alloy.

magnesium could be attributed to the reinforcing effect of *in-situ* formed particles and intermetallics, and also, to the alloying of the matrix by aluminium. But, the lower volume loss in cast *in-situ* composite compared to the cast unreinforced Mg-9 wt% Al alloy is primarily due to *in-situ* formed reinforcing particles and intermetallics.

The wear rates,  $(V_w/S_w)$ , volume loss per unit sliding distance, is determined from the slope of the variation of cumulative volume loss with sliding distance for middle segments of cast ingots of *in-situ* composite, MT14/80, containing 2.45 wt% of reinforcing particles, 2.14 vol% intermetallics and 1 vol% of porosity, unreinforced commercial magnesium and unreinforced Mg-9 wt% Al alloy are shown in Fig. 5.4. In cast commercial magnesium, the wear rate initially increases gradually with increasing normal load till 20 N but at higher loads it increases linearly with a higher slope. In Mg-9 wt% Al alloy, the wear rate increases linearly with increasing normal load. In cast magnesium based *in-situ* composite, the wear rate increases linearly with increasing normal load but at higher normal loads, the wear rate deviates from the line towards a lower value, showing non-linear behaviour. The Fig. 5.5 shows the variation of wear rate with normal load for the bottom, middle and top segments of cast ingots of different cast *in-situ* Mg-Al/Al<sub>3</sub>Ti-Al<sub>2</sub>O<sub>3</sub> composites: (a) MT8/80, (b) MT10/80, (c) MT12/80, (d) MT14/80, (e) MT12/75 and (f) MT12/85. The wear rate increases linearly with increasing normal load but at higher normal loads, the wear rate deviates from the line towards a lower value, showing non-linear behaviour for all cast *in-situ* composites. Also, the wear rate is nearly same for the three segments of cast ingots of *in-situ* composites.

Generally, the cast particulate composites have considerable porosity, which is often originating from the poor wetting of reinforcing particles by molten alloy or dissolution of gases during processing (Ray, 1993), or releasing of gases during the formation of *in-situ* particles/intermetallics. The influence of porosity content on dry sliding wear of three groups of cast *in-situ* composites containing reinforcing particles varying over limited ranges, (a)  $1.55 \pm 0.2$  wt%, (b)  $1.98 \pm 0.2$  wt% and (c)  $2.52 \pm 0.26$  wt% is shown respectively in Figs. 5.6(a), (b) and (c). In these three groups of cast *in-situ* composites, the wear rate remains nearly constant with increasing volume fraction of porosity. However, slightly increasing wear rate trend with increasing volume fraction of porosity is observed for cast *in-situ* composites containing reinforcing particles  $1.55 \pm 0.2$  wt% as shown in Fig. 5.6(a) and  $1.98 \pm 0.2$  wt% as shown in Fig. 5.6(b), while, slightly decreasing wear rate trend with increasing volume fraction of porosity is observed for cast *in-situ* composites containing reinforcing particles  $2.52 \pm 0.26$  wt% as shown in Fig. 5.6(c).

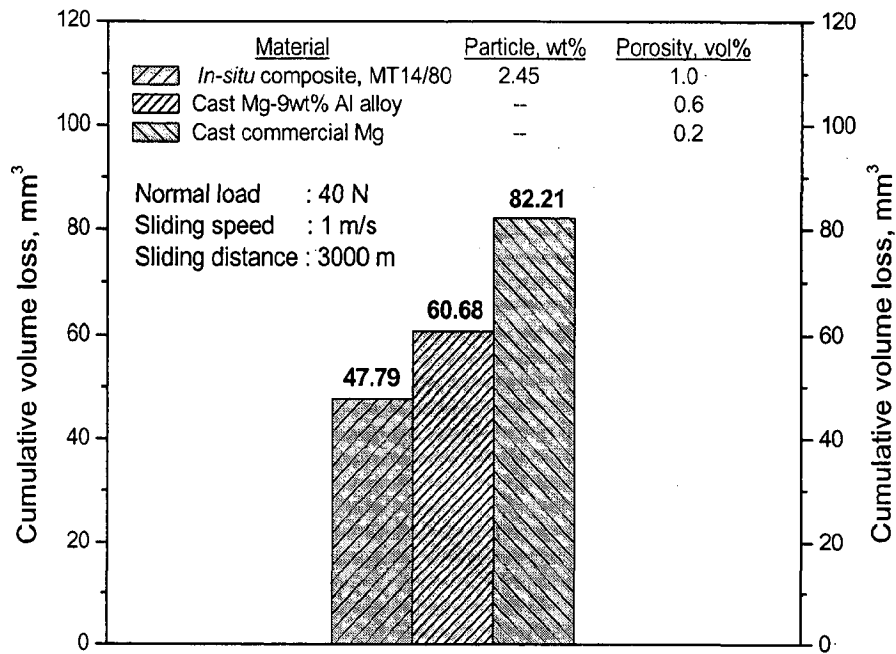
The influence of particle content on dry sliding wear of three groups of cast *in-situ* composites containing porosity varying over limited ranges, (a)  $0.8 \pm 0.2$  vol%, (b)  $1.2 \pm 0.2$  vol% and  $1.6 \pm 0.2$  vol% is as shown in Figs. 5.7(a), (b) and (c) respectively. The wear rate of cast *in-situ* composites decreases slightly with increasing particle content particularly beyond particle content of 2 wt%, for all the loads investigated here.

The wear coefficient,  $k$ , has been calculated by multiplying the slope of the variation of wear rate with normal load by the hardness ( $H$ ) of the specimen and it decreases a little with increasing porosity content, particularly beyond 1.1 vol% for cast *in-situ* composites, as observed in Figs. 5.8(a), (b) and (c). The wear coefficient of cast *in-situ* composites increase with increasing particle content as shown in Fig. 5.9.

### 5.1.2 Cast *In-Situ* Mg-Al/Mg<sub>2</sub>Si Composites

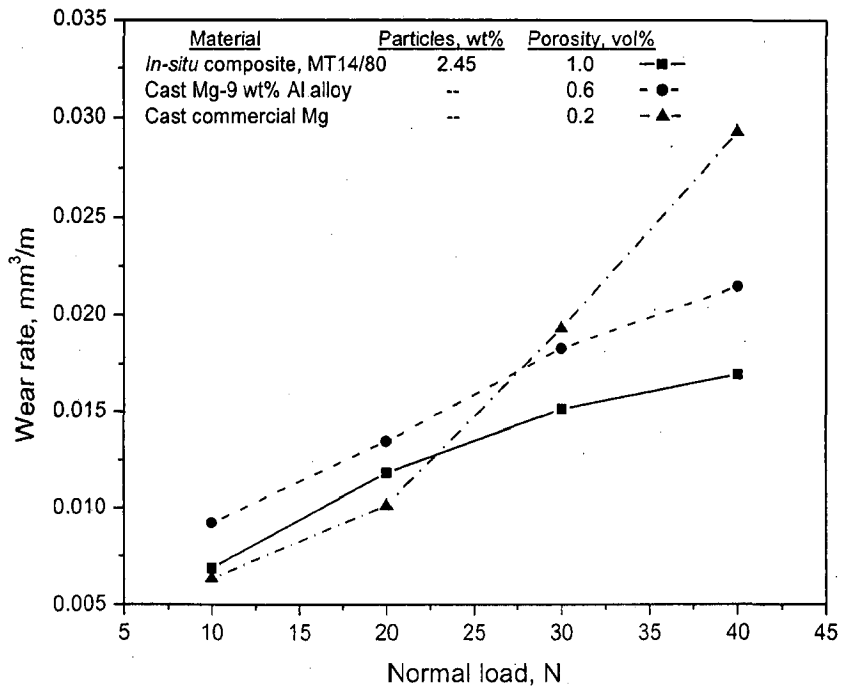
Different cast *in-situ* magnesium based composites containing reinforcement, Mg<sub>2</sub>Si, ranging from 2.36 vol% to 6.54 vol% and porosity ranging from 0.6 vol% to 2.6 vol% are summarized in Table 5.3. This table also contains the processing temperature and silicon particles added in the development of *in-situ* composites. The designation given to cast *in-situ* composites is based on the addition of silicon particles and processing temperature as mentioned in Chapter 3. Cast unreinforced commercial magnesium and cast unreinforced Mg-9 wt% Al alloy have been tested for wear and friction for comparison with the cast *in-situ* composites. The porosity content of cast unreinforced commercial magnesium and cast unreinforced Mg-9 wt% Al alloy is given in Table 5.2. The methods for determination of chemical composition of the matrix alloy, reinforcement, Mg<sub>2</sub>Si, and porosity content of cast *in-situ* composites are discussed in detail in experimental procedure, given in Chapter 3.

The variation of cumulative volume loss with sliding distance at different normal loads of 10, 20, 30 and 40 N and a constant sliding speed of 1 m/s for the bottom, middle and top segments of cast ingots of following *in-situ* Mg-Al/Mg<sub>2</sub>Si composites are shown respectively in Figs. 5.10(a) to (e): (a) MS9/80, (b) MS15/80, (c) MS20/80, (d) MS15/72 and (e) MS15/80. For a given normal load, the cumulative volume loss increases linearly with increasing sliding distance and the lines obtained by linear least square fit for different loads are shown in the Fig. 5.10. There is no significant load-induced wear transition in the load range investigated. However, these lines at different normal loads sometimes converge at low sliding distance where the differences in wear volumes at different loads are relatively small. For each normal load, cumulative volume loss variation is very small among three segments of cast ingots of *in-situ* composites and relatively higher cumulative volume loss is observed for the top segments than that of the bottom segments, which may be due to relatively higher porosities at the top segments.



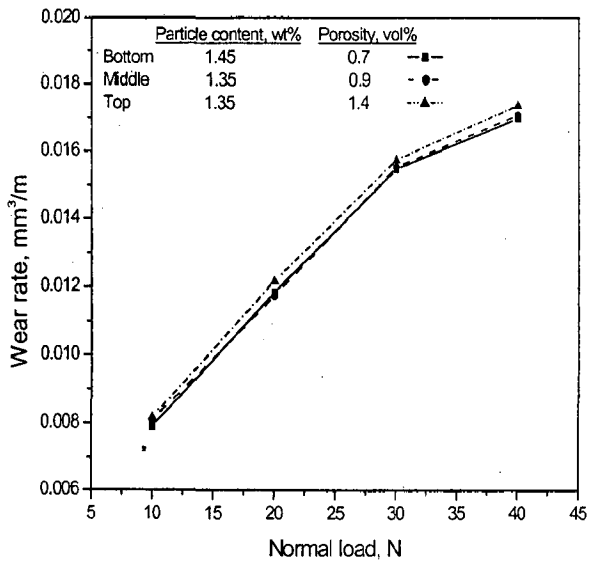
**Fig, 5.3**

A comparison of cumulative volume loss after dry sliding for 3000 m for the middle segments of cast ingots of *in-situ* composite, MT14/85, containing 2.45 wt% reinforcing particles and 1.0 vol% porosity, cast Mg-9 wt% Al alloy and cast commercial magnesium under similar load and sliding conditions.

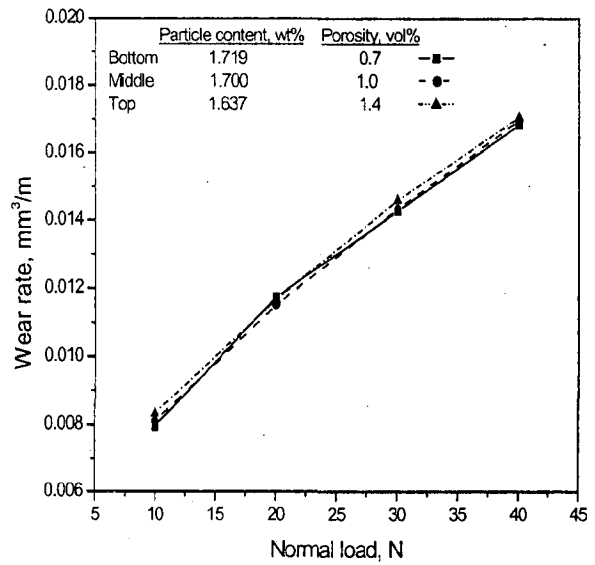


**Fig, 5.4:**

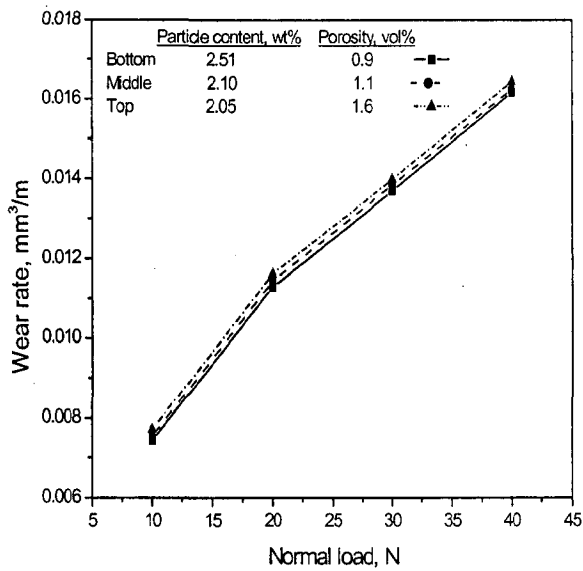
The variation of wear rate with normal load for the middle segments of cast ingots of *in-situ* composite, MT14/80, containing 2.45 wt% reinforcing particles and 1.0 vol% porosity, cast Mg-9 wt% Al alloy and cast commercial magnesium.



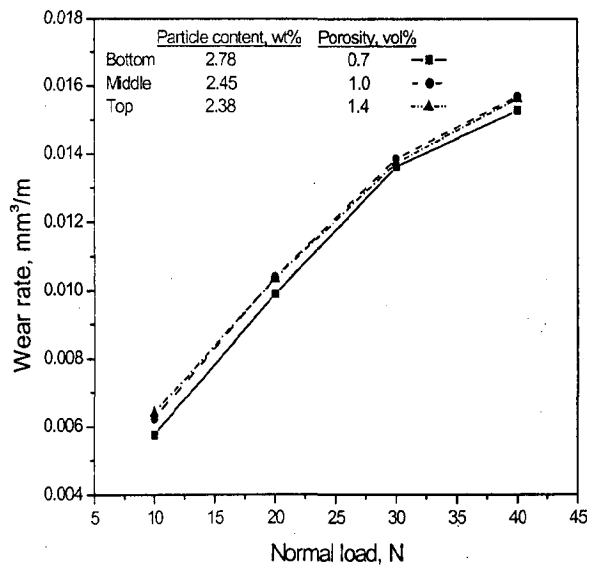
(a) The composite, MT8/80



(b) The composite, MT10/80

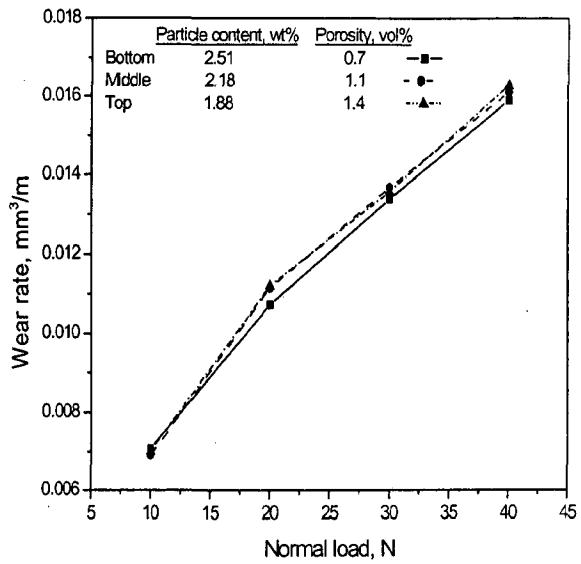


(c) The composite, MT12/80

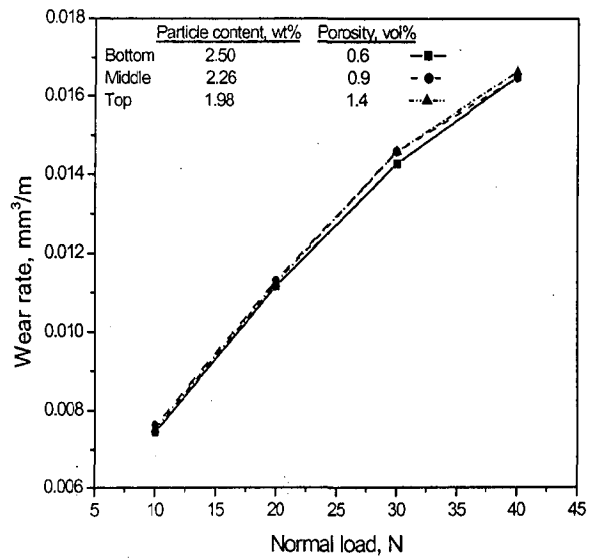


(d) The composite, MT14/80

Continued/-



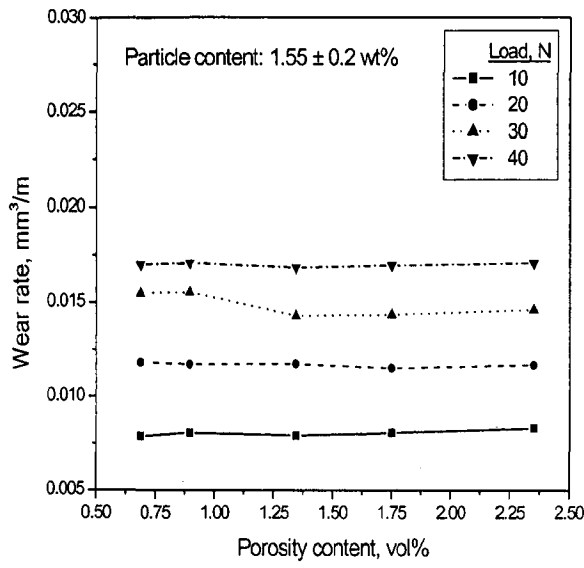
(e) The composite, MT12/76



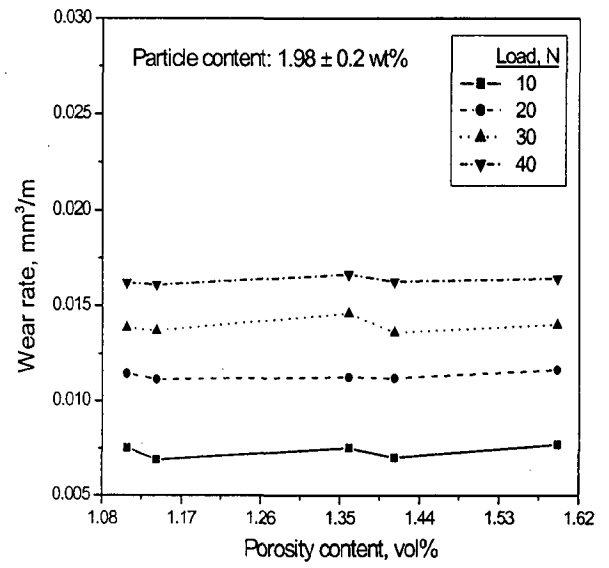
(f) The composite, MT12/85

**Fig. 5.5:** The variation of wear rate with normal load for the bottom, middle and top segments of cast ingots of different *in-situ* Mg-Al/Al<sub>3</sub>Ti-Al<sub>2</sub>O<sub>3</sub> composites: (a) MT8/80, (b) MT10/80, (c) MT12/80, (d) MT14/80, (e) MT12/75 and (f) MT12/85.

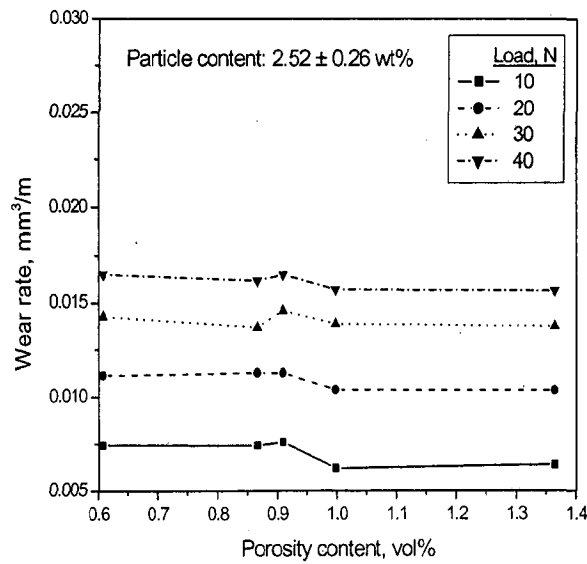




(a)

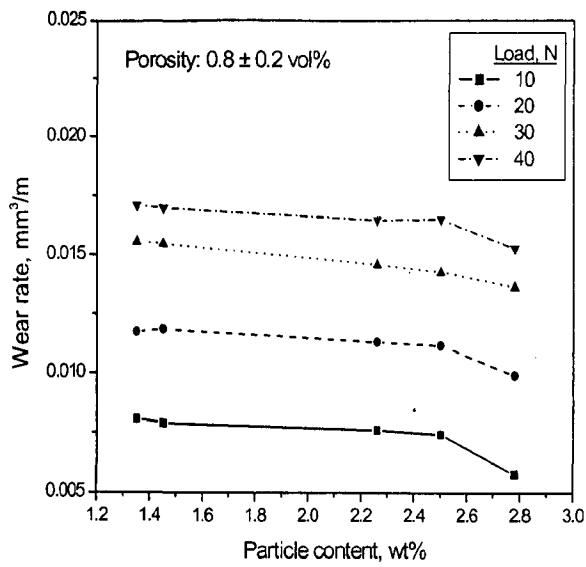


(b)

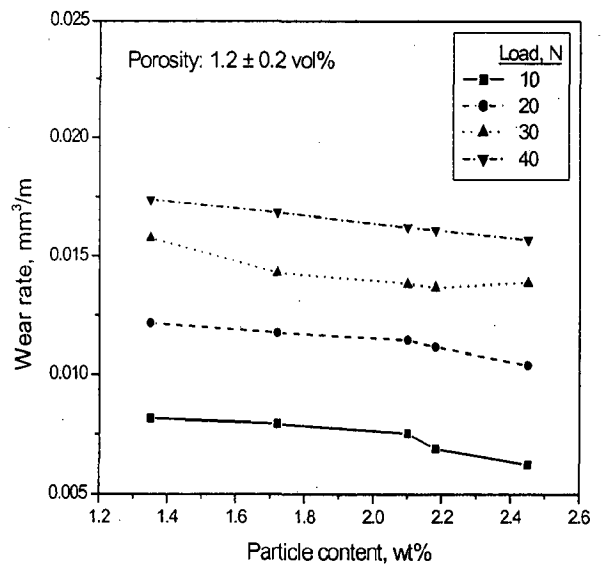


(c)

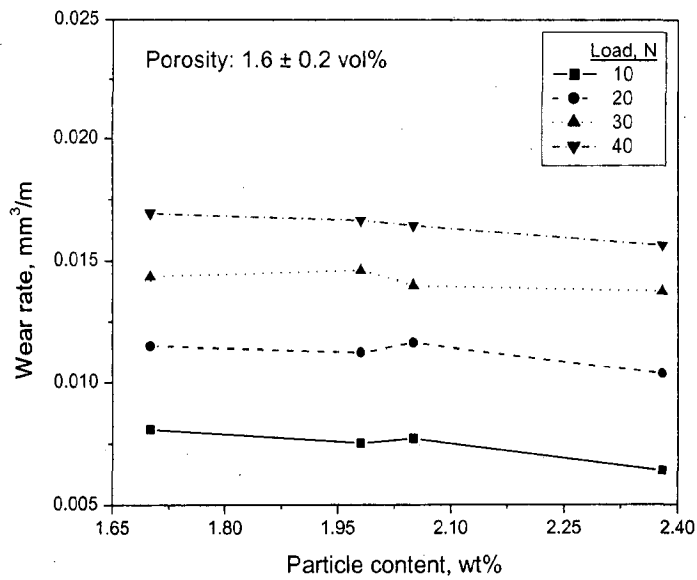
**Fig. 5.6:** The variation of wear rate with porosity content for cast *in-situ* Mg-Al/ $\text{Al}_3\text{Ti}$ - $\text{Al}_2\text{O}_3$  composites containing reinforcing particles varying over a limited range of (a)  $1.55 \pm 0.2$  wt%, (b)  $1.98 \pm 0.2$  wt% and (c)  $2.52 \pm 0.26$  wt%.



(a)

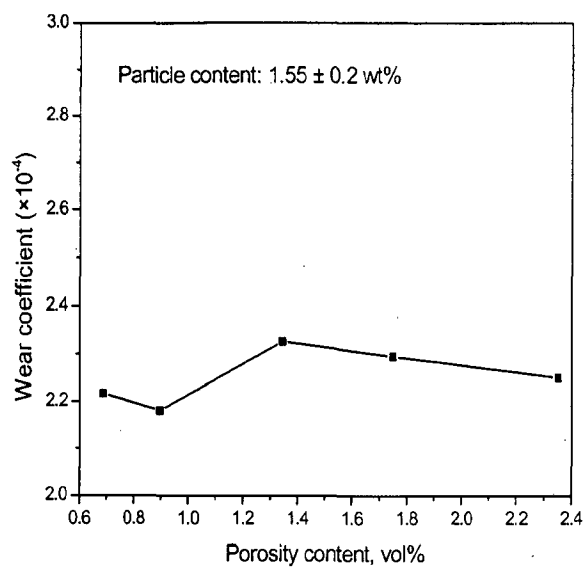


(b)

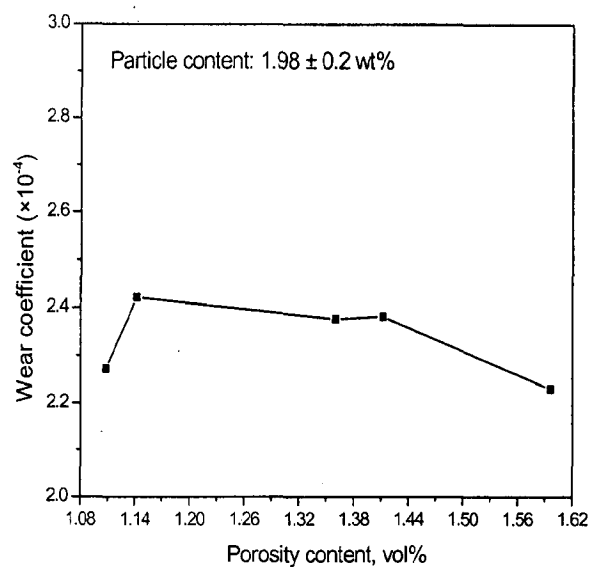


(c)

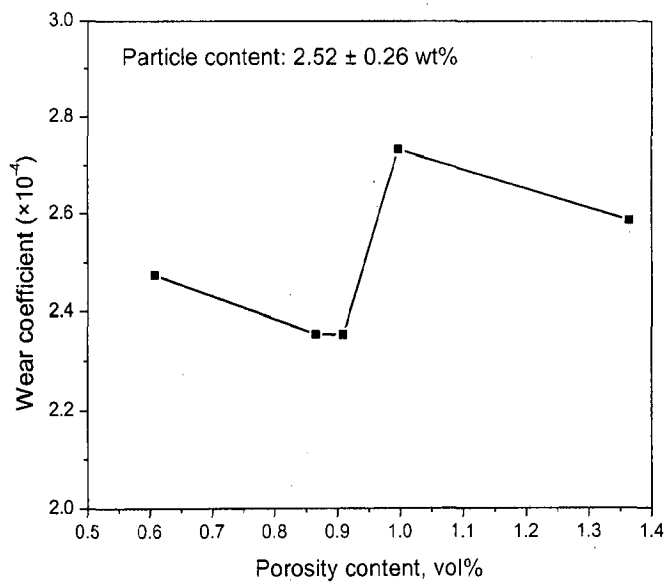
**Fig. 5.7:** The variation of wear rate with particle content for cast *in-situ* Mg-Al/Al<sub>3</sub>Ti-Al<sub>2</sub>O<sub>3</sub> composites containing porosity varying over a limited range of (a)  $0.8 \pm 0.2$  vol%, (b)  $1.2 \pm 0.2$  vol% and (c)  $1.6 \pm 0.2$  vol%.



(a)

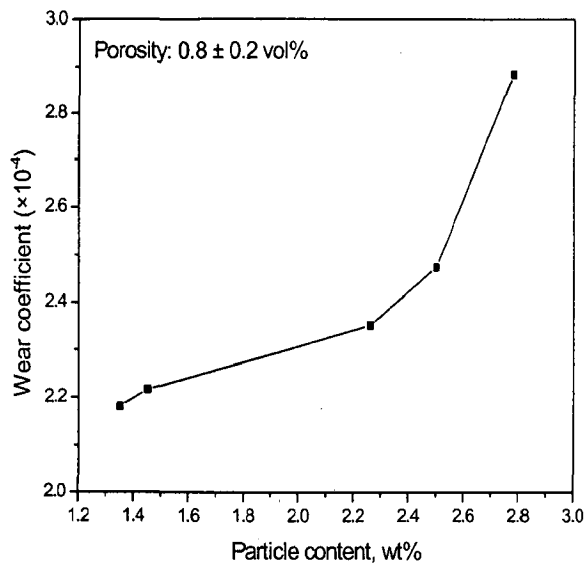


(b)

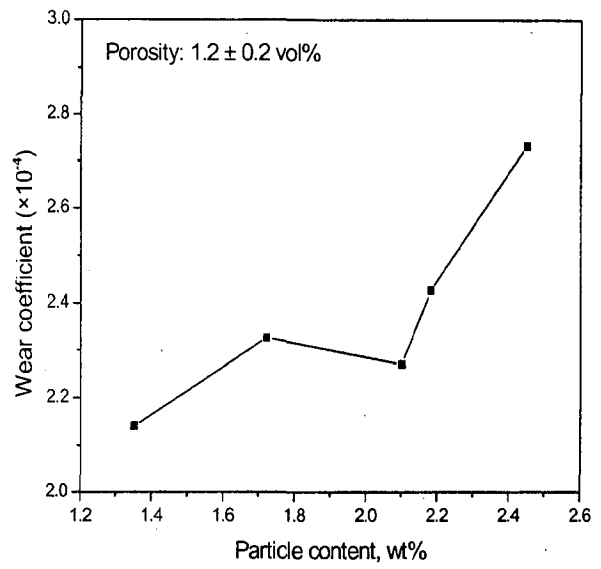


(c)

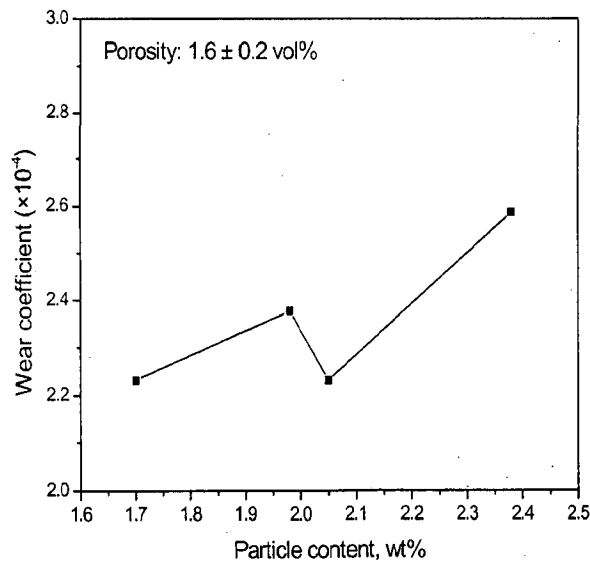
**Fig. 5.8:** The variation of wear coefficient with porosity content for cast *in-situ* Mg-Al/ $\text{Al}_3\text{Ti}$ - $\text{Al}_2\text{O}_3$  composites containing reinforcing particles varying over a limited range of (a)  $1.55 \pm 0.2$  wt%, (b)  $1.98 \pm 0.2$  wt% and (c)  $2.52 \pm 0.26$  wt%.



(a)



(b)



(c)

**Fig. 5.9:** The variation of wear coefficient with particle content for cast *in-situ* Mg-Al/ $\text{Al}_3\text{Ti-Al}_2\text{O}_3$  composites containing porosity varying over a limited range of (a)  $0.8 \pm 0.2$  vol%, (b)  $1.2 \pm 0.2$  vol% and (c)  $1.6 \pm 0.2$  vol%.

**Table 5.3:** Silicon metal particles addition, processing temperature and physical characteristics of different cast *in-situ* Mg-Al/Mg<sub>2</sub>Si composites.

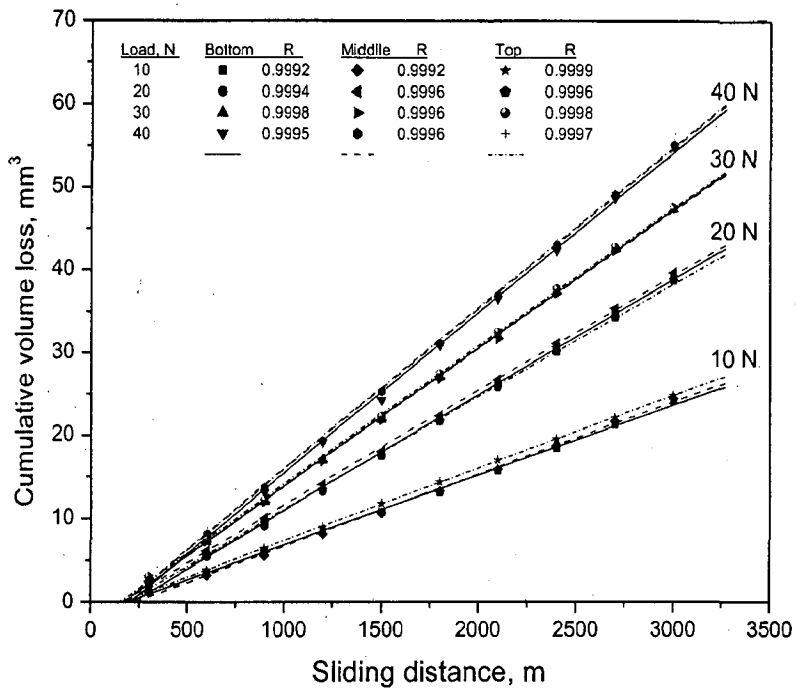
<i>In-situ</i> composite designation	Si particles addition (wt%)	Processing temperature (°C)	Location in ingot	Porosity (vol%)	Reinforcement (vol%)	Brinell hardness (MPa)
MS9/76	9	760	Bottom	0.6	2.43	743
			Middle	0.8	2.42	726
			Top	1.1	2.36	711
MS15/76	15	760	Bottom	0.8	5.16	822
			Middle	1.0	4.80	810
			Top	1.5	4.68	791
MS20/76	20	760	Middle	1.7	6.54	839
			Top	2.6	6.40	812
MS15/72	15	720	Bottom	1.4	3.90	804
			Middle	2.0	3.94	794
			Top	2.3	4.12	784
MS15/80	15	800	Bottom	0.9	4.72	798
			Middle	1.9	4.52	785
			Top	2.2	4.36	776

In order to identify the role of reinforcement, Mg<sub>2</sub>Si, on the wear behaviour, the wear behaviour of the present cast *in-situ* magnesium based composites has been compared with those observed in cast unreinforced commercial magnesium and cast unreinforced Mg-9 wt% Al alloy. A comparison of cumulative volume loss for middle segments of cast ingots of cast *in-situ* composite, MS20/76, containing 6.54 vol% reinforcement, Mg<sub>2</sub>Si, and 1.7 vol% of porosity, unreinforced commercial magnesium and unreinforced Mg-9 wt% Al alloy at the highest normal load of 40 N and sliding distance of 3000 m is shown in Fig. 5.11: The cumulative volume loss in cast *in-situ* composite is significantly lower than those observed in the cast unreinforced commercial magnesium and cast unreinforced Mg-9 wt% Al alloy, by about 38 % and 16 % respectively. The porosity content of the cast unreinforced Mg-9 wt% Al alloy is lower than that of the cast *in-situ* composite and the porosity in cast commercial magnesium is still lower than that in cast *in-situ* composite and cast unreinforced Mg-9 wt% Al alloy. Thus, the reduced volume loss of the cast *in-situ* composite over that of cast unreinforced commercial magnesium could be attributed to the alloying of the matrix by aluminium and also, to the reinforcing effect of *in-situ* formed intermetallics, Mg<sub>2</sub>Si. But, the lower volume loss in cast *in-situ* composite compared to the cast unreinforced Mg-9 wt% Al alloy is primarily due to *in-situ* formed reinforcing intermetallics, Mg<sub>2</sub>Si.

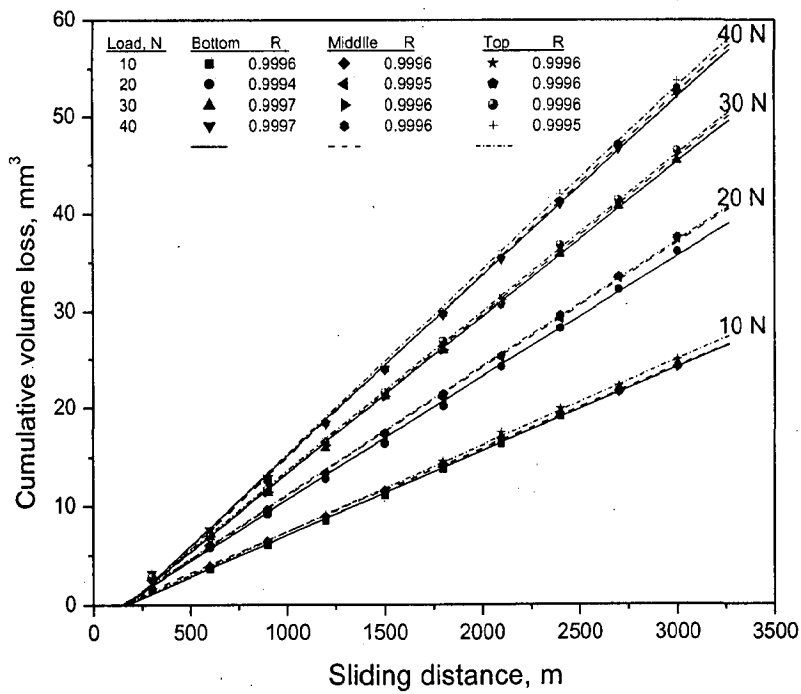
The wear rates, ( $V_w/S_w$ ), volume loss per unit sliding distance, is determined from the slope of the variation of cumulative volume loss with sliding distance for middle segments of cast ingots of *in-situ* composite, MS20/76, containing 6.54 vol% reinforcement, Mg<sub>2</sub>Si, and 1.7 vol% of porosity, unreinforced commercial magnesium and unreinforced Mg-9 wt% Al alloy are shown in Fig. 5.12. In cast commercial magnesium, the wear rate initially increases gradually with increasing normal load till 20 N but at higher loads it increases linearly with a higher slope. In Mg-9 wt% Al alloy, the wear rate increases linearly with increasing normal load. In cast magnesium based *in-situ* composite, the wear rate increases linearly with increasing normal load but at higher normal loads, the wear rate deviates from the line towards a lower value, showing non-linear behaviour. The Fig. 5.13 shows the variation of wear rate with normal load for the bottom, middle and top segments of cast ingots of different *in-situ* Mg-Al/ Mg<sub>2</sub>Si composites; (a) MS9/76, (b) MS15/76, (c) MS20/76, (d) MS15/72 and (e) MS15/80. The wear rate increases linearly with increasing normal load but at higher normal loads, the wear rate deviates from the line towards a lower value, showing non-linear behaviour for all cast *in-situ* composites. Also, the wear rate is nearly same for the three segments of cast ingots of *in-situ* composites.

The influence of porosity content on dry sliding wear of two groups of cast *in-situ* composites containing reinforcement, Mg<sub>2</sub>Si, varying over limited ranges, (a)  $2.4 \pm 0.04$  vol% and (b)  $4.64 \pm 0.52$  vol% is as shown respectively in Figs. 5.14(a) and (b). In both the groups of cast *in-situ* composites, the wear rate remains nearly constant with increasing volume fraction of porosity. The influence of reinforcement on dry sliding wear of two groups of cast *in-situ* composites containing porosity varying over limited ranges, (a)  $0.8 \pm 0.3$  vol% and (b)  $1.8 \pm 0.3$  vol% is as shown in Figs. 5.15(a) and (b) respectively. The wear rate of the second group of cast *in-situ* composites containing relatively higher amount of porosity, varying over limited range between  $1.83 \pm 0.34$  vol% decreases slightly with increasing reinforcement content, over the entire range of particle content investigated as shown in Fig. 5.15(b). On the other hand, in the first group, where the porosity is relatively lower than that in the second group of cast *in-situ* composites, the wear rate remains nearly constant with increasing particle content up to 4.72 vol% and beyond particle content of 5.16 vol%, the wear rate appears to be decreasing as shown in Fig. 5.15(a).

The influence of porosity content on wear coefficient of two groups of cast *in-situ* composites containing reinforcement, Mg<sub>2</sub>Si, varying over limited ranges, (a)  $2.4 \pm 0.04$  vol% and (b)  $4.64 \pm 0.52$  vol% are shown respectively in Figs. 5.16(a) and (b). In group (a), where the particle content is relatively lower than that in group (b) of cast *in-situ* composites,

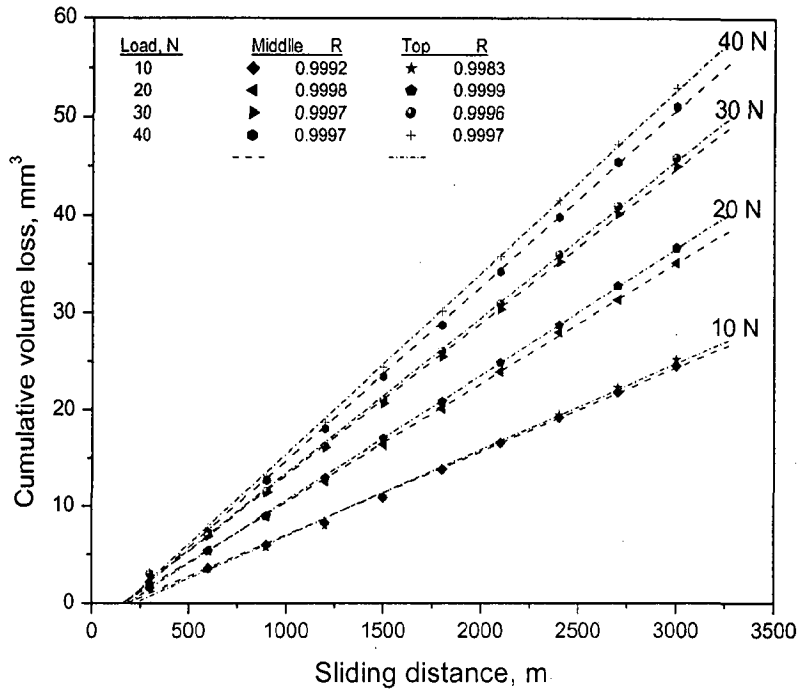


(a) The composite, MS9/76

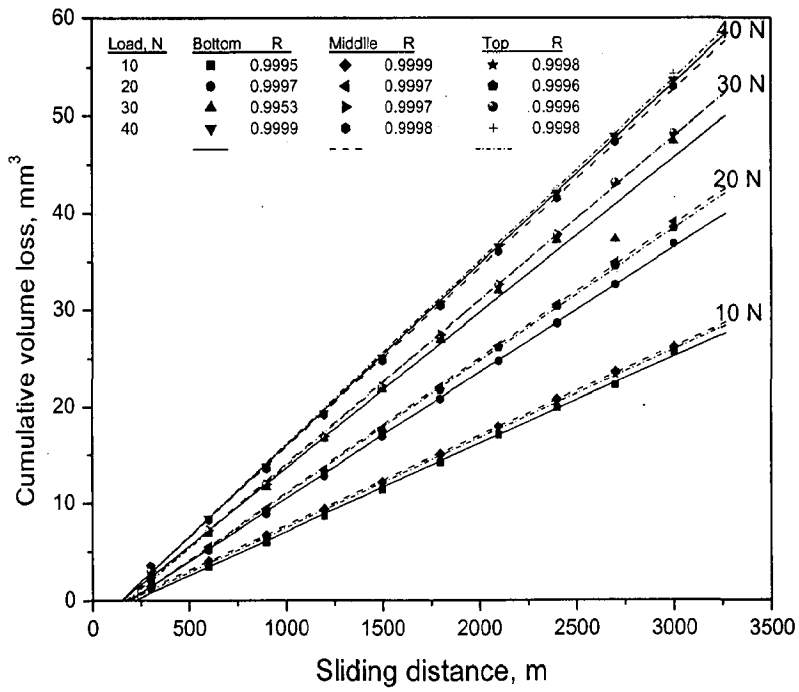


(b) The composite, MS15/76

Continued/-



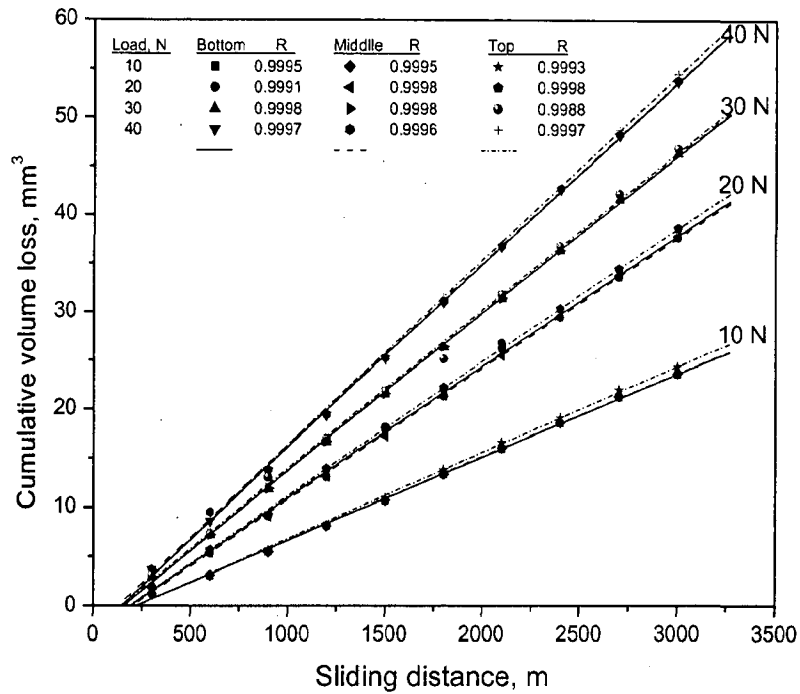
(c) The composite, MS20/76



(d) The composite, MS15/72

Continued/-





(e) The composite, MS15/80

**Fig. 5.10:** The variation of cumulative volume loss with sliding distance at different normal loads of 10, 20, 30 and 40 N and sliding speed of 1 m/s for the bottom, middle and top segments of cast ingots of the following *in-situ* Mg-Al/Mg<sub>2</sub>Si composites: (a) MS9/76, (b) MS15/76, (c) MS20/76, (d) MS15/72 and (e) MS15/80.

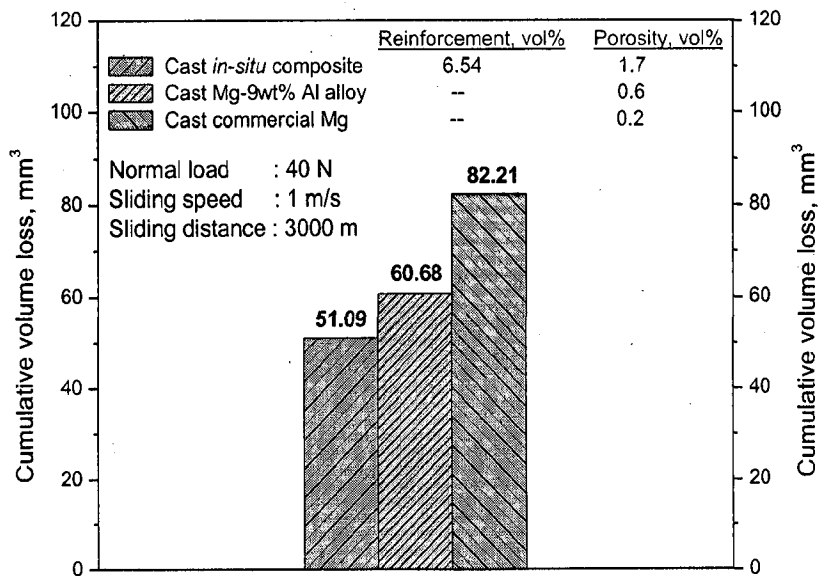


**Fig. 5.11:** A comparison of cumulative volume loss after dry sliding for 3000 m for the middle segments of cast ingots of *in-situ* Mg-Al/Mg<sub>2</sub>Si composite containing 6.54 vol% reinforcement (Mg<sub>2</sub>Si) and 1.7 vol% porosity, cast Mg-9 wt% Al alloy and cast commercial magnesium under similar load and sliding conditions.

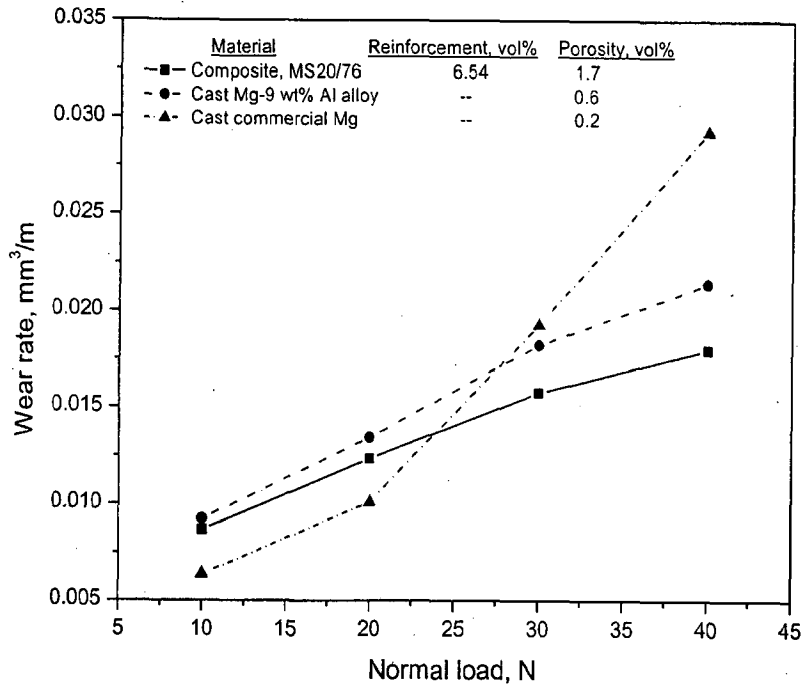
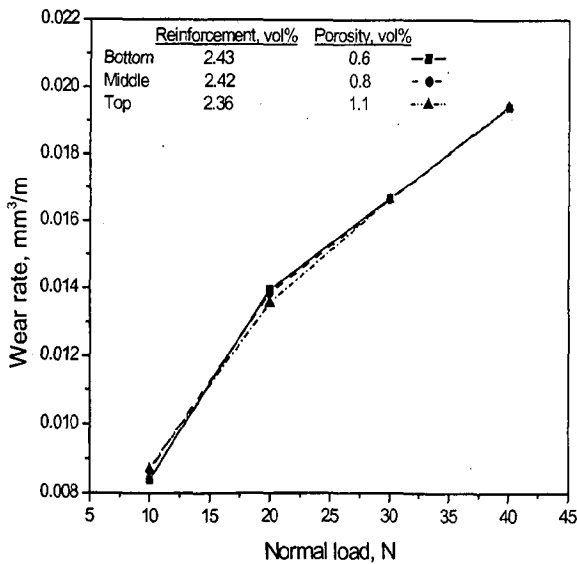
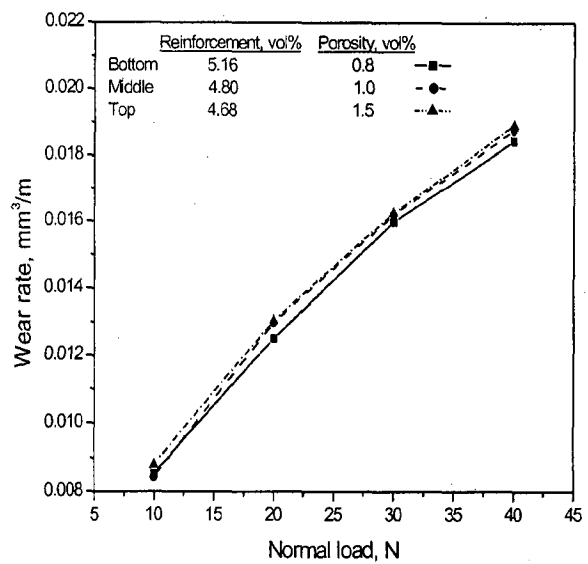


**Fig. 5.12:** The variation of wear rate with normal load for the middle segments of cast ingots of *in-situ* Mg-Al/Mg<sub>2</sub>Si composite, designated as MS20/76, containing 6.54 vol% reinforcement and 1.7 vol% porosity, cast Mg-9 wt% Al alloy and cast commercial magnesium.

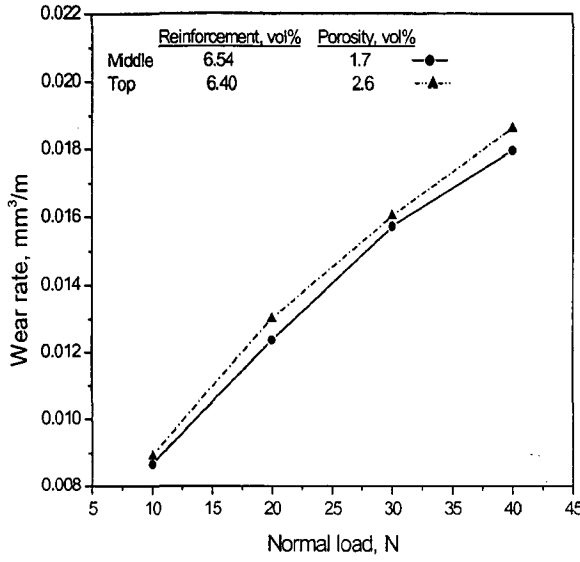


(a) The composite, MS9/76

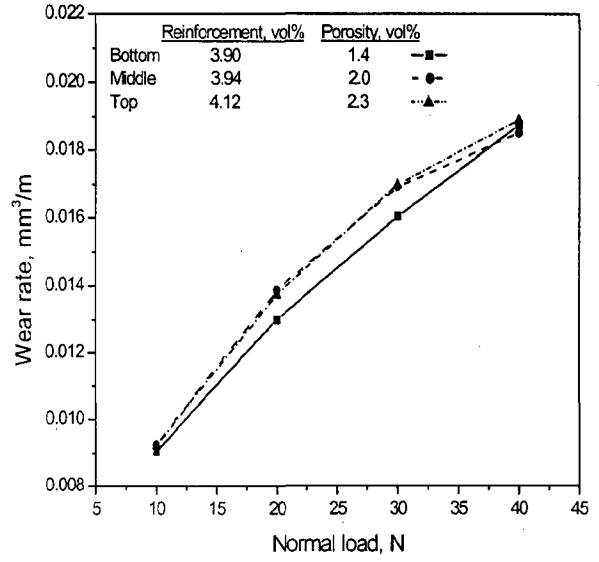


(b) The composite, MS15/76

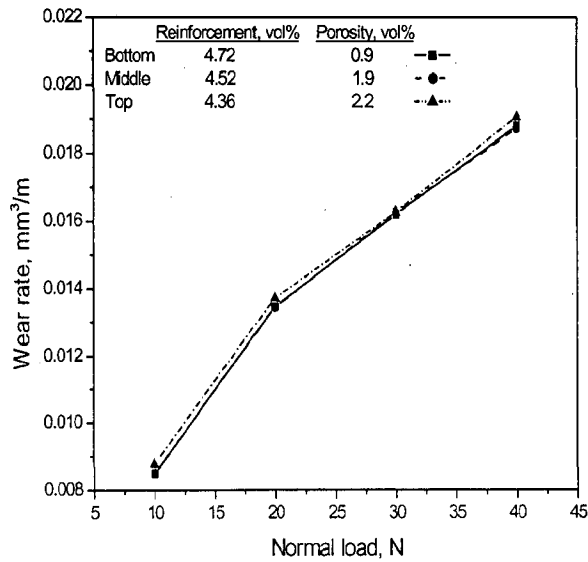
Continued/-



(c) The composite, MS20/76



(d) The composite, MS15/72



(e) The composite, MS15/80

**Fig. 5.13:** The variation of wear rate with normal load for the bottom, middle and top segments of cast ingots of different *in-situ* Mg-Al/Mg<sub>2</sub>Si composites: (a) MS9/76, (b) MS15/76, (c) MS20/76, (d) MS15/72 and (e) MS15/80.

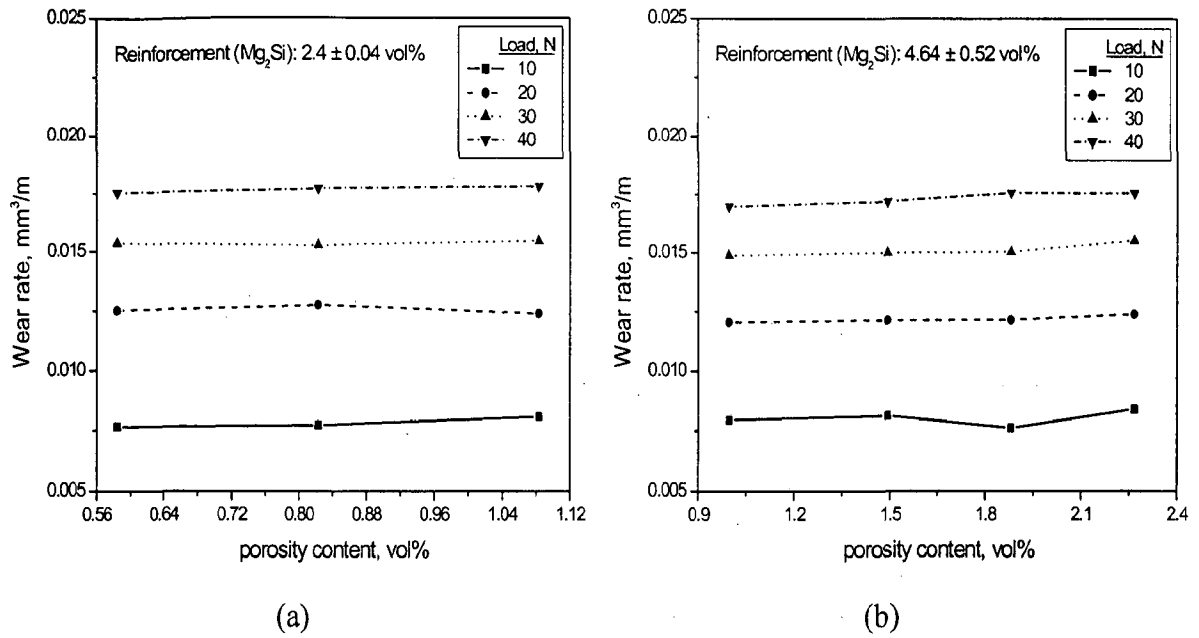


**Fig. 5.14:** The variation of wear rate with porosity content for cast *in-situ* Mg-Al/Mg<sub>2</sub>Si composites containing reinforcing particles varying over a limited range of (a) 2.4 ± 0.04 wt% and (b) 4.64 ± 0.52 wt%.

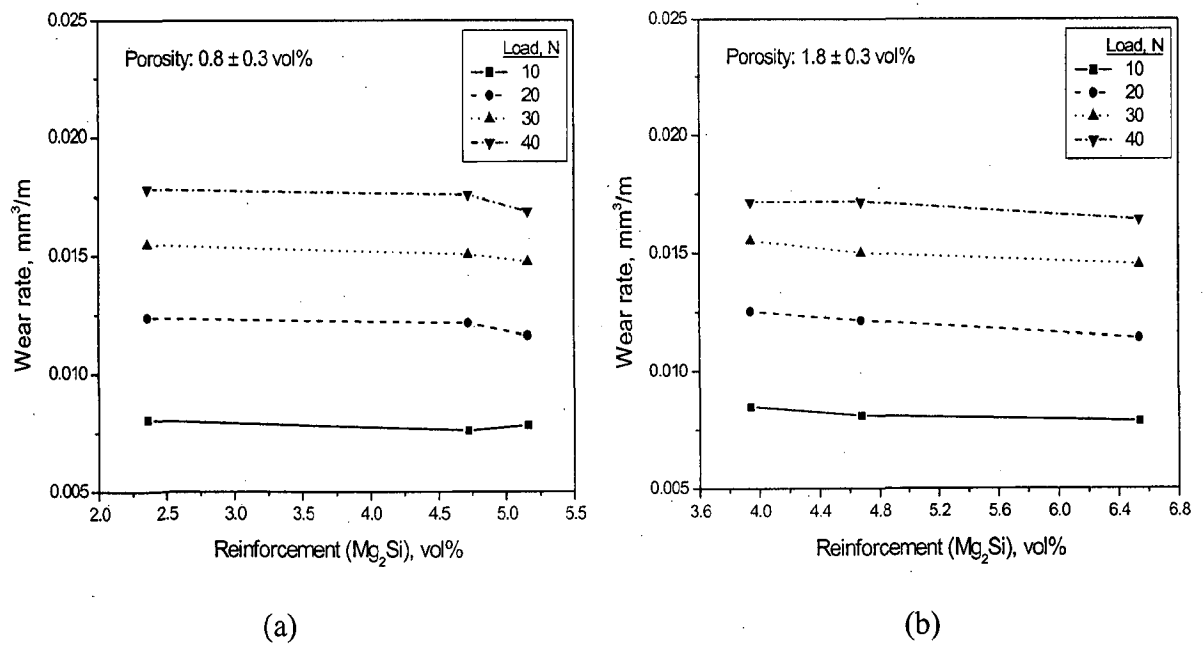


**Fig. 5.15:** The variation of wear rate with particle content for cast *in-situ* Mg-Al/Mg<sub>2</sub>Si composites containing porosity varying over a limited range of (a) 0.8 ± 0.3 vol% and (b) 1.8 ± 0.3 vol%.

the wear coefficient decreases gradually from  $2.408 \times 10^{-4}$  to  $2.297 \times 10^{-4}$  with increasing volume fraction of porosity over entire range of porosity content investigated, as observed in Fig. 5.16(a). For group (b) of cast *in-situ* composites, the wear coefficient decreases with increasing porosity from  $2.637 \times 10^{-4}$  to  $2.399 \times 10^{-4}$  in the porosity range investigated, as shown in Fig. 5.16(b).

The influence of reinforcement on wear coefficient of two groups of cast *in-situ* composites containing porosity varying over limited ranges between (a)  $0.83 \pm 0.25$  vol% and (b)  $1.83 \pm 0.34$  vol% are shown in Figs. 5.17(a) and (b) respectively. The wear coefficient of cast *in-situ* composites is observed to increase a little with increasing particle content as shown in Figs. 5.17(a) and (b).

## 5.2 Friction under Dry Sliding

Dry sliding friction behaviour in different cast *in-situ* Mg-Al/Al<sub>3</sub>Ti-Al<sub>2</sub>O<sub>3</sub> and cast *in-situ* Mg-Al/Mg<sub>2</sub>Si composites synthesized using cast Al-based composites/Ai-Si master alloys is of considerable interest from the standpoint of tribological applications. For comparison with *in-situ* composites, dry sliding friction behaviour in cast commercial magnesium and cast Mg-9 wt% Al base have also considered for investigation. The following subsections show the results on coefficient of friction as determined from the observed torque on pin samples during pin on disc test of dry sliding wear against the counterface of hardened EN-32 steel.

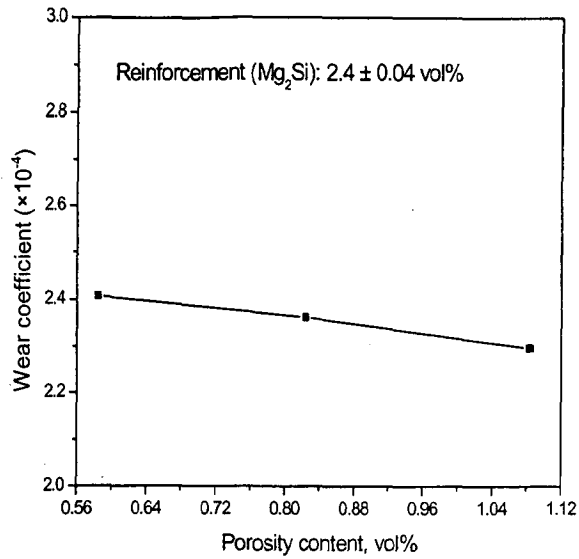
### 5.2.1 Cast *In-Situ* Mg-Al/Al<sub>3</sub>Ti-Al<sub>2</sub>O<sub>3</sub> Composites

The coefficient of friction ( $\mu$ ) is calculated by dividing the recorded frictional force ( $F$ ) by the normal load ( $L_w$ ). The variation of coefficient of friction with sliding distance at different normal loads of 10, 20, 30 and 40 N and a constant sliding speed of 1 m/s, for following cast *in-situ* composites are shown respectively in Figs. 5.18(a) to (f): (a) MT8/80, (b) MT10/80, (c) MT12/80, (d) MT14/80, (e) MT12/75 and (f) MT12/85. For comparison, the variation of the coefficient of friction of cast unreinforced commercial magnesium and cast Mg-9 wt% Al alloy with sliding distance at different normal load and a constant sliding speed of 1 m/s, is shown in Figs. 5.19(a) and (b). The variation of coefficient of friction with sliding distance observed in cast *in-situ* composites and cast Mg-9 wt% Al alloy is approximately similar, but compared to these materials some differences are observed in case of cast commercial magnesium as shown in Fig. 5.19(a). At all normal loads for cast commercial magnesium, the coefficient of friction fluctuates rapidly with sliding distance which may be attributed to the nature of dynamic contact. Also, there is large difference in the average

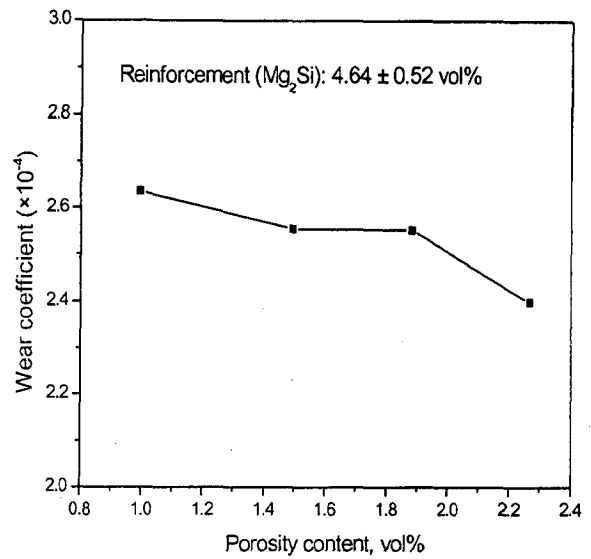
coefficient of friction of (about 0.26) for the lowest and the highest normal load. In case of cast *in-situ* composites and cast Mg-9 wt% Al alloy relatively higher fluctuations in coefficient of friction with sliding distance are observed only for the lowest normal load of 10 N and to some extent for the next lowest normal load of 20 N and for higher normal loads, the fluctuations about mean coefficient of friction are within a small range. At higher normal loads, average coefficient of friction observed is about 0.3 for cast Mg-9 wt% Al alloy and cast *in-situ* composites designated as MT8/80 and MT10/80 which are containing relatively lower particles, and while it is about 0.32 for cast *in-situ* composites designated as MT12/80, MT14/80, MT12/75 and MT12/85 which are containing relatively higher particles. Increasing particle content in case of cast *in-situ* composites designated as MT12/80, MT14/80, MT12/75 and MT12/85 could be responsible for relatively higher value of coefficient of friction than that of the *in-situ* composites with lower particle content. The variation of average coefficient of friction with increasing load, for different cast *in-situ* composites designated as MT8/80, MT10/80, MT12/80, MT14/80, MT12/75 and MT12/85 is shown in Fig. 5.20. It is observed that the average coefficient of friction decreases with increasing normal load and it appears to decrease relatively faster at lower loads than at higher loads. Also, increasing values of the average coefficient of friction are observed for *in-situ* composites with increasing particle content. The variation of average coefficient of friction with normal load at sliding speed of 1 m/s for cast commercial magnesium and cast Mg-9 wt% Al alloy is shown in Fig. 5.21. Similar to cast *in-situ* composites, the average coefficient of friction decreases with increasing normal load for cast Mg-9 wt% Al alloy, but the rate at which the average coefficient of friction decreases with increasing normal load for cast commercial magnesium is more.

### 5.2.2 Cast *In-Situ* Mg-Al/Mg<sub>2</sub>Si Composites

The variation of coefficient of friction with sliding distance at different normal loads and a constant sliding speed of 1 m/s, for following cast *in-situ* Mg-Al/Mg<sub>2</sub>Si composite are shown respectively in Figs. 5.22(a) to (e): (a) MS9/76, (b) MS15/76, (c) MS20/76, (d) MS15/72 and (e) MS15/80. For comparison, the variation of the coefficient of friction of cast unreinforced Mg-9 wt% Al alloy with sliding distance at different normal load and a constant sliding speed of 1 m/s is shown in Figs. 5.19(a) and (b) in the previous sub-section. The variation of coefficient of friction with sliding distance observed in cast *in-situ* composites and cast Mg-9 wt% Al alloy is approximately similar. In case of cast *in-situ* composites and cast Mg-9 wt% Al base alloy relatively higher fluctuations in coefficient of friction with sliding distance are observed only at the lowest normal load of 10 N, particularly for *in-situ* composites designated as

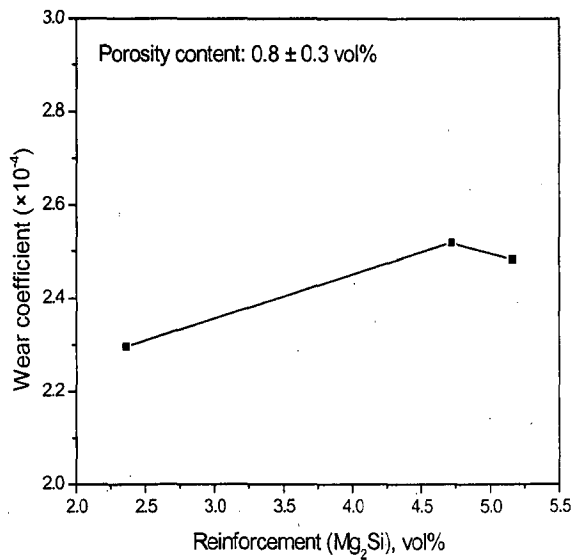


(a)

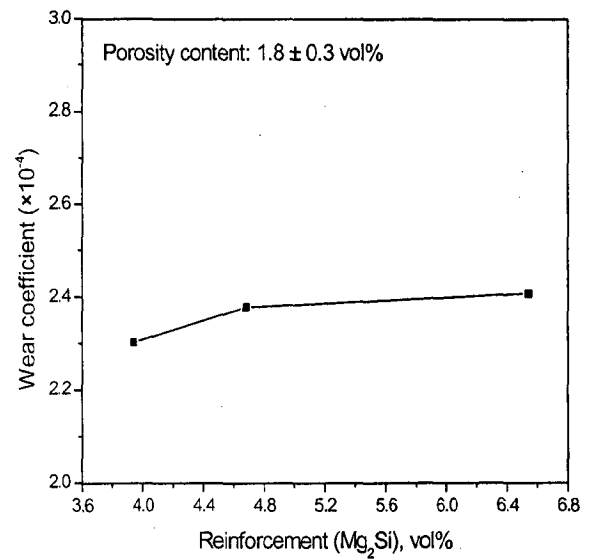


(b)

**Fig. 5.16:** The variation of wear coefficient with porosity content for cast *in-situ* Mg-Al/ $Mg_2Si$  composites containing reinforcing particles varying over a limited range of (a)  $2.44 \pm 0.04$  vol% and (b)  $4.64 \pm 0.2$  vol%.

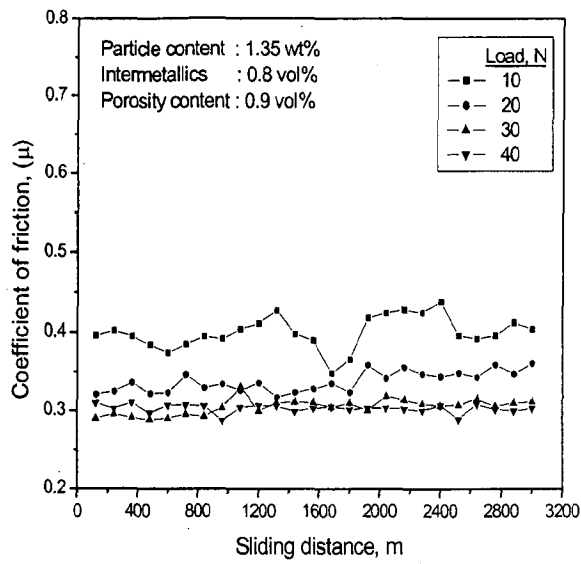


(a)

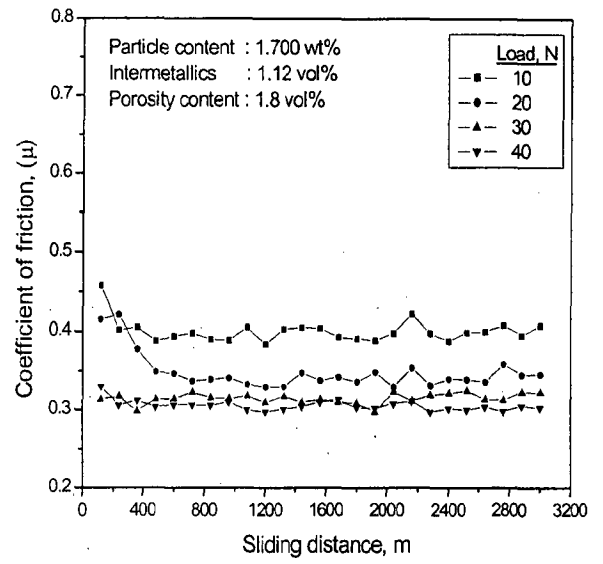


(b)

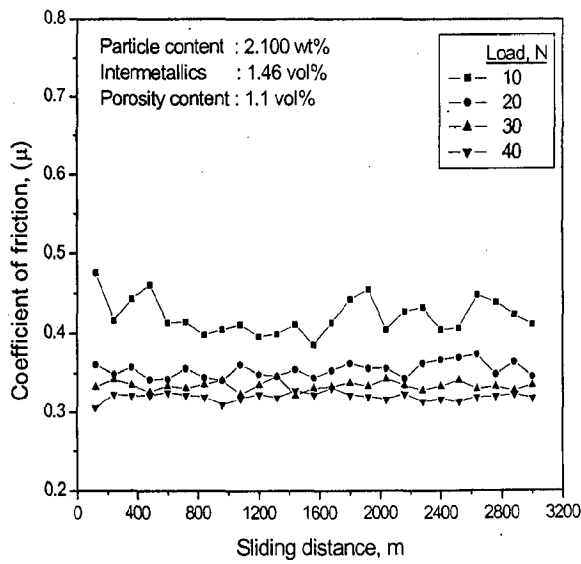
**Fig. 5.17:** The variation of wear coefficient with particle content for cast *in-situ* Mg-Al/ $Mg_2Si$  composites containing porosity varying over a limited range of (a)  $0.8 \pm 0.3$  vol% and (b)  $1.8 \pm 0.3$  vol%.



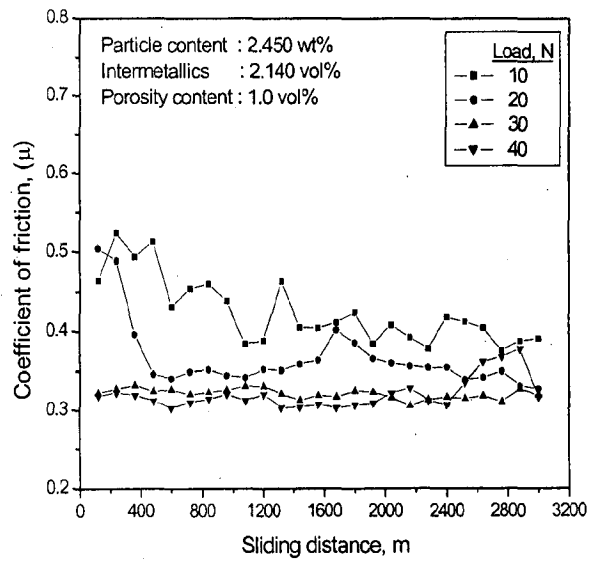
(a) The composite, MT8/80



(b) The composite, MT10/80



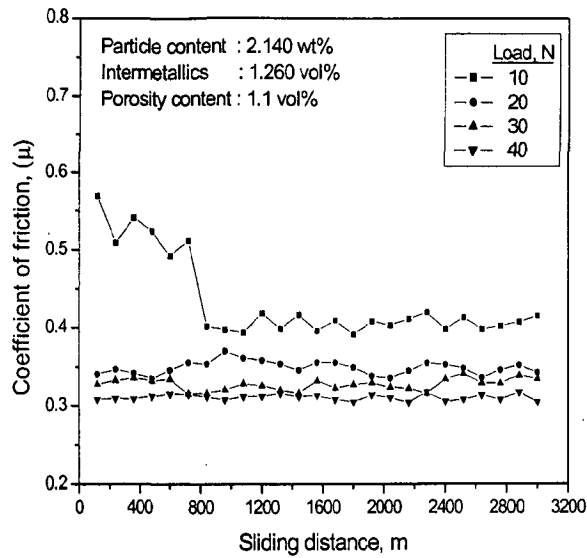
(c) The composite, MT12/80



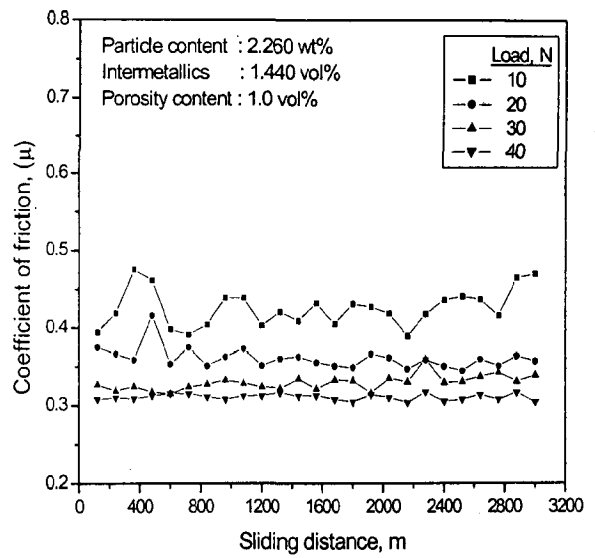
(d) The composite, MT14/80

Continued/-



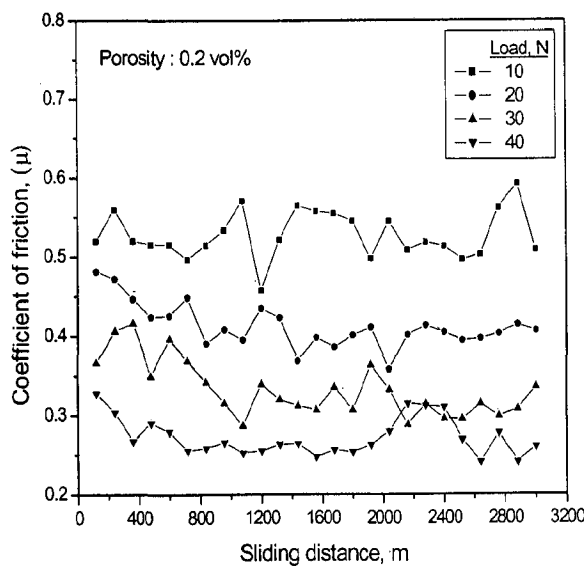


(e) The composite, MT12/75

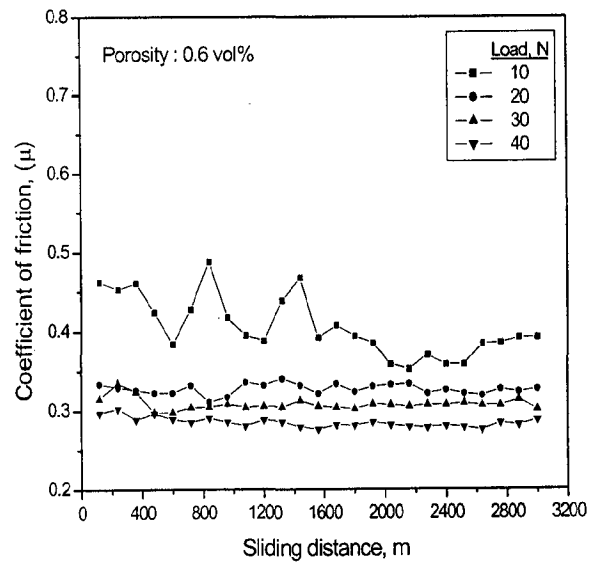


(f) The composite, MT12/85

**Fig. 5.18:** The variation of coefficient of friction with sliding distance at different normal loads of 10, 20, 30 and 40 N and sliding speed of 1 m/s for the following *in-situ* Mg-Al/Al<sub>3</sub>T-Al<sub>2</sub>O<sub>3</sub> composites: (a) MT8/80, (b) MT10/80, (c) MT12/80, (d) MT14/80, (e) MT12/75 and (f) MT12/85.



(a) Cast commercial magnesium and



(b) Cast Mg-9 wt% Al alloy

**Fig. 5.19:** The variation of coefficient of friction loss with sliding distance at different normal loads of 10, 20, 30 and 40 N and sliding speed of 1 m/s for (a) cast commercial magnesium and (b) cast Mg-9 wt% Al alloy.

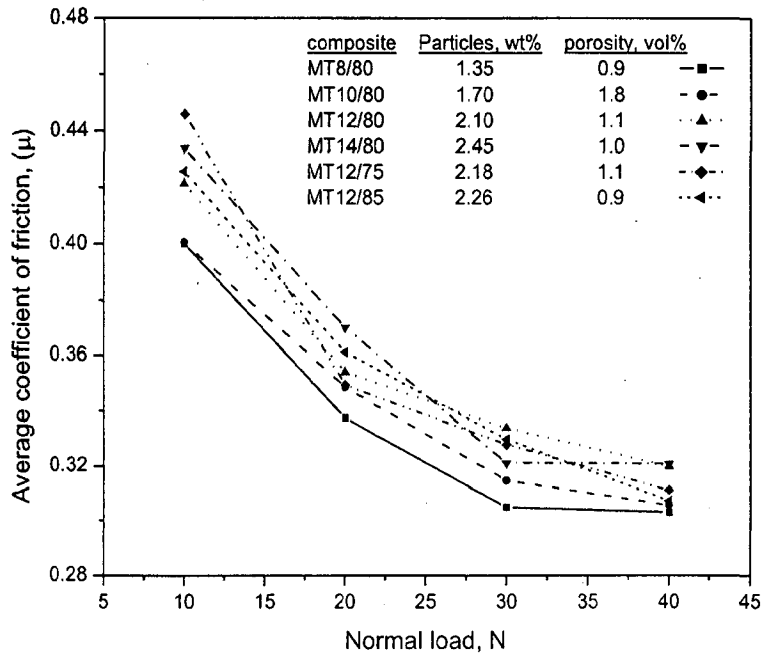


**Fig. 5.20:** The variation of average coefficient of friction with normal load at sliding speed of 1 m/s for different cast in-situ Mg-Al/Al<sub>3</sub>Ti-Al<sub>2</sub>O<sub>3</sub> composites containing reinforcing particle and porosity contents respectively given in the figure.

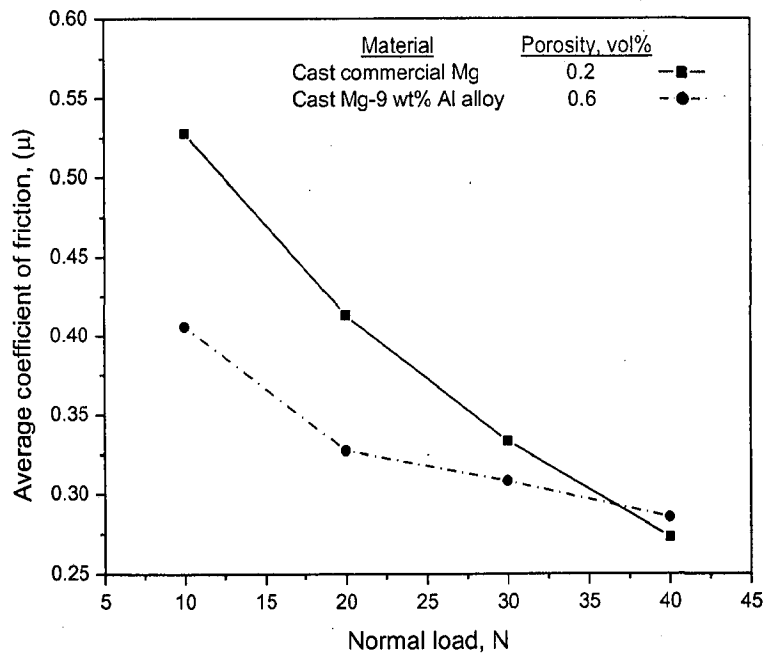


**Fig. 5.21:** The variation of average coefficient of friction with normal load at sliding speed of 1 m/s for cast commercial magnesium and cast Mg-9 wt% Al alloy.

MS9/76, which contains comparatively lower volume fraction of reinforcement,  $Mg_2Si$ , and at higher normal loads, the fluctuations about mean coefficient of friction are too small. At higher normal loads, average coefficient of friction observed is about 0.3 for cast Mg-9 wt% Al alloy and approximately same value is observed in cast *in-situ* composites. There is no much variation of coefficient of friction with increasing reinforcement,  $Mg_2Si$ , for *in-situ* composites. The variation of average coefficient of friction with increasing normal load, for different cast *in-situ* composites designated as (a) MS9/76, (b) MS15/76, (c) MS20/76, (d) MS15/72 and (e) MS15/80 is shown in Fig. 5.23. For comparison, the variation of average coefficient of friction with normal load at sliding speed of 1 m/s for cast Mg-9 wt% Al alloy is also shown in the figure. It is observed that the average coefficient of friction decreases with increasing normal load and it appears to decrease relatively faster at lower loads than at higher loads. Similarly as in *in-situ* composites, decreasing trend of the average coefficient of friction with increasing normal load is observed for cast Mg-9 wt% Al alloy.

### 5.3 Wear Debris and Worn Surfaces

The nature of wear debris generated during dry sliding wear of different cast *in-situ* Mg-Al/ $Al_3Ti$ - $Al_2O_3$  and cast *in-situ* Mg-Al/ $Mg_2Si$  composites synthesized using cast Al-based composites/Ai-Si master alloys is of considerable interest in understanding the wear process under given load and sliding velocity. The following subsections show the results of examination of wear debris and also the worn surfaces of the pin.

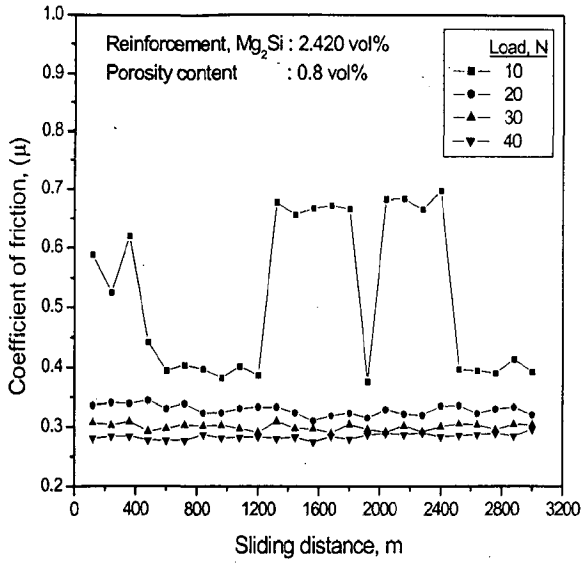
Typical X-ray diffraction patterns for wear debris from cast *in-situ* Mg-Al/ $Al_3Ti$ - $Al_2O_3$  and cast *in-situ* Mg-Al/ $Mg_2Si$  composites are shown respectively in Figs. 5.24(a) and (b). Apart from broad peak initially showing possibly amorphous oxides, the sharp peaks in the patterns of both the types of composites belong to the primary solid solution of magnesium and are similar, except for peaks corresponding to  $Al_3Ti$  which are observed in Fig. 5.24(a) and those corresponding to  $Mg_2Si$  in Fig. 5.24(b). From the patterns it is understood that the wear debris from both the types of composites contain metallic particles from the matrix along with oxides and intermetallics. The physical appearance of the debris is powdery and black in colour along with some shining metallic particles as revealed by optical micrographs of the wear debris generated during dry sliding of pin samples of the composites, MT12/80 and MS20/76, and base alloy, Mg-9 wt% Al as shown in Figs. 5.25 (a), (b) and (c) respectively as representatives of their class. The wear debris, thus, consists primarily of oxides under the conditions of dry sliding used in the present study for both the types of composites.

The examination of the surface of the pin specimens after dry sliding a distance of 3000 m at a normal load of 40 N has been carried out under Scanning Electron Microscope (SEM) and the micrographs show marks of wear tracks along with formation of some transfer layer as shown in Figs. 5.26 for the cast *in-situ* Mg-Al/Al<sub>3</sub>Ti-Al<sub>2</sub>O<sub>3</sub> composites, designated respectively by MT8/80 and MT14/80 as well as for cast Mg-9 wt% Al alloy and cast commercial magnesium.

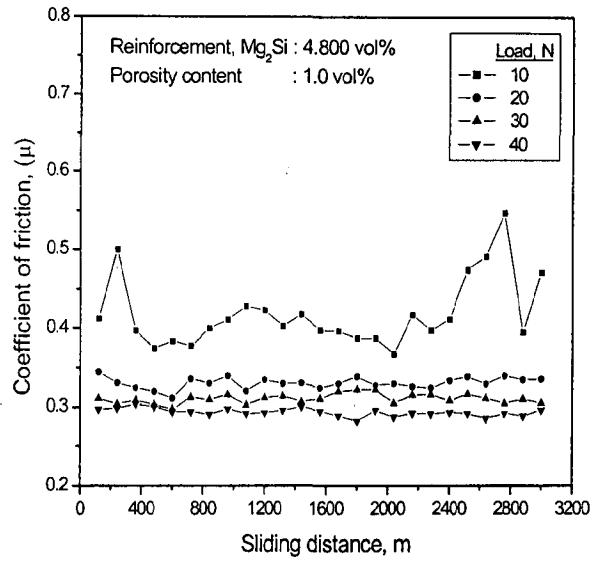
The worn surfaces of the pin of cast *in-situ* Mg-Al/Al<sub>3</sub>Ti-Al<sub>2</sub>O<sub>3</sub> composite developed from aluminium based composite with 12 wt% TiO<sub>2</sub>, designated by MT12/80, after dry sliding at different normal loads show the increasing formation of compacted transfer layer as the load increases from 10 N to 30 N, shown in Fig. 5.27 but increasing the load further to 40 N the compacted oxides are less visible as shown in Fig. 5.27(d). The worn surfaces of pins of cast *in-situ* Mg-Al/Mg<sub>2</sub>Si composites, designated by MS9/76 and MS20/76, after dry sliding under normal loads 10 and 40 N have been examined under SEM and the micrographs are shown in Fig. 5.28. A comparison of worn surfaces of pins of both the composites containing lower and higher amounts of Mg<sub>2</sub>Si shows that formation of transfer layer is relatively easier on the softer surface of the composite designated by MS9/76, which contains relatively lower volume fraction of Mg<sub>2</sub>Si, than on the relatively harder surface of the composite, designated by MS20/76, both at lower and higher loads. In this system also it has been observed that at higher loads the extent of compacted layer observed is less at higher loads of 40 N compared to that at relatively lower loads as shown Fig. 5.28.

#### **5.4 Comparison of Friction and Wear between Cast *In-Situ* Mg-Al/Al<sub>3</sub>Ti-Al<sub>2</sub>O<sub>3</sub> and Cast *In-Situ* Mg-Al/Mg<sub>2</sub>Si Composites**

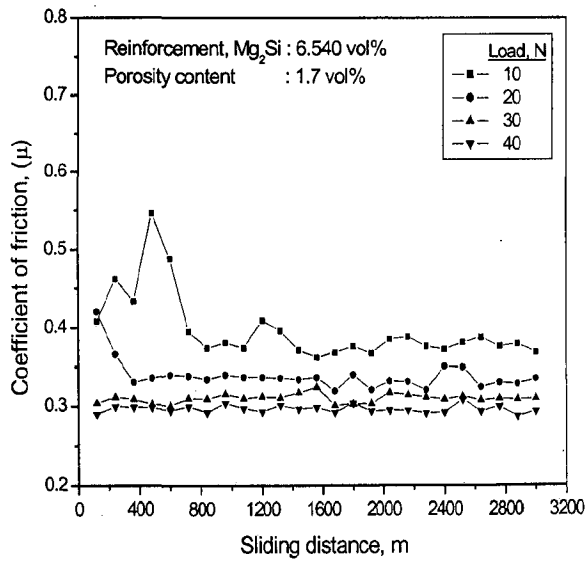
A comparison of the wear rates observed at different loads in different cast *in-situ* Mg-Al/Al<sub>3</sub>Ti-Al<sub>2</sub>O<sub>3</sub> and cast *in-situ* Mg-Al/Mg<sub>2</sub>Si composites along with cast commercial Mg and Mg-9 wt% Al base alloy is shown in Fig. 5.29. Both classes of composites are entirely different, because cast *in-situ* Mg-Al/Al<sub>3</sub>Ti-Al<sub>2</sub>O<sub>3</sub> composite contains both oxide particles as well as intermetallics (Al<sub>3</sub>Ti), but in relatively lower volume fraction, as reinforcement, where as cast *in-situ* Mg-Al/Mg<sub>2</sub>Si composite contains only intermetallics, Mg<sub>2</sub>Si, but in relatively higher volume fraction as reinforcement. However in the range of reinforcement investigated here, cast *in-situ* Mg-Al/Al<sub>3</sub>Ti-Al<sub>2</sub>O<sub>3</sub> composites show lower wear rate than cast



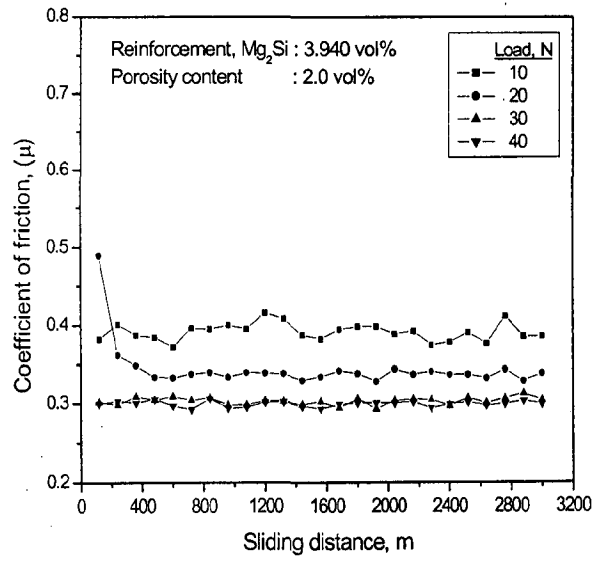
(a) The composite, MS9/76



(b) The composite, MS15/76

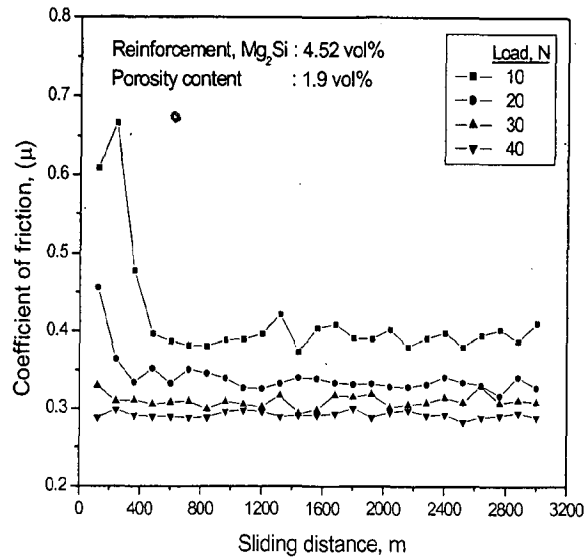


(c) The composite, MS20/76



(d) The composite, MS15/72

Continued/-



(e) The composite, MS15/80

**Fig. 5.22:** The variation of coefficient of friction with sliding distance at different normal loads of 10, 20, 30 and 40 N and sliding speed of 1 m/s for the following *in-situ* Mg-Al/Mg<sub>2</sub>Si composites: (a) MS9/76, (b) MS15/76, (c) MS20/76, (d) MS15/72 and (e) MS15/80.

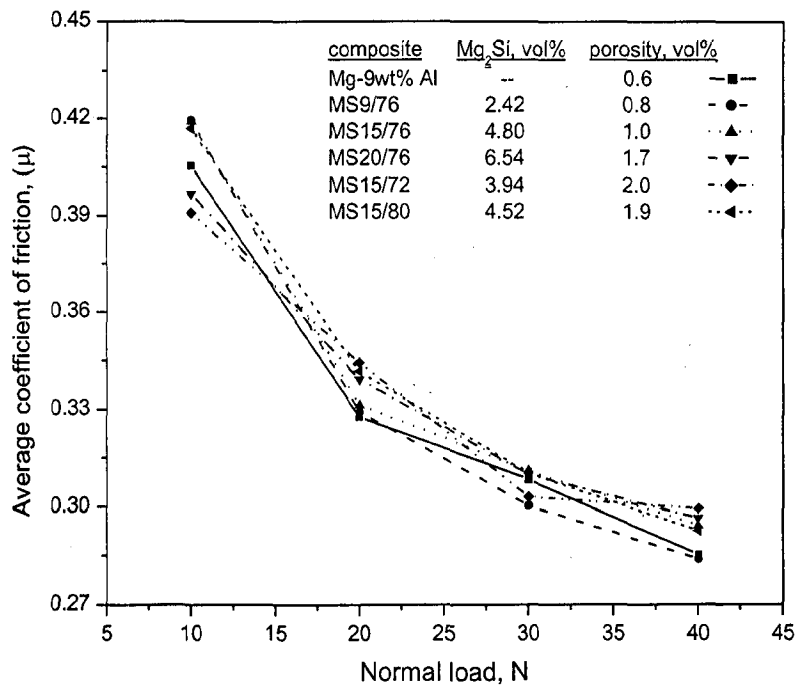
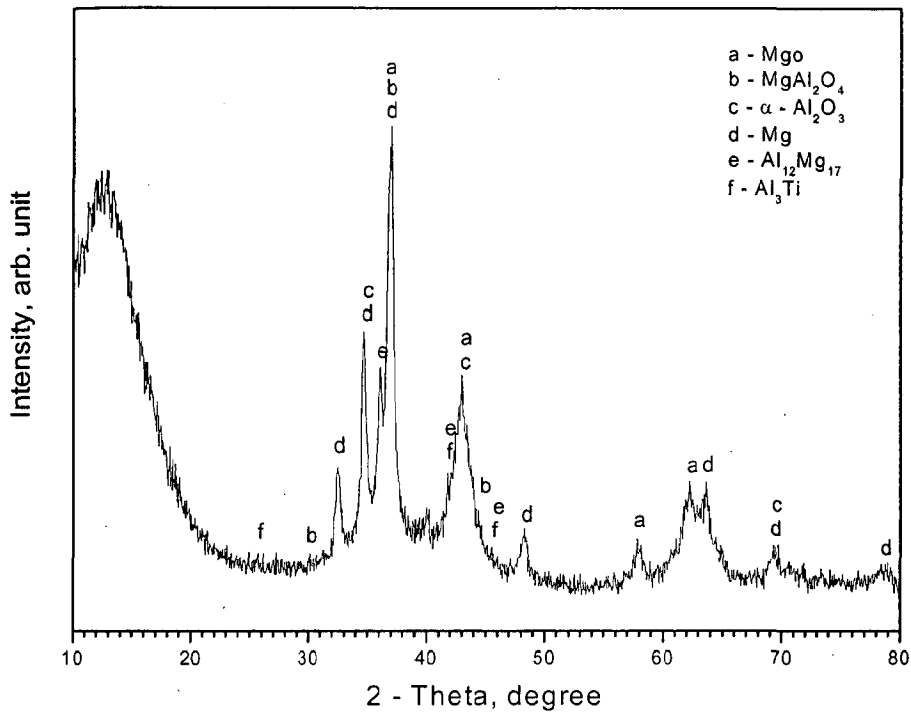
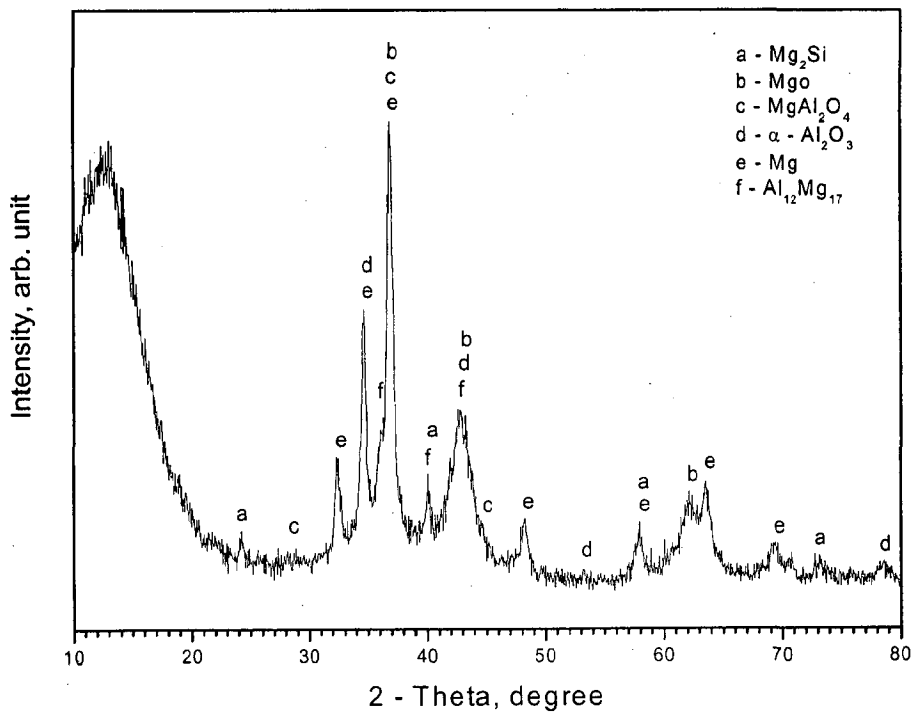


**Fig. 5.23:** The variation of average coefficient of friction with normal load at sliding speed of 1 m/s for different cast *in-situ* Mg-Al/Mg<sub>2</sub>Si composites containing reinforcement, Mg<sub>2</sub>Si, and porosity contents respectively given in the legend of the figure.

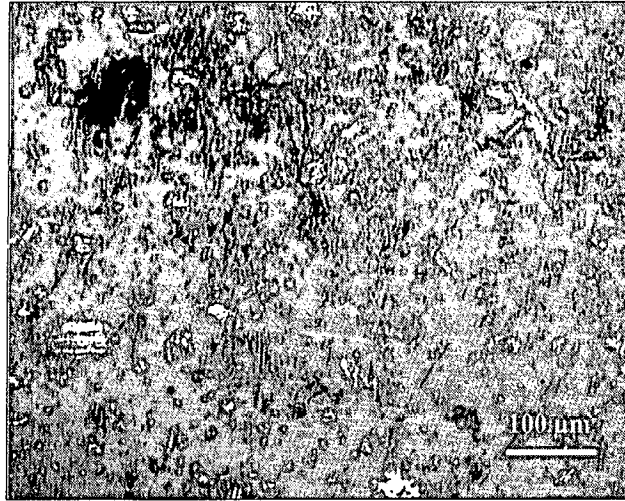


(a) Cast *in-situ* Mg-Al/ $Al_3Ti$ - $Al_2O_3$  composite

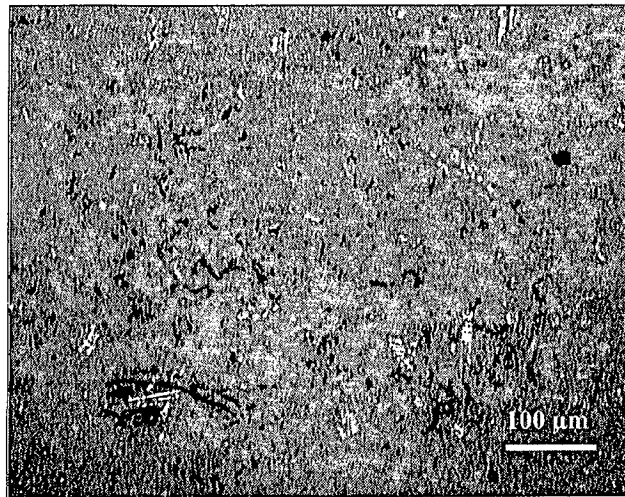


(b) Cast *in-situ* Mg-Al/ $Mg_2Si$  composite

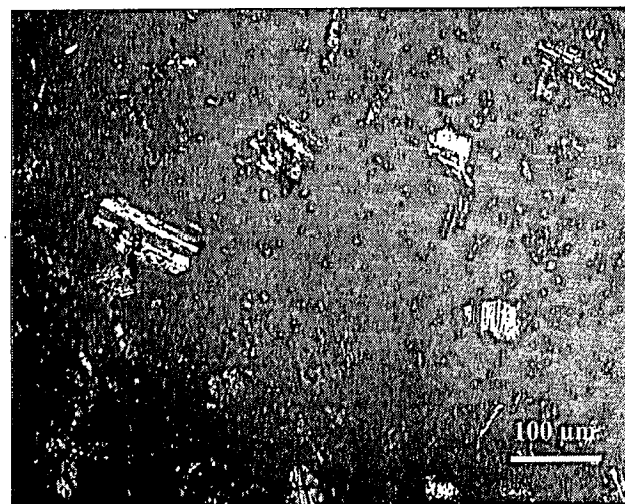
**Fig. 5.24:** X-ray diffraction pattern for wear debris generated during dry sliding wear of (a) cast *in-situ* Mg-Al/ $Al_3Ti$ - $Al_2O_3$  composite (b) cast *in-situ* Mg-Al/ $Mg_2Si$  composite.



(a) The composite, MT12/80



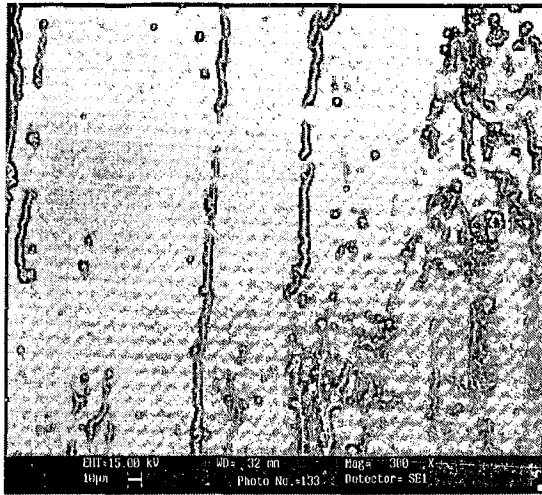
(b) The composite, MS20/76



(c) Mg-9 wt % Al alloy

**Fig.5.25:** Optical micrographs of typical samples of wear debris generated during dry sliding of pin samples of (a) cast *in-situ* Mg-Al/Al<sub>3</sub>Ti-Al<sub>2</sub>O<sub>3</sub> composite (b) cast *in-situ* Mg-Al/Mg<sub>2</sub>Si composite and (c) Mg-9 wt % Al alloy.

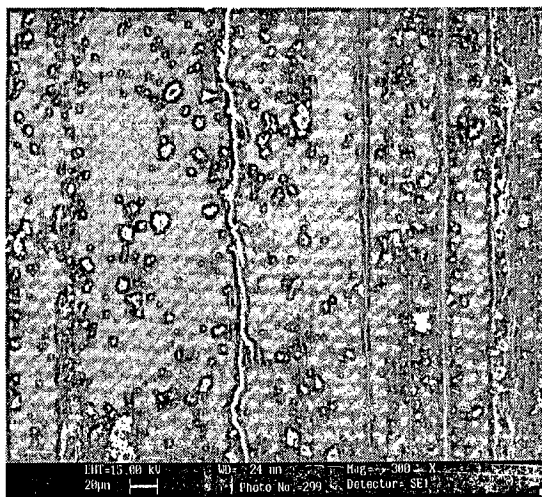




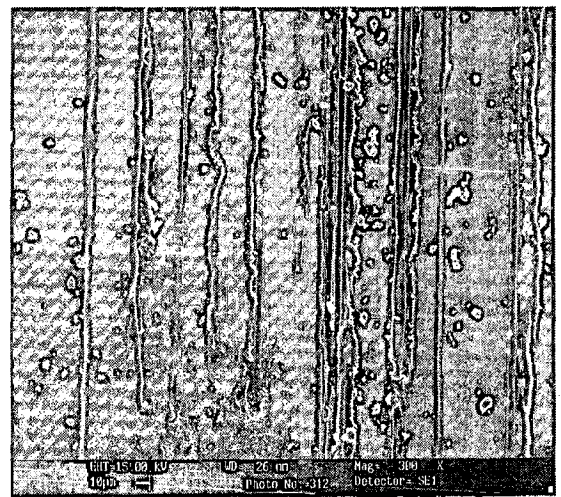
(a) The composite, MT8/80



(b) The composite, MT14/80

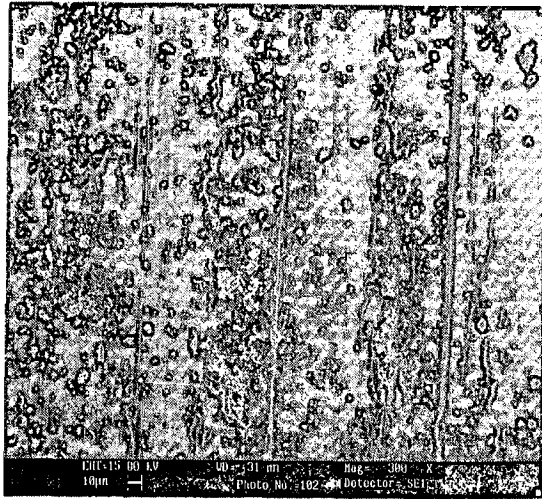


(c) Mg-9 wt% Al alloy



(d) Cast commercial Mg

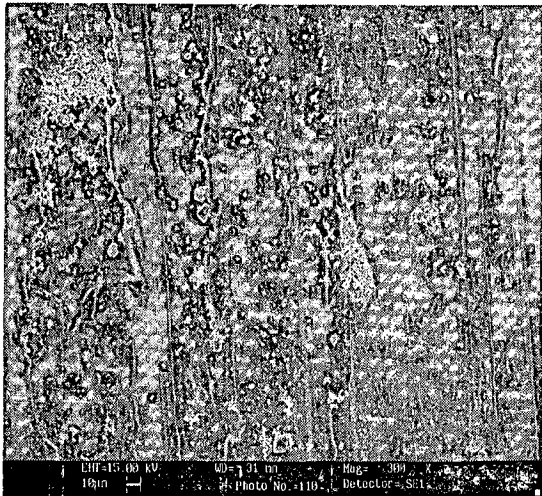
**Fig. 5.26:** Typical SEM micrographs at a magnification, X300, showing the worn surfaces of (a) and (b) cast *in-situ* Mg-Al/Al<sub>3</sub>Ti-Al<sub>2</sub>O<sub>3</sub> composites, designated respectively by MT8/80 containing 0.9 vol% porosity and 1.35 wt% particles and MT14/80 containing 1 vol% porosity and 2.45 wt% particles, (c) cast Mg-9 wt% Al alloy and (d) cast commercial Mg.



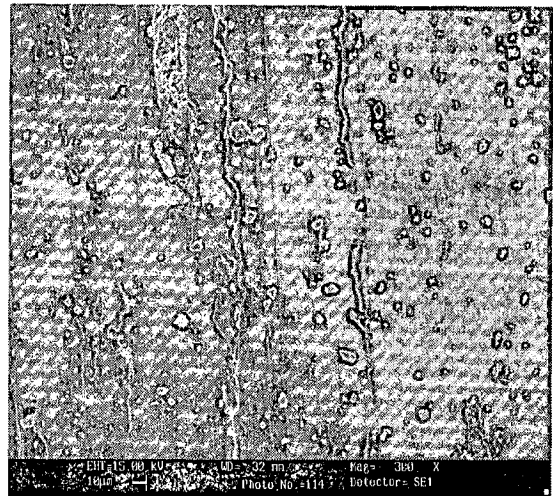
(a) Normal load: 10 N



(b) Normal load: 20 N

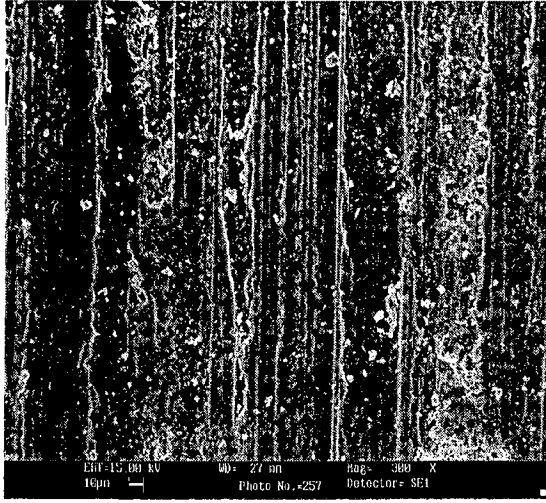


(c) Normal load: 30 N

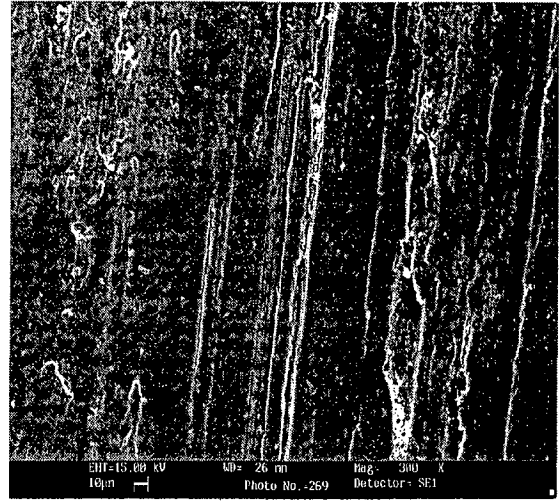


(d) Normal load: 40 N

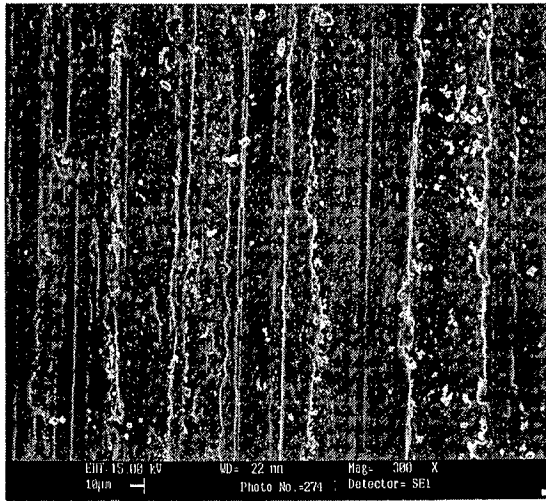
**Fig. 5.27:** SEM micrographs at a magnification, X300, showing the worn surfaces of a cast *in-situ* Mg-Al/Al<sub>3</sub>Ti-Al<sub>2</sub>O<sub>3</sub> composite designated by MT12/80, containing 1.1 vol% porosity and 2.1 wt% particles, at different normal loads.



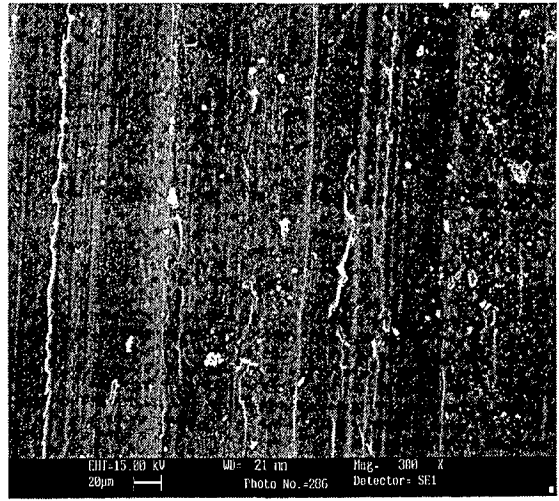
(a) MS9/76, Normal load: 10 N



(b) MS9/76, Normal load: 40 N



(c) MS20/76, Normal load: 10 N



(d) MS20/76, Normal load: 40 N

**Fig. 5.28:** Typical SEM micrographs at a magnification, X300, showing the worn surfaces of cast *in-situ* Mg-Al/Mg<sub>2</sub>Si composites designated by (a) and (b) MS9/76, containing 0.8 vol% porosity and 2.42 vol % reinforcement, Mg<sub>2</sub>Si, at normal loads 10 and 40 N respectively, and (c) and (d) MS20/76, containing 2.6 vol% porosity and 6.4 vol % reinforcement, Mg<sub>2</sub>Si, at normal loads 10 and 40 N respectively.

*in-situ* Mg-Al/Mg<sub>2</sub>Si composites. Lower wear rates for cast *in-situ* Mg-Al/Al<sub>3</sub>Ti-Al<sub>2</sub>O<sub>3</sub> composites could be due to presence of oxide particles. Cast commercial Mg and Mg-9 wt% Al alloy have significantly steeper variation of wear rate with increasing load compared to those of composites, resulting in considerably increased wear rate compared to those in composites particularly at relatively higher normal loads.

A comparison of the variation of coefficient of friction with increasing load shows that alloying of aluminium has significantly decreased coefficient of friction and its variation with load compared to that in cast commercial magnesium as revealed in Fig. 5.30. Cast *in-situ* Mg-Al/Al<sub>3</sub>Ti-Al<sub>2</sub>O<sub>3</sub> composites show slightly higher coefficient of friction than that of Mg-9 wt% Al alloy where as cast *in-situ* Mg-Al/Mg<sub>2</sub>Si composites show the coefficient of friction approximately in the same range as that of Mg-9 wt% Al alloy as observed in Fig. 5.30.

## 5.5 Discussion

The primary aim of the investigation reported in this chapter is to study dry sliding friction and wear behaviour of cast *in-situ* Mg-Al/Al<sub>3</sub>Ti-Al<sub>2</sub>O<sub>3</sub> and cast *in-situ* Mg-Al/Mg<sub>2</sub>Si composites. The hard phases of Al<sub>2</sub>O<sub>3</sub> particles and intermetallics, Al<sub>3</sub>Ti and Mg<sub>2</sub>Si, embedded in a soft matrix like magnesium-aluminium alloy may satisfy textbook prescription for a good bearing material. The soft phase adjusts to the contour of shaft and the hard phase bears the load. Aluminium alloying has significant influence in enhancing the mechanical properties of magnesium, which are very much essential for satisfactory tribological performance of a material. The cast composites contain apart from particles and intermetallics, an amount of porosity as reported in Tables 5.1 to 5.3. The friction and wear in cast commercial magnesium and in Mg-9 wt% Al alloy has also been investigated for comparing these results with those of composites.

The cumulative volume loss in cast commercial magnesium increases linearly with increasing sliding distance at different normal loads following Archard's equation predicting linear variation of cumulative volume loss in wear with normal load, as shown in Fig. 5.2(a). The wear rate increases with increasing load from about  $6 \times 10^{-3}$  mm<sup>3</sup>/m at 10 N to about  $30 \times 10^{-3}$  mm<sup>3</sup>/m at 40 N as shown in Fig. 5.4. Oxidative, delamination and abrasive wear are observed in micrographs of worn surfaces as shown in Fig. 5.26(d). Lim et al. (2005) have investigated dry sliding of cast extruded pure magnesium pin against AISI-O1 tool-steel disc, which had

been oil-hardened to 63 HRC. They have observed a decreasing wear rate from about  $12 \times 10^{-3} \text{ mm}^3/\text{m}$  at a sliding velocity of 1 m/s to about  $6.5 \times 10^{-3} \text{ mm}^3/\text{m}$  at a sliding velocity of 7 m/s at the normal load of 10 N. The results obtained in the present investigation are very close to the results observed by Lim et al (2005).

Lim et al. (2003) have investigated dry sliding wear in Mg-9 wt% Al alloy using a pin on disc set-up very similar to that used in the present investigation. Although the present study has not investigated any new aspect of dry sliding in Mg-Al alloy but the experiments reported is only for the purpose of comparison with the results on composites. The earlier investigators have observed oxidative, delamination and abrasive wear at a sliding speed of 1 m/s under loads of 10 and 30 N and the wear rates are respectively, about  $6 \times 10^{-3}$  and  $10 \times 10^{-3} \text{ mm}^3/\text{m}$ . The present study also observes oxidative, delaminating and abrasive wear in Mg-9 wt% Al alloy as confirmed by appearance of wear debris in Fig. 5.25 (c) SEM micrograph of worn surface in Fig. 5.26 (c). In the present investigation, the cumulative volume loss in cast Mg-9 wt% Al alloy increases linearly with increasing sliding distance, as shown in Fig. 5.2(a) and the wear rate increases linearly with increasing load from about  $9 \times 10^{-3} \text{ mm}^3/\text{m}$  at 10 N to about  $21 \times 10^{-3} \text{ mm}^3/\text{m}$  at 40 N as shown in Fig. 5.4 for the sliding speed of 1 m/s. Sharma et al. (2000) have investigated dry sliding of wrought magnesium alloy, AZ91, which contains mainly, 0.5-1.0 wt% Zn along with 8.5-9.5 wt% Al using a pin-on-disc machine at a sliding speed of 0.62 m/s and reported wear rates of about  $5.5 \times 10^{-3}$  and  $6 \times 10^{-3} \text{ mm}^3/\text{m}$  for normal loads of 20 N and 40 N respectively.

Cast *in-situ* Mg-Al/ $\text{Al}_3\text{Ti}$ - $\text{Al}_2\text{O}_3$  and cast *in-situ* Mg-Al/ $\text{Mg}_2\text{Si}$  composites synthesized by addition of cast Al-based composites/ Al-Si master alloy to magnesium resulting in oxides like alumina and/or intermetallics like  $\text{Al}_3\text{Ti}/\text{Mg}_2\text{Si}$  distributed in the matrix of Mg-Al alloy. These additional intermetallics and the oxide particles increase the hardness of the composites considerably compared to cast commercial magnesium and Mg-9 wt% Al alloy, as shown in Tables 5.1 to 5.3. Although the porosity content in the cast commercial magnesium and Mg-9 wt% Al alloy is lower than that in the cast *in-situ* composites as shown in Table 5.1 to 5.3, there is a significant decrease in cumulative volume loss in dry sliding wear as observed in cast *in-situ* composites in Figs. 5.3 and 5.11, compared to those in cast commercial magnesium and cast Mg-9 wt% Al alloy. The lower volume loss in cast *in-situ* composites is primarily attributed to lowering of real area of contact caused by *in-situ* formed reinforcing particles or intermetallics. The cumulative volume loss in dry sliding wear

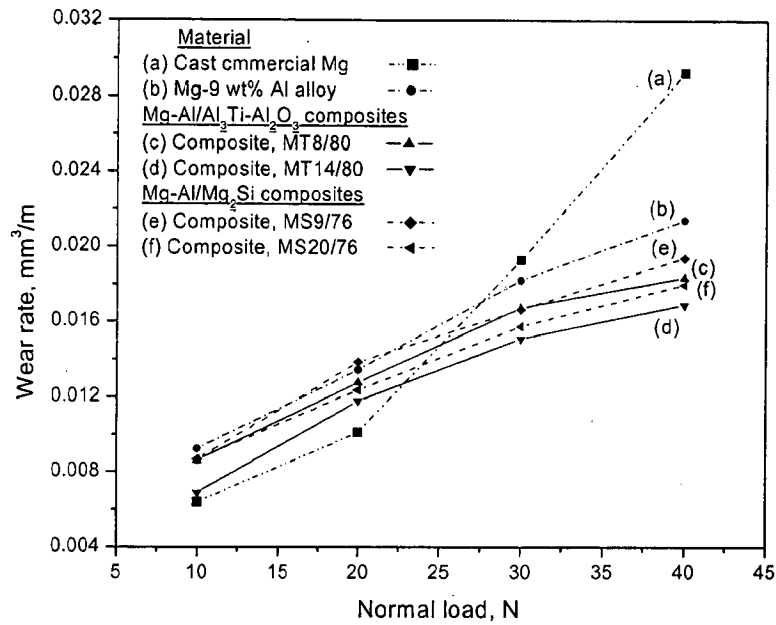


**Fig. 5.29:** Comparison of wear rates with increasing load between cast *in-situ* Mg-Al/Al<sub>3</sub>Ti-Al<sub>2</sub>O<sub>3</sub> composites designated by (c) MT8/80 and (d) MT14/80 and cast *in-situ* Mg-Al/Mg<sub>2</sub>Si composites designated by (e) MS9/76 and (f) MS20/76, along with those of (a) cast commercial Mg and cast Mg-9 wt% Al alloy.

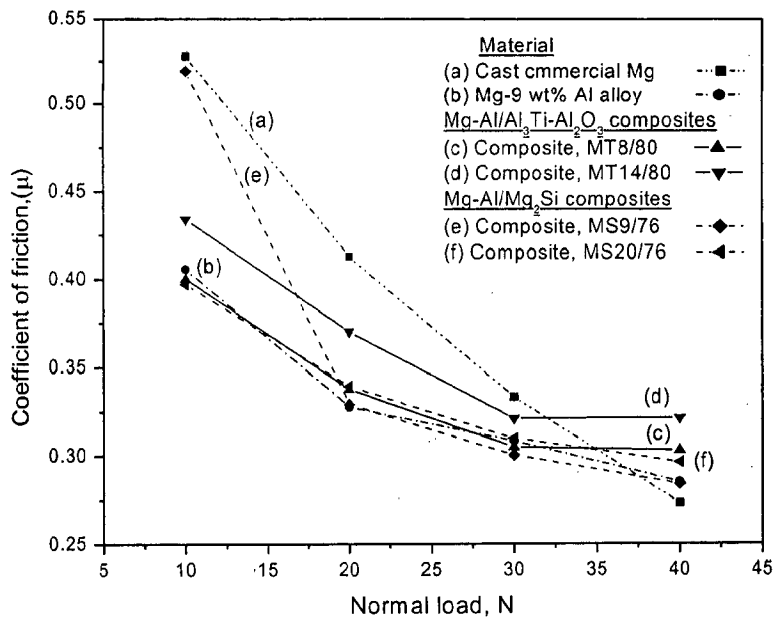


**Fig. 5.30:** Comparison of coefficient of friction with increasing load between cast *in-situ* Mg-Al/Al<sub>3</sub>Ti-Al<sub>2</sub>O<sub>3</sub> composites, designated by (c) MT8/80 and (d) MT14/80, and cast *in-situ* Mg-Al/Mg<sub>2</sub>Si composites, designated by (e) MS9/76 and (f) MS20/76, along with those of (a) cast commercial Mg and cast Mg-9 wt% Al alloy.

increases linearly with sliding distance in both the types of composites as shown in Fig. 5.1 and 5.10 respectively for different amounts of TiO<sub>2</sub> particles/silicon particles. The observed wear behaviour in both the composites agrees well with Archard's equation.

The variation of wear rate with load is fairly linear initially but at higher loads the rate of increase with load slows down in both the types of composites as shown in Figs. 5.5 and 5.13 respectively. The wear rate of cast *in-situ* composites is considerably lower at higher loads of 30 N and beyond, compared to those observed in the cast commercial magnesium and cast Mg-9 wt% Al alloy as shown in Fig. 5.4 and 5.12. But at loads below 20 N, cast commercial magnesium has a wear rate lower than that of the composite but it starts rising beyond 20 N more rapidly than either the composites or the Mg-Al alloy. Also, it is observed from Fig. 5.4 and 5.12 that at loads of 30 N and beyond, the differences in wear rate between the cast *in-situ* composites and cast commercial magnesium or cast Mg-9 wt% Al alloy increases with increasing normal load. For sliding speed, 1 m/s, the wear rates of cast *in-situ* Mg-Al/Al<sub>3</sub>Ti-Al<sub>2</sub>O<sub>3</sub> composite designated as MT14/80, cast *in-situ* Mg-Al/Mg<sub>2</sub>Si composite designated as MS20/76, cast Mg-9 wt% Al alloy and cast commercial magnesium are  $17 \times 10^{-3}$ ,  $18 \times 10^{-3}$ ,  $22 \times 10^{-3}$  and  $30 \times 10^{-3}$  mm<sup>3</sup>/m respectively at normal load, 40 N and  $7 \times 10^{-3}$ ,  $8 \times 10^{-3}$ ,  $9 \times 10^{-3}$  and  $6 \times 10^{-3}$  mm<sup>3</sup>/m respectively at normal load, 10 N. Lim et al. (2005) have reported the wear rates about  $11 \times 10^{-3}$ ,  $10 \times 10^{-3}$  and  $9 \times 10^{-3}$  mm<sup>3</sup>/m respectively in their *ex-situ* composites, magnesium reinforced with 0.22 vol%, 0.66 vol% and 1.11 vol% nano-sized alumina particles during dry sliding against a tool steel disc for normal load of 10 N and sliding speed of 1 m/s. Lim et al. (2003) have also conducted wear tests on *ex-situ* composite of Mg-9wt% Al reinforced with 8 vol% SiC<sub>p</sub>, for two normal loads, 10 and 30 N using pin-on-disc machine and reported wear rates of about  $4 \times 10^{-3}$  and  $10 \times 10^{-3}$  mm<sup>3</sup>/m respectively at the sliding speed of 1 m/s.

The nature of the wear debris has been confirmed to be oxidative primarily although there are some metallic particles which could have resulted due to ploughing by asperities of counterface and three body wear due to entrapped hard particles of reinforcement between the sliding surfaces, as evident from XRD and optical micrographs shown in Figs. 5.24 and 5.25 respectively. There are often chip like long metallic fragments in the debris of the composite indicating the role of micro-cutting by hard oxide particles in the composite which has brought back the peaks of matrix alloy in XRD of wear debris from composites. The oxide debris generated during oxidative wear under dry sliding may have two contradictory roles. They may get locked between the sliding surfaces and promote three body wear, which should enhance volume loss in wear. These oxide particles in the debris may get compacted to form a protective transfer layer, so hard that there are no scoring marks on it. The

relatively brighter compacted oxide transfer layer could be observed in the SEM micrograph of worn pin surfaces of the cast *in-situ* composites in Figs. 5.27 and 5.28. It has also been observed that the extent of transfer layer increases with increasing load but at higher loads of 40 N the extent of transfer layer appear to decrease and it could be attributed to flow of matrix over oxides during dry sliding to cover the particles at higher load of 40 N.

Generally, the cast particulate composites have considerable porosity along with reinforcement. The influence of porosity content on dry sliding wear has been studied by grouping the *in-situ* composites according to reinforcement varying over limited ranges. Accordingly, three groups of cast *in-situ* Mg-Al/Al<sub>3</sub>Ti-Al<sub>2</sub>O<sub>3</sub> composites containing reinforcement in the limited ranges of (a)  $1.55 \pm 0.2$  wt%, (b)  $1.98 \pm 0.2$  wt% and (c)  $2.52 \pm 0.26$  wt%, have been considered and the results as observed in Figs. 5.6(a) to (c), show that the wear rate does not vary significantly with porosity in the range of porosity investigated here. However, there may be a very slow increase in wear rate as it appears in some of the curves shown. Similarly, two groups of cast *in-situ* Mg-Al/Mg<sub>2</sub>Si composites, containing varying reinforcement in the limited ranges, (a)  $2.4 \pm 0.04$  vol% and (b)  $4.64 \pm 0.52$  vol% have been considered and the results as observed in Figs. 5.14(a) and (b), show that wear rate is increasing very slowly with increasing porosity. The decreasing wear rate with porosity content may be attributed to decreasing hardness but the porosity content in these materials are not yet so high as to affect its integrity and contribute to widespread delamination.

The influence of reinforcement on dry sliding wear has been studied by grouping the *in-situ* composites according to porosity content varying over limited ranges. Accordingly, three groups of cast *in-situ* Mg-Al/Al<sub>3</sub>Ti-Al<sub>2</sub>O<sub>3</sub> composites containing porosity in the limited ranges of (a)  $0.8 \pm 0.2$  vol%, (b)  $1.2 \pm 0.2$  vol% and  $1.6 \pm 0.2$  vol%, have been considered and the results as observed in Figs. 5.7(a) to (c) show that wear rate decreases continuously but slowly with increasing reinforcement for all the loads investigated here. Similarly, two groups of cast *in-situ* Mg-Al/Mg<sub>2</sub>Si composites, containing porosity in the limited ranges of (a)  $0.8 \pm 0.3$  vol% and (b)  $1.83 \pm 0.3$  vol% have been considered and the results as observed in Figs. 5.15(a) and (b) show that the wear rate decreases only slightly with increasing reinforcement, particularly for higher volume fraction of reinforcement, for all the loads investigated here. The decreasing wear rate with increasing particle content may be attributed again to increased hardness of the composites with higher particle content and the reinforcements may also contribute to increased cover of transfer layer which could not be established due to limited variation of particle content.

The wear coefficient has been calculated by multiplying the slope of the variation of wear rate with normal load by the hardness ( $H$ ) of the specimen and it decreases a little with



increasing porosity content for three groups of cast *in-situ* Mg-Al/Al<sub>3</sub>Ti-Al<sub>2</sub>O<sub>3</sub> composites containing reinforcement in the limited ranges of (a)  $1.55 \pm 0.2$  wt%, (b)  $1.98 \pm 0.2$  wt% and (c)  $2.52 \pm 0.26$  wt%, particularly beyond 1.2 vol% porosity as observed in Figs. 5.8(a), (b) and (c). The influence of porosity content on wear coefficient of two groups of cast *in-situ* Mg-Al/Mg<sub>2</sub>Si composites containing reinforcement, Mg<sub>2</sub>Si, over limited ranges of (a)  $2.4 \pm 0.04$  vol% and (b)  $4.64 \pm 0.52$  vol% are shown respectively in Figs. 5.16(a) and (b). In group (a), where the particle content is relatively lower than that in group (b) of cast *in-situ* composites, the wear coefficient decreases gradually from  $2.408 \times 10^{-4}$  to  $2.297 \times 10^{-4}$  with increasing porosity over the entire range of porosity content investigated, as observed in Fig. 5.16(a). For group (b) of cast *in-situ* composites, the wear coefficient decreases with increasing porosity from  $2.637 \times 10^{-4}$  to  $2.399 \times 10^{-4}$  in the porosity range investigated, as shown in Fig. 5.16(b).

The wear coefficient for three groups of cast *in-situ* Mg-Al/Al<sub>3</sub>Ti-Al<sub>2</sub>O<sub>3</sub> composites containing porosity in the limited ranges of (a)  $0.8 \pm 0.2$  vol%, (b)  $1.2 \pm 0.2$  vol% and  $1.6 \pm 0.2$  vol%, increases with increasing reinforcement as shown in Figs. 5.9(a), (b) and (c). Increase in the wear coefficient with increasing particle content may be attributed to decreased area of contact, which more than offsets the advantage of lower wear rate with higher particle content. The influence of reinforcement on wear coefficient of two groups of cast *in-situ* Mg-Al/Mg<sub>2</sub>Si composites containing porosity varying over limited ranges between (a)  $0.8 \pm 0.3$  vol% and (b)  $1.8 \pm 0.3$  vol% are shown in Figs. 5.17(a) and (b) respectively. The wear coefficient of cast *in-situ* composites is observed to increase a little with increasing particle content as shown in Figs. 5.17(a) and (b) and the reasons could be as discussed above.

The wear coefficient, which may be considered as the ratio of wear rate and real area of contact, does not reflect the wear resistance of a material. The lowering of both wear rate and real area of contact are good for wear resistance but if real area of contact decreases more compared to decrease in wear rate the wear coefficient will show an increase misleadingly. Similarly, if real area of contact increases more compared to increase in wear rate the material will show a lower wear coefficient.

The friction behaviour in cast *in-situ* Mg-Al/Al<sub>3</sub>Ti-Al<sub>2</sub>O<sub>3</sub> and cast *in-situ* Mg-Al/Mg<sub>2</sub>Si composites have been examined for their friction behaviour determined by variation of coefficient of friction during tests of dry sliding wear under different loads. The friction behaviour in cast commercial magnesium and in Mg-9 wt% Al alloy has also been investigated for comparing these results with those of composites. The variation of the coefficient of friction of cast unreinforced commercial magnesium and cast Mg-9 wt% Al base alloy with sliding distance at different normal load and a constant sliding speed of 1 m/s, is

shown in Figs. 5.19(a) and (b). At all normal loads for cast commercial magnesium, the coefficient of friction fluctuates rapidly with sliding distance which may be attributed to the dynamic nature of contact. Average coefficients of friction of 0.53 and 0.273 have been observed respectively for the lowest load of 10 N and the highest normal load of 40 N, shown in Figs. 5.21 and 5.29. The average coefficient of friction increases with increasing load. In case of cast Mg-9 wt% Al alloy relatively higher fluctuations in coefficient of friction with sliding distance are observed only for the lowest normal load of 10 N and to some extent for the next lowest normal load of 20 N but for higher normal loads, the fluctuations about the mean coefficient of friction is within a small range as shown in Fig. 5.19(b). The average coefficient of friction is significantly lower than that of cast commercial magnesium at a load of 10 N and it decreases with increasing load to become similar to that of magnesium at higher loads as shown in Fig. 5.21. At higher normal load of 40 N, the average coefficient of friction in the alloy is about 0.3 which is similar to the values observed by Balu and Waluk (2000). They have reported that the average sliding friction coefficients in the range of 0.2 to 0.35 against the counterface of stainless steel type 440C, in both unidirectional and reciprocating sliding motion, for magnesium alloy, AZ91D produced by two methods - die casting and thixo-molding. The higher average coefficient of friction in cast commercial magnesium compared to that in alloy at lower load is because of larger area under junction with the counterface requiring larger force to disengage compared to the area under junction in the alloy, in spite of the higher shear strength of the alloy.

The variation of coefficient of friction with sliding distance at different normal loads at a constant sliding speed of 1 m/s, for different cast *in-situ* Mg-Al/Al<sub>3</sub>Ti-Al<sub>2</sub>O<sub>3</sub> composites is shown respectively in Figs. 5.18(a) to (f); (a) MT8/80, (b) MT10/80, (c) MT12/80, (d) MT14/80, (e) MT12/75 and (f) MT12/85. The results are almost similar to those observed in cast Mg-9 wt% Al alloy as shown in Fig. 5.19(b). In cast *in-situ* Mg-Al/Al<sub>3</sub>Ti-Al<sub>2</sub>O<sub>3</sub> composites similar to cast Mg-9 wt% Al alloy, relatively higher fluctuations in coefficient of friction with sliding distance are observed only for the lowest normal load of 10 N and for higher normal loads, the fluctuations about mean coefficient of friction are within a small range. At higher normal load of 40 N, the average coefficient of friction is about 0.3, similar to that in cast Mg-9 wt% Al alloy, for cast *in-situ* composites designated as MT8/80 and MT10/80 which are containing relatively lower amount of particles. For cast *in-situ* composites designated as MT12/80, MT14/80, MT12/75 and MT12/85 which are containing relatively higher amount of particles, it is about 0.32. Increasing particles in case of cast *in-situ* composites designated as MT12/80, MT14/80, MT12/75 and MT12/85 could be responsible for the observed lowering of coefficient of friction in these materials because of relatively weaker junctions

made by the counterface particularly with the oxide particles. Also, a higher hardness results in relatively lower area under junction. The variation of average coefficient of friction with increasing load, for different cast *in-situ* composites designated as MT8/80, MT10/80, MT12/80, MT14/80, MT12/75 and MT12/85 is shown in Fig. 5.20, where it is observed that the average coefficient of friction decreases with increasing normal load and it appears to decrease relatively faster at lower loads than at higher loads. At higher load, the real area of contact increases but higher energy dissipation results in increased temperature, which decreases the strength of the junction at contact. Also, there is relatively higher cover of transfer layer which is oxidative and so, creates weaker junctions. Thus, there is lower coefficient of friction at higher load.

The variation of coefficient of friction with sliding distance at different normal loads and a constant sliding speed of 1 m/s, for cast *in-situ* Mg-Al/Mg<sub>2</sub>Si composite are shown respectively in Figs. 5.22 (a) to (e); (a) MS9/76, (b) MS15/76, (c) MS20/76, (d) MS15/72 and (e) MS15/80. The variation of coefficient of friction with sliding distance observed in cast *in-situ* composites is approximately similar to that of cast Mg-9 wt% Al alloy. In case of cast *in-situ* composites and cast Mg-9 wt% Al alloy relatively higher fluctuations in coefficient of friction with sliding distance are observed only at the lowest normal load of 10 N, particularly for *in-situ* composites designated as MS9/76, which contains comparatively lower volume fraction of reinforcement (Mg<sub>2</sub>Si) but at higher normal loads, the fluctuations about mean coefficient of friction are too small. At higher normal loads, similar to cast Mg-9 wt% Al alloy, the average coefficient of friction in cast *in-situ* composites is about 0.3 as shown in Fig. 5.23. There is only a small change in coefficient of friction with increasing reinforcement, Mg<sub>2</sub>Si, for *in-situ* composites. In *in-situ* composites, it is observed that the average coefficient of friction decreases with increasing normal load similar to that observed in cast Mg-9 wt% Al base alloy and it appears to decrease relatively faster at lower loads than at higher loads as seen in Fig. 5.23 and 5.30. Thus, it appears that the intermetallic Mg<sub>2</sub>Si does not make significant difference in coefficient of friction compared to that alloy because the gain due to lower area under junction with the counterface due to higher hardness appears to be compensated by enhanced shear strength of the composite.

Therefore, the present study clearly reveals the potential of low cost cast *in-situ* Mg-Al/Al<sub>3</sub>Ti-Al<sub>2</sub>O<sub>3</sub> and cast *in-situ* Mg-Al/Mg<sub>2</sub>Si composites synthesized using cast Al-based composites/Ai-Si master alloys as candidate tribological materials for engineering applications.

Cast *in-situ* Mg-Al/Al<sub>3</sub>Ti-Al<sub>2</sub>O<sub>3</sub> and Mg-Al/Mg<sub>2</sub>Si composites have been synthesized by two stage solidification processing. In the first stage, cast aluminium based composite/Al-Si master alloy has been synthesized by dispersing TiO<sub>2</sub>/Si particles into the molten aluminium. In the second stage, the aluminium based composite/Al-Si alloy has been dissolved in molten magnesium to the extent that the matrix alloy of the composite has 9 wt% aluminium. The influences of different key processing parameters like processing temperature and amount of TiO<sub>2</sub>/Si particles added on the microstructure of the resulting cast magnesium based *in-situ* composite including distribution of reinforcing particles and porosity along the height of cast ingot and the mechanical properties have been studied. The tribological behaviour of these cast magnesium based *in-situ* composites has been investigated and compared with those of cast unreinforced commercial magnesium and cast unreinforced Mg-9 wt% Al alloy processed similarly as the cast composites. The influences of the amount of both *in-situ* formed reinforcing phases and porosity on the wear and friction behaviour of cast magnesium based *in-situ* composites are evaluated. The results and discussion have been presented in two segments: (i) processing, microstructural studies and mechanical properties of cast magnesium based *in-situ* composites and (ii) tribological behaviour of cast magnesium based *in-situ* composites. The conclusions of the present study are outlined below for each segment of study.

### 6.1 Processing, Microstructural Studies and Mechanical Properties of Cast *In-Situ* Composites

#### (a) Cast *in-situ* Mg-Al/Al<sub>3</sub>Ti-Al<sub>2</sub>O<sub>3</sub> Composites

1. XRD patterns of the powders of Mg-Al/Al<sub>3</sub>Ti-Al<sub>2</sub>O<sub>3</sub> composite and the particles extracted by partially and fully dissolving the matrix indicate the presence of Al<sub>3</sub>Ti and *in-situ* generated finer reinforcing alumina particles inherited from the aluminium based composite dissolved in the magnesium melt. Existence of oxides and mixed compounds of oxides like MgO, MgAl<sub>2</sub>O<sub>4</sub> and Al<sub>2</sub>TiO<sub>5</sub> are also observed at interfaces which are generally helpful in incorporating the alumina particles in the melt. Existence

of Al<sub>3</sub>Ti and alumina has been further confirmed and identified in the microstructures of *in-situ* composite through EDS analysis at points, along a line scan and by X-ray mapping. Distribution of Al<sub>3</sub>Ti in the *in-situ* composites is fairly uniform.

2. In the cast *in-situ* composites, the intermetallic, Al<sub>3</sub>Ti, occurs in rod shape with an aspect ratio of about nine. Alumina particles are small and nearly spherical with maximum size up to 2 μm.
3. In the cast magnesium based *in-situ* composites, relatively lower porosities, higher volume fraction of intermetallics and the extracted particles are observed at the bottom than at the top of cast ingots. It may be due to gravity segregation due to settling of intermetallics, being heavier than the matrix alloy. Densities of Al<sub>3</sub>Ti, extracted particles and matrix alloy are respectively 3.3, 3.26 and 1.79 g/cm<sup>3</sup>.
4. Increasing addition of TiO<sub>2</sub> in aluminium based composite results in increasing volume fraction of *in-situ* formed reinforcing intermetallic and particle content in magnesium based composite, but Al<sub>3</sub>Ti rods generally becomes thicker without increasing their number significantly.
5. In the magnesium based cast *in-situ* composites, Brinell hardness decreases gradually along the height of cast ingot from the bottom to top, which may be due to combined effect of decreasing volume fraction of reinforcing intermetallics and particle content, and increasing porosity along the height of cast ingot from the bottom.
6. In the cast magnesium based *in-situ* composite, the hardness improves significantly compared to those observed in the unreinforced cast Mg-9 wt% Al alloy and unreinforced cast commercial magnesium, by factors of about 1.4 and 2 respectively. The hardness of the unreinforced cast Mg-9 wt% Al alloy and unreinforced cast commercial magnesium are similar to those reported in the literature.
7. Brinell hardness in the middle height segment of the cast ingot of magnesium based *in-situ* composites decreases gradually with increasing processing temperature, primarily due to increasing porosity.
8. In the cast magnesium based *in-situ* composites, Brinell hardness increases with increasing volume fraction of reinforcing intermetallics, Al<sub>3</sub>Ti, and particle content.
9. In the cast magnesium based *in-situ* composites, comparatively better tensile properties (ultimate tensile strength and percentage elongation) are observed at the bottom than that at the top of cast ingots, where particle content is relatively less and porosity is more.

10. In the magnesium based *in-situ* composites, the ultimate tensile strength increases with increasing processing temperature, but the percentage elongation decreases slightly with increasing processing temperature.
11. Both of the tensile properties, ultimate tensile strength and percentage elongation, decreases with increasing porosity in the cast magnesium based *in-situ* composites, and are relatively lower than those obtained in Mg-9 wt% Al alloy. It may be due to inadequate strength of interfacial bonding between intermetallics, Al<sub>3</sub>Ti and the matrix.
12. The fractured surfaces of the tensile specimens of cast *in-situ* Mg-Al/Al<sub>3</sub>Ti-Al<sub>2</sub>O<sub>3</sub> composites revealed the evidence of mixed-mode failure involving primarily brittle and partially ductile fracture.
13. The tensile properties, ultimate tensile strength and percentage elongation, in the magnesium based *in-situ* composites extrapolated to zero porosity, decreases with increasing particle content.

**(b) Cast *in-situ* Mg-Al/Mg<sub>2</sub>Si Composites**

14. XRD patterns of the powders of cast *in-situ* Mg-Al/Mg<sub>2</sub>Si composite and Al-Si alloy indicate complete reaction of silicon with magnesium for *in-situ* formation of intermetallic reinforcement, Mg<sub>2</sub>Si. Further existence of Mg<sub>2</sub>Si is confirmed in the microstructures of *in-situ* composite through EDS analysis. Distribution of Mg<sub>2</sub>Si in the *in-situ* composites is fairly uniform.
15. In the cast *in-situ* Mg-Al/Mg<sub>2</sub>Si composites, the intermetallic, Mg<sub>2</sub>Si, occurs in blocky shapes with an average size of about 20 μm.
16. In the cast *in-situ* composites, relatively lower porosities, higher volume fraction of intermetallics and the extracted particles are observed at the bottom of cast ingots than at the top. It may be due to gravity segregation due to settling of intermetallics, being heavier than the matrix alloy. Densities of Mg<sub>2</sub>Si, and matrix alloy are respectively 1.99 and 1.79 g/cm<sup>3</sup>.
17. In cast *in-situ* Mg-Al/Mg<sub>2</sub>Si composites, the volume fraction of Mg<sub>2</sub>Si and the porosity increases with increasing addition of silicon through Al-Si alloy.

18. In the cast magnesium based *in-situ* composites, Brinell hardness decreases gradually along the height of cast ingot from the bottom to top, which may be due to combined effect of decreasing volume fraction of the intermetallic,  $Mg_2Si$ , content and increasing porosity along the height of cast ingot from the bottom to the top.
19. There is a significant improvement in hardness in cast *in-situ* composites compared to those observed in unreinforced cast Mg-9 wt% Al alloy and unreinforced cast commercial magnesium by factors about 1.4 and 2 respectively.
20. Brinell hardness in the middle height segment of the cast ingot of magnesium based *in-situ* composites increases slightly with increasing processing temperature, however, at higher processing temperatures it decreases, which may be attributed to higher porosities.
21. In the cast *in-situ* composites, Brinell hardness increases with increasing volume fraction of reinforcing intermetallics,  $Mg_2Si$ .
22. In the cast *in-situ* composites, comparatively better tensile properties (ultimate tensile strength and percentage elongation) are observed at the bottom than those at the top of cast ingots where particle content is relatively less and porosity is more.
23. In the cast *in-situ* composites, both the tensile properties, ultimate tensile strength and percentage elongation increases initially but decreases at higher processing temperatures, which might be due to higher porosity content at higher processing temperatures.
24. Both of tensile properties, ultimate tensile strength and percentage elongation, decrease with increasing porosity in the cast *in-situ* composites. Lower tensile properties are obtained in the cast *in-situ* composites compared to Mg-9 wt% Al alloy. It may be due to inadequate interfacial bond strength between intermetallic,  $Mg_2Si$  and matrix.
25. The fractured surfaces of the tensile specimens of cast *in-situ* Mg-Al/ $Mg_2Si$  composite revealed the evidence of mixed-mode failure involving primarily brittle and partially ductile fracture.
26. The tensile properties, ultimate tensile strength and percentage elongation, in the *in-situ* composites extrapolated to zero porosity, decreases with increasing volume fraction of reinforcement,  $Mg_2Si$ .

## 6.2 Tribological Behaviour of Cast *In-Situ* Mg-Al/Al<sub>3</sub>Ti-Al<sub>2</sub>O<sub>3</sub> and Mg-Al/Mg<sub>2</sub>Si Composites

27. In both the cast magnesium based *in-situ* composites as well as in cast Mg-9 wt% Al alloy and commercial magnesium, the cumulative volume loss increases linearly with increasing sliding distance at a given normal load between 10N to 40N, following Archard's law.
28. In both of the cast *in-situ* composites, the cumulative volume loss and wear rate decreases considerably, particularly at higher loads, compared to those observed in Mg-9 wt% Al alloy and cast commercial magnesium. The wear rates obtained in the unreinforced cast Mg-9 wt% Al alloy and unreinforced cast commercial magnesium are matching with the data given in the literature.
29. In cast commercial magnesium, the wear rate initially increases gradually with increasing normal load till 20N but at higher loads it increases linearly with a higher slope. In Mg-9 wt% Al alloy, the wear rate increases linearly with increasing normal load. In both the types of cast magnesium based *in-situ* composites, the wear rate increases linearly with increasing normal load but at higher normal loads, the wear rate deviates from the line towards a lower value, showing non-linear behaviour.
30. In cast *in-situ* Mg-Al/Al<sub>3</sub>Ti-Al<sub>2</sub>O<sub>3</sub> composites of similar but lower particle contents, the wear rate increases gradually with porosity. Similarly, in cast *in-situ* Mg-Al/Mg<sub>2</sub>Si composites having similar particle contents, the wear rate of *in-situ* composite increases with increasing volume fraction of porosity due to its combined effect on the real area of contact and on delamination by the subsurface crack propagation.
31. The wear coefficients in both types of composites are observed to increase with increasing particle content but decrease with increasing porosity, at least in certain ranges, contrary to expectations because of the inherent weakness of wear coefficient as decreasing wear rate may lead to higher wear coefficient if real area of contact decreases relatively more and vice-versa. Thus, wear coefficient is not a discriminating parameter to characterize wear resistance.
32. In both the cast *in-situ* composites containing similar porosity content, the wear rate decreases gradually with increasing reinforcing phase whereas the wear coefficient increases with increasing reinforcing phase, presumably due to influence of lower real area of contact.



33. In both type of cast *in-situ* magnesium based composites and Mg-9 wt% Al alloy, there are large fluctuations in the coefficient of friction during sliding at the lowest load, 10 N, where as large fluctuations in the coefficient of friction are observed at all the normal loads for cast commercial magnesium. This has been attributed to dynamic nature of the contact.
34. In cast *in-situ* Mg-Al/Al<sub>3</sub>Ti-Al<sub>2</sub>O<sub>3</sub> composites, the average value of coefficient of friction is slightly higher than those observed in cast Mg-9 wt% Al alloy whereas for cast *in-situ* Mg-Al/Mg<sub>2</sub>Si composites, it is similar to those observed in cast Mg-9 wt% Al alloy.
35. The coefficient of friction decreases with increasing normal load in both of cast *in-situ* magnesium based composites and Mg-9 wt% Al alloy and it decreases at a higher rate for lower loads than that at higher normal loads. This may be attributed to higher temperature at contact decreasing the shear force required to disengage and also, to a higher cover of transfer layer on the sliding surface.
36. From the examination of the worn surfaces of wear specimens and the debris, oxidative as well as abrasive wear mechanisms are observed operate during dry sliding of both the types of cast *in-situ* composites against the counterface of EN32 hardened steel, in the load range from 10 N to 40 N.

**Table A-1:** Mechanical properties, density and porosity content at the bottom, middle and top height segments of cast Mg-9 wt% Al alloy and commercial magnesium.

Material	Location in ingot	Tensile strength (MPa)	Percentage elongation (%)	Brinell hardness (MPa)	Density (g/cm <sup>3</sup> )	Porosity (vol%)
Cast commercial Magnesium	Bottom	156 ± 6	17.53 ± 0.32	439 ± 9	1.738	0.1
	Middle	149 ± 1	17.16 ± 0.04	431 ± 17	1.737	0.2
	Top	143 ± 6	12.84 ± 0.37	423 ± 14	1.736	0.3
Cast Mg-9 wt% Al alloy	Bottom	215 ± 10	9.63 ± 1.44	615 ± 8	1.792	0.3
	Middle	192 ± 10	9.32 ± 0.87	607 ± 12	1.788	0.6
	Top	190 ± 9	7.23 ± 0.87	594 ± 17	1.786	0.7

**Table A-2:** Mechanical properties, density, porosity and reinforcement content at the bottom, middle and top height segments of cast *in-situ* Mg-Al/Al<sub>3</sub>Ti-Al<sub>2</sub>O<sub>3</sub> composites.

<i>In-situ</i> composite	Location in ingot	Tensile strength (MPa)	Percentage elongation (%)	Brinell hardness (MPa)	Density (g/cm <sup>3</sup> )	Porosity (vol%)	Reinforcement	
							Intermetallics (vol%)	Particles (wt%)
MT8/80	Bottom	185 ± 11	5.38 ± 0.6	718 ± 8	1.817	0.7	0.84 ± 0.28	1.45
	Middle	171 ± 6	4.62 ± 0.18	707 ± 21	1.815	0.9	0.80 ± 0.29	1.35
	Top	162 ± 7	4.43 ± 0.15	686 ± 16	1.814	1.4	0.73 ± 0.3	1.35
MT10/80	Bottom	139 ± 2	2.65 ± 0.11	796 ± 8	1.821	1.3	1.18 ± 0.35	1.72
	Middle	131 ± 1	2.66 ± 0.04	781 ± 11	1.819	1.8	1.12 ± 0.36	1.70
	Top	116 ± 2	2.45 ± 0.11	774 ± 27	1.817	2.4	1.10 ± 0.36	1.64
MT12/80	Bottom	142 ± 9	2.63 ± 0.26	824 ± 16	1.838	0.9	1.94 ± 0.36	2.51
	Middle	140 ± 4	2.84 ± 0.07	798 ± 25	1.834	1.1	1.46 ± 0.47	2.10
	Top	135 ± 9	2.51 ± 0.25	782 ± 21	1.832	1.6	1.30 ± 0.39	2.05
MT14/80	Bottom	155 ± 2	2.72 ± 0.04	892 ± 23	1.850	0.7	2.22 ± 0.56	2.78
	Middle	155 ± 7	2.78 ± 0.19	857 ± 26	1.847	1.0	2.14 ± 0.43	2.45
	Top	143 ± 3	2.39 ± 0.04	833 ± 22	1.845	1.4	1.82 ± 0.44	2.38
MT12/75	Bottom	138 ± 3	2.78 ± 0.07	837 ± 16	1.838	0.7	1.74 ± 0.4	2.51
	Middle	136 ± 3	2.86 ± 0.03	803 ± 21	1.834	1.1	1.26 ± 0.36	2.18
	Top	135 ± 8	2.80 ± 0.34	789 ± 24	1.831	1.4	1.22 ± 0.41	1.88
MT12/85	Bottom	147 ± 6	3.31 ± 0.26	817 ± 12	1.838	0.6	1.50 ± 0.41	2.50
	Middle	142 ± 3	2.83 ± 0.13	787 ± 17	1.835	0.9	1.44 ± 0.38	2.26
	Top	139 ± 1	3.08 ± 0.22	774 ± 16	1.832	1.4	1.34 ± 0.42	1.98

**Table A-3:** Mechanical properties, density, porosity and reinforcement content at the bottom, middle and top height segments of cast *in-situ* Mg-Al/ Mg<sub>2</sub>Si composites.

<i>In-situ</i> composite	Location in ingot	Tensile strength (MPa)	Percentage elongation (%)	Brinell hardness (MPa)	Density (g/cm <sup>3</sup> )	Porosity (vol%)	Reinforcement (vol%)
MS9/76	Bottom	199 ± 3	5.30 ± 0.64	743 ± 11	1.790	0.6	2.43 ± 0.43
	Middle	197 ± 2	5.18 ± 0.01	726 ± 24	1.785	0.9	2.42 ± 0.74
	Top	194 ± 10	5.05 ± 0.2	711 ± 21	1.781	1.1	2.36 ± 0.47
MS15/76	Bottom	174 ± 7	3.95 ± 0.12	822 ± 12	1.797	0.8	5.16 ± 0.65
	Middle	174 ± 10	4.27 ± 0.22	810 ± 22	1.792	1.0	4.80 ± 0.54
	Top	168 ± 1	3.70 ± 0.08	791 ± 19	1.783	1.5	4.68 ± 0.68
MS20/76	Middle	163 ± 2	3.26 ± 0.16	839 ± 11	1.795	1.7	6.54 ± 0.76
	Top	129 ± 6	2.75 ± 0.13	812 ± 22	1.763	2.6	6.40 ± 0.71
	Bottom	152 ± 4	3.07 ± 0.07	804 ± 13	1.784	1.4	3.90 ± 0.55
MS15/72	Middle	143 ± 6	3.90 ± 0.26	794 ± 18	1.775	2.0	3.94 ± 0.54
	Top	142 ± 11	2.69 ± 0.19	784 ± 13	1.769	2.3	4.12 ± 0.57
	Bottom	168 ± 9	3.73 ± 0.18	798 ± 12	1.793	1.0	4.72 ± 0.62
MS15/80	Middle	165 ± 13	3.33 ± 0.37	785 ± 11	1.776	1.9	4.52 ± 0.74
	Top	150 ± 3	3.48 ± 0.04	776 ± 8	1.771	2.2	4.36 ± 0.77

## REFERENCES

---

---

1. Abdulhaqq, A.H., (2005), Ph.D. Thesis, "Aluminium Based *In-situ* Composites – Synthesis, Mechanical and Tribological Properties", Indian Institute of Technology Roorkee, Roorkee, India.
2. Abdulhaqq, A.H., Ghosh, P. K., Jain, S.C., Ray, S., (2005), "Processing, Microstructure, and Mechanical Properties of Cast In-Situ Al(Mg,Mn)-Al<sub>2</sub>O<sub>3</sub>(MnO<sub>2</sub>) Composite", *Metall. and Mater. Trans.*, Vol. 36A, p. 2211.
3. Abdulhaqq, A.H., Ghosh, P. K., Jain, S.C., Ray, S., (2006), "Processing, Microstructure, and Mechanical Properties of Cast In-Situ Al(Mg,Ti)-Al<sub>2</sub>O<sub>3</sub>(TiO<sub>2</sub>) Composite", *Metall. and Mater. Trans.*, Vol. 37A, p. 469.
4. Aikin, Jr., R. M., (1997), "The Mechanical Properties of In-Situ Composites", *JOM*, Vol. 49, No. 8, pp. 35-39.
5. Alpas, A. T. and Embury, J. D., (1990), "Sliding and Abrasive Wear Behaviour of an Aluminium 2014-SiCp Reinforced Composite", *Scr. Metall.*, Vol. 24, pp. 931-935.
6. Alpas, A. T. and Zhang, J., (1992 A), "Wear Rate Transition in cast Aluminium-Silicon Alloys Reinforced with SiC Particles", *Scr. Metall.*, Vol. 26, pp. 505-509.
7. Alpas, A. T. and Zhang, J., (1992 B), "Effect of SiC Particle Reinforcement on the Dry Sliding Wear of Aluminium-Silicon Alloys (A356)", *Wear*, Vol. 155, pp. 83-104.
8. Alpas, A. T. and Zhang, J., (1993), "Wear Regimes and Transitions in Al<sub>2</sub>O<sub>3</sub> Particulate Reinforced Aluminium Alloys", *Mater. Sci. Engg.*, Vol. A161, pp. 273-284.
9. Alpas, A.T. and Zhang J., (1994), "Effect of Microstructure (Particulate Size and Volume Fraction) and Counterface Materials on the Sliding Wear Resistance of Particulate-Reinforced Aluminum Matrix Composites", *Metall. Mater. Trans. A*, Vol. 25A, pp. 969-983.
10. Anand, K. and Kishore, (1983), "On the Wear of Aluminium-Corundum Composites", *Wear*, Vol. 85, pp. 163-169.
11. Archard, J. F., (1980), "Wear Theory and Mechanisms", *Wear Control Hand Book*, Edited by Peterson, M. B. and Winer, W. O., ASME, NY, pp. 35-79.
12. ASM Handbook, (1990), Properties and selection: non-ferrous alloys and special-purpose materials, Vol. 2, p.1134, *ASM International*, Ohio, USA.
13. ASM Handbook, Vol. 15, (1992), *ASM International, Materials Park*, Ohio 44073-0002, pp. 798-810.

14. Aune T. Kr., (1995), "Magnesium Die Casting-Alloys and Properties", *IMA Automotive Seminar*, Frankfurt, October.
15. Badia, F. A. and Rohatgi, P. K., (1969), *Trans. AFS*, Vol. 79, pp. 346-354.
16. Bansal, S. and Ray, S., (2005), "Applications of Metal Matrix Composites: A Status Report", 53<sup>rd</sup> Indian Foundry Congress, 21-23 January, Kolkata, India, pp. 159-168.
17. Bengisu, M.T. and Akay, A., (1997), "Relation of Dry-Friction to Surface Roughness", *J. of Tribology*, Vol. 119, pp. 18-25.
18. Bhushan, B., and Gupta, B.K., (1991), "Hand Book of Tribology", *McGraw-Hill, Inc.* New York, U.S.A.
19. Bradley, E.F., (1988), "Superalloys: A Technical Guide", *ASM Inter., Metals Park*, Ohio, USA, p. 122.
20. Caracostas, C.A., Chiou, W.A., Fine, M.E., Cheng, H.S., (1992), "Wear mechanisms during lubricated sliding of XD 2024-Al/TiB<sub>2</sub> metal matrix composites against steel", *Scr. Metall. et Mater.*, Vol. 27, pp. 167-172.
21. Caron, S. and Masounave, J., (1990A), "Fabrication of MMCs by a Bottom Mixing Foundry Process", Proc. Conf. in "Fabrication of particulates Reinforced Metal Composites", Edited by Masounave, J. and Hamel, F. G., *Montréal, Québec*, Canada, 17-29 September, pp. 107-112.
22. Caron, S. and Masounave, J., (1990B), "A Literature Review on Fabrication Techniques of Particulate Reinforced Metal Composite", Proc. Conf. in "Fabrication of Particulates Reinforced Metal Composites", Edited by Masounave J. and Hamel, F. G., *Montréal, Québec*, Canada, 17-29 September, pp. 79-86.
23. Carreño-Morelli, E., Cutard, T., Schaller, R., Bonjour, C., (1998), "Processing and characterization of aluminium-based MMCs produced by gas pressure infiltration", *Mater. Sci. and Engg. A*, Vol. 251, pp. 48-57.
24. Cense, W.A., Klerk, M. and Albers, W., (1977), "Aligned in situ growth of fibrous Ni-Nb<sub>2</sub>O<sub>5</sub> composite by preferential internal oxidation", *J. Mater. Sci.*, Vol. 12, pp. 2184-2188.
25. Cherepin, V.K., and Mallik, A.K., (1967) "Experimental techniques in physical metallurgy", *Asia publishing House*, Bombay, India.
26. Choi, Y., Mullins, M.E., Wijayatilleke, K., Lee, J.K., (1992), "Fabrication of metal matrix composites of TiC-Al through self-propagating synthesis reaction", *Metall. Trans. A*, Vol. 23A, pp. 2387-2392.
27. Chrysanthou, A., Erbaccio, G., (1995), "Production of copper-matrix composites by in situ processing", *J. of Mater. Sci.*, Vol. 30, pp. 6339-6344.

28. Chua, B.W. Lu, L., Lai, M.O., (1999), "Influence of SiC particles on mechanical properties of Mg based composite", *Composite Structures*, Vol. 47, pp. 595-601.
29. Daniel, B.S.S., Murthy, V.S.R., Murthy, G.S., (1997), "Metal-ceramic composites via in-situ methods", *J. of Mater. Processing Tech.*, Vol. 68, pp. 132-155.
30. Davies, P.J, (1987), "Development of Cast Aluminium MMCs", *London Scandinavian Metall. Company Limited*, United Kingdom.
31. Davies, P.J., Kellie, J.L.F., Wood, J.V., (1992), U.K. Patent No. 2, 257985A, *ASM*, Paris, September.
32. Davis, J.R., (2003), "ALLOYING: Understanding the basics", *ASM International, Materials Park*, Ohio 44073-0002.
33. Dong, Q., Chen, L.Q., Zhao, M.J., Bi, J., (2004), "Synthesis of TiC<sub>p</sub> reinforced magnesium matrix composites by in situ reactive infiltration process", *Mater. Letters*, Vol. 58, pp. 920-926.
34. Duhl, D.H, (1989), "Single Crystal Superalloys", in J.K. Tien and T. Caulfield (Eds.), *Superalloys, Supercomposites and Superceramics, Mater. Sci. and Tech. series, Academic press*, San Diego, pp. 149-182.
35. Dunand, D.C., Sommer, J.L., Mortensen, A., (1993), "Synthesis of bulk and reinforced nickel aluminides by reactive infiltration" *Metall. Trans. A*, Vol. 24A, pp. 2161-2170.
36. Dvorina, L.A., Popova, O.I. and N. A. Derenovskaya, N.A., (1969), "Preparation and some Chemical Properties of Magnesium Silicide", *Inst. of Mater. Sci., Academy of Sciences of the Ukrainian SSR*. Translated from *Poroshkovaya Metallurgiya*, No. 5, Vol. 77, pp. 29-32.
37. Ebisawa, M. Hara, T., Hayashi, T. and Ushio, H., "Production Process for Metal Matrix Composite (MMC) Engine Block", *SAE Special Paper Series*, 910835.
38. Eyre, T. S., (1976), "Wear Characteristics of Metals", *Tribology International*, vol. 11, pp. 203-212.
39. Feng, C. F. and Froyen, L., (2000), "Formation of Al<sub>3</sub>Ti and Al<sub>2</sub>O<sub>3</sub> from an Al-TiO<sub>2</sub> System for Preparing In-Situ Aluminium Matrix Composites", *Composites; Part A: Applied Sci. and Manf.*, Vol. 31, pp. 385-390.
40. Feng, C.F., Froyen, L., (2000), "Formation of Al<sub>3</sub>Ti and Al<sub>2</sub>O<sub>3</sub> from an Al-TiO<sub>2</sub> system for preparing in-situ aluminium matrix composites", *Composites: Part A*, Vol. 31, pp. 385-390.
41. Foltz, J. V., (1997), "Metal-Matrix Composites", *ASM Handbook*, Edited by Henry, S. D., Vol. 2, pp. 903-912.

42. Friedrich, H., Schumann, S., (2001), "Research for a 'new age of magnesium' in the automotive industry", *J. of Mater. Processing Tech.*, Vol. 117, pp. 276-281.
43. Friedrich, H.E., Mordike, B.L., (2006), "Magnesium Technology", *Springer-Verlag Berlin Heidelberg, Germany*.
44. Fukunaga, H., Wang, X. and Aramaki, Y., (1990), *J. Mater. Sci. Letters.*, Vol. 9, pp. 23-29.
45. Ghosh, P. K. and Ray, S., (1988A), "Fabrication and Properties of Compocast Aluminium-Alumina Particulate Composite", *Indian J. of Technology*, Vol. 26, pp. 83-94.
46. Ghosh, P. K. and Ray, S., (1988B), "A Model Study on the Particle Dispersion and Fluid-Particle Interaction in Slurry of Liquid Alloy and Ceramic Particle", *Trans. JIM.*, Vol. 29, pp. 502-508.
47. Ghosh, P. K. and Ray, S., (1988C), "Particle Dispersion and Fluid-Particle Interaction in a Slurry of Liquid Al-Mg Alloy and Al<sub>2</sub>O<sub>3</sub> Particles", *Trans. JIM*, Vol. 29, pp. 509-519.
48. Ghosh, P. K. and Ray, S., (1988D), "Influence of Process Parameters on the Porosity Content in Al(Mg)-Al<sub>2</sub>O<sub>3</sub> Cast Particulate Composite Produced by Vortex Method", *AFS Trans.*, Vol. 214, pp. 775-781.
49. Ghosh, P. K., (1986), *Ph.D. Thesis*, "Mixing Characteristics and Mechanical Properties of Cast Al(Mg)-Al<sub>2</sub>O<sub>3</sub> Particulate Composite", *University of Roorkee, Roorkee, India*.
50. Ghosh, P. K., Prasad, P. R. and Ray, S., (1984A), "Effect of Porosity on the Strength of Particulate Composites", *Z. Metallkde.*, Vol. 75, pp. 934-939.
51. Ghosh, P. K., Ray, S. and Rohatgi, P. K., (1984B), "Incorporation of Alumina Particles in Aluminium-Magnesium Alloy by Stirring in Melt", *Trans. of JIM*, Vol. 25, No. 6, pp. 440-444.
52. Giessen, B. C., (1985), U. S. Patent No. 4, 540, 546, September, 10.
53. Glasco, F.S., (1967), "Unidirectionally Solidified Eutectics for Optical, electronic and Magnetic Applications", *J. Met.*, Vol. 19, pp. 17-21.
54. Gotman, I., Koczak, M.J., Shtessel, E., (1994), "Fabrication of Al matrix in situ composites via self-propagating synthesis", *Mater. Sci. and Engg. A*, Vol. 187, pp. 189-199.
55. Graham, R.L., Edge, D.A and Moore, D.C., (1970), "Dispersion-hardened copper and chemically prepared powders: Copper and its alloys", *The Institute of Metals, London*.
56. Grant, N.J., (1970), "A Look at Dispersion Strengthening of Powder Metallurgy Methods", in *Progress in Powder Metallurgy*, Vol. 16, *Metal Powder Industries Federation, New York*, p. 99.



57. Gupta, M., Lai, M.O., Saravananathan, D., (2000), "Synthesis, microstructure and properties characterization of disintegrated melt deposited Mg/SiC composites", *J. of Mater. Sci.*, Vol. 35, pp. 2155-2165.
58. Hanumanth, G. S., Irons, G. A. and Lafreniere, S., (1992), "Particle Sedimentation During Processing of Liquid Metal-Matrix Composites", *Metall. Trans.*, Vol. 22B, pp. 753-763.
59. Harnby, N., Edwards, M.F., Nienow, A.W., (1985), "Mixing in the process industries", *Butterworth & Co (Publishers) Ltd.*, pp. 113-118.
60. Hassan, S. F., Gupta, M., (2005), "Development of high performance magnesium nanocomposites using nano-Al<sub>2</sub>O<sub>3</sub> as reinforcement", *Mater. Sci. and Engg. A*, Vol. 392, pp. 163-168.
61. Hassan, S. F., Gupta, M., (2006), "Effect of primary processing on the microstructure, CTE and mechanical properties of magnesium/alumina nano-composites", *Composite Structures*, Vol. 72, pp. 19-26.
62. Hassan, S.F., Gupta, M., (2002), "Development of ductile magnesium composite materials using titanium as reinforcement", *J. of Alloys and Compounds*, Vol. 345, pp. 246-251.
63. Ho, K.F., Gupta, M., Srinivasan, T.S., (2004), "The mechanical behaviour of magnesium alloy AZ91 reinforced with fine copper particulates", *Mater. Sci. and Engg. A*, Vol. 369, pp. 302-308.
64. Hoffman, A.V., and Mantell, C.L., (1966), "Mechanism of co-deposition of alumina with electrolytic copper", *Trans. Metall. Soc. AMIE*, Vol. 236, p. 1015.
65. Holt, J.B., Munir, Z.A., (1986), "Combustion synthesis of titanium carbide: theory and experiment", *J. of Mater. Sci.*, Vol. 21, pp. 251-259.
66. Hosking, F. M., Folgar Portillo, F., Wunderlin, R. and Mehrabian, R., (1982), "Composites of Aluminium Alloys: Fabrication and Wear Behaviour", *J. Mater. Sci.*, Vol. 17, pp. 477-498.
67. How, H. C. and Baker, T. N., (1997), "Dry Sliding Wear Behaviour of Saffil Reinforced A6061 Composites", *Wear*, Vol. 210, pp. 263-272.
68. How, H. C. and Baker, T. N., (1999), "Characterisation of Sliding Friction-Induced Subsurface Deformation of Saffil-Reinforced AA6061 Composites", *Wear*, Vol. 232, pp. 106-115.
69. Huashun, Y., Hongmei, C., Liming, S., and Guanghui, M., (2006), "Preparation of Al-Al<sub>3</sub>Ti in situ composites by direct reaction method", *Rare Metals*, Vol. 25, No. 1, p. 32.
70. Hutchings, I. M., Wilson, S. and Alpas, A. T., (2000), "Wear of Aluminium-based Composites, Comprehensive Composite Materials", *MMCs*, Vol. 3, pp. 501-519.

71. Ibrahim, I. A., Mohamed, F. A. and Lavernia, E. J., (1991), "Particulate Reinforced Metal Matrix Composites – a Review", *J. Mater. Sci.*, Vol. 26, No. 5, pp. 1137-1156.
72. Jangg, G., (1988), in: E. Arzt, L. Schultz, (Eds.), *New Materials by Mechanical Alloying Techniques*, Proceedings of the DGM Conference, Calw-Hirsau, p. 39.
73. Jiang, Q.C., Li, X.L., Wang, H.Y., (2003), "Fabrication of TiC particulate reinforced magnesium matrix composites", *Scr. Mater.*, Vol. 48, pp. 713-717.
74. Jiang, Q.C., Wang, H.Y., Ma, B.X., Wang, Y., Zhao, F., (2005), "Fabrication of B<sub>4</sub>C particulate reinforced magnesium matrix composite by powder metallurgy", *J. of Alloys and Compounds*, Vol. 386, pp. 177-181.
75. Jiang, Q.C., Wang, H.Y., Wang J.G., Guan, Q.F., Xu, C.L., (2003), "Fabrication of TiCp /Mg composites by the thermal explosion synthesis reaction in molten magnesium", *Mater. Letters*, Vol. 57, pp. 2580-2583.
76. Jiang, Q.C., Wang, H.Y., Wang, Y., Ma, B.X., Wang, J.G., (2005), "Modification of Mg<sub>2</sub>Si in Mg-Si alloys with yttrium", *Mater. Sci. and Engg. A*, Vol. 392, pp. 130-135.
77. Jin, I. and Lloyd, D. J., (1990), "Solidification of SiC Particulate Reinforced Al-Si Alloy Composites", Proc. Conf. in "Fabrication of Particulates Reinforced Metal Composites", Edited by Masounave, J. and Hamel, F. G., *Montréal, Québec, Canada*, 17-29 September, pp. 47-52.
78. Jokinen, A. and Anderson, P., (1990), "Tribological Properties of P/M Aluminium Alloy Matrix Composites", Annual Powder Metallurgy Cong., Proc., *American Powder Metallurgy Institute*, Princeton, N J, pp. 517-530.
79. Jombor, A., beyer, M., (1997), "Technical Report: New cars – new materials", *Materials & Design*, Vol. 18, Nos. 4/6, pp. 203-209.
80. Kanthal Handbook, "Appliance Heating Alloys", *Kanthal Lab*, Hallstahammer, Sweden.
81. Kevorkijan, V., Smolar, T., Jelen, M., (2003), "Fabrication of Mg-AZ80/SiC Composite Bars by Pressureless and Pressure-Assisted Infiltration", *American Ceramic Society Bulletin*, July, p. 9201.
82. Koczak, M. J. and Kumar, K. S., (1989), U. S. Patent No. 4, 808, 372.
83. Koczak, M. J. and Premkumer, M. K., (1993), "Emerging Technologies for the In-situ Production of MMCs", *JOM*, vol. 45, No.1, pp. 44-48.
84. Kothari, N.C., (1984), "Dispersion hardening by powder metallurgy", in G.S. Upadhyaya (ed.), *Sintered Metal-Ceramic Composites*, *Elsevier*, Amsterdam, pp. 71-85.

85. Krajewski, P.E., Allison, J.E., Jones, J.W., (1993), "The influence of matrix microstructure and particle reinforcement on the creep behavior of 2219 aluminum", *Metall. Trans. A*, Vol. 24A, pp. 2731-2741.
86. Krishnadev, M.R., Angers, R., Nair, C.G.K., Huard, G., (1993), *JOM*, Vol. 45, p. 52.
87. Kuruvilla, A. K., Prasad, K. S., Bhanuprasad, V. V. and Mahajan, Y. R., (1990), "Microstructure-Property Correlation in Al/TiB<sub>2</sub> (XD) Composites", *Scr. Metall. Materialia*, Vol. 24, pp. 879-883.
88. Kuruvilla, A.K., Prasad, K.S., Bhanuprasad, V.V., Mahajan, Y.R., (1990), "Microstructure-property correlation in Al/TiB<sub>2</sub> (XD) composites", *Scr. Metall. Materialia*, Vol. 24, pp. 873-878.
89. Laden, K., Guerin, J. D., Watremez, M. and Bricout, J. P., (2000), "Frictional Characteristics of Al-SiC Composite Brake Discs", *Tribology, Letters*, Vol. 8, pp. 237-247.
90. Laurent, V. Jarry, Regazzoni, G., (1992), "Processing, microstructure relationships in compocast magnesium/SiC", *J. of Mater. Sci.*, Vol. 27, pp. 4447-4459.
91. Lee, D.M., Suh, B.K., Kim, B.G., Lee, L.S., Lee, C.H., (1997), "Fabrication, microstructure, and tensile properties of magnesium alloy AZ91/SiC<sub>p</sub> composites produced by powder metallurgy", *Mater. Sci. and Tech.*, Vol. 13, p. 590.
92. Lee, Y.C., Dahle, A.K., StJon, D.H., (2000), "The Role of Grain Refinement of Magnesium", *Metall. and Mater. Trans.*, Vol. 31A, p. 2895
93. Leonard, A. J., Perrin, C. and Rainforth, W. M., (1997), "Microstructural Changes Induced by Dry Sliding Wear of a A357/SiC MMC", *Mater. Sci. and Tech.*, Vol. 13, pp. 41-48.
94. Lewis II, D., (1991) "In-situ Reinforcement of Metal Matrix Composites", In *Metal Matrix Composites: Processing and Interfaces (Treatise on Materials Science and Technology)*, Edited by Arsenault, R. J. and Everett, R. K., Chapter 6, *Academic press, Inc., U.S.A.*, Vol. 32, pp. 121-150.
95. Lim, C.Y.H., Leo, D.K., Ang, J.J.S., Gupta, M., (2005), "Wear of magnesium composites reinforced with nano-sized alumina particulates", *Wear*, Vol. 259, pp. 620- 625.
96. Lim, C.Y.H., Lim, S.C., Gupta, M., (2003), "Wear behaviour of SiC<sub>p</sub>-reinforced magnesium matrix composites", *Wear*, Vol. 255, pp. 629-637.
97. Lin, Y., Zee, R.H., Chin, B.A., (1991), "In situ formation of three-dimensional TiC reinforcements in Ti-TiC composites", *Metall. Trans. A*, Vol. 22A, pp. 859-865.

98. Liu, Y. B., Lim, S. C., Ray, S., and Rohatgi, P. K., (1992), "Friction and Wear of Aluminium-Graphite Composite: The Smearing Process of Graphite during Sliding", *Wear*, Vol. 159, pp. 201-205.
99. Liu, Y. B., Rohatgi, P. K., and Ray, S., (1993), "Tribological Characteristics of Aluminium-50 Vol. Pct. Graphite Composite", *Metall. Trans.*, Vol. 24A, pp. 151-159.
100. Lloyd, D.J., (1994), "Particle Reinforced Aluminium and Magnesium Matrix Composites", *International Materials Reviews*, Vol. 39, pp. 1-23.
101. Lu, L., Lai, M.O., Chen, F.L., (1997), "Al-4 wt% Cu composite reinforced with in-situ TiB<sub>2</sub> particles", *Acta Materialia*, Vol. 45, pp. 4297-4309.
102. Lu, L., Lai, M.O., Niu, X.P., Ho, H.N., (1998), "In-situ formation of TiB<sub>2</sub> reinforced aluminium via mechanical alloying", *Zeitschrift fur Metallkunde*, Vol. 89, pp. 567-572.
103. Lu, L., Lim, C.Y.H., Yeong, W.M., (2004), "Effect of reinforcements on strength of Mg-9%Al composites", *Composite Structures*, Vol. 66, pp. 41- 45.
104. Lu, L., Thong, K.K., Gupta, M., (2003), "Mg-based composite reinforced by Mg<sub>2</sub>Si", *Composites Sci. and Tech.*, Vol. 63, pp. 627-632.
105. Lu, Y.X., Bi, J., Li, D.X., Ping, D.H., Ma, Z.Y., Shen, H.W., (1992), in: C.T. Sun, T.T. Loo (Eds.), *Proceedings of the Second International Symposium on Composite Materials and Structures*, *Peking University Press*, Beijing, p. 882.
106. Luo, A., (1995), "Processing, microstructure and mechanical behaviour of cast magnesium metal matrix composites", *Metall. Mater. Trans.*, Vol. 26A, pp. 2445-2455.
107. Ma, B. X., Wang, H. Y., Wang, Y., Jiang, Q. C., (2005), "Fabrication of (TiB<sub>2</sub>-TiC)<sub>p</sub>/AZ91 magnesium matrix hybrid composite", *J. of Mater. Sci.*, pp. 4501- 4504.
108. Ma, Z. Y. and Tjong, S. C., (1997), "In-Situ Ceramic Particle-Reinforced Aluminum Matrix Composites Fabricated by Reaction Pressing in the TiO<sub>2</sub> (Ti)-Al-B (B<sub>2</sub>O<sub>3</sub>) Systems", *Metall. Mater. Trans. A*, Vol. 28A, pp. 1931-1942.
109. Ma, Z. Y., Li, J. H., Li, S. X., Ning, X. G., Lu, Y. X. and Bi, J., (1996), "Property-microstructure correlation in situ formed Al<sub>2</sub>O<sub>3</sub>, TiB<sub>2</sub> and Al<sub>3</sub> Ti mixture-reinforced aluminium composites", *J. of Mater. Sci.*, Vol. 31, pp. 741-747.
110. Ma, Z. Y., Li, J. H., Li, S. X., Ning, X. G., Lu, Y. X. and Bi, J., (1996), *J. of Mater. Sci.*, Vol. 31, pp. 741-748.
111. Ma, Z. Y., Li, J. H., Luo, M., Ning, X. G., Lu, Y. X. and Bi, J., (1994), "In-Situ Formed Al<sub>2</sub>O<sub>3</sub> and TiB<sub>2</sub> Particulates Mixture-Reinforced Aluminium Composite", *Scr. Metall. Materialia*, Vol. 31, No. 5, pp. 635-639.

112. Ma, Z. Y., Ning, X. G., Lu, Y. X., Bi, J. and L. S., (1994A), "In-situ Al<sub>4</sub>C<sub>3</sub> Dispersoid and SiC Particle Mixture-Reinforced Aluminium Composite", *Scr. Metall. et Materialia*, Vo. 31, No. 2, pp. 131-135.
113. Ma, Z.A., Li, J.H., Luo, M., Ning, X.G., Lu, Y.X., Bi, J., Zhang, Y.Z., (1994), "In-situ formed Al<sub>2</sub>O<sub>3</sub> and TiB<sub>2</sub> particulates mixture-reinforced aluminum composite", *Scr. Metall. et Materialia*, Vol. 31, pp. 635-639.
114. Ma, Z.Y., Ning, X.G., Lu, Y.X., Bi, J., Wen, L.S., Wu, S.J., Jangg, G., Daninger, H., (1994), "In-situ Al<sub>4</sub>C<sub>3</sub> dispersoid and SiC particle mixture reinforced aluminum composite", *Scr. Metall. et Materialia*, Vol. 31, pp. 131-135.
115. Maity, P. C. and Panigrahi, S. C., (1995), "Metal and Intermetallic Matrix In-Situ Particle Composites", *Key Engg. Mater.*, Vols. 104-107, pp. 313-328.
116. Maity, P. C., Chakraborty, P. N. and Panigrahi, S. C., (1994), "Preparation of Al-MgAl<sub>2</sub>O<sub>4</sub>-MgO in situ particle-composites by addition of MnO<sub>2</sub> particles to molten Al-2 wt% Mg alloys", *Materials Letters*, Vol. 20, pp. 93-97.
117. Maity, P. C., Chakraborty, P. N. and Panigrahi, S. C., (1995), "Processing and Properties of Al-Al<sub>2</sub>O<sub>3</sub> (TiO<sub>2</sub>) In-Situ Particle Composite" *J. Mater. Proc. Tech.*, Vol. 53, pp. 857-870.
118. Maity, P. C., Panigrahi, S. C. and Chakraborty, P. N., (1993), "Preparation of Aluminium-Alumina In-Situ Particle Composite by Addition of Titania to Aluminium Melt", *Scr. Metall. et Materialia*, Vol. 28, pp. 549-552.
119. Martin, J.W., (1980), "Micro-mechanism in Particle Hardened Alloys", *Cambridge University Press*, Cambridge.
120. Matin, M.A., Lu, L., Gupta, M., (2001), "Investigation of the reactions between boron and titanium compounds with magnesium", *Scr. Materialia*, Vol. 45, pp. 479-486.
121. Metals Handbook, (1990), "Properties and selection: nonferrous alloys and special-purpose materials", 10<sup>th</sup> Edition, Vol. 2, *ASM International*, Materials Park, OH, USA.
122. Mitra, R., Chiou, W.A., Weertman, J.R., Fine, M.E., Aikin R.M., Jr., (1991), "Relaxation mechanisms at the interfaces in XD Al/TiC<sub>p</sub> metal matrix composites", *Scr. Metall. et Materialia*, Vol. 25, pp. 2689-2694.
123. Mordike, B.L., Ebert, T., (2001), "Magnesium: Properties – applications – potential", *Mater. Sci. and Engg. A*, Vol. 302, pp. 37-45.
124. Munir, Z.A., Holt, J.B.,(1987), "The combustion synthesis of refractory nitrides- I. Theoretical analysis", *J. of Mater. Sci.*, Vol. 22, pp. 710-714.
125. Murthy, V.S.R., Rao, B.S., (1995), "Microstructural development in the directed melt-oxidized (DIMOX) Al-Mg-Si alloys", *J. of Mater. Sci.*, Vol. 30, pp. 3091-3097.

126. Muscat, D., Drew, R.A.L., (1994), "Modeling the infiltration kinetics of molten aluminum into porous titanium carbide", *Metall. and Mater. Trans. A*, Vol. 25A, pp. 2357-2370.
127. Nagata, S., (1975), "Mixing-Principles and Applications", *John Wiley & Sons*, New York (NY), pp. 250-252.
128. Nakamura, M., Kimura, K., (1991), "Elastic constants of  $TiAl_3$  and  $ZrAl_3$  single crystals", *J. of Mater. Sci.*, Vol. 26, pp. 2208-2214.
129. Nakata, H., Choh, T., Kanetake, N., (1995), "Fabrication and mechanical properties of in situ formed carbide particulate reinforced aluminium composite", *J. of Mater. Sci.*, Vol. 30, pp. 1719-1727.
130. Nayak, S.S., Murty, B.S., (2004) "Synthesis and stability of  $L1_2$ - $Al_3Ti$  by mechanical alloying", *Mater. Sci. and Engg. A*, Vol. 367, pp. 218-224.
131. Orowan, E. (1948), in: Symposium on Internal Stress in Metals and Alloys, *Institute of Metals*, London, p. 451.
132. Pan, Y. M., Fine, M. E. and Cheng, H. S., (1990), "Wear Mechanism of Aluminium-Based Metal Matrix Composites", Proc. Conf. In "Tribology of Composites Materials", Edited by Rohatgi, P. K., Balu, P. J., and Yust, C. S., *Oak Ridge, Tennessee*, pp. 93-101.
133. Peng Yu, Cheng-Ji Deng, Nan- Gang Ma, and Dickon H. L. Ng; (2004), " A New Method of Producing Uniformly Distributed Alumina Particles in Al-Based Metal Matrix Composite", *Mater. Letters.*, Vol. 58, pp. 679-682.
134. Perez, P., Garces, G., Adeva, P., (2004), "Mechanical properties of a Mg 10 (vol%)Ti composite", *Composite Science and Technology*, Vol. 64, pp. 145-151.
135. Peter, B. Madakson, (1983), "The Frictional Behavior of Materials", *Wear*, Vol. 87, pp. 191-206.
136. Philpot, K.A., Munir, Z.A., Holt, J.B., (1987), "An investigation of the synthesis of nickel aluminides through gasless combustion", *J. of Mater. Sci.*, Vol. 22, pp. 159-169.
137. Polmear, I.J., (1995), "Light alloys. Metallurgy of the light metals", 3<sup>rd</sup> Edition, *Arnold*, London, England.
138. Pramila, Bai B. N., Ramasesh, B. S., and Surappa, M. K., (1992), "Dry Sliding of A356-Al-SiC<sub>p</sub> Composites", *Wear*, Vol. 157, pp. 295-304.
139. Prasad, B.K., (1999), "Sliding Wear Response of Zn-Al Alloy as Affected by SiC Particle Dispersion and Test Conditions", *J. of Mater. Sci. Letters*, Vol. 18, pp. 1731-1734.

140. Prasad, B.K., (2002), "Influence of Some Test Parameters on Dry Sliding Wear Characteristics of a Zinc-11.5% Aluminium Alloy", *J. of Mater. Engg. and Performance*, Vol. 11, pp. 461-468.
141. Prasad, B.K., Singh, M., Mondal, D.P. and Jha, A.K., (2001), "Dry Sliding Wear Behaviour of an Aluminium Alloy-Granite Particle Composite", *Tribology International*, Vol. 43, pp. 557-567.
142. Prasad, P. R., Ray, S., Gaindhar, J. L. and Kapoor, M. L., (1982), "Microstructure and Mechanical Properties of Rheocast Al-10 wt% Cu Alloy", *Zeitschrift fur Metallkunde*, Vol. 73, pp. 420-429.
143. Prasad, S.V., Asthana, R., (2004), "Aluminum Metal Matrix Composites for Automotive Applications: Tribological Considerations", *Tribology Letters*, Vol.17, pp. 445.
144. Q.C. Jiang, B.X. Ma, H.Y. Wang, Y. Wang, Y.P. Dong, (2006) "Fabrication of steel matrix composites locally reinforced with in situ TiB<sub>2</sub>-TiC particulates using self-propagating high-temperature synthesis reaction of Al-Ti-B<sub>4</sub> C system during casting", *Composites: Part A*, Vol. 37, pp. 133-138.
145. Qin, Q.D., Zhao, Y.G., Liang, Y.H., Zhou, W., (2005), "Effects of melt superheating treatment on microstructure of Mg<sub>2</sub>Si/Al-Si-Cu composite", *J. of Alloys and Compounds*, Vol. 399, pp. 106-109.
146. Rabinowicz, E., (1977), "Proceedings of International Conference on Wear of materials", Louis, *ASME*, New York, pp. 36-40.
147. Rabinowicz, E., (1980), "Factors modifying the erosive wear equation for metals", *Israel J. of Technology*, Vol. 18, pp.193-197.
148. Rabinowicz, E., (1984), "The least wear", *Wear*, Vol. 100, pp. 533-541.
149. Rana, F. and Stefanescu, D. M., (1989), *Metall. Trans. A.*, Vol. 20A, pp. 1564-1566.
150. Ranganath, S., Vijayakumar, M., Subrahmanyam, J., (1992), "Combustion-assisted synthesis of Ti-TiB-TiC composite via the casting route", *Metall Trans. A*, Vol. 149A, pp. 253-257.
151. Ray S., (1969), *Master of Technology Dissertation*, "Fabrication of Aluminium-Alumina Composite by Foundry Method", Indian Institute of Technology Kanpur, Kanpur, India.
152. Ray, S., (1993), "Review Synthesis of Cast Metal Matrix Particulate Composites", *J. of Mater. Sci.*, Vol. 28, pp. 5397-5413.
153. Ray, S., (1995), "Casting of Metal Matrix Composites", *Key Engg. Mater.*, Vol. 104-107, pp. 417-446.

154. Ray, S., Daniel, B.S.S. and Sivalingappa, D., (2007), Indian patent ( Patent application No. 1384/DEL/2007), "An improved process for preparation of Magnesium based composite and an improved magnesium based *in-situ* composite".
155. Razavizadeh, K., and Eyre, T. S., (1982), "Oxidative Wear of Aluminium Alloys", *Wear*, Vol. 79, pp. 325-333.
156. Richardson, J. F., and Zaki, W. N., (1954), "Sedimentation and Fluidisation, Part I", *Trans. Instit. Chem. Engrs.*, Vol. 32, p. 3.
157. Rohatgi, P. K., (1995), "Future Directions in Solidification of Metal Matrix Composites", *Key Engg. Mater.*, Vols. 104-107, pp. 293-312.
158. Rohatgi, P. K., Asthana, R., and Das, S., (1986), "Solidification Structure and Properties of Cast Metal-Ceramic Particle Composites", *International Metals Review*, Vol. 31, No. 3, pp. 115-139.
159. Rohatgi, P. K., Liu, Y. and Ray, S., (1992), "Friction and Wear of Metal-Matrix Composites", *ASM Handbook*, Edited by Scott, D. Henry, Vol. 18, pp. 802-811.
160. Roy, M., Venkataraman, B., Bhanuprasad, V., Mahajan, Y. R. and Sundararajan, G., (1992), "The effect of Particulate Reinforcement on the Sliding Wear Behaviour of Aluminium Matrix Composites", *Metall. Trans.*, Vol. 23A, pp. 2833-2847.
161. Sahay, S.S., Ravichandran, K.S., Atri, R., Chen, B., Rubin, J., (1999), "Evolution of microstructure and phases in in situ processed Ti-TiB composites containing high volume fractions of TiB whiskers", *J. of Mater. Research*, Vol. 14, pp. 4214-4223.
162. Sahoo, P., Koczak, M.J., (1991), "Microstructure-property relationships of in situ reacted TiC/Al-Cu metal matrix composites", *Mater. Sci. and Engg. A*, Vol. A131, pp. 69-76.
163. Sampath, S. Khatri, E. Shtessel, M.J. Koczak, in: V.A. Ravi, T.S. Srinivatsan (Eds.), *Processing and Fabrication of Advanced Materials for High Temperature Applications II*, TMS, Warrendale, PA, 1993, p. 223.
164. Sannino A. P. and Rack, H. J., (1995 A), "Surface Topography Evolution During Sliding Wear of 2009 Al-SiCp/17-4 PH", *Proc. Int. Conf. in Wear of Materials*, Boston, *Wear*, Vol.181-183, pp. 202-211.
165. Sannino, A. P. and Rack, H. J., (1995B), "Dry Sliding Wear of Discontinuously Reinforced Aluminum Composites: Review and Discussion", *Wear*, Vol.189, pp. 1-19.
166. Saravanan, R.A., Surappa, M.K., (2000), "Fabrication and characterization of pure magnesium-30 vol% SiC<sub>p</sub> particle composite", *Mater. Sci. and Engg. A*, Vol. 276, pp. 108-116.
167. Sarkar, A. D., (1980), "Friction and wear", *Academic Press Inc.*, London, Great Britain.



168. Sato, A. and Mehrabian, R., (1976), "Aluminium Matrix Composites: Fabrication and Properties", *Metall. Trans.*, Vol. 7B, pp. 443-451.
169. Serikawa, T., Henmi, M., Yamaguchi, T., Oginuma, H., Kondoh, K., (2006), "Depositions and microstructures of Mg-Si thin film by ion beam sputtering", *Surface & Coatings Tech.*, Vol. 200, pp. 4233-4239.
170. Sharma, S.C., Anand, B., Krishna, M., (2000), "Evaluation of sliding wear behaviour of feltspar particle-reinforced magnesium alloy composites", *Wear*, Vol. 241, pp. 33- 40.
171. Sin, H. C., Saka, N. and Suh, N. P., (1979), "Abrasive Wear Mechanisms and Grit Size effect", *Wear*, Vol. 55, pp. 163-190.
172. Sprigg's, R.M., (1961), *J. of American Ceramics Society*, Vol. 44, pp. 628-629.
173. Srikanth, N., Zhong, X.L., Gupta, M., (2005), "Enhancing damping of pure magnesium using nano-size alumina particulates", *Mater. Letters*, Vol. 59, pp. 3851-3855.
174. Standard terminology related to erosion and wear, Annual Book of Standards, Vol. 3.02, *ASTM*, Philadelphia, PA, 1993.
175. Stefanescu, D. M., and Dhindaw, B. K., (1988), "Behavior of Ceramic Particles at the Solid-Liquid Metal Interface in Metal Matrix Composites", *Principles of Solidification, Metals Handbook, ASM International*, Vol. 15, pp. 142-147.
176. Stefanescu, D. M., Dhindaw, B. K., Kacar, S. A., and Moitra, (1988), "Behavior of Ceramic Particles at the Solid-Liquid Metal Interface in Metal Matrix Composites", *Metall. Trans. A*, Vol. 19A, pp. 2847-2855.
177. Straffelini, G., Bonollo, F., Molinari, A. and Tiziani, A., (1997), "Influence of Matrix Hardness on the Dry Sliding Behaviour of 20 vol% Al<sub>2</sub>O<sub>3</sub> Particulate Reinforced 6061 Al Metal Matrix Composite", *Wear*, Vol. 211, pp. 192-197.
178. Suh, N. P., (1977), "An Overview of the Delamination Theory of Wear", *Wear*, Vol. 44, pp. 1-16.
179. Suh, N. P., (1986), "Tribophysics", *Prentice-Hall, Inc., A Division of Simon and Schuster Englewood Cliffs*, New Jersey, USA, pp.
180. Suh, N.P. and Sin, H.C., (1981), "The genesis of friction", *Wear*, Vol. 69, pp. 91-114.
181. Suh, N.P., (1973), "The delamination theory of wear", *Wear*, Vol. 25, No. 1, pp.111-124.
182. Surappa M. K. and Rohatgi P. K., (1978), "Technical Note", "Production of Aluminium-Graphite Composites Using Copper-Coated Graphite particles", *Metal Tech.*, pp. 358-361.
183. Surappa, M. K., Prasad, S. V. and Rohatgi, P. K., (1982), "Wear and Abrasion of Cast Al-Alumina Particle Composites", *Wear*, Vol. 77, pp.295-301.

184. Surappa, M.K., (1997), "Microstructure evolution during solidification of DRMMCs discontinuously reinforced metal matrix composites: state of art", *J. of Mater. Processing Tech.*, Vol. 63, pp. 325-333.
185. Surappa, M.K., Blank, E., Jaquet, J.C., (1986), "Effect of macro-porosity on the strength and ductility of cast Al-7Si-0.3Mg alloy", *Scr. Metall.*, Vol. 20, pp. 1281-1286.
186. Taheri-Nassaj, E., Kobashi, M., Choh, T., (1996), "Fabrication and analysis of an in situ TiB<sub>2</sub>/Al composite by reactive spontaneous infiltration", *Scr. Mater.*, Vol. 34, pp. 1257-1265.
187. Taheri-Nassaj, E., Kobashi, M., Choh, T., (1997), "Fabrication and analysis of in situ formed boride/Al composites by reactive spontaneous infiltration", *Scr. Mater.*, Vol. 37, pp. 605-614.
188. Thakur, S.K., Dhindaw, B.K., (2001), "The influence of interfacial characteristics between SiC<sub>p</sub> and Mg/Al metal matrix on wear, coefficient of friction and microhardness", *Wear*, Vol. 247, pp. 191-201.
189. Tjong, S.C., Ma, Z.Y., (2000), "Microstructural and mechanical characteristics of in situ metal matrix composites". *Mater. Sci. and Engg. A*, Vol. 29, pp. 49-113.
190. Tjong, S.C., Wang, G.S., Mai, Y.W., (2003), "Low-cycle fatigue behavior of Al-based composites containing in situ TiB<sub>2</sub>, Al<sub>2</sub>O<sub>3</sub> and Al<sub>3</sub>Ti reinforcements", *Mater. Sci. and Engg. A*, Vol. 358, pp. 99-106.
191. Tsang, H.T., Chao, C.G., Ma, C.Y., (1996), "In situ fracture observation of a TiC/Ti MMC produced by combustion synthesis", *Scr. Mater.*, Vol. 35, pp. 1007-1012.
192. Tsang, H.T., Chao, C.G., Ma, C.Y., (1997), "Effects of volume fraction of reinforcement on tensile and creep properties of in-situ TiB/Ti MMC", *Scr. Mater.*, Vol. 37, pp. 1359-1365.
193. Tsuzuki, R., Kondoh, K., (2004), "In-situ solid-state synthesis of Mg composite with Mg<sub>2</sub>Si dispersoids", *The Fifth Pacific Rim International Conference on Advanced Materials and Processing*, November 2-5, Beijing, China.
194. Vardavoulias, M., Jouannt-Tresy C. and Jeandin M., (1993), "Sliding-Wear Behaviour of Ceramic Particle-Reinforced High-Speed Steel Obtained by Powder Metallurgy", *Wear*, Vol. 165, pp. 141-149.
195. Venkataraman, B. and Sundararajan, G., (1996), "Sliding wear behaviour of Al-SiC particulate composites – II: The characterization of subsurface deformation and correlation with wear behaviour", *Acta Materialia*, Vol. 44, pp. 461-467.
196. Videm, M., Hansen, R.S., Tomac, N., Tonnesen, K., (1994) "Metallurgical Considerations for Machining Magnesium Alloys", SAE Transactions, *J. of Mater. and Manf.*, Vol. 103, pp. 213-220.

197. Vijayamohan, V., Gopalakrishna, V., (1996), "Technology for magnesium metal matrix composites", *Indian Foundry Journal*, pp. 5-9.
198. Vyletel, G.M., Aken, D.C.V., Allison, J.E., (1991), "Effect of microstructure on the cyclic response and fatigue behavior of an XD aluminum metal matrix composite", *Scr. Metall. et Materialia*, Vol. 25, pp. 2405-2410.
199. Vyletel, G.M., Allison, J.E. Aken, D.C.V., (1995), "Effect of matrix microstructure on cyclic response and fatigue behavior of particle-reinforced 2219 aluminum: Part I. Room temperature behavior", *Metall. Tran. A*, Vol. 26A, pp. 3143-3154.
200. Vyletel, G.M., Allison, J.E., Aken, D.C.V., (1993), "The influence of matrix microstructure and TiC reinforcement on the cyclic response and fatigue behavior of 2219 Al", *Metall. Trans. A*, Vol. 24A, pp. 2545-2557.
201. Wang, A. and Rack, H. J., (1991), "Transition Wear Behaviour of SiC-Particulate and SiC-Whisker-Reinforced 7091 Al MMCs", *Mater. Sci. Engg.*, Vol. A147, pp. 211-224.
202. Wang, H.Y., Jiang Q.C., Wang, Y., Ma, B.X. Zhao, F., (2004), "Fabrication of TiB<sub>2</sub> particulate reinforced magnesium matrix composites by powder metallurgy", *Materials Letters*, Vol. 58, pp. 3509-3513.
203. Wang, H.Y., Jiang Q.C., Wang, Y., Ma, B.X.. Zhao, F., (2004), "Fabrication of TiB<sub>2</sub> particulate reinforced magnesium matrix composites by powder metallurgy", *Materials Letters*, Vol. 58, pp: 3509-3513.
204. Wang, H.Y., Jiang, Q.C., Li, X.L., Zhao, F., (2004), "Effect of Al content on the self-propagating high-temperature Synthesis reaction of Al-Ti-C system in molten magnesium", *J. of Alloys and Compounds*, Vol. 366, pp. L9-L12.
205. Wang, H.Y., Jiang, Q.C., Li, X.L., Zhao, F., (2004), "Effect of Al content on the self-propagating high-temperature Synthesis reaction of Al-Ti-C system in molten magnesium", *J. of Alloys and Compounds*, Vol. 366, pp. L9-L12.
206. Wang, H.Y., Jiang, Q.C., Zhao, Y.G., Zhao, F., (2004), "In situ synthesis of TiB<sub>2</sub>/Mg composite by self-propagating high-temperature synthesis reaction of the Al-Ti-B system in molten magnesium", *J. of Alloys and Compounds*, Vol. 379, pp. L4-L7.
207. Wang, H.Y., Jiang, Q.C., Zhao, Y.Q., Zhao, F., Ma, B.X., Wang, Y., (2005), "Fabrication of TiB<sub>2</sub> and TiB<sub>2</sub>-TiC particulates reinforced magnesium matrix composites", *Mater. Sci. Engg.,A* Vol. 372, pp. 109-114.
208. Wang, L., Niinomi, M., Takahashi, S., Hagiwara M., Emura, S., Kawabei, Y., Kim, S.J., (1999), "Relationship between fracture toughness and microstructure of Ti-6Al-2Sn-4Zr-2Mo alloy reinforced with TiB particles", *Mater. Sci. Engg., A*, Vol. A263, pp. 319-325.
209. Wang, X., Jha, A., Brydson, R., (2004), "In situ fabrication of Al<sub>3</sub>Ti particle reinforced aluminium alloy metal-matrix composites", *Mater. Sci. Engg., A*, Vol. 364, pp. 339-345.

210. Wang, X., Jha, A., Brydson, R., (2004), "In situ fabrication of Al<sub>3</sub>Ti particle reinforced aluminium alloy metal-matrix composites", *Mater. Sci. Engg., A*, Vol. 364, pp. 339-345.
211. Wang, Yan; Wang, Hui-Yuan; Xiu, Kun; Wang, Hong-Ying; Jiang, Qi-Chuan, (2006), "Fabrication of TiB<sub>2</sub> particulate reinforced magnesium matrix composites by two-step processing method", *Mater. Letters*, Vol. 60, pp. 1533-1537.
212. Wang, Yan; Wang, Hui-Yuan; Xiu, Kun; Wang, Hong-Ying; Jiang, Qi-Chuan, (2006), "Fabrication of TiB<sub>2</sub> particulate reinforced magnesium matrix composites by two-step processing method", *Mater. Letters*, Vol. 60, pp. 1533-1537.
213. Weiss, H., (1971), "Electromagnetic Properties of Eutectic Composites", *Metall. Trans.*, Vol. 2, pp. 1513-1521.
214. Westwood, A. R. C. and Winzer S. R., (1987), in : P. A. Psaras, edited by Langford H. D., *Advanced Materials Research, National Academy Press*, Washington, DC, pp. 225-226.
215. Wilson, S. and Alpas, A. T., (1997), "Wear Mechanism Maps for Metal Matrix Composites", *Wear*, Vol. 212, pp. 41-49.
216. Wood, J.V., Davies, P., Kellie, J.L.F., (1993), "Properties of reactively cast aluminium-TiB<sub>2</sub> alloys", *Mater. Sci. Tech.*, Vol. 9, pp. 833-840.
217. Xi, Y.L., Chai, D.L., Zhang, W.X., Zhou, J.E., (2006), "Titanium alloy reinforced magnesium matrix composite with improved mechanical properties", *Scr. Mater.*, Vol. 54, pp. 19-23.
218. Xing, Z. P. Dai, J.Y. Guo, J.T. An, G.Y. and Hu, Z.O., (1994), "Compression Behaviour and Interfaces of NiAl-TiB<sub>2</sub> In-situ Composites", *Scr. Metall. et Materialia*, Vol. 31, No. 9, pp. 1141-1144.
219. Y. Miyamoto, K. Hirao, M. Koizumi, in: Proceedings of the International Symposium on Fundamental Research Strategy in Development of New Materials for Efficient Energy Conversion, Osaka, 1987.
220. Yarandi, F. M., Rohatgi P. K. and Ray, S., (1992), "The Phase Flow Behaviour and Microstructure in Aluminium Alloys-SiC Particulate Reinforced Composites", Proc. Conf. in "Semi-Solid Alloys and Composites", MIT, U.S.A., pp. 447-465.
221. Yen B. K. and Ishiharas, T., (1996), "Effect of humidity on Friction and Wear of Al-Si Eutectic Alloy and Al-Si-Graphite Composites", *Wear*, Vol. 198, No. 1-2, pp. 169-175.
222. Yen, B. K., (1997), "The Effect of Humidity on Friction and Wear of an Aluminium-Silicon Eutectic Alloy", *J. of Mater. Sci.*, Vol. 32, pp. 821-828.
223. Zam Zam, M. A., (1989), *Metalwissenschaft Technik*, Vol. 43, pp. 1158-1161.

224. Zhang, E., Zeng, S., Yang, B., Li Q., Ma, M., (1999A), "A Study on the Kinetic Process of Reaction Synthesis of TiC: Part I. Experimental Research and Theoretical Model", *Metall. and Mater. Trans.*, Vol. 30A, p. 1147.
225. Zhang, E., Zeng, S., Yang, B., Li Q., Ma, M., (1999B), "A Study on the Kinetic Process of Reaction Synthesis of TiC: Part II. Theoretical Analyses and Numerical Calculation", *Metall. and Mater. Trans.*, Vol. 30A, p. 1153.
226. Zhang, X., Wang, H., Liao, L., Teng, X., Ma, N., (2005), "The mechanical properties of magnesium matrix composites reinforced with (TiB<sub>2</sub> + TiC) ceramic particles", *Mater. Letters*, Vol. 59, pp. 2105-2109.
227. Zhao, Y.G., Qin, Q.D., Zhao, Y.Q., Liang, Y.H., Jiang Q.C., (2004), "In situ Mg<sub>2</sub>Si/Al-Si composite modified by K<sub>2</sub>TiF<sub>6</sub>", *Mater. Letters*, Vol. 58, pp. 2192-2194.